

Solidification Microstructure Simulation of Ti6Al4V in Laser Wire Deposition Additive Manufacturing

by

Jinghao Li

Doctor of Philosophy

Department of Mechanical Engineering

Faculty of Engineering

McGill University, Montreal

2021 October

A thesis submitted to McGill University in partial fulfillment of the requirements of the degree of
Doctor of Philosophy

© **Jinghao Li**

Abstract

Metal additive manufacturing (MAM) technology is now changing the pattern of the high-end manufacturing industry, among which microstructure simulation gradually shows its importance and attracts many research interests. Until today, the simulation of solidification microstructure in MAM remains challenging because of the complex solidification conditions. This research develops a data-driven model to investigate the competitive grain growth behaviour and a novel method to quantitatively simulate the topology structures of the columnar grains in laser wire directed energy deposition (DED) fabricated Ti6Al4V.

With a thorough review of the literature, the development of existing solidification microstructure simulation methods as well as their capacity and applicability on MAM are discussed. Traditional solidification microstructure simulation methods all have their merits as well as drawbacks when applied in MAM processes. To fill the gaps in the rapid solidification theory, a data-driven approach is developed to analyze the anisotropic grain growth effect under a rapid directional solidification condition in laser wire DED fabricated Ti6Al4V. A series of laser wire DED, optical microscope, and electron backscatter diffraction (EBSD) experiments were carried out under the experimental design to gather the training and testing data for the artificial neural network (ANN), which is used as an engine to predict the transient grain boundary angles. After parameter tuning and model testing, the strategy and ANN model developed in this work is demonstrated to be an efficient way to describe the competitive grain growth behaviour in laser wire DED fabricated Ti6Al4V. In conjunction with the regression relation found by the ANN, a deterministic solidification microstructure simulation model named the “invasion model”, is established to avoid the essential defects of traditional methods, such as the high computational cost and the handling of rapid solidification phenomena. This model focuses on the interaction between the neighbouring bi-crystals instead of simulating the growth kinetics of each columnar grain or deriving the field form of

variables. Within a bi-crystal system, the grain boundary tilt from the vertical direction of solidification front is understood as a transient invasion behaviour of one grain to another, and the competitive grain growth behaviour along the buildup process of MAM is an accumulation of all the invasions in bi-crystal systems. Laser wire DED fabricated Ti6Al4V thin wall samples with full dendritic columnar grains (prior beta) are used as a benchmark to test the validation of the novel simulation model. The grain structure of reconstructed prior beta grains along the build-up direction has a good agreement with the simulation result which shows the unique capabilities of the invasion model compared to the traditional ones. In the end, the crystal (prior beta grain) introducing mechanism in laser wire DED fabricated Ti6Al4V is investigated. Recrystallization is found to be the main reason that introduces new crystals into the printing domain and influences the resultant solidification microstructure. The formation tendency of the early-stage recrystallized grain indicates its strong dependency on the grain boundary alpha phase. Some of the recrystallized grains are able to participate in the following competitive grain growth, thus influencing the solidification microstructure in the fabricated part dramatically.

Résumé

La technologie de fabrication additive métallique (MAM) change l'industrie de fabrication de pointe, incluant l'adoption d'outils de simulation de microstructure progressivement démontre son importance et par le fait même le nombre de travaux de recherche. Jusqu'à aujourd'hui, la simulation de la microstructure lors de solidification dans MAM reste difficile en raison des conditions de solidification complexes. La présente recherche est basé sur le développement d'un modèle pour étudier le comportement compétitif de croissance des grains et inclut une nouvelle méthode pour simuler quantitativement les structures topologiques des grains colonnaires dans une structure Ti6Al4V produite par dépôt d'énergie dirigée (DED) au fil.

Suite à une revue approfondie de la littérature, le développement de méthodes de simulation de microstructure de solidification existantes ainsi que leurs capacités et applicabilités sur MAM sont discutées. Les méthodes traditionnelles de simulation de microstructure de solidification possèdent des avantages et inconvénients lorsqu'elles sont appliquées aux procédés MAM. Pour combler les lacunes émergeant de la théorie de la solidification rapide, une approche basée sur les données est développée pour analyser l'effet de croissance anisotrope des grains dans des conditions de solidification directionnelle rapide pour le DED laser fil du Ti6Al4V. Une série d'expériences de DED laser au fil, de microscopie optique et de diffraction par rétrodiffusion d'électrons (EBSD) ont été menées selon un plan d'expérience pour rassembler une base de données pour entraîner et tester un réseau de neurones artificiels (ANN), outil utilisé pour prédire l'angle de transition des joints de grains. Suite au réglage des paramètres et des tests du modèle, la stratégie et le modèle ANN développés dans ce travail s'avèrent être un moyen efficace pour décrire le comportement compétitif de croissance des grains dans le DED laser fil du Ti6Al4V. En conjonction avec la relation de régression trouvée par l'ANN, un modèle de simulation de microstructure de solidification déterministique nommé « modèle d'invasion », fut établi pour éviter les limites

essentielles des méthodes traditionnelles, tels que le coût de calcul élevé et la gestion des phénomènes de solidification rapide. Ce modèle se concentre sur l'interaction entre les bi-cristaux voisins au lieu de simuler la cinétique de croissance de chaque grain colonnaire ou de dériver la forme de champ des variables. Dans un système bicristallin, l'inclinaison des joints de grains par rapport à la direction verticale du front de solidification est considérée comme un comportement d'invasion transitoire d'un grain à un autre, et le comportement compétitif de croissance des grains le long du processus d'accumulation de MAM est une accumulation de toutes les invasions. Des échantillons à paroi mince de Ti6Al4V fabriqués par DED laser fil avec des grains colonnaires dendritiques complets (pré-bêta) sont utilisés comme référence pour tester la validation du nouveau modèle de simulation. La structure des grains pré-bêta reconstruits le long de la direction de fabrication présente une bonne symétrie avec le résultat de la simulation, qui démontre les capacités uniques du modèle d'invasion par rapport aux modèles traditionnels. Finalement, le mécanisme d'invasion du cristal (grain pré-bêta) dans le DED laser fil pour le Ti6Al4V est étudié. La recristallisation s'avère être la principale raison qui germe de nouveaux cristaux dans la structure imprimée et influence la microstructure de solidification résultante. La formation de grain recristallisé à un stade hâtif indique sa forte dépendance à la phase alpha au joint de grain. Certains des grains recristallisés sont capables de participer à la croissance compétitive des grains subséquent, influençant ainsi considérablement la microstructure de solidification dans la pièce fabriquée.

Acknowledgment

Foremost, I would like to express my deepest gratitude to my supervisor Prof. Yaoyao Fiona Zhao for her unlimited support, trust, and encouragement throughout my Ph.D. program. Her insight and knowledge in this field have steered me through this research. As a scientist, her serious work and dedication as well as her professional attitude will always be the role model for my research career in the future.

I would also like to acknowledge my co-supervisor and good friend Prof. Mathieu Broch, who is always available for support and guidance. Thank you, “M”, for your help and for carrying the research forward. I want to thank Prof. Xianglin Zhou for his continuous guidance throughout my research career. The collaboration on multiple topics broads my mind and enables me to see the problems at a higher level.

Many thanks to all my lab-mates at Additive Design and Manufacturing Lab for sharing their experiences, the scientific discussion, their timely help, and their suggestions for my projects.

I would also like to thank Prof. JY Hascoët for sharing the powder DED equipment and the inspiration for understanding the transport phenomena in the melt pool. I would like to thank Prof. Nikolas Provatas for the fruitful discussion in terms of phase field simulations. I would like to give my special thanks to Liburdi Automation Weld Lab, especially to Dr. Nejib Chekir and Mr. JJ Sixsmith. Without your continuous support, it is impossible to enclose this research. I’m grateful to Materials and Characterization Laboratories and McGill Institute for Advanced Materials of McGill. I thank Stéphanie and Nicolas at the Facility for Electron Microscopy Research of McGill University for the help in microscope operation and data collection who have always been professional, supportive, and open to discussions.

I would like to thank my parents Maodong Li and Huaping Chen for their unwavering support. I thank my girlfriend Dr. Yuan Yao for being aside and cheering me up. Also, my best friend Jason, thank you for the

company and the happiness you brought to me even during the pandemic time. Thanks to Covid or this thesis should be finished half-year earlier.

Last but not least, I would like to thank the Natural Sciences and Engineering Research Council of Canada (NSERC) Collaborative Research and Development Grant CRDPJ 479630-15, the NSERC Collaborative Research and Training Experience (CREATE) Program Grant 449343 for funding this research, as well as McGill Engineering Doctoral Award (MEDA) grant and China Scholarship Council (201706460027).

Claim of Originality

The author claims the originality of the main ideas and results reported in this thesis. Major contributions from this thesis are listed as the following:

- It analyzes the merits and drawbacks of existing solidification microstructure simulation methods when applied in MAM cases.
- It introduces a novel solidification microstructure simulation method, called the “invasion model”, to the community to quantitatively simulate the solidification microstructure in wire DED processed Ti6Al4V.
- It establishes a unique database for the competitive grain growth behaviour of the columnar prior beta grains in wire DED fabricated Ti6Al4V.
- For the first time, the prior beta grain structure of DED fabricated Ti6Al4V is compared quantitatively with the experimental result. This also approved the validation of the “invasion model”.
- It investigates the recrystallization behaviour of the prior beta grains during the deposition process of laser wire DED process.

Some contents of this thesis have been published in some journal and conference articles. The abstracts of these papers are listed in Appendix.

List of Abbreviations

AM	Additive Manufacturing
ANN	Artificial Neural Network
ASTM	American Society for Testing and Materials
BCC	Body Centred Cubic
BOR	Burgers Orientation Relation
CA	Cellular Automata
CET	Columnar to Equiaxed Transition
CFD	Computational Fluid Dynamics
CNT	Classical Nucleation Theories
CPU	Central Processing Unit
DED	Directed Energy Deposition
DNN	Dendritic Needle Network
EBSD	Electron Backscatter Diffraction
EBSM	Electron Beam Selective Melting
EDX	Energy Dispersive X-ray Spectroscopy
FCC	Face Centred Cubic
FEM	Finite Element Method
FIB	Focused Ion Beam
G	Thermal Gradient
GL	Geometrical Limit
GPU	Graphics Processing Units
HCP	Hexagonal Close-Packed
KAM	Kernel Average Misorientation
KMC	Kinetic Monte Carlo
LENS	Laser Engineered Net Shaping
MAM	Metal Additive Manufacturing
MC	Monte Carlo
ML	Machine Learning
MSE	Mean Squared Error
PBF	Powder Bed Fusion
PF	Phase Field
PFC	Phase Field Crystal
PSP	Process-Structure-Property
R	Solidification Rate
ReLU	Rectified Linear Unit
SEM	Scanning Electron Microscope
SLM	Selective Laser Melting
SVM	Support Vector Machines
XPS	X-Ray Photoelectron Spectroscopy

Table of Contents

Abstract.....	II
Résumé.....	IV
Acknowledgment	VI
Claim of Originality	VIII
List of Abbreviations	IX
Table of Contents	X
List of Figures	XIV
List of Tables	XVIII
Chapter 1. Introduction and motivations	1
1.1. Metal additive manufacturing	1
1.2. Solidification in metal additive manufacturing.....	3
1.2.1 Nucleation v.s. epitaxial grain growth	4
1.2.2 Grain Growth	6
1.3. General Microstructural Features in MAM.....	12
1.3.1. Columnar Grain, Texture and Anisotropy	12
1.3.2. Hierarchical Phase Composition.....	15
1.4. Metallurgy of MAM Ti6Al4V	17
1.5. Fundamentals of Machine Learning and Application in MAM.....	20
1.6. Research objectives	23
1.7. Thesis organization	24
Chapter 2. Literature review	25
2.1. Introduction	25
2.2. Current Solidification Microstructure Simulation Methods in MAM	25

2.2.1. Cellular Automata (CA) Method	33
2.2.2. Phase Field (PF) Method	37
2.2.3. Monte Carlo Method.....	40
2.2.4. Needle-Network Method	42
2.3. Discussion and Perspectives.....	42
2.4. Chapter summary	48
Chapter 3. The proposed methodological framework	50
Chapter 4. Machine Learning-Enabled Competitive Grain Growth Behavior Study in Laser Wire DED Fabricated Ti6Al4V	55
4.1. Introduction	55
4.2. Methodology	55
4.3. Experimental Data Gathering.....	62
4.4. Artificial Neural Network and Results.....	73
4.5. Chapter Summary.....	79
Chapter 5. Deterministic modelling of solidification microstructure formation in laser wire DED fabricated Ti6Al4V	80
5.1. Introduction	80
5.2. Solidification Background.....	80
5.2.1. Dendritic Columnar Grains.....	83
5.2.2. Nucleation and epitaxial grain growth.....	84
5.2.3. Preferred grain growth direction and grain selection mechanism	85
5.3. Crystal orientations	90
5.4. Local Solidification Condition.....	90
5.5. Grain Boundary Invasion	95
5.6. Model Verification.....	97
5.7. Experimental Validation	100

5.7.1.	Characterizations of microstructures	101
5.7.2.	Grain boundary extraction & grain topological structure reconstruction	103
5.7.3.	Transient Melt Pool Geometry Attributes.....	105
5.8.	Results and discussion.....	109
5.9.	Conclusions	113
Chapter 6.	Crystal Introducing Mechanism in Laser Wire DED fabricated Ti6Al4V	114
6.1.	Introduction	114
6.2.	Nucleation in MAM solidification microstructure models	117
6.3.	Experimental Methods	119
6.3.1.	Laser wire DED fabricated Ti6Al4V thin wall structure.....	119
6.3.2.	Experimental design.....	124
6.3.3.	Solidification microstructure and grain size analysis	127
6.4.	Results	132
6.4.1.	Contamination (gas impurities of oxygen, nitrogen)	132
6.4.2.	Early stage of crystallization at the grain boundary, 3D tomography analysis and chemical composition (segmentation).....	136
6.4.3.	Validation on a single beta grain substrate	141
6.5.	Conclusions	143
Chapter 7.	Conclusions and future research	144
7.1.	Conclusions	144
7.2.	Future Research.....	147
References.....		149
APPENDIX I: Lists of publications.....		165
Journal papers.....		165
Publication under review or revision		166

Peer-reviewed conference papers	166
APPENDIX II : Abstract of major journal publications	167
Journal publication D1	167
Journal publication D2	168
Journal publication D3	169

List of Figures

Figure 1-1 (a) LAWS 1000 automated welding system (Liburdi) (b) schematic diagram of a gantry front feed laser wire DED process [8]	2
Figure 1-2 Basic solidification modes (observed in carbon tetrabromide): (a) planar solidification; (b) cellular solidification; (c) columnar dendritic solidification; (d) equiaxed dendritic solidification.	7
Figure 1-3 Effect of temperature gradient G and growth rate R on the morphology and size of solidification microstructure (left). Variation in solidification mode across the fusion zone (right) [18].	8
Figure 1-4 A solidification map using Ti6Al4V as an example highlighting the grain type dominating under varying regimes of solidification front velocity and temperature gradient across the solidification front [19].	9
Figure 1-5 Effect of constitutional supercooling on solidification mode: (a) planar; (b) cellular; (c) columnar dendritic; (d) equiaxed dendritic (S, L, and M denote solid, liquid, and mushy zone, respectively) [18].	11
Figure 1-6 Schematic diagram of the grain growth mechanism of Ti–8.5Cu and Ti6Al4V alloys. TA is the profile of the temperature of the melt and TE is the profile of the equilibrium liquidus temperature [22].	11
Figure 1-7 Column grains in Ti6Al4V parts produced by (a) DED [35] (b) SLM [36] (c) Gas Tungsten Arc Welding (GTAW) [29]; (d) Column grains in Inconel 718 parts produced by DED [37] (e) SLM [38] (f) Electron beam smelting layered solidification [39] (g) Column grains in 316L parts produced by DED [40] (h) SLM [41] (i) EBSM [42]	13
Figure 1-8 (a) Simulated temperature profile and thermal gradient versus deposited time of DED fabricated part; (b) Simulated temperature profile and the measured temperature versus deposited time at different locations [54].	16
Figure 1-9 Microstructural evolution map of Ti6Al4V fabricated by DED as each layer is deposited (reproduced from [44, 55, 56]).	17
Figure 1-10 Phase Composition of Ti6Al4V fabricated by DED: (a-b) Micrographs of macrostructure and fine microstructure of DED sample [78]	19
Figure 2-1 An example of 2D microstructure simulation using CA method: (a) SLM process which involves multiple layers of material deposited on a polycrystalline substrate (b) Schematic of single dendritic grain growth in the melt (left) and its CA representation (right). [112]	35

Figure 2-2 PF simulation on dendrite morphology evolution along with solidification time, colours indicate dendrites with different crystal orientations. [154]	39
Figure 2-3 KMC simulation of grain structures in a weld with different scanning speeds. [170].....	41
Figure 3-1 Framework of the solidification microstructure simulation of Ti6Al4V in laser wire DED ..	50
Figure 3-2 Flow chart of the microstructure simulation for Ti6Al4V in laser wire DED applying invasion model.....	51
Figure 4-1 Flow chart of the methodology of the ANN model establishment for X-Z plane	57
Figure 4-2 Local solidification condition for a bi-crystal system in MAM.....	58
Figure 4-3 Comparison between the experimental melt pool bottom geometry (red) and the analytical solution (blue) in the Y-Z plane.....	59
Figure 4-4 Schematic representation of 3D melt pool geometry with the normal direction (n) and tangential direction (t) at the melt pool bottom	60
Figure 4-5 Schematic representation of Marangoni convection in a melt pool of DED fabricated Ti6Al4V with negative surface tension-temperature coefficient	61
Figure 4-6 Specimens fabricated via wire DED process under the Taguchi experiment design for Y-Z plane data collection.	64
Figure 4-7 Optical microscope image of columnar beta grains on the Y-Z plane.....	65
Figure 4-8 Grain structure on the X-Y plane	66
Figure 4-9 Optical microscope image stitching of columnar beta grains on the X-Z plane, layer 0 to layer 50 indicated by the black mark on the right every 10 layers.	67
Figure 4-10 Optical microscope image of duplex phase microstructure in the hot roll substrate.	68
Figure 4-11 Optical microscope image of the initial competitive grain growth at the initial several layers of material deposition.	69
Figure 4-12 The crystal structure in the center of the printed thin wall structure	70
Figure 4-13 Grain boundary angle measurement of columnar beta grains on the X-Z plane	71
Figure 4-14 EBSD characterization of a single prior beta grain domain on the X-Z plane: band contrast map (left) and inverse pole figure (IPF Z) map colouring perpendicular to the sample surface	72
Figure 4-15 Scanning electron microscope (SEM) image and EBSD on the additive portion in Y-Z plane, and the EBSD result reconstruction from three Euler angles maps.....	73
Figure 4-16 Structure of the neural network used for Y-Z plane samples.....	75
Figure 4-17 Structure of the neural network used for X-Z plane samples.....	76

Figure 4-18 The evolution of training loss and validation loss during training for Y-Z plane samples...	77
Figure 4-19 Comparison between experimental data and ANN model.....	78
Figure 5-1 One timestep in the invasion model. a. Schematic of local solidification condition. b. Numerical representation of the simulation domain.....	89
Figure 5-2 The origin of constitutional supercooling on both sides of dendrite under the Marangoni effect. (a) Composition profile across solid/liquid interface with direction point away from the interface. (b) The temperature profile (TL) ahead of the interface with the difference between TL and equilibrium liquidus temperature (TE) represents the different constitutional supercooling on both sides. T1 and T0 stand for the equilibrium temperature of the solidus and liquidus line.....	94
Figure 5-3 Deviation of the represented angle (percentage): (a) 5 degree (b) 10 degree (c) 20 degree (d) 30 degree.....	98
Figure 5-4 Representation of tilting angles with deviation (percentage): (a) 10 degree (b) 20 degree (c) 30 degree (d) 40 degree (e) 50 degree (f) 60 degree.....	99
Figure 5-5 Building configuration and surface topology comparison of the wire (a, c) & powder (b, d) DED fabricated Ti6Al4V thin wall structures	101
Figure 5-6 Microstructure of wire DED fabricated Ti6Al4V thin wall structure. (a) Electron microscope of the basketweave structure (fully alpha prime phase). (b) Three detected areas (spaced at 50 μ m) within the same prior beta grain. (c) The three corresponding Euler angle maps of alpha prime grain and the reconstructed crystal orientation present of the prior beta grain.....	102
Figure 5-7 Laser confocal imaging and 3D optical image and contour map with the extracted cross-section height profile of grain boundary area.....	104
Figure 5-8 Grain boundary recognition under image segmentation from sample XZ_1.....	105
Figure 5-9 Deposition process of a single track: (a) Laser positioning at 0s (b) 1s (c) 2s (d) 3s (e) 4s (f) 5s (g) 6s (h) 7s (i) 8s.....	106
Figure 5-10 Laser stop and feeding wire retract at (a) 7.3s (b) 7.4s (c) 7.5s	107
Figure 5-11 Melt pool geometry validation. (a) High-speed imaging of transient melt pool geometry with L and W representing the length and width of the melt pool. (b) Melt pool geometry extracted from the CFD simulation.	108
Figure 5-12 The application of the invasion model on the thin wall structure. (a) The simulation domain on a wire DED fabricated thin wall structure. (b) Grain boundary extraction on the three corresponding layers. (c) Grain structure reconstruction result. (d) Simulation result of the invasion model.....	110

Figure 5-13 Average grain size comparison between experimental and simulation results.....	111
Figure 6-1 Comparison on both sides of a thin wall structure.....	120
Figure 6-2 Crystal introducing (b) and end (c) position in a laser wire DED fabricated thin wall structure (a).....	121
Figure 6-3 Solidification microstructure in the last 12 layers of material deposition	123
Figure 6-4 Grain structure reconstruction of the introduced crystal.....	124
Figure 6-5 Sample matrix of the experimental design. Sample CI_1. continuous deposition of 180 layers (control group). Sample CI_2. Cool down to room temperature for every 60 layers (hypothesis 1). Sample CI_3. Annealing treatment for every 60 layers (hypothesis 2). Sample CI_4. Heat treatment at alpha-beta transform temperature for every 60 layers (hypothesis 3).....	126
Figure 6-6 Grain size measurement of Sample NI_1 at 160th – 180th layers (every ten layers) on the middle plane of Y direction.	128
Figure 6-7 The grain size analysis of the control group (sample CI_1) along the build-up direction....	129
Figure 6-8 Crystal introducing position marking for the experimental sample matrix in layer 60-120: (a) CI_1 control group (b) CI_2 cooling to room temperature (c) CI_3 annealing (4) CI_4 heat treatment above the alpha-beta transformation temperature.....	130
Figure 6-9 The crystal introducing position in sample CI_4 (layer 120-180).....	131
Figure 6-10 XPS testing position of intergrain and grain boundary area within a bi-crystal system (from sample CI_1).....	132
Figure 6-11 XPS survey of the intergrain and grain boundary area within a bi-crystal system.....	133
Figure 6-12 The FIB SEM of a grain boundary area.	134
Figure 6-13 The grain boundary morphology in the XY plane in the fabricated part	135
Figure 6-14 EDX result of the grain boundary area: (a) SEM image (b) Ti element map (c) Al element map (d) V element map.....	136
Figure 6-15 Forescatter diodes (FSD) mixed and band contract image of the recrystallized grain at the grain boundary	137
Figure 6-16 EDX mapping of the (a) small crystal area (b) combined Al and V mapping (c) Al mapping (d) V mapping.....	138
Figure 6-17 EBSD mapping of the small crystal and its neighbouring area.	139
Figure 6-18 The KAM mapping of the recrystallized small crystal area showing the misorientation value of the subcrystals.....	140

Figure 6-19 The two-step fabrication of a validation thin wall structure 141

Figure 6-20 Grain structure at the first layer and the adjacent substrate 142

List of Tables

Table 2-1: Solidification Microstructure Simulation Methods in Grain Level..... 30

Table 4-1 Taguchi experimental design orthogonal arrays for Y-Z plane sample fabrications 62

Table 4-2 Experimental design arrays for X-Z plane samples 63

Table 5-1 Process parameters of the laser wire DED fabricated Ti6Al4V for model validation 101

Chapter 1. Introduction and motivations

1.1. Metal additive manufacturing

Additive manufacturing (AM, also known as 3D printing) refers to a process by which digital 3D design is fabricated in a layer-by-layer fashion. Metal additive manufacturing (MAM) methods based on powder, wire, sliced metals and alloys are famous for their flexibility, efficiency, and accuracy [1]. Due to the nature of MAM process, which adds material only at the desired place, the lead-time and material waste are reduced to a relatively low level. More importantly, since the tooling is no longer needed, MAM unlocks a significant amount of constraints for the designers to design products with complex geometry [2]. The technical features of MAM make it suitable for industries with small batch and high complexity part geometry, especially hollow structures, and complex curved surfaces. There are already relatively mature applications at present in aerospace, remanufacturing, medical industries and so on [3].

Following American Society for Testing and Materials (ASTM) classification, MAM technologies can be broadly classified into two categories, namely directed energy deposition (DED) and powder bed fusion (PBF) [4]. There are several technologies under each category branded by different manufacturers [5-7]. The PBF technologies (electron beam selective melting EBSM and selective laser melting SLM) enable the building of complex features, hollow cooling passages and high precision parts; however, they are limited by building envelop, single material per build, and horizontal layer-building ability. In contrast, the DED technologies feature a larger build envelop and higher deposition rate but their ability to build finer and complex geometry is limited. DED technology also offers the ability to deposit multiple materials in a single build and add metal material on existing parts; thus, it is suitable for large component printing and remanufacturing industries [5]. Commercially available MAM technologies are mainly based on three types of heat sources: laser, electron beam and plasma arc, for melting the feedstock (powder or wire).

Laser and arc-based systems are usually operated under an inert atmosphere (especially for titanium processing) compared to the vacuum environment for electron beam processes. Even though the high vacuum systems are more expensive, they offer the advantage of low residual stress and gas element contamination, and electron beam-processed parts can be used without any stress-relieving operation [7].

DED is an important branch in MAM, now showing strong potentials in the rapid fabrication of large component prototypes and remanufacturing industry. A typical DED machine consists of a nozzle mounted on a multi-axis arm or a gantry system, which deposits melted material onto the specified surface, where it solidifies under a gas protection environment. Figure 1-1a shows the DED system (LAWS 1000 automated welding system equipped with a 1 kW YAG solid fibre laser) used in this research and Figure 1-1b is the schematic representation of a front feed laser wire DED process. The key process parameters in this process are laser power, scanning speed, wire feed rate and angle, hatching space, dwelling time between tracks and so on. To avoid gas contamination, a protection environment (Argon as shielding gas) is provided during the sample fabrication process.

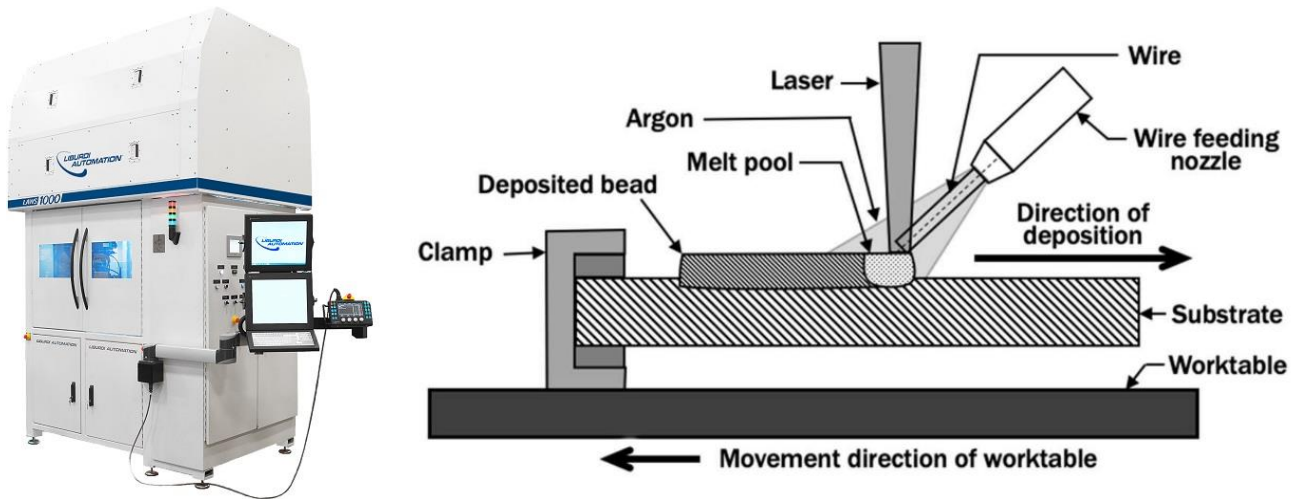


Figure 1-1 (a) LAWS 1000 automated welding system (Liburdi) (b) schematic diagram of a gantry front feed laser wire DED process [8]

Different from casting and forging, DED processes are characterized by heterogeneous nucleation, epitaxial grain growth and rapid, directional solidification due to the layer-by-layer build-up fashion. Uncertainties in the process-structure-property (PSP) linkage are restricting the development and application of this technique [9], and recognizing the interplay between PSP linkage is crucial for quality control and development of this technology. Modelling approaches and numerical simulations are the ideal tools to fill the gap by saving time and experimental costs [10]. These models enable mechanical property predictions from the process and material parameters and serve as a guideline for design, process control, and optimization. Before going to the simulation methods, a detailed understanding of the solidification process in MAM and the common resultant microstructural features (simulation targets) is necessary.

1.2. Solidification in metal additive manufacturing

Solidification is never an easy problem since it involves the phenomena of heat and mass transfer, phase transformation and interface movement. The solidification condition of MAM within a melt pool is more complex than casting as the solidification interface in a melt pool is a relatively small, highly nonlinear free-form interface. It usually takes place under a rapid and steep thermal gradient condition where various physical parameters are difficult or even impossible to be quantified. Another problem for solidification microstructure simulation techniques comes from the highly nonlinear interface evolution during the solidification process, especially the frequently encountered dendritic structures in MAM. To depict the microscale features of material microstructure, simulation techniques need to mesh the investigated domain in an even finer manner, which is typically recommended to be ten times finer than the feature scale to stabilize the simulation result. This leads to the requirement of enormous computational power usually making it impossible for a part-level solidification microstructure simulation.

In metallurgy, solidification is considered to have two steps: nucleation and grain growth. The following section begins with the issues of these two aspects in MAM first. As welding is usually considered as the core of MAM techniques, the solidification phenomena in the welding technique are then elaborated. The grain growth section mainly focuses on a constrained growth case of dendritic columnar grain case which matches the research scope of this thesis.

Among the limited number of printable alloy systems including Ti-based, Fe-based, Al-based, Ni-based, and Co-based alloys, MAM technologies inevitably lead to unique microstructural characteristics w.r.t. traditional forming and manufacturing methods. These differences are inevitable results of the melting, solidification and cooling condition provided by MAM, and the material aspects including nucleation, grain growth behaviours and solid phase transformation, hence the different resultant mechanical properties and defects. In this Chapter, the Ti6Al4V alloy is selected to explain the common microstructural characteristics in MAM, including columnar grains, nucleation, and epitaxial grain growth behaviour as well as the solid phase composition. These characteristics are also frequently observed in other printable alloy systems. Most of the materials have all the mentioned microstructural features, and the rest should be investigated individually. The dendritic columnar grains of as-solidified phases, such as the primary beta of Ti6Al4V, are simulation targets and referred to as ‘grains’ or ‘column grains’ for simplicity.

1.2.1 Nucleation v.s. epitaxial grain growth

Nucleation is the first step of the solidification process. Here, the basic introduction of traditional nucleation theory is skipped to avoid redundancy. The detailed derivative from a thermodynamic point of view can be found in most of the solidification books [11]. In the deterministic models of solidification, the heterogeneous nucleation theory is widely used to explain the small undercooling needed for a

conventional solidification process. In the heterogeneous nucleation theory, if the nuclei are simultaneously generated at a critical undercooling value, it is unable to account for the grain density changes in different cooling conditions. This is contrary to observation, where the grain size will decrease drastically at a higher cooling rate. Currently, the instantaneous nucleation theory is broadly accepted by researchers and has been implemented in solidification microstructure simulation where the nucleation phenomenon is considered as a thermally activated process. Based on the experimental observation from Oldfield [12] that the density of the grains is positively correlated to maximum undercooling, the nuclei density increased by supercooling can be formed under a log Gaussian distribution [13]:

$$\frac{dn}{d(\Delta T)} = \frac{n_{max}}{\Delta T_{\sigma} \sqrt{2\pi}} \frac{1}{\Delta T} \exp \left[-\frac{1}{2} \left(\frac{\ln \Delta T - \ln \Delta T_0}{\Delta T_{\sigma}} \right)^2 \right] \quad \text{Equation 1.1}$$

where n_{max} is the total nucleus number per unit volume; ΔT_{σ} and ΔT_0 are the standard deviation and mean value of the log of supercooling respectively. Here, how to obtain the n_{max} is a critical question that eventually decides the average grain size. Some research directly counts the grains in a unit volume or calculates from the measured grain size [14, 15] before implementing the instantaneous nucleation theory. This practice goes against the prediction nature of simulation, but it is a compromise of the reality that the total nucleus number calculated from the traditional nucleation theory has a deviation of several magnitudes of difference from the experimental result [16].

In term of nucleation behaviour in laser wire DED fabricated Ti6Al4V, epitaxial growth is a common phenomenon and a single crystal (prior beta) usually run through multiple layers of material deposition [17]. In some cases, the column grains even grow throughout the entire length of the printed part. If the partially melted crystal is considered as the substrate for nucleation to start, there will be perfect compatibility between the solid and the liquid phases. Theoretically, there is no nucleation energy barrier, and the wetting angle is zero. It means there are little or no newly formed nuclei in the material deposition

process if the columnar to equiaxed transition (CET) cannot be achieved. Thus, the instantaneous nucleation can also be neglected in most cases, and the column grains directly epitaxially grow from a crystallographic orientation and grain geometry-defined substrate in many MAM solidification microstructure simulations. However, external factors such as impurity, defects and recrystallization are the main reason for new nuclei in MAM. These external factors also provide additional nucleation positions and in turn change the microstructure dramatically.

1.2.2 Grain Growth

1.2.2.1 Solidification mode

Based on the morphology of the liquid and solid interface, the solidification is usually described in four modes (shown in Figure 1-2): planar, cellular, columnar dendritic, and equiaxed dendritic. The planar solidification model is believed to only take place for pure metal and is rarely encountered in real industrial practice. The effect of the thermal gradient (G) and the solidification rate (R) on the resultant solidification microstructure of an alloy is shown in Figure 1-3. The ratio G/R determines the mentioned four modes of solidification while the product $G \cdot R$ decides the average size of the solidification structure.

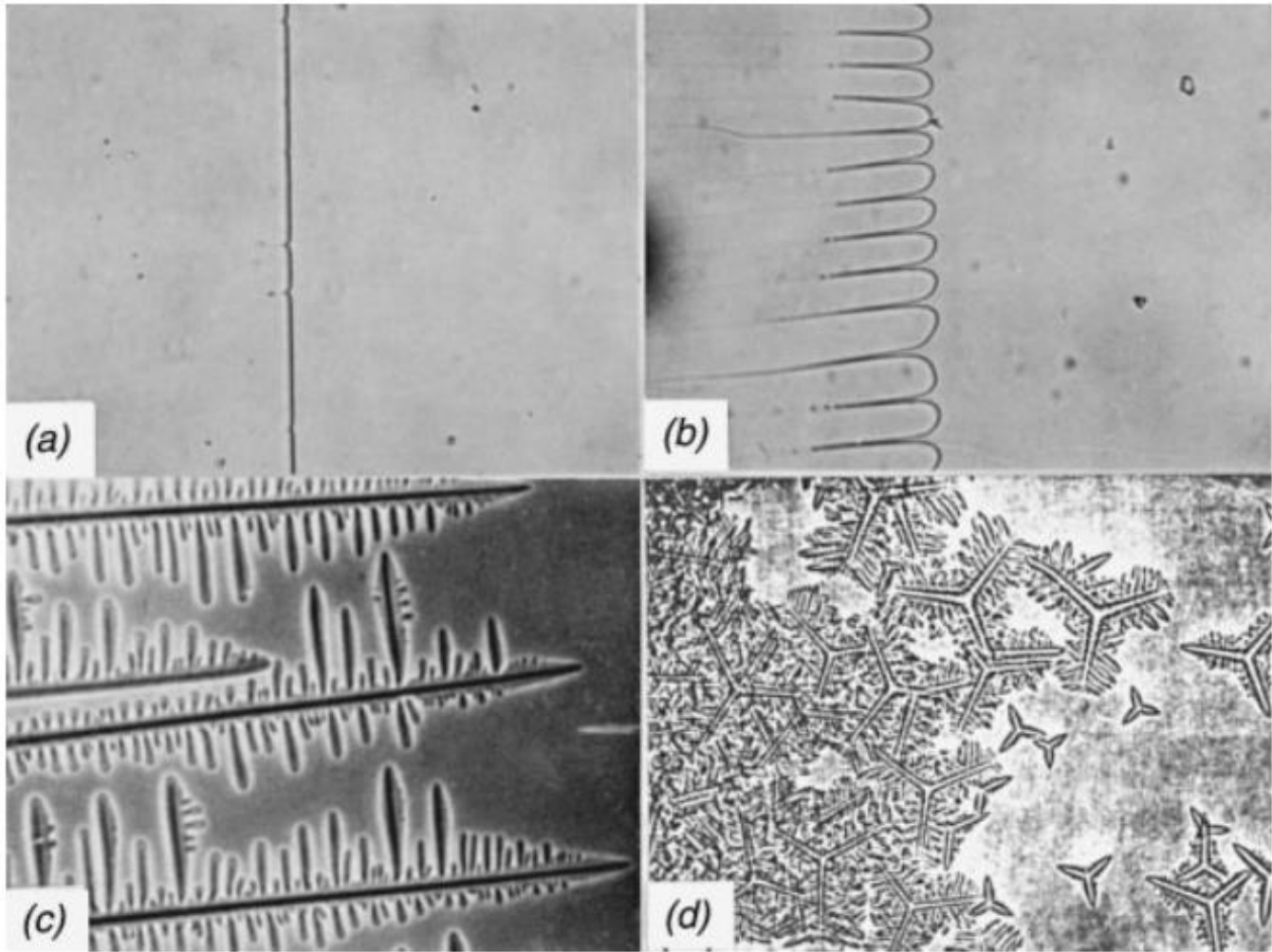


Figure 1-2 Basic solidification modes (observed in carbon tetrabromide): (a) planar solidification; (b) cellular solidification; (c) columnar dendritic solidification; (d) equiaxed dendritic solidification.

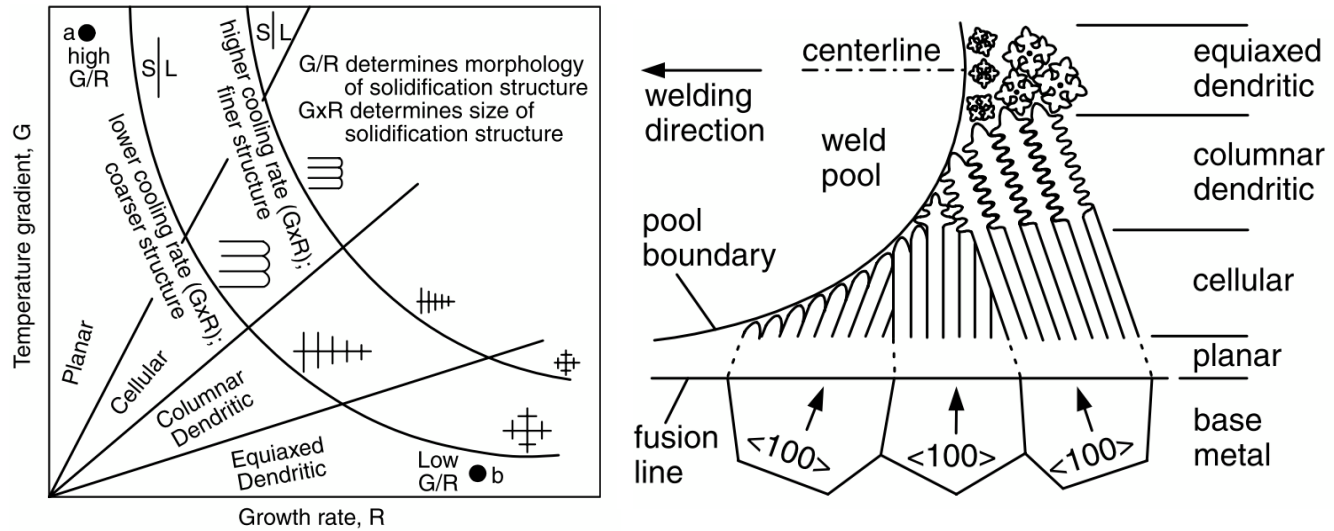


Figure 1-3 Effect of temperature gradient G and growth rate R on the morphology and size of solidification microstructure (left). Variation in solidification mode across the fusion zone (right) [18].

Considering a solidification condition within a moving melt pool, the solidification rate increases from zero at the fusion line to the scanning speed at the centerline. However, the value of the thermal gradient decreases accordingly. The G/R ratio decreases from the fusion line toward the center line. The solidification mode may change from planar to cellular, columnar dendritic, and equiaxed dendritic across the fusion zone, as shown in Figure 1-3 right. The solidification mode transitions have been observed in several different alloy systems in MAM. However, MAM fabrication of a fully equiaxial grain structure for Ti6Al4V is difficult, especially for the DED process. As shown in Figure 1-4, the solidification conditions provided by MAM techniques are analyzed in the G/R graph. The process window of the DED is mainly located at fully columnar grain and mixed area. The scenario of PBF processes is similar but the size of the developed microstructure is finer as a result of a higher solidification rate (scanning speed of PBF is usually higher than DED processes).

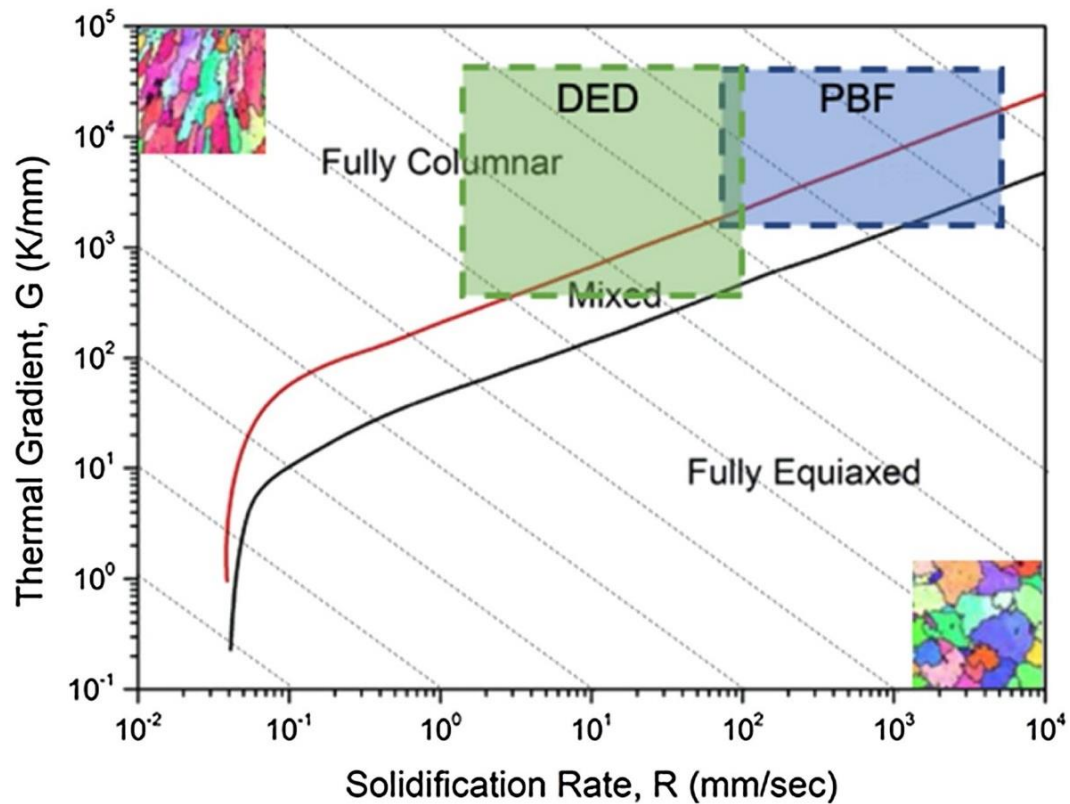


Figure 1-4 A solidification map using Ti6Al4V as an example highlighting the grain type dominating under varying regimes of solidification front velocity and temperature gradient across the solidification front [19].

1.2.2.2 Constitutional supercooling

Supercooling, also known as undercooling, is the driving force for the phase transformation from liquid to solid. The constitutional supercooling which is due to the compositional changes ahead of the solid-liquid interface results in cooling a liquid below the freezing point. For the solidification of an alloy system, constitutional supercooling is usually believed to be the main contribution. And by increasing the degree of constitutional supercooling, the solidification mode can also be changed from cellular/dendritic to the equiaxed dendritic grain (Figure 1-5). The area where the solid (columnar or equiaxed dendrites) and liquid phase co-existed is called the mushy zone (represented as M in Figure 1-5). With a very high value

of constitutional supercooling, the mushy zone becomes so wide that allows the nucleation to start directly in the liquid. Two major recent breakthroughs to understand this problem are the *Free Growth Theory* from Greer et al. [20] and the *Interdependence Theory* from StJohn et al. [21, 22]. By investigating the growth restriction factor Q , a titanium-copper type of alloy is found to have sufficient constitutional supercooling compares to the inadequate constitutional supercooling in Ti6Al4V at the solidification front (Figure 1-6) which results in a fine equiaxed solidification structure and promising mechanical properties [22]. Unfortunately, there is still no commercial grain refiner for Ti6Al4V that is able to achieve this type of CET transformation as its constitutional supercooling is inadequate. Thus, the major effort of this thesis focuses on the accurate simulation of the columnar grain structures in laser wire DED processed Ti6Al4V. The recrystallization of the prior beta grains is studied in Chapter 6 as it is found to have an influence on the columnar grain structures. When the fully equiaxed grain structure is achieved in the fabrication, the number of nucleation sites and the average grain size become more important than the actual grain structure morphology. Thus, the development of equiaxed grain structure is not include in the scope of this thesis.

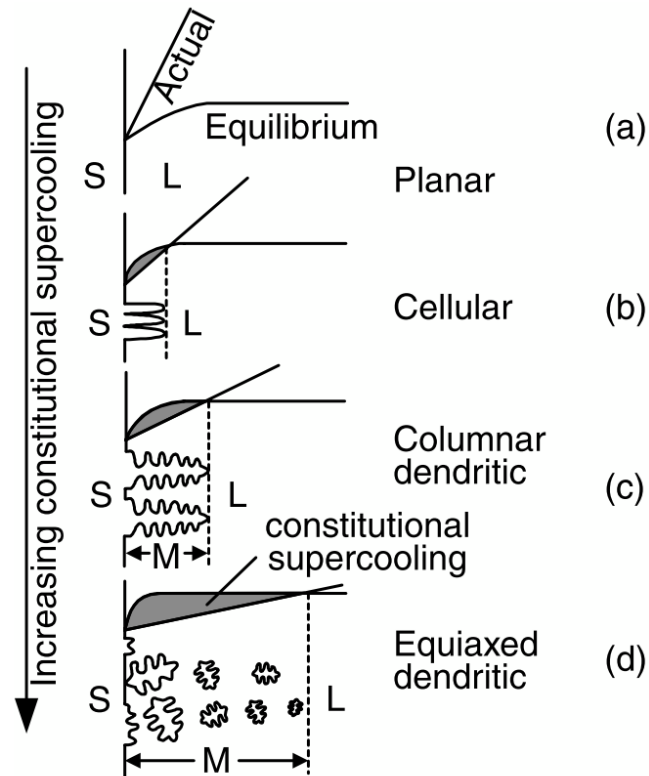


Figure 1-5 Effect of constitutional supercooling on solidification mode: (a) planar; (b) cellular; (c) columnar dendritic; (d) equiaxed dendritic (S, L, and M denote solid, liquid, and mushy zone, respectively) [18].

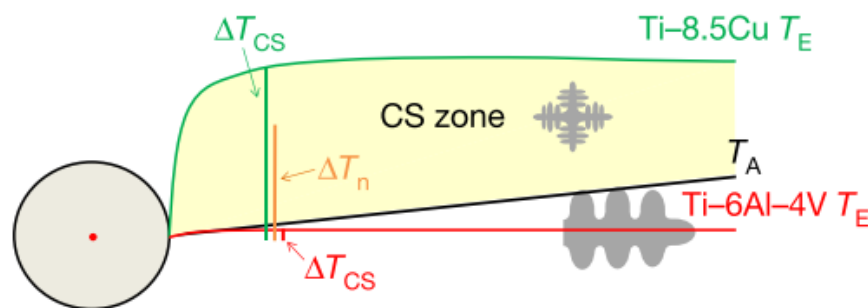


Figure 1-6 Schematic diagram of the grain growth mechanism of Ti-8.5Cu and Ti6Al4V alloys. T_A is the profile of the temperature of the melt and T_E is the profile of the equilibrium liquidus temperature [22].

1.3. General Microstructural Features in MAM

1.3.1. Columnar Grain, Texture and Anisotropy

MAM studies have shown that columnar grain is a common microstructural characteristic in the fabricated samples [17, 23-30]. When considering the cooling condition of the bottom of the melt pool in terms of the thermal gradient (G) and solidification rate (R), the cooling conditions of MAM technologies are mostly located at the columnar zone of the G - R diagram (with a relatively large G and small R in Figure 1-4) [31-33]. The columnar grains frequently observed in MAM fabricated parts tend to elongate along the build direction (e.g., the columnar grains of Ti6Al4V, Inconel 718 and 316L fabricated via multiple MAM techniques in Figure 1-7), approximately parallel to the preferentially growing directions of crystals or generally the buildup direction. This is the result of the onset of solidification where the fusion transfers into crystallographically ordered solid phase characterized by body-centred cubic (bcc), face-centred cubic (fcc) or hexagonal closed-packed (hcp) crystal structure.

The reason for the columnar grains going through multiple layers is the so-called ‘epitaxial growth’ behaviour in MAM [34]. From the energy point of view, it will save more free energy if nucleation starts from partially melted grains in the previous layer rather than generating a new one. The newly formed grains will inherit crystallographic information like crystal orientations and grain size from existing crystals. Those with their preferred grain growth directions aligned with the thermal gradient direction tend to stand out from the competitive grain growth and develop even bigger through MAM build-up process. In the buildup direction of MAM, the steep thermal gradient of the melt pool provides a perfect selection environment for grain growth. The columnar grains with their preferred grain growth direction align with the thermal gradient direction have the growth advantage, and they are able to kill the adjacent grains during the competitive grain growth process. In a single weld track of MAM, the columnar grains tend to tilt towards the scanning direction to align their preferred growth direction with the maximum

thermal gradient direction. Theoretically, if the columnar grains grow steadily and align with the thermal gradient direction, it will result in a curvature of the grain shape because the grain will experience a changing thermal gradient direction along the melt pool tail. However, this kind of grain curvature can also be inhibited due to the constrained solidification among the highly textured grains (preferential growth direction in the build-up direction) and the remelting in MAM.

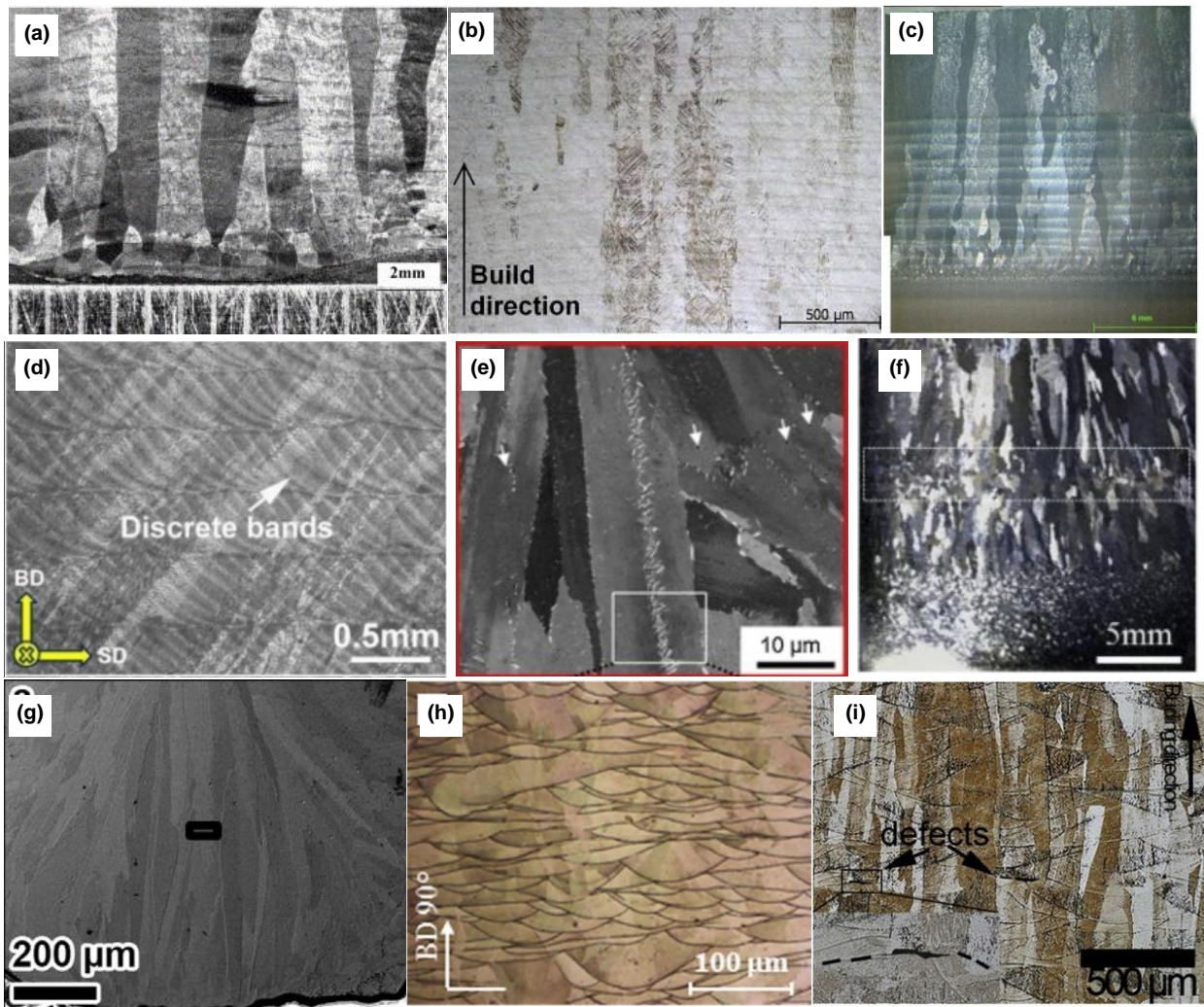


Figure 1-7 Column grains in Ti6Al4V parts produced by (a) DED [35] (b) SLM [36] (c) Gas Tungsten Arc Welding (GTAW) [29]; (d) Column grains in Inconel 718 parts produced by DED [37] (e) SLM [38] (f) Electron beam smelting layered solidification [39] (g) Column grains in 316L parts produced by DED [40] (h) SLM [41] (i) EBSM [42]

Different from conventional manufacturing methods like casting, forging, and rolling, the solidification texture of MAM fabricated parts is usually more emphasized than the deformation texture. Most of the conventional metallic materials processed by MAM are cubic crystal systems (either bcc or fcc). When they are processed by this layer-by-layer building strategy, highly crystallographic solidification textures are frequently encountered with the preferred grain growth direction of the crystals parallel with the buildup direction (Nz) of MAM process (e.g., the strong $\langle 001 \rangle // Nz$ solidification fibre texture). The texture becomes stable after a few layers of deposition when the competitive grain growth is complete [43].

Also, the developed microstructure in MAM tends to generate anisotropic microstructural features like the mentioned columnar grains, texture, networks of dislocation, precipitates, harmful phases and so on. Combining with the manufacturing deficiencies during the printing process, this can further result in anisotropic mechanical properties of the printed metal parts [44]. As the columnar grains are generally parallel with the building direction, the dislocations within the crystals are easier to be accumulated on the grain boundaries areas and result in stress concentration under a force loading on the build-up direction. And on the other hand, in the vertical loading direction, more elongation before failure is found [45]. However, this conclusion is not always true as some study shows that cracks also have the propensity to propagate along columnar grain boundaries in some cases [46, 47], like Ti, Ni and Al alloys [44]. Researchers attribute this mostly to the morphology of the columnar grain, as in the build-up direction of MAM where grain boundaries lose their effect of cleavage-cracking resistance [48]. The segregation at the grain boundary in some of the alloy systems also leads to a risk of hot cracking as a result of thermal stress and segregation-induced liquation, especially at high-angle grain boundaries [49]. As a result, the morphology of columnar grains in MAM samples leads to anisotropic mechanical properties in the as-built condition [44]. Depending on the loading direction with respect to the morphological orientation of

columnar grains, ductility differences were discovered between horizontally and vertically built test specimens [47, 50, 51]. The frequently encountered cellular/dendritic solidification microstructure in MAM is usually in a fine manner as a result of the rapid solidification. Compared to casting, it presents a higher strength and superior mechanical properties. On the other hand, great efforts have also been made to achieve the equiaxial grain morphology by investigating the CET phenomenon with the help of numerical models [24, 52, 53].

1.3.2. Hierarchical Phase Composition

During MAM, local temperature history varies depending on the different spatial positions in the printed part, and this has been extensively proved from both experimental and simulation points of view. As shown in Figure 1-8, at a single point within a fabricated part, the material experienced a complicated cooling and heating history. The combination of this repetitive thermal cycling and associated residual stress developed during printing provides the activation energy for solid-phase transformations, which gives a chance for the unstable solid phase (from rapid solidification) to dissolve. This is especially exemplified for materials with solid-solid phase transformations, where hierarchical phase composition within the printed part can be found.

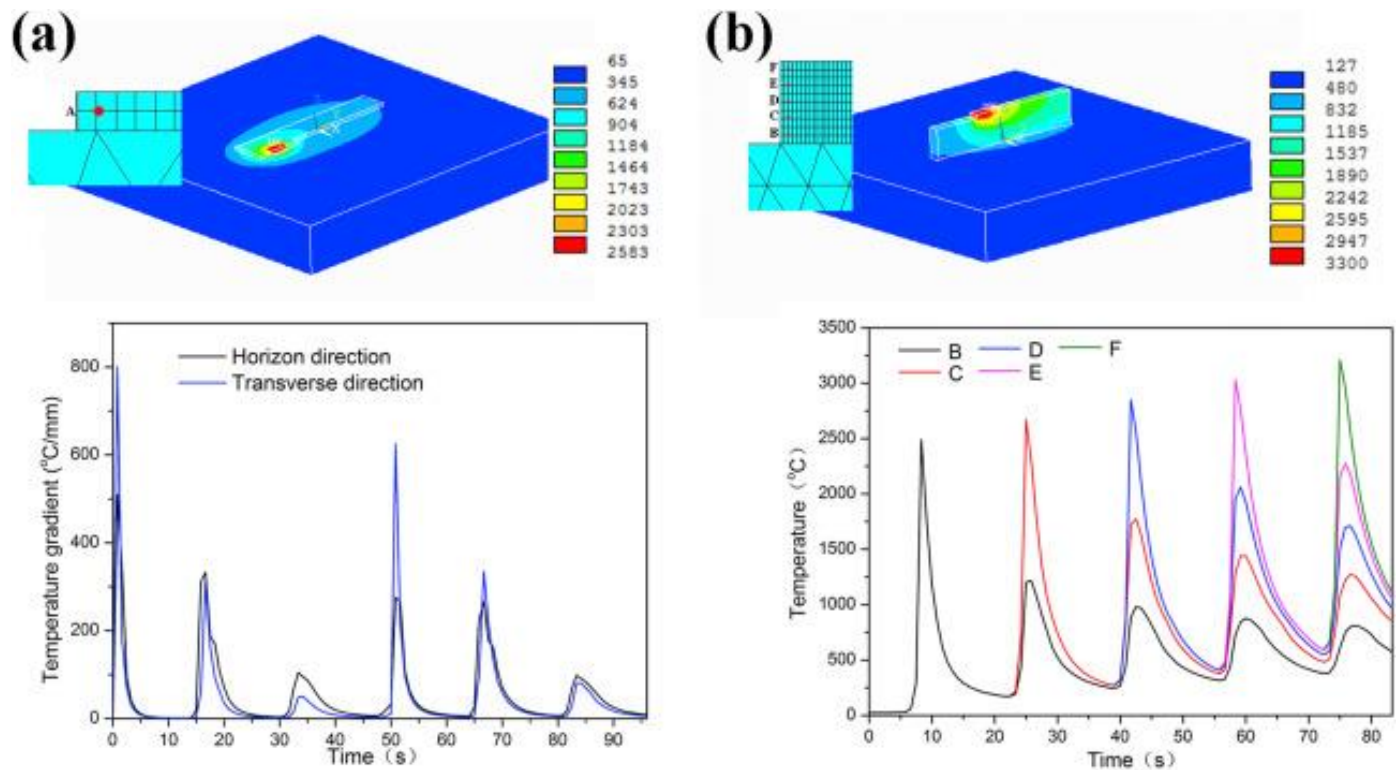


Figure 1-8 (a) Simulated temperature profile and thermal gradient versus deposited time of DED fabricated part; (b) Simulated temperature profile and the measured temperature versus deposited time at different locations [54].

Various solid phase compositions along with the newly added deposition layers can be depicted as position-dependent microstructural “maps”, based on known relationships from the thermal history and microstructural evolution. As in DED fabricated Ti6Al4V (Figure 1-9), the complex solid phase transformation even takes place within several layers of printing. This type of microstructural evolution map can be coupled with thermo-mechanical models to make predictions of the phase composition after printing and provide the guideline for process parameters selection and optimization.

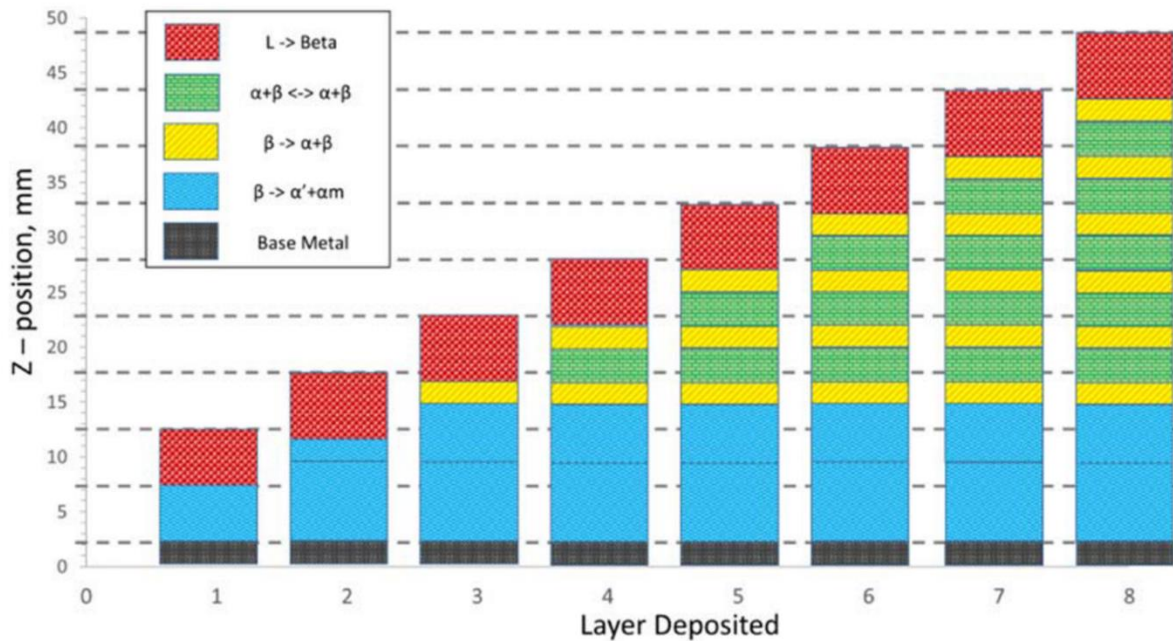


Figure 1-9 Microstructural evolution map of Ti6Al4V fabricated by DED as each layer is deposited (reproduced from [44, 55, 56]).

The microstructures in MAM tend to be finer than traditional manufacturing methods because of the rapid solidification. If a sufficient cooling rate is imposed, diffusionless solid-solid phase transformation can be activated.

1.4. Metallurgy of MAM Ti6Al4V

Titanium alloys are famous for their light weight, high strength, heat, and corrosion-resistant properties [57-61]. However, titanium is hard to extract as pure metal and normally used for high-value-added products [62]. In the past few decades, titanium and its alloys are found to be a good combination with AM. To date, there have been only a limited number of commercial alloys used in AM, among which Ti6Al4V has been by far the most extensively investigated. This can be attributed to the strong business

case of complex and low production volume titanium parts [27]. Titanium alloys are among the most important categories of advanced materials being widely used in aerospace and terrestrial systems [7]. The conventional titanium alloys are categorized based on the phases present at room temperature. With the addition of different stabilizer elements, three types of titanium alloys predominately consist of alpha (hcp), beta (bcc) and alpha + beta phase. Considering the combination of strength, workability, and formability, Ti6Al4V becomes the most widely used titanium alloy. This argument also applies to the case of AM with a lot of research and applications of titanium alloys focusing on Ti6Al4V because of its high weldability. However, there are still several studies on other types of titanium alloys [63, 64]. Beyond Ti6Al4V, another class being extensively investigated in MAM is Ti6242 (Ti-6Al-2Sn-4Zr-2Mo) [65]. This near-alpha titanium alloy composition shows promising properties compared to Ti6Al4V in aspects of good toughness, high-temperature stability and good creep resistance [66]. Studies are also conducted to understand the porosity formation [66], the effect of heat-treatment [67], alloy composition optimization [68] and so on.

In Ti6Al4V MAM studies, the as-built microstructure is usually composed of the martensitic alpha prime phase with little alpha or beta phases in a high cooling rate (diffusionless solid phase transformation in PBF) [36, 69, 70]. And in EBSM and DED cases with a relatively lower cooling rate, it typically presents an alpha-beta Widmanstätten structure. The heat input in the DED processed samples is usually higher than that in SLM; thus, the relatively slow cooling rate gives the opportunity for diffusion-controlled solid phase transformation. This sometimes results in the alpha phase forming at the grain boundary of prior beta grains (pointed out in Figure 1-10b). The thermal cycles in MAM process usually result in a changing phase composition along the build-up direction. In most cases of Ti6Al4V, the secondary or higher-order branches of dendritic columnar grains merge [71], and the solid-phase transformation eliminates the original grain morphology. To investigate the original solidification microstructure of MAM fabricated

Ti6Al4V, the EBSD technique is frequently used [50, 51, 72-76]. The prior beta grain can be characterized by the EBSD reconstruction result to provide the crystal orientation information and the approximate grain morphology as well. Detailed methodology is explained in Chapter 4 of this thesis. Post-processing can also influence the microstructure in Ti6Al4V dramatically, this includes stress relieving, annealing, and ageing, hot isostatic pressing and so on. The corresponding resultant microstructure under different cooling conditions can be found in the titanium alloy handbook [77].

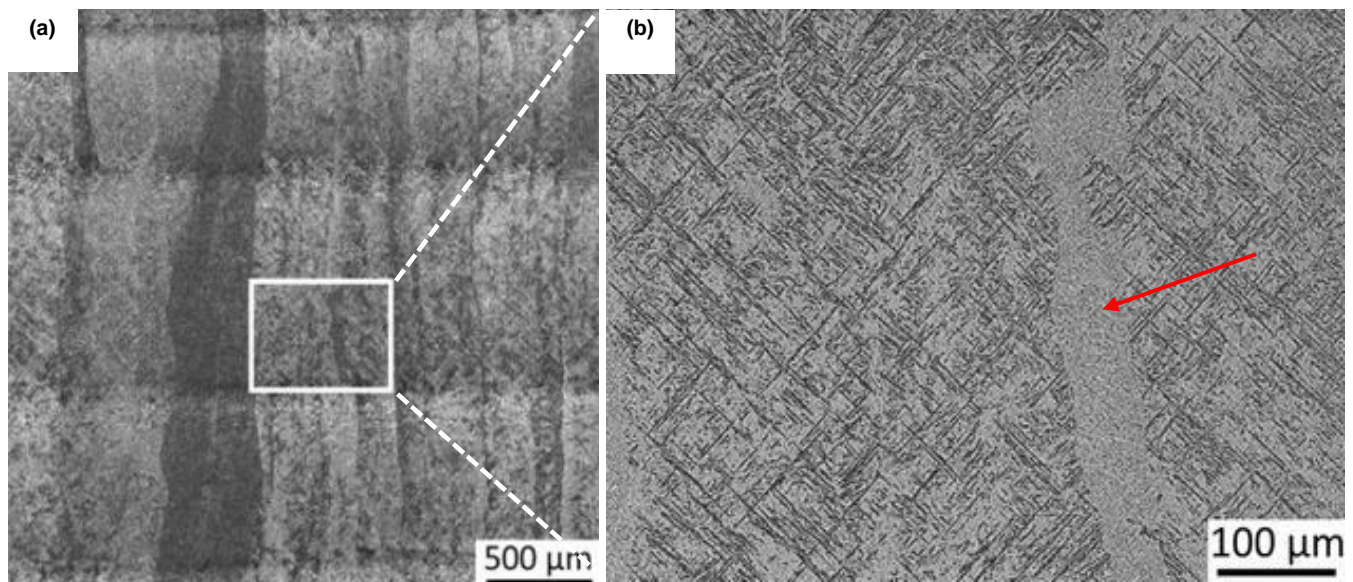


Figure 1-10 Phase Composition of Ti6Al4V fabricated by DED: (a-b) Micrographs of macrostructure and fine microstructure of DED sample [78]

Studies also show that primarily alpha prime microstructure results in low ductility, and unlike the martensite in steels, alpha prime in titanium alloys contributes little to the strength of the material. The size of the alpha colony is a determining factor for the mechanical properties [79]. By applying post-process heat treatments to decompose alpha prime into microstructures consisting of alpha and beta phases (i.e., lamellar microstructure), ductility can be improved significantly [36]. Besides Ti6Al4V, post-

processing and heat treatment are also powerful tools for MAM fabricated alloy systems to control their solid phase composition and mechanical properties [26].

1.5. Fundamentals of Machine Learning and Application in MAM

A widely accepted definition of machine learning (ML) is given by Tom Mitchell as “a computer program is said to learn from experience E with respect to some class of tasks T and performance measure P if its performance at tasks in T, as measured by P, improves with experience E” [80]. The most commonly used machine learning algorithms are categorized as supervised or unsupervised. Supervised machine learning algorithms make the prediction from the learning of labelled data. Based on whether the prediction is made on concrete or continuous value, the task can be further divided into classification or regression. Starting from the analysis of a known training dataset, the learning algorithm produces an inferred function to model the relationships and dependencies between the target prediction output and the input features. The trained model can make predictions with new input and evaluate the accuracy, then modify the model accordingly. The commonly used algorithms include nearest neighbour, naive Bayes, decision trees, linear regression, support vector machines (SVM) and ANN. In contrast, unsupervised machine learning algorithms work on data neither classified nor labelled. Unsupervised learning studies how systems can infer a function to describe a hidden structure from unlabeled data like finding clusters of instances or simplifying it through the removal of high-entropy features. The main types of unsupervised learning algorithms include clustering algorithms and association rule learning algorithms.

Semi-supervised machine learning algorithms fall somewhere in between supervised and unsupervised learning since they use both labelled and unlabeled data for training – typically a small amount of labelled data and a large amount of unlabeled data. The systems that use this method can considerably improve learning accuracy. Usually, semi-supervised learning is chosen when the acquired labelled data requires

skilled and relevant resources in order to train and learn from it. Otherwise, acquiring unlabeled data generally doesn't require additional resources.

Reinforcement machine learning algorithms are a relatively new learning method that interacts with its environment by producing actions and discovering errors or rewards. Trial and error search and delayed reward are the most relevant characteristics of reinforcement learning. This method allows machines and software agents to automatically determine the ideal behaviour within a specific context to maximize its performance. Simple reward feedback is required for the agent to learn which action is best; this is known as the reinforcement signal.

Compared to conventional manufacturing methods, there are more uncertainties in AM processes as they usually involve complex designs, transport phenomena, phase transformation, and in-process control to achieve the desired microstructure and properties. In the meantime, the enormous data generated from design and PSP linkage [81, 82] in AM techniques brings challenges to researchers, and the traditional trial and error methods are usually not efficient. Considering the melt pool size alone, it can change from hundreds of micrometres in PBF to several millimetres in DED, and this may eventually result in very different microstructures and properties. Modelling approaches and numerical simulations are the ideal tools to fill the gap and save experimental costs [10, 83]. However, establishing mechanistic models [84] usually requires domain knowledge and model validation process before their reliable applications. In recent years, an increasing number of studies are looking into solutions by directly applying data-driven approaches. ML continuously shows its advantages to dealing with the uncertainties and multiple types of data from AM for various reasons. First, it avoids solving complex equations in many physical models. Second, it fills the gap where traditional theories are either non-existent or lose function due to their inability to solve application-specific problems. Finally, it is able to make a prediction for a long process range based on the well-tested and reliable ML algorithms encoded by the open-source software [84].

Thus, apart from physical-based mechanistic models, great efforts have been spent towards developing the correlation in between by using the advanced data mining techniques of machine learning [85]. The increasing interest in data-driven analysis, now, also extends to the field of AM [86-88]. Lu et al. investigated the effect of main parameters (laser power, scanning speed and powder feeding rate) on the depositing height of a single track in Laser Engineered Net Shaping (LENS). The backpropagation (BP) based network improved with Adaptive learning rate and Momentum coefficient (AM) algorithm, and the least square support vector machine (LS-SVM) network are both adopted. The performance of different algorithms was compared [89]. Karimzadeh et al. used an ANN within a Bayesian framework to model the effect of welding current and speed on average grain size in Ti6Al4V alloy weldments [90]. Ghosh et al. developed a data-driven multilayer perceptron-based neural network model to predict the percentage of total porosity and mechanical properties in A356 aluminum alloy during the solidification process [91]. Krol et al. have analyzed the impact of various process parameters on the dimensional accuracy of AM fabricated part, at the meantime, calculated their decisive importance [92].

In the material deposition process of MAM, the melt pools generated from all kinds of high energy sources are vital to the resultant microstructure and mechanical properties. Studies on weld bead modelling carried out under regression analysis [93] are substituted into ML to achieve higher efficiency and accuracy. Especially, the neural network has a greater capacity for approximating and predicting any nonlinear processes than the traditional regression models. Xiong et al. established a neural network model to predict the desired bead geometry in terms of bead width and height. The neural network performs better than the second-order regression model with a higher efficiency [94]. Garg et al. proposed a modified multi-gene genetic programming approach to reveal the hidden relation between process parameters and bead width [95]. Ding et al. determine the relationship between single bead geometry and welding process parameters

through an ANN model. The adaptive medial axis transformation (MAT) algorithm for void-free deposition is introduced to achieve high geometrical accuracy [96].

The advantage of data-driven modelling is its efficiency and fidelity achieved. It turns out to be a more realistic approach compared to the direct simulation when the physics behind are ambiguous and yet not fully understood. However, data-driven modelling remains a challenge because enormous experimental data is needed as training data to guarantee the accuracy under adapted machine learning algorithms. Along with the booming of computer science and machine learning algorithm, there is a vast number of opportunities for improvement of data-driven approaches in AM when investigating the PSP linkage and controlling the uncertainties. It becomes an additional way aside from the direct numerical simulations and has already shown great potentials.

1.6. Research objectives

The main goal of this research is to develop a practical model that is able to quantitatively simulate the solidification microstructure in laser wire DED fabricated of Ti6Al4V, with the support of a data-driven approach. The specific objectives of this research are listed as follows:

- Develop a database to investigate the anisotropic grain growth behaviour in laser wire DED fabricated Ti6Al4V and establish the regression relation between the crystal orientation, solidification conditions and the resultant grain boundary angle.
- Develop a novel model focusing on the interaction within a bi-crystal system under different solidification conditions of MAM and simulate the solidification microstructure in laser wire DED fabricated Ti6Al4V on a practical scale.
- Validate the “invasion model” under the configuration of laser wire DED fabricated Ti6Al4V thin wall structure.

- Investigate the crystal introducing mechanism in laser wire DED fabricated Ti6Al4V which influences the solidification microstructure dramatically.

1.7. Thesis organization

This thesis is composed of 7 Chapters. Chapter 1 presents an overview of the research background of the thesis project and introduces the fundamentals of the related concepts, objectives and significance of the study. Chapter 2 reviews the relevant literature of the current solidification simulation methods together with their corresponding methodology. The difficulties and drawbacks are discussed at the end. Chapter 3 describes the proposed methodological framework. This strategy addresses the difficulties in MAM and avoids the essential defects of traditional methods. Chapter 4 outlines the development of the ANN enabled database recording the anisotropic grain growth behaviour of Ti6Al4V in laser wire DED process. Chapter 5 presents the establishment of a novel deterministic model, called the “invasion model”, and the experimental validation process. Chapter 6 investigates the crystal introducing mechanism in laser wire DED fabricated Ti6Al4V. Chapter 7 concludes the major findings of the thesis and provides recommendations for future research directions.

Chapter 2. Literature review

2.1. Introduction

This Chapter aims to provide a comprehensive review of the state-of-art microstructure simulation methods for MAM fabricated parts to accurately predict the solidification microstructure in terms of grain morphology and texture. These microstructural features can be further applied to mechanical property prediction and process optimization. Existing thermal welding models were found to be inadequate for describing MAM process due to inconsistencies in predictions of the microstructures [90, 97, 98]. MAM deposition processes are characterized by rapid, directional solidification due to the layer-by-layer build-up process; the microstructure and mechanical properties of the deposited materials depend strongly on the cooling condition and subsequent thermo-mechanical cycles. The grain-scale simulation approaches used to numerically model the solidification process in MAM are discussed in detail and compared w.r.t. their respective capacity and applicability. Finally, the challenges and opportunities in the area of microstructure simulation for MAM are addressed.

2.2. Current Solidification Microstructure Simulation Methods in MAM

One principal aim of material science is to relate macroscopic sample behaviour to microstructure [47] quantitatively, and simulation is a good option to bridge the gap. Following this, a microstructure simulation is not necessarily carried out on a microscale as long as its simulation target is the microstructure. For all the metal solidification processes including MAM, microstructure simulation can be roughly divided into macroscale (solid-state phase transformation, concentration field, etc.), mesoscale (grain texture) and microscale (nucleation and grain growth). Furthermore, with the aid of advanced analytic capabilities of the supercomputer, nucleation behaviours are simulated at an atomic scale [99,

100]. All the simulation works are facing the trade-off between computational efficiency and accuracy. In this Chapter, the computational efficiency is analyzed by the computational time and simulation domain including its dimension. For the accuracy of the solidification microstructure simulation methods, the smallest time and length scale captured by the three methods are considered. A solid physical background is needed in order to guarantee the accuracy of the method, but the most straightforward method to test the simulation accuracy is experimental validation.

Melt pool models in welding have been used as a guide for the development of MAM process and solidification microstructure simulation [101-104]. Factors such as the solidification front velocity, temperature gradient, melt pool shape, travel speed, undercooling, and alloy constitution are vital in the solidification process of MAM to determine the cooling conditions and resultant solidification microstructure in a single melt pool [105]. Extensive literature has documented the polycrystalline microstructures as well as the significant differences in the resulting mechanical properties of MAM components [106-109]. However, due to the rapid development of MAM techniques, it is recognized that matching detection and simulation systems are becoming increasingly important [110-114].

The study of dendritic growth and features of crystal grain is another prominent fundamental research topic in solidification microstructure modelling and simulation. It provides a better understanding of the solidification process and resultant microstructure. In the modern sense of solidification microstructure simulation, physical models act as the foundation providing a formal description of the crystal nucleation and grain growth behaviour. Microstructural information such as grain size and morphology are gathered under different algorithms through numerical simulation and implemented on computer visualization. With the rapid development of computer technology, some established macro-transmission models have been used to describe the transport phenomenon and movement of solid-liquid interfaces in space and in time [115]. From these models, temperature and other field data can be extracted and used in the

subsequent steps of microstructure simulation. Currently, there are four conventional methods used in the field of solidification microstructure simulation, namely Cellular Automata (CA), Phase Field (PF), Monte Carlo (MC) and deterministic method. The deterministic method is based on solidification kinetics, usually with clear physical implications and application background. In this work, the first three probabilistic (subject to or involving stochastic variables or factors) models in MAM are discussed in the following sections.

The blooming of microstructure simulation on MAM, especially in the last decade, is a result of the rapid development of MAM technologies and simulation methods. Compared to casting, MAM provides more opportunities for cooling condition controllability by manipulating the process parameters in a much smaller region. Simulation increasingly reveals its importance in this area to hit the target of quantitative control on MAM fabricated microstructure. From all the reviewed solidification microstructure simulation methods shown in table 2-1, CA is currently the most used method for MAM processes with relatively low computational cost, and it provides the information of rough outline of solidification grain structures. It has also been widely implemented in MAM-related topics to investigate the PSP linkage. With the help of the macro-transmission models, the CA method can be launched at a 3D level with a scope of multiple layers.

PF methods are capable of high accuracy and resolution in the representation of physical models. It can capture subgrain features in the solidification microstructure, such as secondary or higher-order dendrites. However, there is no “free lunch”. PF models are usually computationally expensive and can only generate one or a limited number of grains in the simulation region. The extension of the PF method to 3D models renders the level of computational resources required prohibitive. Other challenges arise when modelling rapid solidification. Specifically, it is not well accepted how to map the asymptotic interface dynamics of PF models onto appropriate non-equilibrium kinetics that incorporate solute trapping and drag; indeed, it

is not even well known what the kinetics at the interface should be when solidification rates become as high as they do in rapid solidification. For example, it is typically assumed that the continuous growth model of Aziz and co-workers holds at rapidly moving interfaces [116]. However, there is also compelling evidence from Molecular Dynamics (MD) that the non-equilibrium two-time kinetics of Sobolev and other workers holds at rapidly moving interfaces. The existence of an interface in PF models naturally leads to the phenomenology of solute trapping and drag [117]. However, the degree of trapping and drag exhibited by each PF model depends on the size of the interface, the interpolation functions used, both of which effects can couple to the rate of solidification. Recent PF models have considered how to integrate non-equilibrium effects consistently and quantitatively into PF models [118-120].

As for the MC method, it is simple and effective in simulating grain growth behaviour, especially the recrystallization, but it can only provide the result after a large number of ‘trial and error’. In the kinetic Monte Carlo (KMC) simulations for MAM, the subgrain microstructure such as cells and dendrites are simplified, in some cases, even the crystal orientations are neglected. Thus, the competitive grain growth behaviour described by this method has a relatively weak physical background compared to CA and PF methods. CA and KMC methods usually combine with the thermal history sources to predict the microstructure evolution during the solidification process. The thermal history source data normally come from the well-developed macro-transmission models based on finite element, finite difference, or Lattice Boltzmann method. However, PF models are mostly carried out under the ‘frozen temperature’ assumption, which is only valid under an extremely small region.

Experiments validate most of the simulation results in the reviewed works in terms of grain structure, size, crystal orientation, and texture. Because of the PF method’s capacity on capturing subgrain microstructural features, dendrite arm spacing is frequently measured in the validation of PF models to compare with the simulation result. However, only a limited number of CA and PF models would validate

the melt pool geometry before launching the solidification microstructure simulation. The accuracy of the simulation result is thus discredited by using a non-validated boundary condition.

The computation efficiency is usually an issue to consider when a solidification microstructure simulation is launched in 3D level or multiple layers' region in MAM. Parallel computation is widely applied to arrange the computation task into a multi-core Central Processing Unit (CPU) or Graphics Processing Units (GPU) to increase the processing speed. To save the memory space: iterative data reuse and dynamic allocation strategies are used in the CA method; for the PF method, this can also be achieved by deriving new evolution equations. Along with the progress and development of microstructure simulation, new methods, theories, and techniques continuously come forth — for example, the needle-network method which has already shown the potentials of its further application in MAM process.

Table 2-1: Solidification Microstructure Simulation Methods in Grain Level

Simulation Method	Simulation Objective	Dimension	Scope	Thermal History Source	Experimental Validation Method	Computational Efficiency Improve Strategy	Reference
Cellular Automata	Melt Pool Solidification	3D	Multiple Layers	Finite Volume	EBSD Measurement	--	[121]
				Analytical Solution	EBSD Measurement	Parallel computations	[122]
				Finite Difference	Grain Structure and Geometry Analysis	--	[123]
				Finite Element	Grain Structure and Size	Iterative Reuse of Thermal Field Data	[124]
			Single Track	Finite Element	--	Parallel Computations	[125]
				Finite Element and Finite Volume	EBSD Measurement	--	[126]
				Finite Element	Grain Structure	--	[127]
			Melt pool	Analytical Solution	Comparison of Primary Dendrite Arm Spacing	--	[128]
				Thermal– Computational Fluid Dynamics (CFD)	Observations from Literature	--	[129]
			Constant Thermal Gradient Area	Frozen Temperature Approximation	--	--	[130]
		2D	Multiple Layers with Powder	Lattice Boltzmann	Grain Structure and Texture	--	[131]
				Lattice Boltzmann	Grain Size and Texture	--	[114]
			Multiple Layers	Finite Element	Grain Structure and Size	--	[132]
				Finite Difference	Grain Structure and Texture	--	[112]
				Phase Filed Model	Grain Structure and Texture	--	[110]
				Finite Element	Grain Size Measurement	--	[113]
Finite Element	Grain Structure	--	[133, 134]				

			Single Crystal	Lattice Boltzmann model	--	Avoids Large Equation Systems	[135]
	Casting or Directional Solidification	3D	Ingot	Finite Element	Temperature Field Measurement	--	[136]
Finite Element				Grain Structure	Dynamic Allocation	[137]	
Finite Element				--	Parallel Computations	[138]	
Finite Element				--	--	[139]	
			Constant Thermal Gradient Area	Finite Element	Primary Dendrite Spacing	--	[140]
		2D	Section of Ingot	Isothermal	Grain Structure	--	[14, 141, 142]
Phase Field	Melt Pool Solidification	3D	$0.65 \times 0.65 \times 10.0 \mu\text{m}^3$	Frozen Temperature	Grain Structure and Primary Dendritic Arm Spacing	--	[143]
			$1 \times 1 \times 2.4 \mu\text{m}^3$	Finite Element (Frozen Temperature Approximation)	--	--	[144]
		2D	Multiple Layers	Phase Filed Model	Observations from Literature	Formulation of New Free Energy Expression	[145]
			Single Track	CFD	Grain Structure and Segregation Analysis	--	[146]
			$6 \text{ mm} \times 12 \text{ mm}$	Finite Element	Grain Structure and Arm Spacing Measurement	--	[147]
			$150 \mu\text{m} \times 150 \mu\text{m}$	Lattice Boltzmann	--	--	[148]
			$50 \mu\text{m} \times 50 \mu\text{m}$	Finite Element	Grain Structure and Dendritic Arm Spacing	--	[149]
			$12 \mu\text{m} \times 12 \mu\text{m}$	Frozen Temperature	Grain Structure and Primary Dendritic Arm Spacing	--	[150]

			12 μm \times 32.4 μm	Frozen Temperature	Grain Structure and Primary Dendritic Arm Spacing	--	[151]
			150 μm \times 100 μm	Analytical Solution	Dendrite Arm Spacing from Literature	--	[152]
	Casting or Directional Solidification	3D	3.072 \times 3.078 \times 3.072 mm^3	Analytical Solution	--	GPU and Parallel Computation	[153]
			768 \times 768 \times 768 μm^3	Frozen Temperature	Grain Structure	Parallel Computation and Asynchronous Concurrent Algorithm	[154]
			1.6 \times 1.6 \times 1.7 mm^3	Analytical Solution	Grain Structure	--	[155]
			1.058 \times 1.058 \times 1.058 mm^3	Frozen Temperature	--	New Evolution Equation	[156]
		2D	600 μm \times 600 μm	Frozen Temperature	Grain Structure	--	[157, 158]
			2 mm \times 1.2 mm	Frozen Temperature Profile	In Situ X-Ray Imaging	--	[159]
			5 μm - 5 mm	Frozen Temperature or Analytical Solution	Grain Structure	--	[160-167]
	Monte Carlo	Melt Pool Solidification	3D	Multiple Layers	CFD	Grain Structure and EBSD	--
Single Track				CFD	Grain Structure and Melt Pool Geometry	--	[169-171]
2D		Multiple Layers	CFD	Grain Structure, Crystal Orientation and Melt Pool Geometry	--	[172, 173]	

2.2.1. Cellular Automata (CA) Method

CA is a type of algorithm reflecting the states of a collection of cells based on transformation rules, the complex evolution of investigated area in discrete space happens automatically when the rules are applied iteratively. The conventional CA uses local rules where the instantaneous state/value of cellular is a function of its neighbours. Recently, variants of the CA method also consider intermediate or long-range interactions [174]. Even though each cellular consists of many identical simple components, together, they are capable of complex behaviour and can be used to simulate complex problems [175]. Unlike general dynamics models, CA is not strictly defined by physical equations, but by rules constructed with a set of models [176].

Typically, A CA model is composed of the cell, cellular state, cellular space, cellular neighbours, the function of rule and time. The local interaction between the cell and its neighbours (different types of neighbour algorithms are developed) is specified through deterministic or stochastic transformation rules. Considering two time steps of a one-dimensional CA as an example, the evolution of the model can be simply expressed as [174]:

$$\xi_j^{t_0+\Delta t} = f\left(\xi_{j-1}^{t_0-\Delta t}, \xi_j^{t_0-\Delta t}, \xi_{j+1}^{t_0-\Delta t}, \xi_{j-1}^{t_0}, \xi_j^{t_0}, \xi_{j+1}^{t_0}\right) \quad \text{Equation 2.1}$$

where ξ is the state variable of a cellular, j is the location subscript, t_0 is the time superscript, and Δt is the timestep. The value of an arbitrary state assigned to cellular at a time ($t_0 + \Delta t$) is determined by its present state ($\xi_j^{t_0}$) and/or its last states ($\xi_j^{t_0}, \xi_j^{t_0-\Delta t}$, etc.) together with the states of its two neighbouring cells.

When dealing with complex, dynamic, and random questions, CA has significant advantages due to its flexible definition of neighbour and action rules. Its application is not limited to a specific

area. Now, CA has been used to develop simulation models for sociology, ecology, computer science, physics, chemistry, and other subjects [175, 177, 178].

In the past 25 years, CA has successfully been used in microstructure simulations, for example, the static recrystallization [179-183], the dynamic recrystallization [184, 185] and the grain growth behaviours [112-114, 127, 186]. The first CA model to incorporate the solidification behaviour was developed in the 1990s [14]. These CA models, initially developed in 2D, were later extended to 3D and coupled with finite element (FE) heat flow calculations resulting in the so-called Cellular Automaton-Finite Element (CAFE) models [13, 14, 137, 187-190]. They are widely applied in investment casting [188], directional solidification [137] and an extensive range of microstructure evolution phenomena including dendrites, micro-segregation, defects in different alloy systems [71, 191-198]. Also, different kinds of defect formation in the casting production process during the last stage of solidification are controlled by CA simulations to achieve the desired microstructure [191]. With the rapid development of MAM, the CA method is also widely applied in the solidification microstructure simulations for MAM. For example, the CA method was used in a 2D numerical model to simulate the evolution of solidification grain structure during the laser MAM process in multiple layers (Figure 2-1a). The influence of the different heat source parameters on the resultant microstructure was also investigated [112].

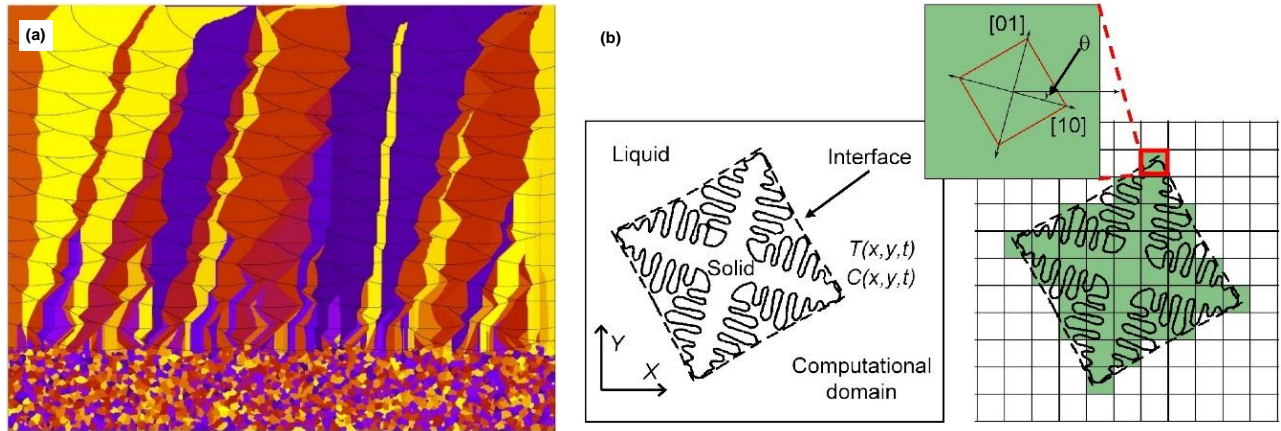


Figure 2-1 An example of 2D microstructure simulation using CA method: (a) SLM process which involves multiple layers of material deposited on a polycrystalline substrate (b) Schematic of single dendritic grain growth in the melt (left) and its CA representation (right). [112]

In terms of solidification microstructure simulation, a CA model is usually achieved by short-term relations or local rules. Every single grain defined by a specific crystal orientation and a nucleation position can develop on its own, and this self-organized behaviour will depict the grain boundary geometry as a result of the competitive grain growth.

The physical-based CA models predict the competitive grain growth behaviour and interactions between the grains under the dendrite tip growth kinetics. In the area of fusion zone and mushy zone, the total supercooling of a dendrite tip, ΔT , is the sum of four contributions

$$\Delta T = \Delta T_{th} + \Delta T_c + \Delta T_k + \Delta T_r \quad \text{Equation 2.2}$$

Where ΔT_{th} is the pure thermal undercooling for fluctuation of temperature at solid/liquid interface caused by thermal diffusion, ΔT_c stands for the undercooling contributions associated with solute diffusion, ΔT_k is the kinetic supercooling influenced by the rate at which atoms attach to the solid phase, ΔT_r is the curvature supercooling due to curvature of the solid-liquid interface, also called

Gibbs-Thomson supercooling. Based on the solidification situation, some contributions on the RHS of equation (3) are neglected in different cases. Then, the growth rate of both columnar and equiaxed grains is calculated as a function of supercooling with the aid of the KGT model [199]. The dendrite tip grain growth rate V_{tip} and its undercooling are related by using the solute supersaturation, Ω , as an intermediate variable under Ivantsov function of the solute Peclet number: $Iv(Pe)$. The relationship between dendrite tip growth rate and undercooling can finally be expressed as

$$V_{tip}(\Delta T) = \frac{D_L}{5.51\pi^2(-m(1-k)^{1.5})\Gamma} \left(\frac{\Delta T^{2.5}}{C_0^{1.5}} \right) \quad \text{Equation 2.3}$$

where V_{tip} is the dendrite tip growth velocity, D_L is the solute diffusion coefficient in the liquid, m is the liquidus slope, k is the partition coefficient, Γ is the Gibbs-Thomson coefficient, C_0 is the initial concentration, detailed derivation can be found in [200]. It should be emphasized here that the dendrite tip growth kinetics we derived above only consider the supercooling contributed by the solute diffusion (ΔT_c). In the case of MAM, the cooling rate is in the order of 10^5 K/sec and it usually leads to an enormous supercooling. So, the influence of supercooling due to grain tip curvature (ΔT_r) and kinetic supercooling are significant and cannot be neglected.

The crystal structure is another aspect that influences the dendrite geometry significantly [201, 202]. To reflect the preferential growth direction of grains (e.g., the $\langle 001 \rangle$ directions of prior beta in Ti6Al4V), Gandin and Rappaz [189] developed the decentered square growth technique in the CA method. The algorithm was then improved by Wang and Peter D. Lee to adapt coarser grids with a concomitant loss in resolution [140]. By using the decentered square growth algorithm, the crystallography symmetry and the orientation information are stored in each cell of the grain growth area (Figure 2-1b). Subsequently, the grain cells are capable of growing faster in their

preferential growth directions according to the total supercooling and reflect the competitive grain growth behaviour quantitatively.

2.2.2. Phase Field (PF) Method

PF method is a powerful computational approach to solve interfacial problems, such as micro and mesoscale crystal morphology and microstructure evolution [203]. It is widely applied in the research topics such as solidification [155, 163-165, 204], microstructure evolution [205, 206], grain growth [152, 161, 207], dislocation [208], crack propagation [209] and so on.

PF method is a continuum description of the free boundary problem which allows the interface to be smeared over a diffuse region for numerical expedience [210]. Order parameters representing the diffused interface can be used to locate the position of arbitrary and highly non-linear interfaces without explicitly tracking them. This avoids the difficulties led by the sharp interface descriptions (maximum velocity, marginal stability, microscopic solvability, interfacial wave) [211-214] in terms of topological complexity, phenomenon descriptions and so on.

In PF models, both the compositional/structural domain and the interface are described by a set of conserved and non-conserved field variables. Governed by Cahn-Hilliard [215, 216] nonlinear diffusion equation and the Allen-Cahn relaxation equation, the field variables are continuous across the interfacial regions, and hence the interfaces in a phase-field model can be diffused to avoid the problem of meshing the highly non-linear interfaces. This strategy can also be understood as metallurgical derivatives of the theories of Onsager and Ginzburg-Landau [174, 217]. In the phase field theory (diffuse interface), the total free energy can be described by

$$F = \int [f(c_1, c_2, \dots, c_n, \eta_1, \eta_2, \dots, \eta_n) + \sum_{i=1}^n a_i (\nabla c_i)^2 + \sum_{i=1}^3 \sum_{j=1}^3 \sum_{k=1}^p \beta_{ij} \nabla_i \eta_k \nabla_j \eta_k] d^3r + \iint G(r - r') d^3r d^3r' \quad \text{Equation 2.4}$$

where F is the total free energy of an inhomogeneous microstructure system, f is the local free-energy density, G is the function of the long-range interactions, a_i and β_{ij} are the gradient energy coefficients, $c_{1...n}$ are conserved field variables, $\eta_{1...n}$ are non-conserved field variables [218].

In equation 2.4, the gradient energy terms come into play at and around the interfaces and contribute to the total free energy. The way to treat the contribution from various terms to the total free energy is the main difference among different PF models [210, 219].

Crystallographic structures in metal are always representing a highly ordered phase in the format of bcc, fcc and hcp. For instance, the Ti6Al4V represents a bcc structure after the first order transformation from liquid to its beta phase. In a two-dimensional PF model, the fourfold surface energy anisotropy at the solid-liquid interface of a cubic system crystal can be given by

$$a(\theta) = 1 + \varepsilon \cos(4\theta) \quad \text{Equation 2.5}$$

where ε is the strength of anisotropy and θ is the interface normal direction [150].

When PF models are used to describe the crystalline materials, the basic principle is to use a free energy functional which is minimized by periodic density to represent the periodic and symmetrical nature of a crystal lattice [206]. PF method is also capable of simulating crystal grains with different orientations by introducing multiple order parameters, one for each orientation. An interaction term in the model can be tuned to control coalescence and grain boundary energy during the solidification process. However, the large number of crystal orientations also leads to an equal quantity of order parameters, which increases the computational cost. Due to the extensive computer power required by the PF method, there is a limited number of PF models implemented in a melt pool level, let along the whole MAM process. To solve this problem, considerable progress has been made in recent years to increase the efficiency of the PF method: In order to

keep the numerical scheme of the PF model efficient, a new formulation of free energy was derived in [145], and the solidification microstructure simulation was carried out in a region of multiple layers. [156] introduced the nonlinearly preconditioned quantitative PF formula to solve the evolution equations on a computational mesh coarser than those in the conventional method. The quantitative simulations of a large number of dendritic growths are carried out on the scale of centimetres. Parallel computing using GPU is another way to unchain the length scale limitation of PF, in [154], the problem of insufficient GPU memory was circumvented by employing an asynchronous concurrent algorithm. The competitive grain growth behavior was also studied in a 3D PF model under different crystal orientations (shown in Figure 2-2).

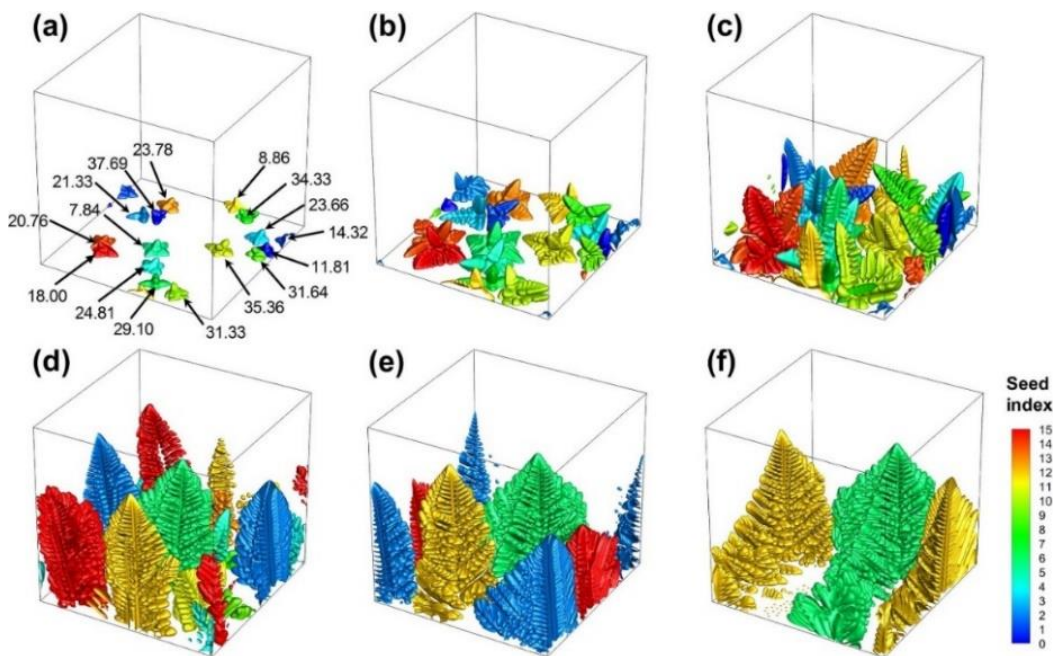


Figure 2-2 PF simulation on dendrite morphology evolution along with solidification time, colours indicate dendrites with different crystal orientations. [154]

To represent the periodic structure of metal crystals in the atomic scale, an extension of the PF method is introduced and known as the Phase-Field Crystal (PFC) method [220]. It describes the evolution of the atomic density of a system according to dissipative dynamics driven by free energy minimization. In the PFC approach, solid-phase free-energy density is also constructed to be minimized by periodic density states with crystal symmetries. PFC models are derived directly from, and thus inherit some of, the principles of classical density functional theory. So, it is still an atomic-scale model in space. On the other hand, its parameterization is not fully quantitative, which also hinders its application in practical problems including MAM.

2.2.3. Monte Carlo Method

MC simulations involve the use of random numbers and probability to solve complex problems based on trial and error. With the help of statistical theories, MC models are generally concerned with large numbers of numerical experiments using uncorrelated random numbers instead of deterministic algorithms. The main idea of solving state function integrals by randomly sampling from the non-uniform distribution of numbers was given by [221].

In the field of grain growth simulation, the MC method discrete computation domain for the same and regular patterns. Each grid in the simulation domain is assigned with an integer number representing different crystals. Those adjacent grids with the same crystallographic orientation belong to a single crystal grain. Based on the minimization of system free energy, the randomly selected nodes will change their orientations and be visualized as the grain growth behaviour. One thing to notice is that: this kind of MC model is only suitable for solid-state grain growth, for example, the recrystallization and second-phase precipitation [222-226]. The limitation of the MC method is obvious that the growth kinetics are not considered in the simulation.

To achieve the solidification microstructure simulation for MAM process, the KMC method is adapted to investigate microstructure developed at the melt pool bottom [168, 170, 171]. The microstructure developed by different process parameters is compared, e.g., the scanning speed influence on microstructure shown in Figure 2-3. The average size of the columnar grains in the fusion zone and the equiaxed grains in the heat affected zone was investigated and compared quantitatively with experiments. This can be attributed to the computational efficiency of the KMC method which can be launched in experimentally accessible time and length scales providing practical simulation results [227]. Due to the epitaxial grain growth in MAM, the grain growth from the liquid to the solid phase is simply treated as inheriting information from the partially melted grains according to the maximum heat flow direction. In the deposit layers, grain growth is simulated by KMC models as the migration of grain boundaries caused by the MC time [228].

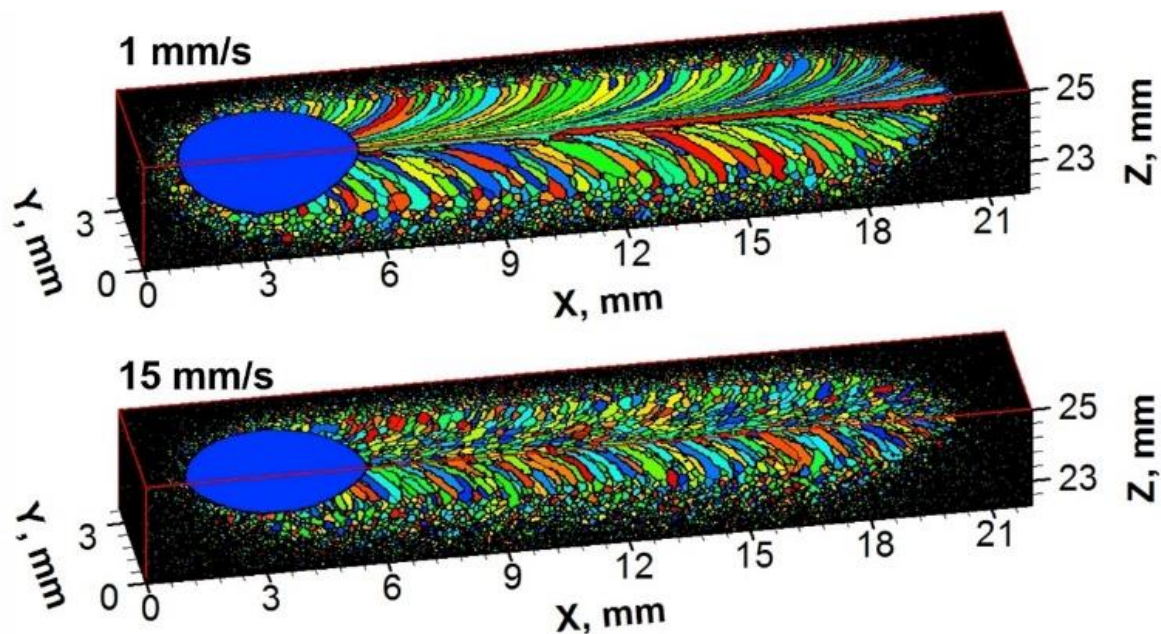


Figure 2-3 KMC simulation of grain structures in a weld with different scanning speeds. [170]

2.2.4. Needle-Network Method

In recent years, a novel dendritic needle network (DNN) method is introduced by [229] to unchain the scale limitation of the PF method. This model represents the primary and high order branches of dendrites by thin needles which develop their own solute diffusion field and interact with each other. The growth dynamics of the needle crystals are derived from the Laplacian growth theory [230]. The tip velocity and radius are computed by considering two conditions: the standard solvability condition on the scale of the dendrite tip and an additional flux balance condition on the outer scale of the dendritic network [231]. The target of this method is to bridge the scale gap between PF and CA methods in the area of dendritic microstructure formation. Different from the PF method, DNN does not focus on the tip scale solid-liquid interface but extends to the grain scale with an acceptable loss of accuracy. On the other hand, this method reflects the competitive grain growth in a more natural way than the CA method by considering both the history-dependent selection and the intergrain dendrite interactions. This model is implemented for both isothermal and directional solidification in 2D and validated by comparison with analytical solutions for equiaxed growth and PF simulations [231]. In their recently published works, a 3D version of needle-network was proposed and validated with an in-situ X-ray imaging of Al-Cu alloy solidification experiments [232].

2.3. Discussion and Perspectives

Until now, most research works on MAM microstructure simulation still focus on the deterministic methods based on experiments, for example, the effects of various process parameters on microstructure evolution in thermo-material models [17]. These models are sought by using the thermal history to predict microstructure evolution and the resulting temperature-dependent

material properties [56, 233, 234]. However, these methods are inadequate to describe the unique characteristics in MAM such as nucleation behaviour, column grains, epitaxial growth, and anisotropy of material behaviours.

The reviewed solidification microstructure simulation methods all have their merits as well as the essential defects when applied in MAM. CA is currently the most suitable one among the reviewed methods for the solidification microstructure simulation in MAM with a relatively lower computational cost than PF, and a more solid physical basis compared to KMC. It has recently been adapted as a module in commercial software (Ansys), which will accelerate its application and development significantly. To describe the grain growth behaviour, CA models are established based on the physics of dendrite tip kinetic to guarantee simulation accuracy. On the other hand, the CA method requires relatively low computation power, and the simulation can be applied to macroscale where it has more practical significances. PF method is firmly based on physical models, and it is capable of providing a high reproduction of reality. It is also capable of describing the subgrain features like high order dendrites, micro-segregation, solid-phase transformation and so on. However, PF models inherit minimal time and length scales from physical theories. The time steps of PF models are usually in the magnitude of microsecond or nondimensional number which must be small enough to stable the simulation result. Attaining a PF simulation even on a micrometre level requires massive computer power. A large amount of computation needed in the PF models makes it only feasible on supercomputers, therefore becoming an obstacle in the application. In order to simulate the grain competition during solidification, CA and PF methods have different strategies to endow the crystallographic structure of the grains considering their symmetry and preferential growth direction. KMC method has the advantage of efficiently simulating the migration of grain boundaries that occur in the solid-state, but the crystallographic

structures are not considered in most reviewed works, so its physical basis is not solid. It is also interesting to notice that the three methods start from different philosophical thoughts and methodologies but are applied to simulate the same objective in the case of MAM: CA method investigates the relationship between the part and the whole, it believes the physical state of the system is an aggregation of local state change; PF method attempts to describe the state of a system by field parameters continuously, so it can avoid the difficulties lead by the sharp interface; for MC method, it uses a large number of sampling to approximate the truth, step by step. Even though there are significant differences among the three methods, they are all developed rapidly, especially in the field of microstructure simulation for MAM over the past decade.

MAM fabricated parts are composed of a large number of welds, the microstructure in a single weld bead will finally decide the initial microstructure of MAM fabricated part at a specific position. Literature has already shown the importance of melt pool geometry to the final solidification microstructure in welding. It is very important to note that: the melt pool geometry is crucial for the resultant microstructure in MAM processes, and an accurate melt pool geometry is the prerequisite of an accurate microstructure simulation result. Solidification microstructure simulation for MAM must take proper consideration of melt pool geometry in terms of G&R and the boundary conditions established for each time step of the simulation. Melt pool geometry at the melt pool bottom is a curved surface to distinguish the solid and liquid phases. The thickness of this surface is the ambiguous area which is usually referred to as a mushy zone. The cooling condition along the melt pool bottom changes dramatically in terms of G&R, and in turn, influences the solidification microstructure developed subsequently. The melt pool geometry can be considered as a direct reflection of the cooling condition at the melt pool bottom, where solidification happens. Furthermore, the melt pool geometry follows the isothermal surface of the

material, and the maximum thermal gradient direction can be captured from the geometric method. Then, the thermal gradient direction which means the maximum heat flux direction should be compared with the preferential growth direction of the crystal to reflect the competitive grain growth behaviour accurately. Qualified CA and KMC work in MAM microstructure simulation always consider the melt pool geometry explicitly or implicitly. However, it is still a problem for PF models as these models calculate hundreds of millions of cells/time steps over millions of time steps to place out the physics of the process long enough to be relevant. That is the reason why the PF models are mostly operated under the “frozen temperature approximation” not a field form of temperature representing the melt pool.

The melt pool geometry can also be used to bridge the scale gap. It can validate the simulation result at a macro level and provide the boundary condition for the meso- and micro-level simulation. Some of the reviewed works used the melt pool simulation result directly as a boundary condition for solidification microstructure simulation. However, it usually leads to a more significant deviation when another simulation result is used as an input. Thus, the accuracy of these microstructure simulations is reduced as they do not have appropriate boundary conditions. Currently, highly developed techniques like CMOS camera [235, 236] and synchrotron X-ray [237, 238] can provide transient melt pool geometry with relatively high accuracy. These melt pool geometry reconstructions can be used as experimental validation for simulations and improve accuracy.

The nucleation rule for the solidification microstructure simulation in MAM is still an open question in the literature. The assumption of epitaxial grain growth with no nucleation can only be applied to a small number of extreme cases in MAM. For powder bed, external factors (e.g., impurity and cracks) leave more opportunities for the nucleation in each weld and cannot be

neglected. The contour of the melt pool always provides new nucleation positions for the solidification at the melt pool bottom. On the other hand, the grains in the DED process are typically considered to develop from the substrate, and the grains will stop growing at the contour without any new nucleation. This is close to the observed fact that the grains are able to develop extremely big and go through multiple layers, e.g., DED processed Ti6Al4V. Thus, in the case of the solidification microstructure simulations under “no nucleation assumption”, it is more reasonable to establish the boundary condition of crystallographic orientation by experimental results (e.g., EBSD) instead of a random orientation assumption at the substrate.

Competitive grain growth is the subsequent step following nucleation. When the research area of the melt pool bottom is divided into a very small length scale, the cooling condition can be considered as constant within a small timestep. The competitive grain growth of bi-crystal simulations is carried out under different methods and criteria where significant deviation on resultant grain boundary orientations is observed [239]. This is caused by the different assumptions and emphasis in different simulation methods: CA methods consider the problem on the kinetics aspect which links the dendrite tip growth rate with the supercooling; while the PF method is derived on the thermodynamic aspects to represent the pattern change along with the free energy minimization. Unfortunately, this deviation on grain boundary orientations will become even larger when these models are applied to a more complicated problem. For example, MAM microstructure simulation includes multiple crystals and a complicated cooling condition. A reasonable way to improve the microstructure simulation accuracy is the proper model validation as well as the database establishment for each recognized phenomenon during the physical process.

The rapid solidification phenomenon makes the solidification microstructure simulation in MAM more difficult, especially the highly non-equilibrium phase transformation and the solute trapping

effect in alloy systems. Typically for the DED process, it is believed to have a grain growth rate geometrically related to laser scanning speed because the melt pool geometry is relatively stable. However, for some rapid scanning MAM processes in PFB, whether the solidification rate can still catch up with the scanning speed is still an open question in the literature. In the CA method, the dendrite tip growth kinetics typically assume local equilibrium which is not valid under rapid cooling conditions. Another problem for CA models is that they typically use one layer of cells to represent the interface between liquid and solid with a solid fraction from zero to one [240], so it is difficult to naturally represent the solute trapping phenomenon. Also, as a rule of thumb, the cell size should be at least ten times smaller than the morphological features it captures. This methodology provides the CA method with high computational efficiency, however, limits its smallest morphological length scale to depict finer microstructures (e.g., higher-order branches) compared to the interface thickness. PF method is very quantitative in its description of solid-liquid interface kinetics. Recently, a work [118] introduced a strategy to quantitatively map the thin interface behaviour of an ideal dilute binary alloy PF model on the continuous growth model. This strategy can be implemented in different phase field models, which will address this problem to a fair degree.

The simulation model for solid-state phase transformation also referred to as the thermo-microstructural model, is an indispensable part of the mechanical property prediction in MAM. It can be combined with the solidification microstructure simulation result then achieve the mechanical property prediction with failure models. These simulation efforts attempt to use the local thermal history data (e.g., the thermal cycles profile in MAM) to predict the material-dependent microstructural evolution including phase fraction and morphology [56, 241-247]. Recently, the density type simulation methods have been generally used for predicting

microstructural evolution during solid-state phase transformations in MAM, especially for large-scale thermal/mechanical/metallurgical coupled problems. The phase fractions of diffusional and diffusionless phase transformation products and dependent properties could be effectively predicted using these methods if they are calibrated, accurately [248].

Model validation is essential for all kinds of simulation works. For the solidification microstructure simulation in MAM, however, the solid-state transformation, secondary or higher-order branches merging, and the migration of grain boundaries brings great difficulties to recognizing the original state and pattern of the solidification microstructure. Even though the reconstructed EBSD results provide accurate information in terms of crystallographic orientation and texture, they are only able to show the obscured grain geometry with no high-order branch. Also, the grain geometry recognized by EBSD, and the microscopes are usually operated at room temperature when the migration of grain boundaries has already occurred after the thermal cycles of MAM.

2.4. Chapter summary

Developing a robust and accurate simulation model on a long scale to describe the grain growth behaviour in a moving melt pool is still a challenge for MAM solidification microstructure simulation. An overview of all the microstructure simulation methods indicates that it is indeed important to develop an integrated and generalized model for MAM process, as a function of melt pool geometry and resultant microstructure. This Chapter further explains the sequential dependency of each physical process during the solidification of MAM that is still open questions in the literature. To achieve an accurate simulation, database establishment between the recognized phenomena is the ideal method to fill these gaps so far. It is also important to know that making a model with all the expected outcome does not lead to novel insights. As for the microstructure

simulations in MAM, it is better to develop models carrying fundamental rules or model components from which more complex grain structure and texture can develop on their own. Otherwise, the simulation models are not predictive and are just pictures without new understanding.

Chapter 3. The proposed methodological framework

A comprehensive review in Chapter 2 indicates the need for a robust and practical model that is able to deterministically predict the solidification microstructure in MAM processes, especially the columnar grains in laser wire fabricated Ti6Al4V. Different from the probabilistic methods, a computational efficient microstructure simulation model, named invasion model, is established to quantitatively analyze the solidification microstructure in the DED process. The framework of the solidification microstructure simulation of Ti6Al4V in laser wire DED is shown in Figure 3-1, before the implementation of invasion model, the melt pool geometry and crystal orientation reconstruction are needed. With the transient grain boundary tilt angle predicted by the invasion model, solidification microstructure can be reconstructed and compared with the experimental result quantitatively.

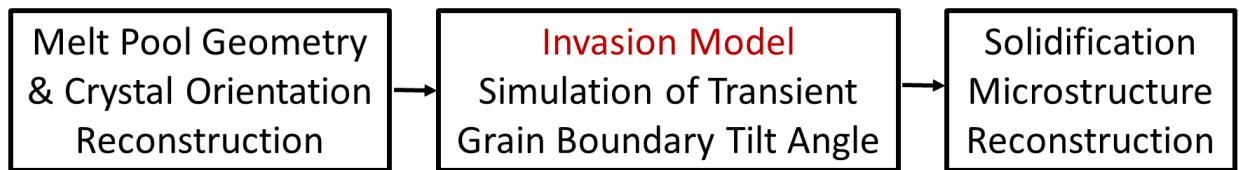


Figure 3-1 Framework of the solidification microstructure simulation of Ti6Al4V in laser wire DED

The overall modelling framework of applying the proposed invasion model is shown in Figure 3-2. The simulation scheme starts from the reconstruction of the transient melt pool geometry as it is a direct reflection of the solidification conditions. The crystal orientation information extracted from EBSD is then combined with the solidification conditions and form the three inputs to the ANN model. The predicted grain boundary angles within the bi-crystal systems at each timestep depict the overall solidification microstructure in the simulation domain. Together with the

information of solid-phase composition and process defects, the properties of the printed part can be predicted.

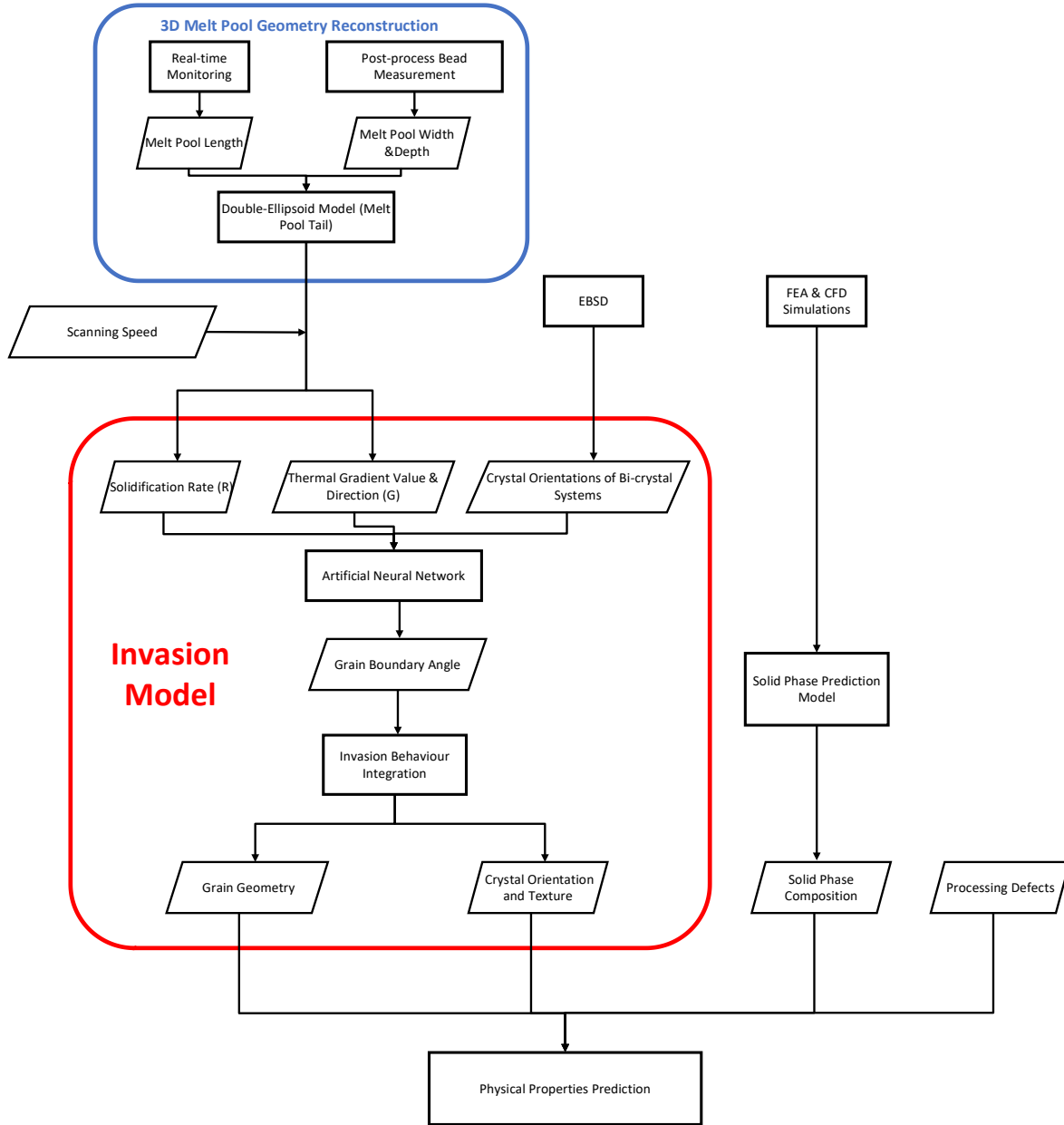


Figure 3-2 Flow chart of the microstructure simulation for Ti6Al4V in laser wire DED applying invasion model

In this thesis, the grain geometrical structure of the primary beta dendritic columnar grains in laser wire DED fabricated Ti6Al4V is the simulation target. The microstructural simulation work is implemented under the following assumptions: (1) The prior beta grains are perfect body center cubic single crystals with no defect and sub crystal above the alpha-beta transfer temperature. (2) There is no nucleation behaviour or other factors that can introduce crystals with new crystal orientation along the material deposition process. (3) Melt pool geometry does not change in a single weld and the transport phenomena within this melt pool is a stable state problem. This research only focuses on the solidification microstructure prediction section, and the explanation of the sub-steps in the simulation scheme is provided in the following paragraphs.

DED parts are composed of a large number of welds. The microstructure of DED fabricated components depends strongly on the cooling condition of the melt pool and the solid phase transformation in a single weld. Thus, an accurate melt pool reconstruction is the first step of the solidification microstructure simulation scheme. The real-time monitoring data and simulation results from the finite element method (FEM) or CFD are the two options for melt pool reconstruction. This thesis selected the experimental way to extract the key factors of a melt pool geometry including length, width and depth (Chapter 4.2 & Chapter 5.4). The width and depth of the melt pool can be gathered from the post-process bead measurement (Y-Z cross-section samples), and the real-time monitoring thermal data indicates the length of the moving melt pool (as shown in Chapter 5.7). To calculate the transient solidification rate and temperature gradient located at the bottom of the melt pool, a double-ellipsoid model is adapted for both experimental data gathering (Chapter 4.3) and invasion model (Chapter 5) to represent the geometry of the melt-pool tail at each discrete time step. Combining with the scanning speed, the solidification rate (R) and thermal gradient (G) can be derived.

The crystal orientations of the bi-crystal systems are detected via EBSD characterization on corresponding cross-sections (Y-Z and X-Z). G&R together with the crystal orientation information of the bi-crystal systems are selected as the input features for an ANN model and the regression relation is established between these three features and the resultant grain boundary angles. Considering the influence of the flowing fusion to the constitutional supercooling on the side of paralleling dendrites, a Marangoni effect correction is included for the case of X-Z plane in the model instead of the direct input as a feature (Y-Z plane) for the ANN model. The experimental data gathering process of the invasion model is described in Chapter 4.3, there are 50 training samples collected on the X-Z and Y-Z plane, respectively. After the ANN model is trained, the regression relation found is used as the engine to drive the solidification microstructure simulation.

By calculating all the grain boundary angles at the transient solidification fronts, the competitive grain growth is understood as the “invasion behaviour” between the bi-crystal systems. An ‘invasion factor’ which means the distance (or cell number) that one single crystal can invade its adjacent crystals in a single time step is introduced in Chapter 5.5. Following this, the integration of all the invasion behaviour depicts the solidification microstructure including grain topology structure (prior beta), crystal orientation and texture.

For a three-dimensional solidification microstructure simulation validation, the simulation domain is discretized into uniformed square cells. The invasion model is implemented on the X-Z and Y-Z cross-sections sequentially. In most of the related literature, the substrate is set up with equiaxed grains with random crystallographic orientation which is the basic reason that the simulation result cannot compare with the experimental quantitatively. This thesis used the reconstructed EBSD result on the substrate section as the boundary condition, so the grain structure can be compared

quantitatively. The model verification is carried out for a simple bi-crystal case in Chapter 5.6 to test whether the methodology of the invasion model can accurately represent the grain boundary angle. The convergence analysis of the model will be implemented on different cell scales and time step lengths. A selected area in laser wire DED fabricated Ti6Al4V thin wall structure under the assumptions is used to test the validation of the proposed invasion model. This area is carefully selected with no nucleation and other factors introducing new crystals into the domain during the process. The grain structure and size are compared quantitatively between the simulation and experimental results.

Based on the observation that CET is not achieved in the fabricated parts and recrystallization provides the additional crystals for epitaxial grain growth, it is logical to investigate the competitive grain growth first and then discuss nucleation (introduce new crystals in the process). This is also the sequence of this thesis. As the recrystallization introduces new crystals into the printing domain and influences the solidification microstructure dramatically, the experimental investigation of the recrystallization phenomenon is carried out in Chapter 6 based on the three hypotheses (contamination, heat and stress accumulation, solid-phase transformation) and the early stage of the recrystallized crystals is detailed investigated in Chapter 6.4.2.

Chapter 4. Machine Learning-Enabled Competitive Grain Growth Behavior Study in Laser Wire DED Fabricated Ti6Al4V

4.1. Introduction

This Chapter presents an ANN model to investigate the relation between grain boundary tilt angle and three causative factors, namely thermal gradient, solidification rate and crystal orientations. A series of wire feedstock DED, optical microscope and EBSD experiments were carried out under experimental design to gather the training and testing data for the ANN. It is the first time that the competitive grain growth behaviour is studied by a data-driven approach. Compared to conventional microstructure simulation methods, the strategy and ANN model developed in this work was demonstrated to be a valid way to describe the competitive grain growth behaviour in DED fabricated Ti6Al4V. They can be deployed to achieve a quantitative microstructure simulation and extended to other polycrystal material solidification processes.

4.2. Methodology

This model believes that a grain boundary angle, under an absolute coordinate system, tilts from the buildup direction because of three causative effects: solidification condition (G/R), Marangoni effect and crystal orientations. These three effects on a two-dimensional cross-section will be converted and presented as angles that indicate their effects on the resultant grain boundary tilt angle. The advantage is that angles are non-dimensional numbers that can be directly multiplied by their influencing coefficients and added with each other without considering the scale. During the alloy solidification of the DED process, the Marangoni effect results in the circulation of fusion within the melt pool and affects the solute concentration. This solute concentration change beside the growing dendrites provides different constitutional supercooling, thus resulting in a vertical

grain growth velocity. This effect is studied as an input to the ANN model for Y-Z plane samples. And on the X-Z plane, the detailed analysis is provided in Chapter 5 and a correction of grain boundary angle is used to counteract the grain boundary tilt because of the Marangoni effect. Before the implementation of the invasion model in a DED case, the grain boundary angle caused by the Marangoni effect is added to the predicted grain boundary angle from ANN.

Several assumptions are made in this model to make the data gathering and ML process more practical.

- The material deposition in the DED process is assumed to be a full epitaxial grain growth without any nucleation. In the network experimentation, data is only gathered between the bi-crystals that are not influenced by nucleation or other crystal introducing effects.
- The melt pool tail bottom geometry is under double ellipsoid consumption and the geometry is stable during the material deposition process [249]. This allows a mathematical expression of the melt pool geometry which makes the data gathering process and calculation more efficient.
- Subgrain structures, for example, the secondary and higher-order dendrites, are ignored because the solid phase transformation eliminates the original solidification microstructure of DED fabricated Ti6Al4V.
- The solidification front is assumed to be strictly attached to the isothermal surface of solidus temperature [250]. The reason for this assumption is that the high thermal gradient achieved by the DED process compresses the mushy zone into an extremely thin film where its thickness can be ignored.
- The grain boundary migration caused by reheating during the solid-state is ignored.

Following the methodology illustrated in the flow chart (Figure 4-1), laser wire DED fabricated Ti6Al4V samples with cross-sections on X-Z and Y-Z planes are used to extract data and train the ANN model. After optimizing the network's hyperparameters and determining the training configurations leading to the smallest testing error, the trained ANN model can be used as an engine for the prediction of grain boundary tilt angle with experimental or hypothetical data as an input.

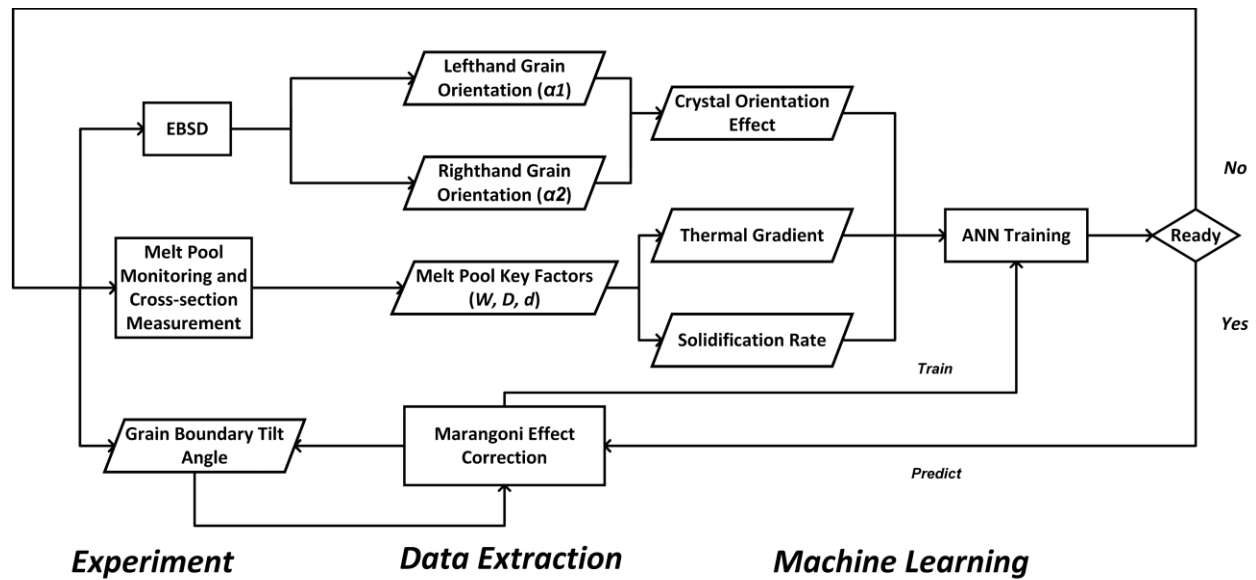


Figure 4-1 Flow chart of the methodology of the ANN model establishment for X-Z plane

Experiments including real-time monitoring, melt pool cross-section observation, EBSD and grain boundary tilt angle measurement are carried out, then fit the assumptions and simplifications made. The three causative effects demonstrated in Figure 4-2 are vectors representing the benchmark of each effect. The coordinate systems for thermal gradient direction measurement and EBSD characterization are exactly under the same Cartesian coordinate system: The X axis refers to the scanning direction of the melt pool, the Y axis to be the normal direction of the X axis on the

horizontal plane, and the Z axis is the build-up direction of the DED process. This guarantees the appropriate vector correlation between the three causative effects. The EBSD experiment and data process strategies will be explained in detail in the experimentation section. $\langle 001 \rangle$ direction tilt angle of the left-hand side and right-hand side grains in a bi-crystal system will be extracted.

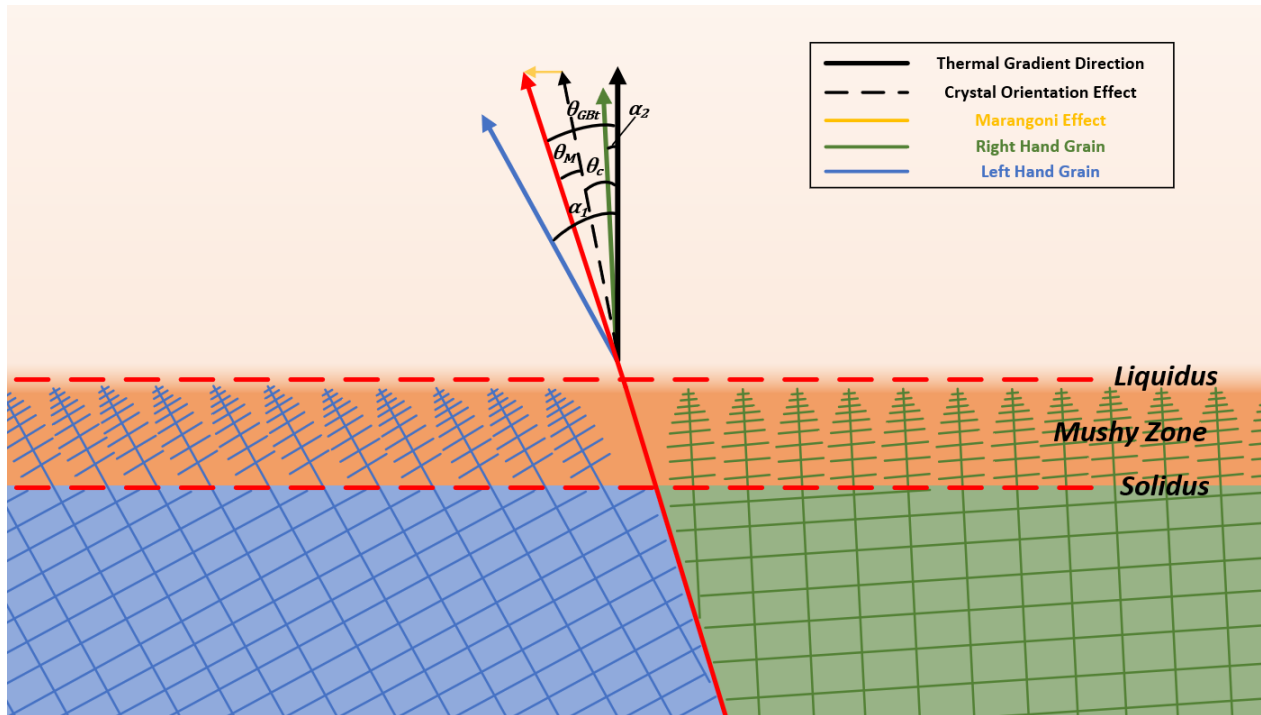


Figure 4-2 Local solidification condition for a bi-crystal system in MAM.

Melt pool geometry is vital for the solidification microstructure developed in the DED process and the melt pool bottom geometry is a direct reflection of the solidification condition. In order to accurately measure the thermal gradient direction from experimental specimens, key factors including melt pool width (W), depth (D-d) and geometric tangent direction at the melt pool boundary are measured from fusion lines in the Y-Z cross-section of the samples to reproduce the 2D melt pool bottom geometry. The tilt angle of the melt pool from the build-up direction is also

measured when there is an overlap between adjacent welds (as the Y-Z cross-section shown in Figure 4-3). This melt pool tilt angle does not exist on the X-Z cross-section samples as the thin wall structures are all fabricated under single track multiple layer configurations with constant scanning direction. The thermal gradient direction measurement only takes place at the region where the actual melt pool bottom boundary (fusion line) perfectly matches with the ellipsoid analytical equation. Following the “double ellipsoid approximation”, the segment of an ellipsoid can be mathematically defined by:

$$\frac{x^2}{L^2} + \frac{y^2}{W^2} + \frac{(z-d)^2}{(D+d)^2} = 1, \quad (z \leq 0) \quad \text{Equation 4-1}$$

Where L is the length of melt pool tail, with W being half the maximum width, D being the maximum depth of the melt-pool, and d is the displacement in the buildup direction.

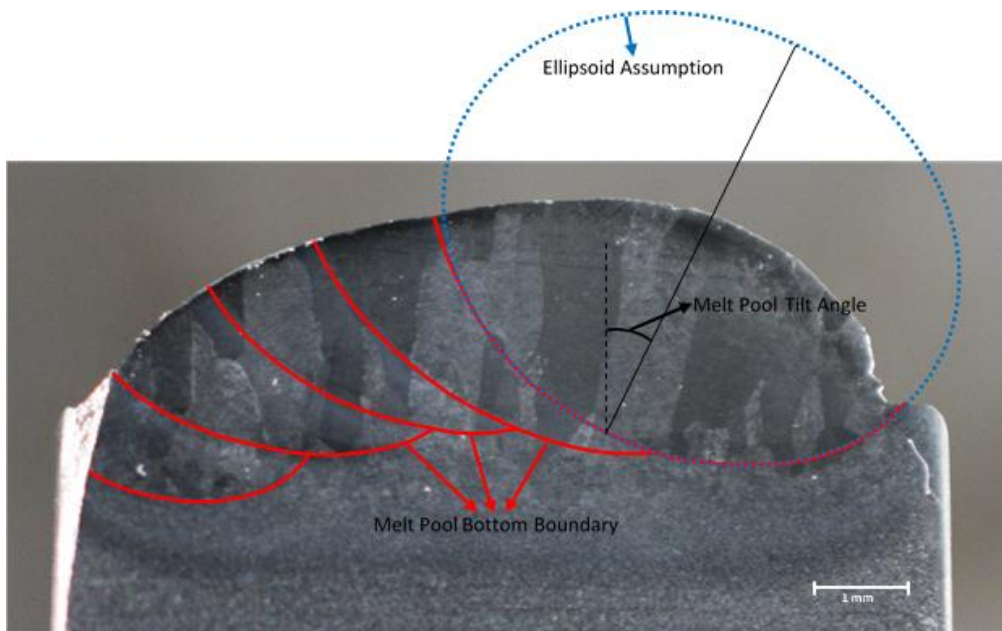


Figure 4-3 Comparison between the experimental melt pool bottom geometry (red) and the analytical solution (blue) in the Y-Z plane.

The boundary shape of the melt pool is closely related to the Marangoni effect that is triggered by the variable surface tension due to temperature and/or solute concentration gradients. The molten metal tends to flow from low surface tension areas to high surface tension areas. If free convection is not significant, a shallow but wide melt pool can be seen when the surface tension-temperature coefficient is negative, while a deep but narrow shape is present with a positive relationship. For relationships such as concave or convex surface tension-temperature profiles, more complex melt-pool profiles are expected. In the case of DED fabricated Ti6Al4V, the surface tension-temperature coefficient is negative. Hence, the molten metal from the laser exposure area with higher temperature tends to flow towards the boundary of the melt-pool and result in a shallow but wide melt pool geometry, as represented in Figure 4-4.

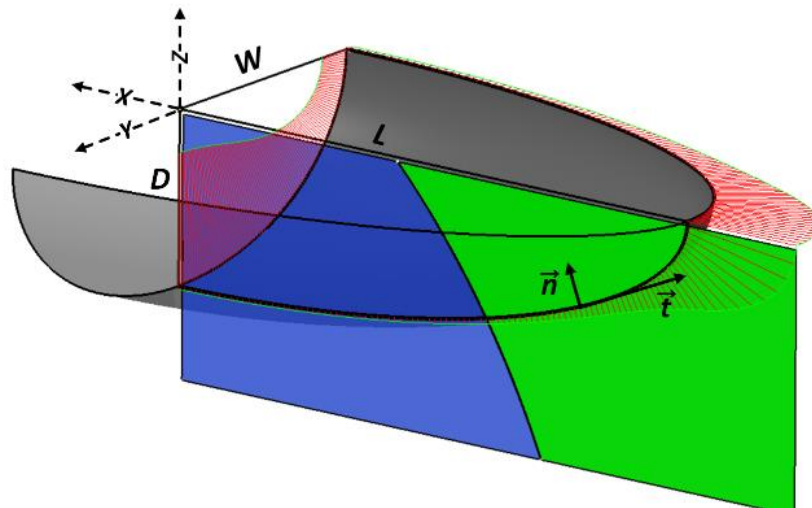


Figure 4-4 Schematic representation of 3D melt pool geometry with the normal direction (n) and tangential direction (t) at the melt pool bottom

The liquid flow was proven in previous work to have an influence on the solidification microstructure [251] and grain growth direction [252]. A schematic representation of the Marangoni effect in DED fabricated Ti6Al4V is shown in Figure 4-5. This can be attributed to the

influence of liquid flow on the solute concentration at the liquid and solid interface, which leads to constitutional supercooling and affects the growth kinetics of grain tips. As one input of the ANN, both tangential direction (dz/dy) and its opposite directions at the melt pool bottom are considered to limit this effect for the Y-Z plane samples. Another reason why the melt pool bottom geometry is vital to the resultant microstructure in DED is that it is a direct reflection of the thermal gradient direction. The normal direction of the liquid and solid interface, which indicates the maximum thermal gradient direction, provides the greatest driven force for grain growth and the grain boundaries naturally tend to follow the thermal gradient direction. In this work, the X-Z plane represents the cross-section vertical to the Y direction located at the center of the thin wall structure, and the Y-Z planes are the cross-sections vertical to the scanning direction (X direction). The negative reciprocal value of dz/dy is the tangent value of the thermal gradient direction on the Y-Z plane. The principle is the same on the X-Y and X-Z plane and the thermal gradient direction is shown as the red filament in Figure 4-4 with their length representing the local curvature.

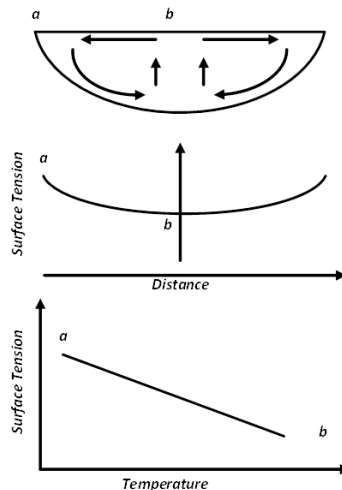


Figure 4-5 Schematic representation of Marangoni convection in a melt pool of DED fabricated Ti6Al4V with negative surface tension-temperature coefficient

4.3. Experimental Data Gathering

The samples were fabricated with a 1 kW YAG solid fibre laser automated welding system (LAWS 1000) using Ti6Al4V ELI wire feedstock under an Argon gas protection environment. Taguchi experimental design is used to fabricate the samples and gather the data on the Y-Z plane, and the orthogonal arrays are shown in Table 4-1. The process parameter in terms of laser power, scanning speed and feeding rate is separated into three intensity levels. The spot size used in this thesis is constant with a diameter of 0.9 mm. Due to the intellectual property concern, the detailed deposition process parameters on the Y-Z plane can not be disclosed.

Table 4-1 Taguchi experimental design orthogonal arrays for Y-Z plane sample fabrications

Deposition on hot-roll Ti6Al4V substrate				Deposition on the existing layer			
Specimen Number	Parameters			Specimen Number	Parameters		
	Laser Power	Scanning Speed	Wire Feeding Rate		Laser Power	Scanning Speed	Wire Feeding Rate
YZ_1	1	1	1	YZ_10	1	1	1
YZ_2	1	2	2	YZ_11	1	2	2
YZ_3	1	3	3	YZ_12	1	3	3
YZ_4	2	1	2	YZ_13	2	1	2
YZ_5	2	2	3	YZ_14	2	2	3
YZ_6	2	3	1	YZ_15	2	3	1
YZ_7	3	1	1	YZ_16	3	1	1
YZ_8	3	2	1	YZ_17	3	2	1
YZ_9	3	3	2	YZ_18	3	3	2

Similarly, 9 thin wall structures are selected from the fabricated samples to gather the data on the X-Z plane. The data gathering samples do not have a requirement on the dimensions of the thin

wall. Typically, the samples used in this research have a length of 60 mm, an average thickness of 2 mm and a height of more than 180 layers of deposition (around 110 mm). The printed samples have fully dense (100%) with no cracks and porosities. All the samples are cut from the center plane (X-Z) for characterization. The process parameters design shown in table 4-2 does not straightly follow the Taguchi experimental design as a successful thin wall structure fabrication needs some process parameter tuning.

Table 4-2 Experimental design arrays for X-Z plane samples

Deposition on hot-roll Ti6Al4V substrate			
Specimen Number	Parameters		
	Laser Power	Scanning Speed	Wire Feeding Rate
XZ_1 – XZ_3	625 W	16.9 ipm	35 ipm
XZ_4 – XZ_6	650 W	16.9 ipm	50 ipm
XZ_7 – XZ_9	750 W	16.9 ipm	63 ipm

To achieve the different cooling conditions for the melt pools, the DED experiments are carried out from substrate (specimens YZ_1-9 in Figure 4-6) and existing layer (specimens YZ_10-18).



Figure 4-6 Specimens fabricated via wire DED process under the Taguchi experiment design for Y-Z plane data collection.

For microstructural observation, the as-fabricated samples were cut along X-Z and Y-Z cross-sections and polished. Then, the cross-sections were etched in an etchant (5% HF, 5% H₂O₂ and 90% H₂O) for 15s. After that, an OM (Keyence digital microscope) was used to achieve a metallographic structure observation at several millimetre levels. The following observation of the microstructure in the laser wire DED fabricated part is first launched on the overview of the geometry of the prior beta columnar grains and compared with the microstructure of the substrate (hot-roll Ti6Al4V metal sheet). Then, it is focuses on the grain boundary area of the prior beta

grains and shows how the grain boundary tilt angle is measured which is the prediction target of this machine learning model.

As shown in Figure 4-7 and Figure 4-8, the columnar beta grains in DED fabricated Ti6Al4V are generally parallel with the build-up direction. The column grains are able to go through the weld bead boundaries (epitaxial grain growth) and achieve a width of 500 μm , even up to several millimetres in length.

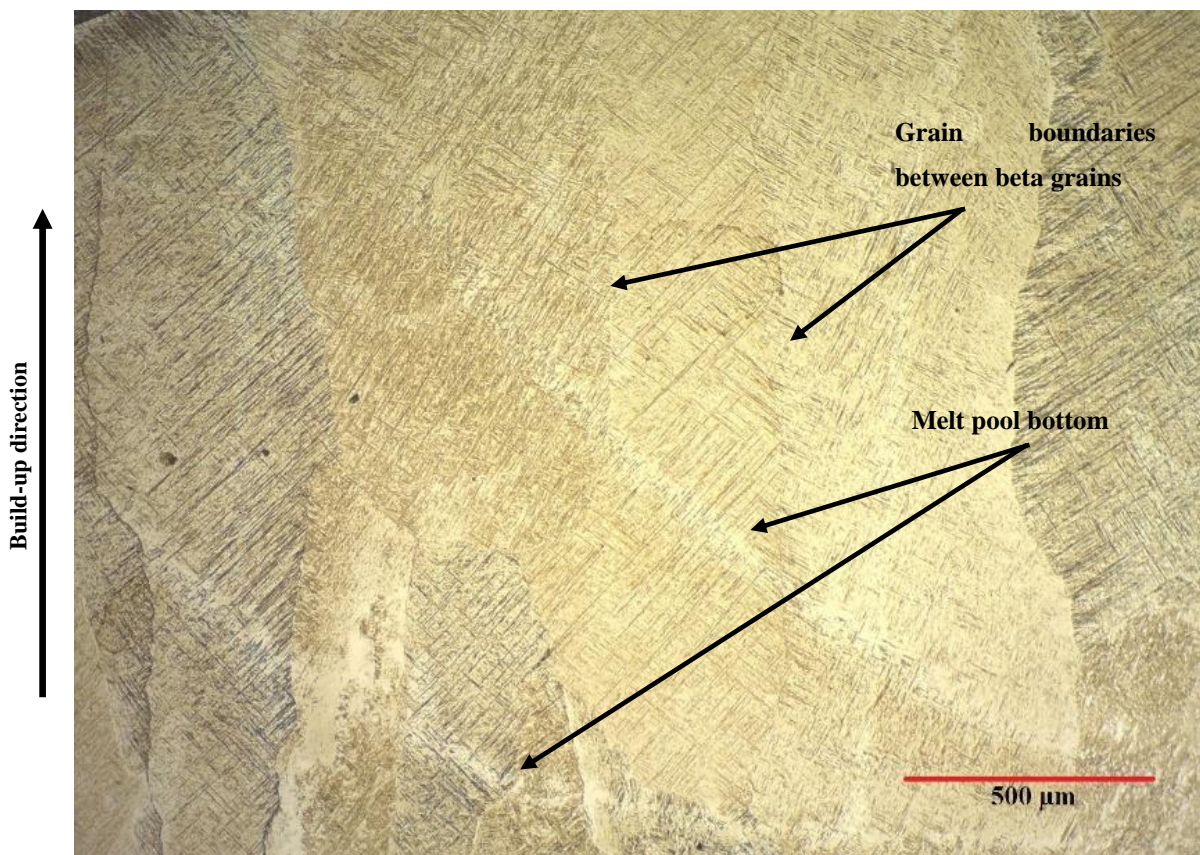


Figure 4-7 Optical microscope image of columnar beta grains on the Y-Z plane

The columnar grains are also observed from the X-Y cross-section to have a full view of the prior beta in laser wire DED Ti6Al4V. In Figure 4-8, an equiaxed prior beta structure is observed. Combining with the X-Z images, an intuitive of the 3D topological structure of the prior beta grains

can be obtained. A 3D grain topological reconstruction is also shown in Chapter 6 to investigate the crystal introducing mechanism.

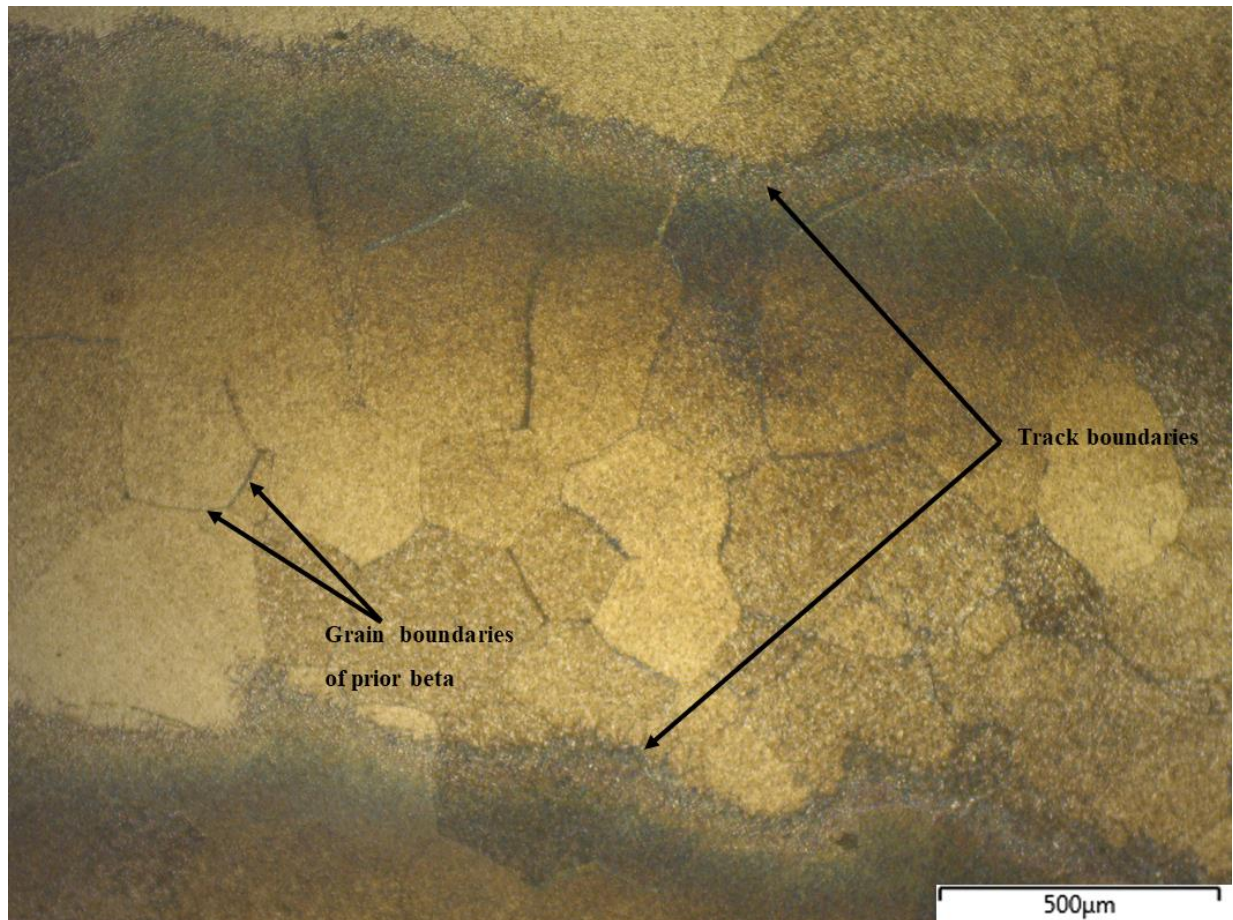


Figure 4-8 Grain structure on the X-Y plane

Under the as-build condition, the solid phase in the column grains is fully martensite with the orthogonal patterns indicating the column grains with different crystal orientations. The grain boundary angles were measured from OM images with an image segmentation software (Dragonfly). The measurement used a 200 μm line as benchmark length at the melt pool bottom and ignored the grain boundary fluctuation in the melt pool center for the Y-Z plane samples.

For a grain boundary angle measurement on the X-Z plane, the image stitching technique is used to achieve an observation on a larger scope (Figure 4-9). The scanning direction and build-up direction of the sample fabrication are shown in the figure, the horizontal white bands are the layer boundaries which are also understood as the bottom of the melt beads. The vertical patterns represent the prior beta grains, as the crystals with different crystal orientations have a different etching resistance and capacity of the light absorption, these patterns are easily recognized from the samples.

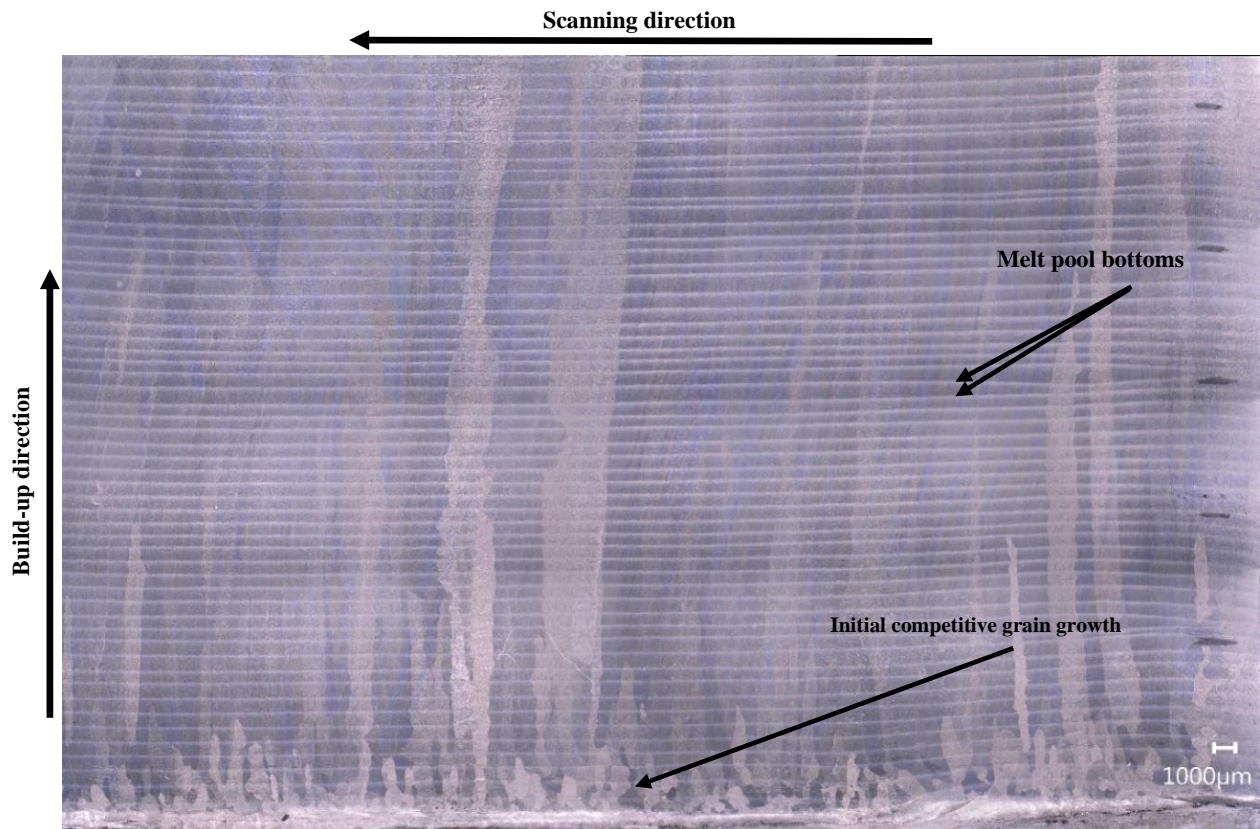


Figure 4-9 Optical microscope image stitching of columnar beta grains on the X-Z plane, layer 0 to layer 50 indicated by the black mark on the right every 10 layers.

The microstructure of the substrate is shown in Figure 4-10 with an average grain size of 16 μm . The ultrafine-grained Ti6Al4V hot roll substrate presents a typical equiaxed duplex phase

microstructure. It consists of equiaxed prior alpha titanium grains and Widmanstatten colonies. These colonies could be characterized by lamellar structures (alpha/beta colonies) with beta phase in-between the colony boundary.

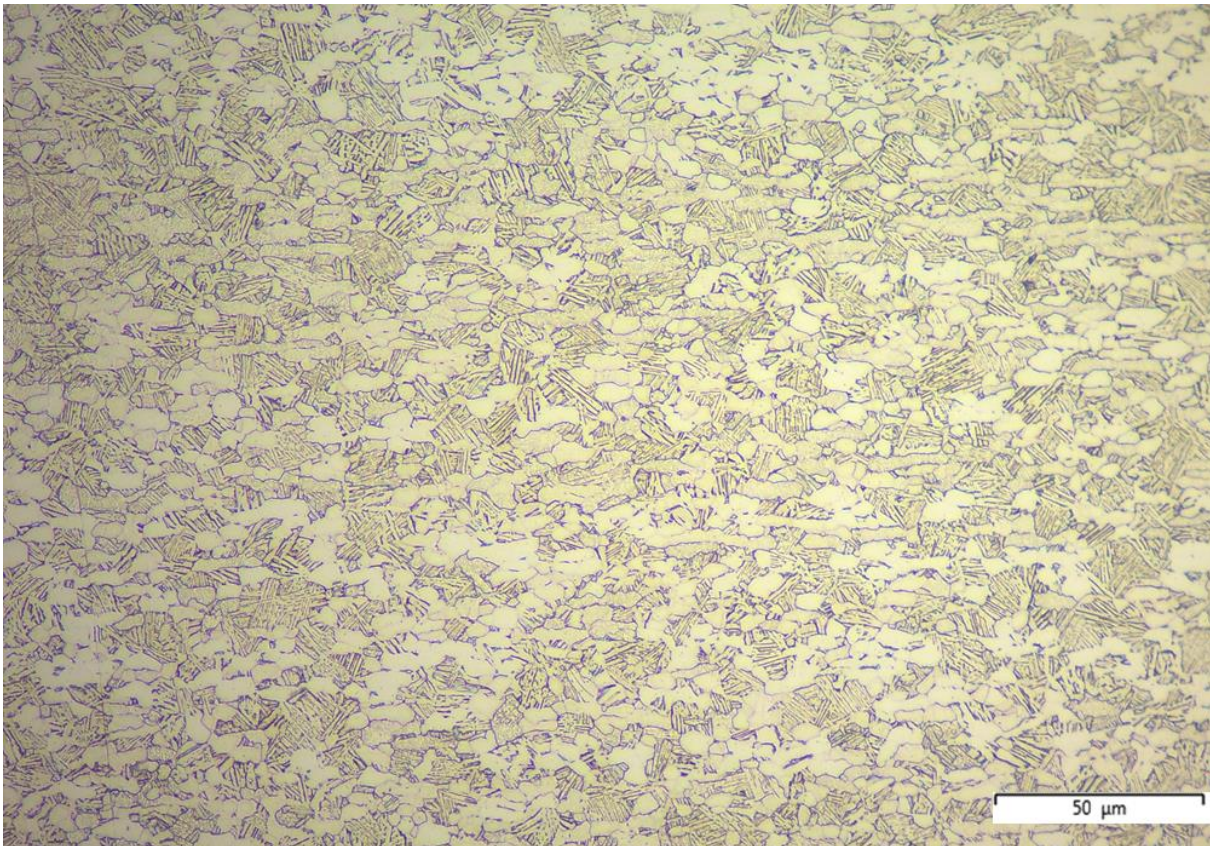


Figure 4-10 Optical microscope image of duplex phase microstructure in the hot roll substrate.

In the first several (7-10 layers) layers of material deposition, the newly deposited material epitaxially grows from the hot-roll substrate. And in this section of material deposition, as shown in Figure 4-11, the grain size immediately increases to the millimetre level. After this, the selected columnar grains with their preferred grain growth direction approximately parallel with the

thermal gradient directions develops further into the printed domain. The efficiency of competitive grain growth decreases from here as the textured crystals emerge.

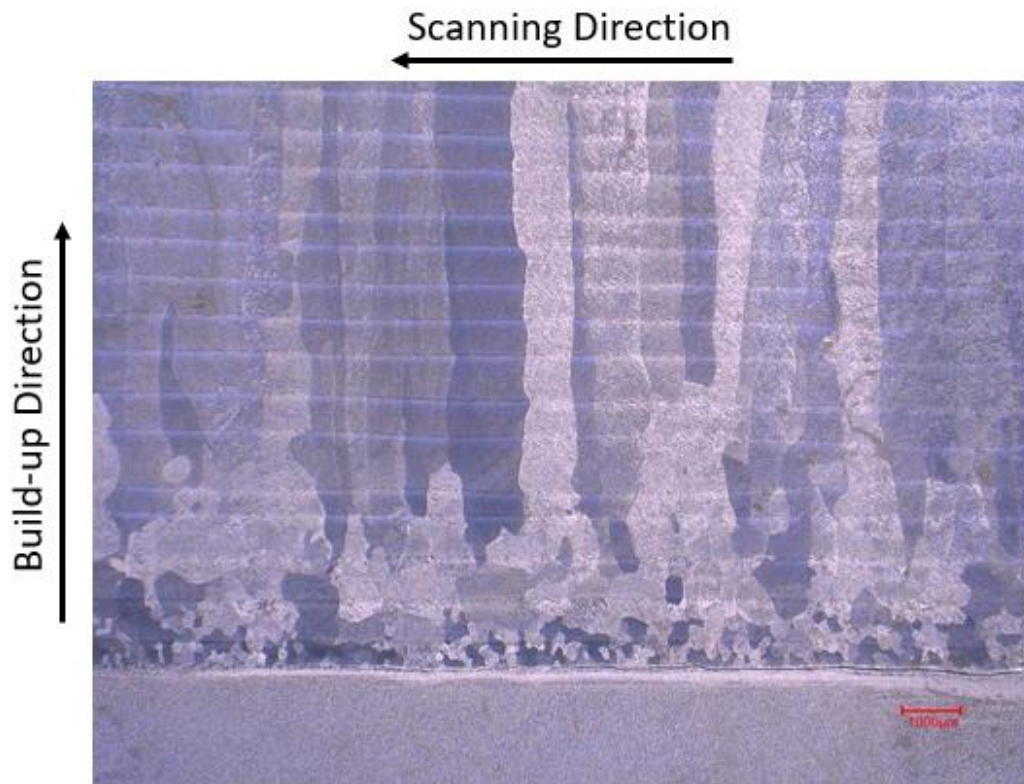


Figure 4-11 Optical microscope image of the initial competitive grain growth at the initial several layers of material deposition.

As shown in Figure 4-12, the crystal geometrical structure is more stable in the center area of the printed thin wall structure. The horizontal black bands are the layer boundaries and there are a total of 19 layers of material deposition represented in the figure. The grain boundary presents a straight line even with tens of layers of material deposition, this is the basic reason that the grain boundary angles in laser wire DED fabricated Ti6Al4V can be modelled quantitatively.

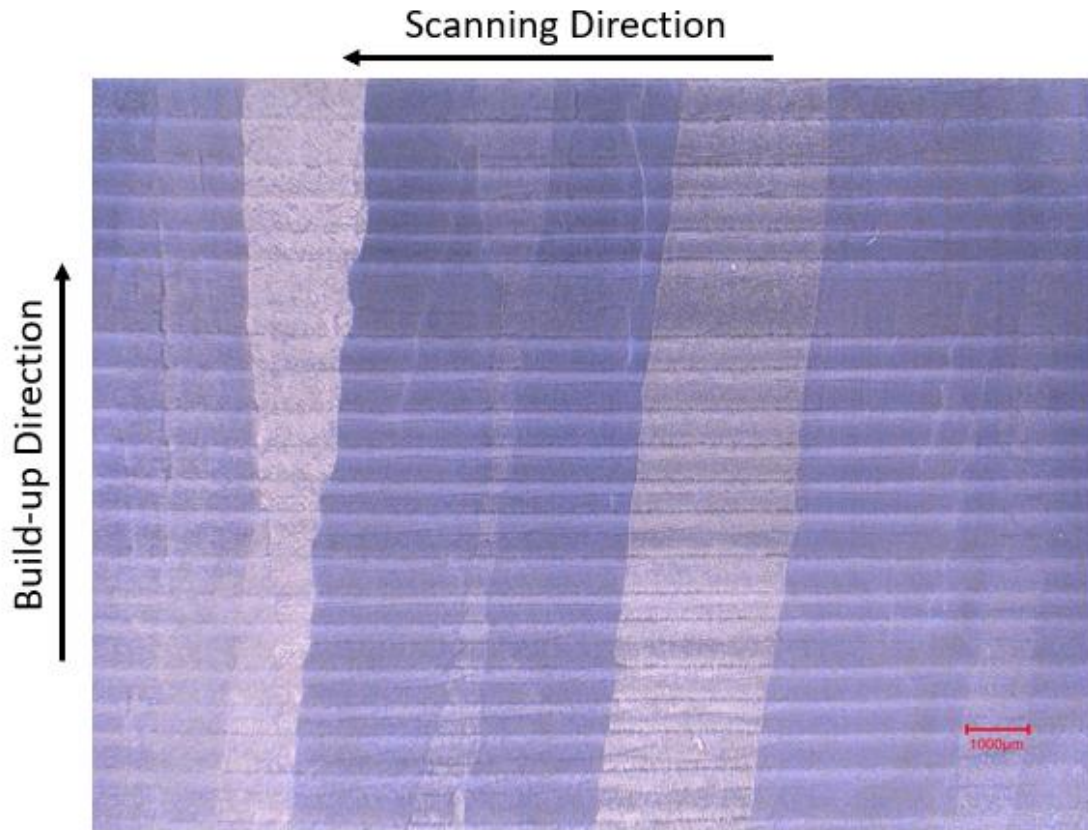


Figure 4-12 The crystal structure in the center of the printed thin wall structure

The grain boundary angles measurement on the X-Z plane from OM images is also achieved under Dragonfly. To get a more stable and representative grain boundary angle result, the measurement used a length of 10 layers of material deposition (around 7 mm) as benchmark length. As shown in Figure 4-13, the grain boundaries are first recognized at the bottom of the deposition layer and then regressed into a straight line with a minimized distance from the recognized grain boundary points.

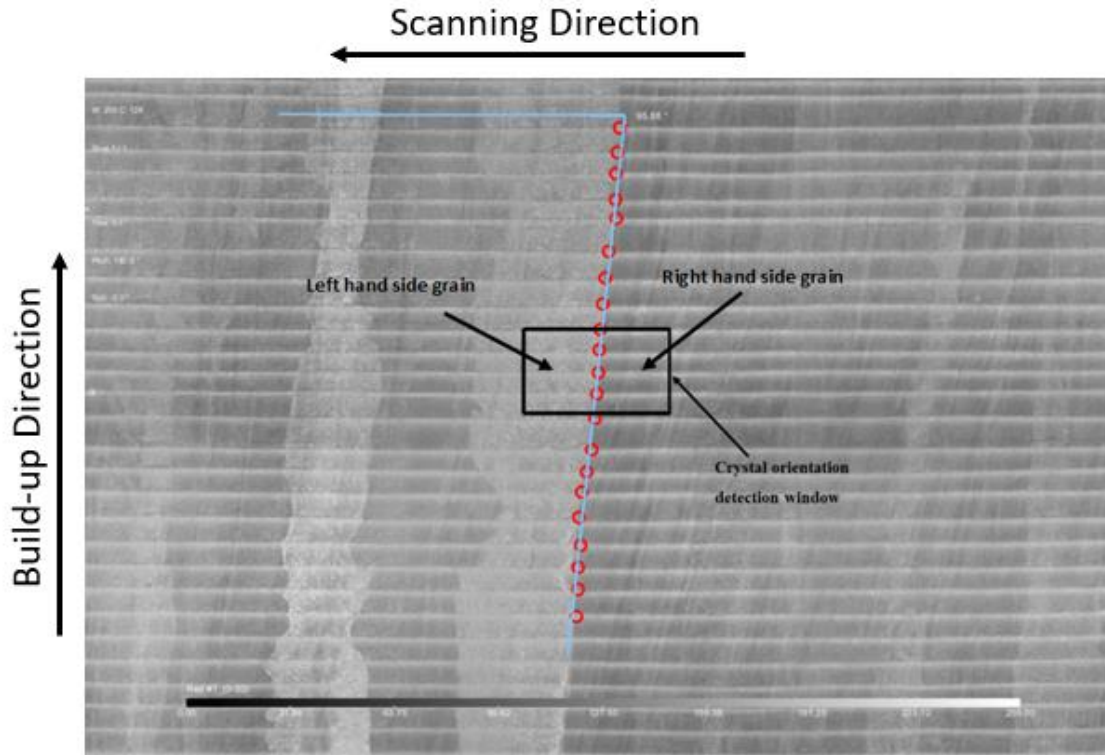


Figure 4-13 Grain boundary angle measurement of columnar beta grains on the X-Z plane

The EBSD experiment was carried out using a Hitachi SU-3500 scanning electron-microscope equipped with an Oxford EBSD module, and the analysis was under Channel 5 software. As for X-Z samples, the detection window of EBSD characterization strictly follows the position of grain boundary angle measurement (detection window shown in Figure 4-13). The EBSD result of a single prior beta crystal is shown in Figure 4-14, the band contrast map shows the structures of the basketweave alpha grains and on the right presents their corresponding crystal orientations. The detected phase percentages are 99.49% (hcp) and 0.51% (bcc) respectively.

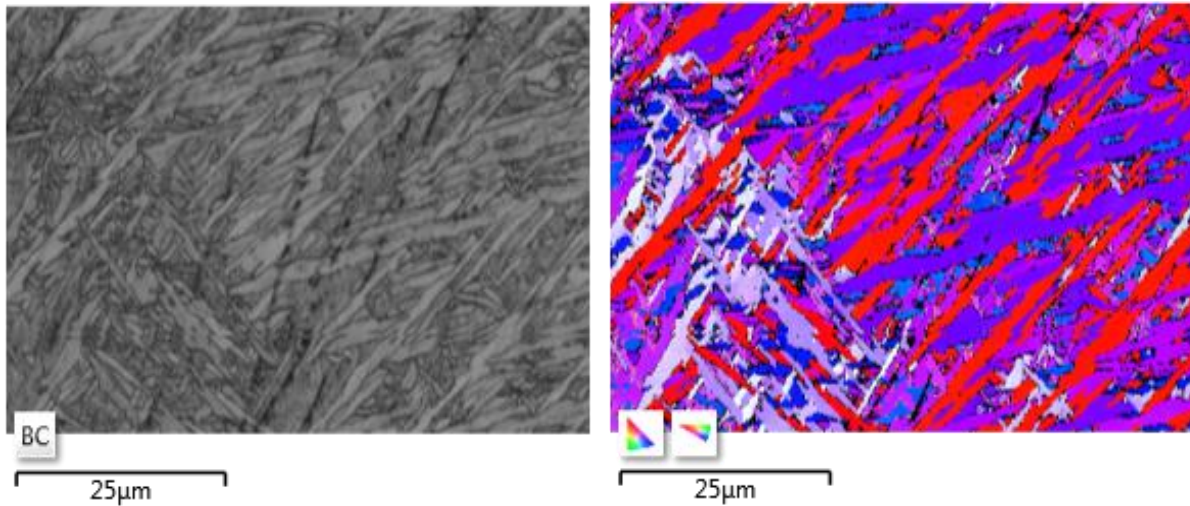


Figure 4-14 EBSD characterization of a single prior beta grain domain on the X-Z plane: band contrast map (left) and inverse pole figure (IPF Z) map colouring perpendicular to the sample surface

In order to measure the exact crystal orientations of the prior beta grains on the Y-Z plane samples, EBSD was performed near the bottom of the deposited portion, as shown in Figure 4-15 left. The coordinate systems for thermal gradient direction measurement and EBSD characterization are exactly under the same Cartesian coordinate system of MAM machine: X axis refers to the scanning direction of the melt pool, Y axis refers to the normal direction of the X axis on the horizontal plane, and the Z axis is the build-up direction of laser wire DED process. This guarantees the appropriate vector correlation between the thermal gradient direction and the crystal orientation. However, the solid phase transformation hides the crystal orientation information of prior beta grains. Thus, the reconstruction following the Burgers orientation relation (BOR) was launched using Arpge software [253]. In the right-hand side of Figure 4-15, two beta grains are reconstructed from the three Euler angle maps. The projection of the preferred grain growth direction $\langle 001 \rangle$ on a 2D plane (X-Z or Y-Z) is operated under a self-developed MATLAB code

based on the rotation matrix operations of the Euler angles. The crystal orientations, which are represented by 2D vectors, are transformed into angles between these vectors and the thermal gradient directions. The grain boundary angle result from the criterion is used as the input for the ANN model representing the crystal orientation effect. In total, 50 groups of data including crystal orientation, solidification condition (G&R), Marangoni effect as well as the grain boundary tilt angle were gathered from the experiment for both X-Z and Y-Z planes and used for the ANN model evaluation in the next section.

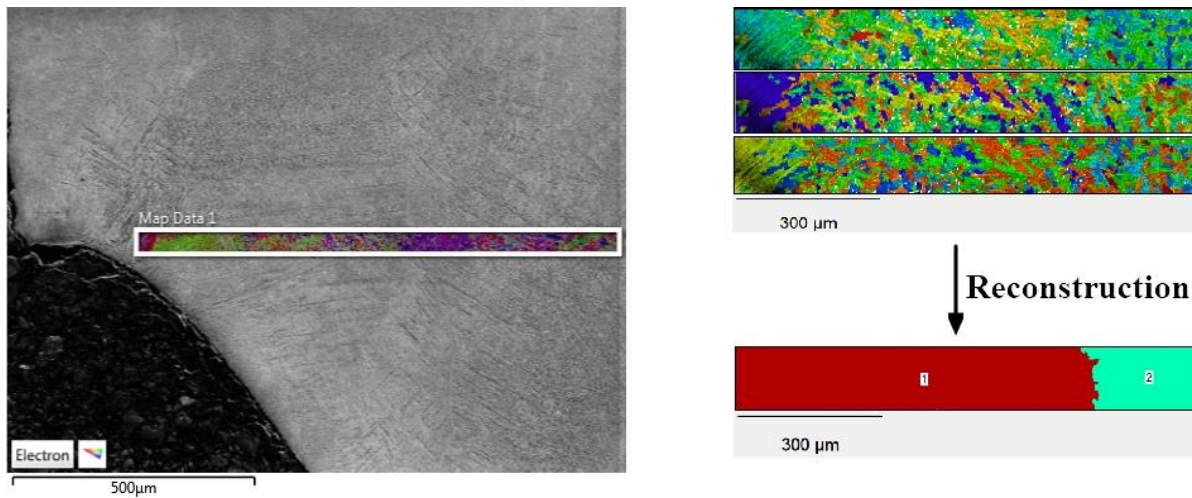


Figure 4-15 Scanning electron microscope (SEM) image and EBSD on the additive portion in Y-Z plane, and the EBSD result reconstruction from three Euler angles maps.

4.4. Artificial Neural Network and Results

The strategies used to investigate the competitive grain growth on Y-Z and X-Z cross-sections are slightly different with regard to the treatment of the Marangoni effect. This attributes to the fact that on the Y-Z cross-sections competitive grain growth at different melt pool bottom positions experiences a different flow velocity. On the contrary, the grain boundary angle measurement on

the X-Z plane is under multiple-layer condition and all the measurement is launched on the middle plane of the fabricated part. Under the constant melt pool assumption, theoretically, all the grain boundaries experience the same fusion flow condition. Thus, for X-Z planes, the integration of the Marangoni effect along the grain boundary throughout the layer distance is represented by a constant angle, and a correction is made during the data collection procedure. The detailed derivative of this angle is elaborated in Chapter 5.

For the implementation of the machine learning algorithm, the open-source machine learning platform PyTorch was used. 50 sample datasets for both Y-Z and X-Z planes are used to train the network after dividing them randomly into training (80%) and test set (20%). The mean squared error (MSE) was chosen as a training and evaluation metric. It calculates the squared difference between the target value and the output of the model. Thus, far-off predictions are penalized exponentially stronger than predictions close to the target value are.

The goal of the learning process is to determine weight and bias terms for each neuron in the network so that the MSE loss at the output layer is as small as possible. The algorithm achieves that via a technique called backpropagation. During training, information is fed in a forward mode through the network. The effect of weight and bias terms of every neuron on the output and thus, the error metric is then computed backwards, using the derivative of the error function. The model is trained in epochs, where one epoch denotes that all training instances are fed into the network and backpropagated once.

For the Y-Z plane samples, the structure of the built feed-forward neural network with two hidden layers is visualized in Figure 4-16. The network's input consists of three different angles: thermal gradient, Marangoni effect and crystal orientation effect. The crystal orientation effect is analyzed under the geometrical limit (GL) criterion (a slow solidification rate under which all the dendrites

get fully developed), a detailed derivation can be found in [239]. The input layer is followed by two hidden layers with five and ten neurons, respectively. The last layer of the fully connected network consists of a single neuron that outputs the prediction for the grain boundary tilt angle. For this relatively simple ML task, the described structure was found to lead to reasonable results yet not to make the model unnecessarily complex. As for the machine learning model training on the X-Z plane, four factors are selected as the features for a bi-crystal system including solidification rate, thermal gradient value, crystal orientations of the left- and the right-hand side crystals. The Marangoni effect is treated as a correction for the data gathering and grain boundary angle prediction process. As shown in Figure 4-17, the structure of the X-Z plane ANN model has four neurons on the input layer and one neuron on the output layer (representing the resultant grain boundary angle). The two hidden layers are set with seven and ten neurons, respectively.

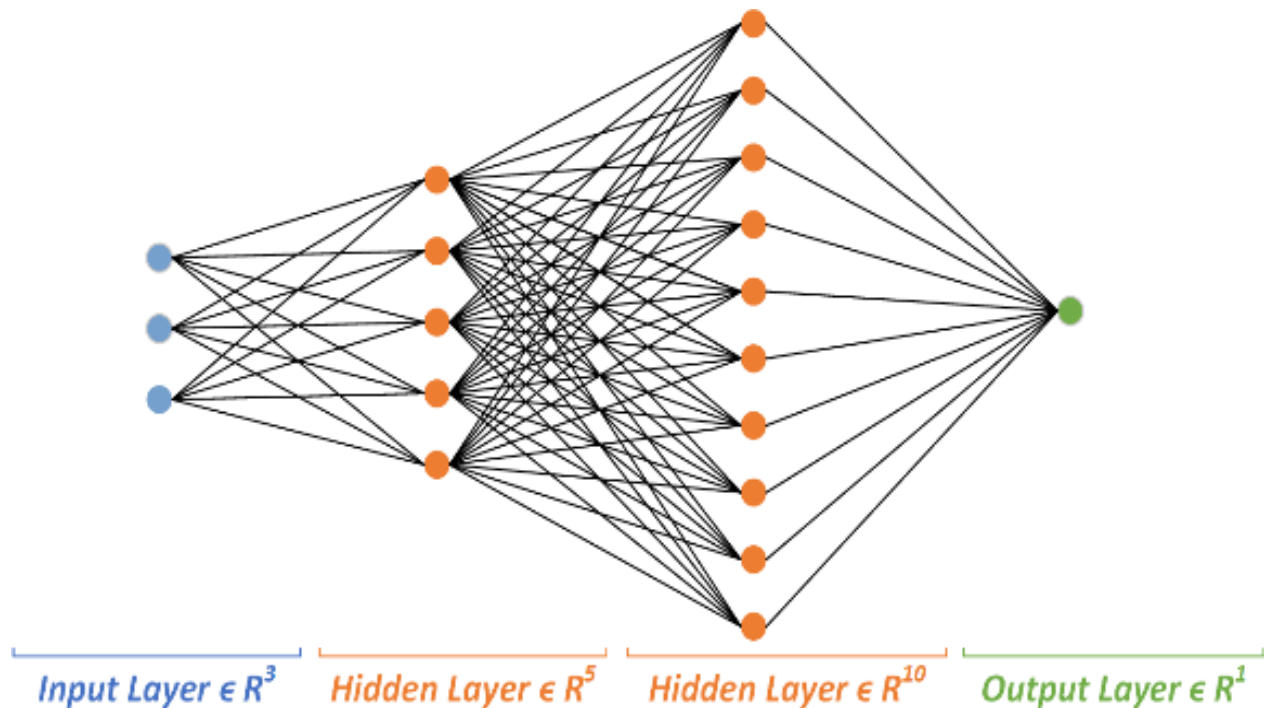


Figure 4-16 Structure of the neural network used for Y-Z plane samples

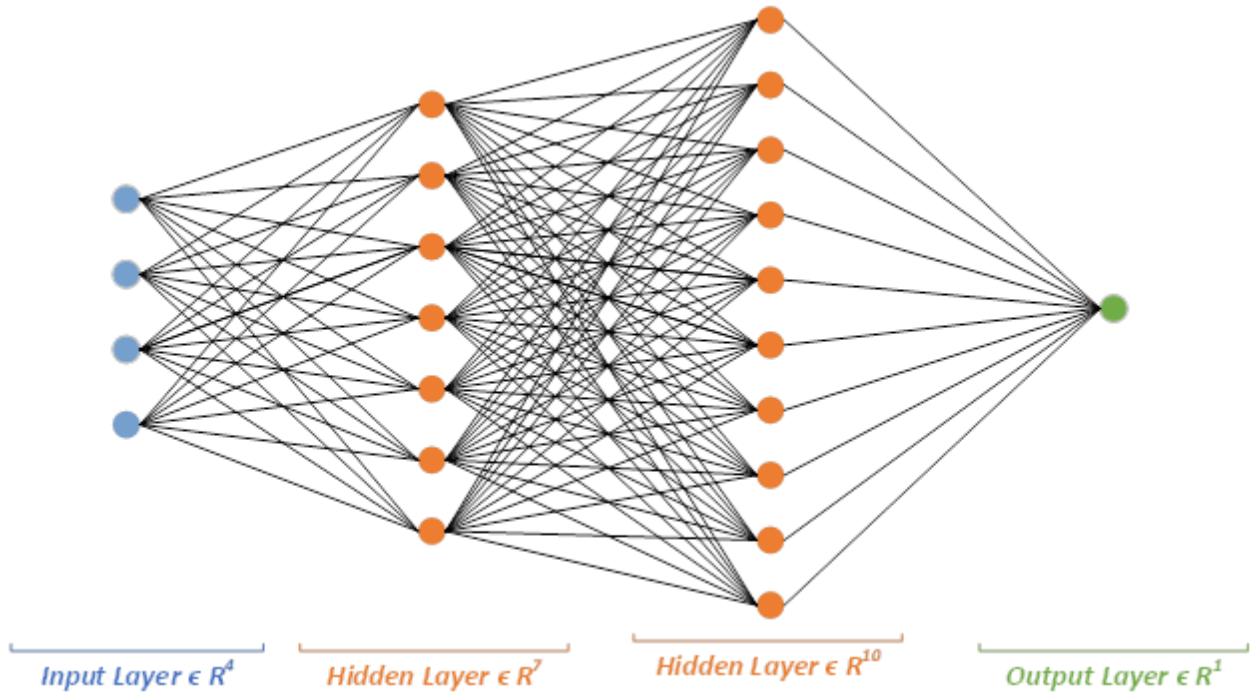


Figure 4-17 Structure of the neural network used for X-Z plane samples

Besides structure and loss function, the following settings and hyperparameters were identified to perform the best: Adam, an adaptive optimization algorithm capable of adaptively scaling the learning rate depending on the training progress, was chosen with an initial learning rate of 0.001. Rectified linear unit functions (ReLU) were taken as non-linear activation functions and the model was trained for 1,000 epochs. The learning curve is shown in Figure 4-18.

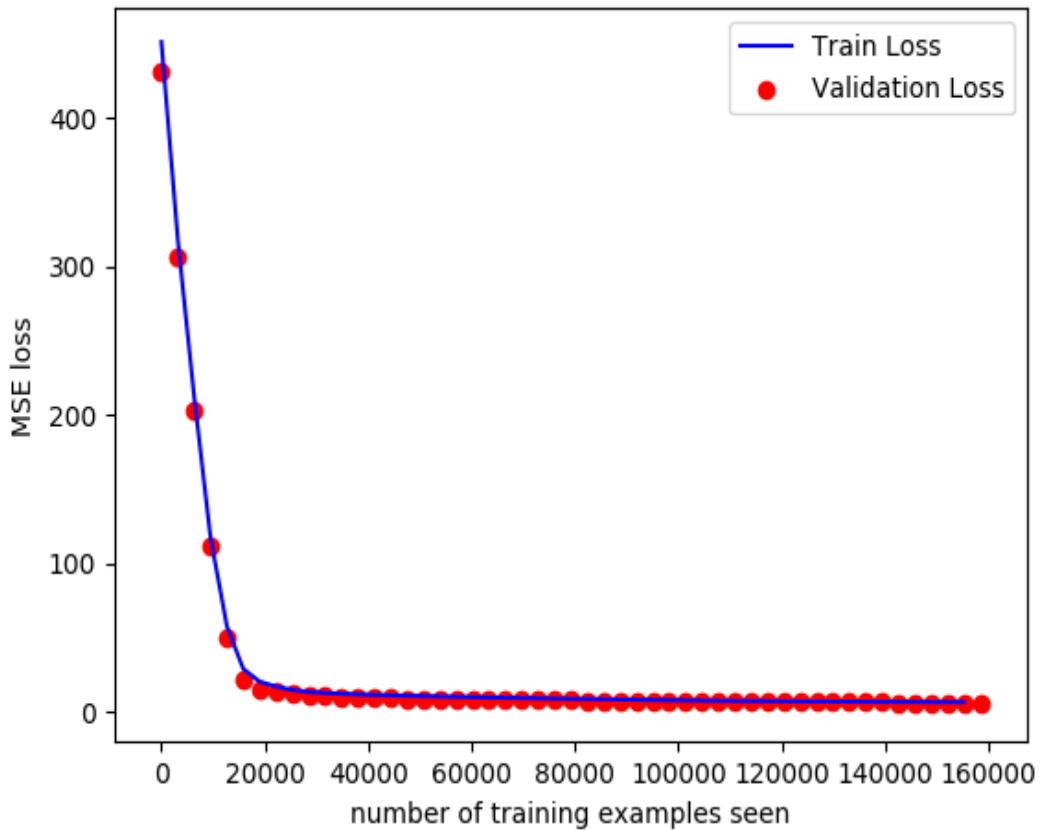


Figure 4-18 The evolution of training loss and validation loss during training for Y-Z plane samples.

Due to the small amount of data available for training and testing, the ANN experiences a high variance in its output despite a long training procedure with many epochs. Depending on the choice of the training set and testing set, the MSE varies too much to report the result of a single run. Therefore, the ANN was run twenty times with randomly changing training and test sets in order to determine the mean MSE and the corresponding variance. As a result, the neural network scored a mean MSE-loss on training data of 3.45 and 6.42 on testing data. Taking the square root of the error made by the ANN, the average distance between the prediction of grain-boundary angle and their experimental results is only 1.83° when training and 2.43° when testing, with a standard

deviation of 0.32° and 0.73° , respectively. The worst prediction of the twenty runtimes resulted in an average difference of 3.94° between the model's guess and the true angle. For Y-Z plane, Fig. 4-19 displays the result of the training process visualizing the networks guess for the grain-boundary angle with thermal gradient and crystal orientation as input, neglecting the Marangoni effect (set as zero) to allow a graphical representation. The red dots represent the 50 training instances obtained from experiments. The ANN was compared to a simple linear regression model with stochastic gradient descent that was implemented using the Scikit Learn platform and attempts to find the plane that describes the training data the best. With an average prediction discrepancy of 3.91° after taking the square root, this approach performed worse and justifies the usage of a neural network. However, the corresponding standard deviation of 0.21° is slightly better than the one of the ANN.

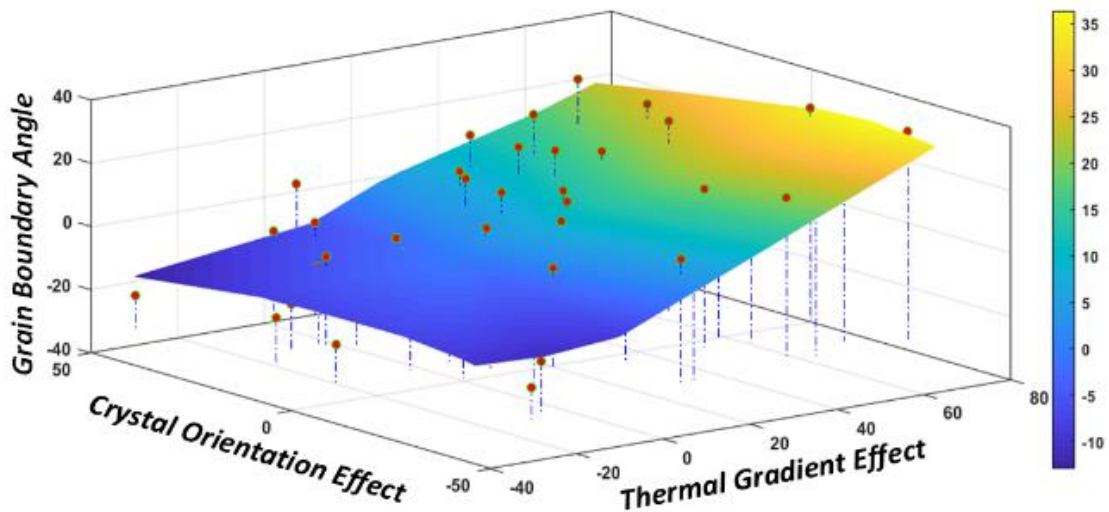


Figure 4-19 Comparison between experimental data and ANN model.

Compared to earlier attempts with the ANN, adding the Marangoni angle to the input helped to improve the performance of the Y-Z plane ANN model. This might be because the thermal gradient has a greater influence on the grain-boundary angle than the crystal orientation and the Marangoni angle is linearly dependent on the thermal gradient (either + or -90°), thus emphasizing this part of the input more. The Marangoni effect correction treatment on the X-Z plane makes the ANN model straight to the point, and the implementation is detailedly described in Chapter 5.

4.5. Chapter Summary

The section has demonstrated that ANN can be employed to investigate the competitive grain growth behaviour in DED fabricated Ti6Al4V efficiently by attributing the grain boundary tilt angle to three causative effects: thermal gradient, crystal orientation and Marangoni effect. Despite the limited amount of experimental data, the ANN model developed in this work can be employed within a tolerance range of about $\pm 4^\circ$. An average prediction error of 2.43° shows that a feed-forward neural network is an appropriate tool for the task described in this paper. However, for future investigations, more experimental data will be generated to improve the model's performance regarding accuracy and stability. A dataset of a few hundred instances obtained from experiments is suggested to achieve more stable results and a prediction performance within the resolution of experimental instruments. With a sufficient dataset, this ANN can be used as an engine to support the microstructure simulation of DED fabricated Ti6Al4V and further extend to other topics in terms of microstructure development in the polycrystal material solidification process.

Chapter 5. Deterministic modelling of solidification microstructure formation in laser wire DED fabricated Ti6Al4V

5.1. Introduction

Different from the reviewed solidification microstructure simulation models, this Chapter aims to develop a deterministic model for solidification microstructure formation in laser wire DED fabricated Ti6Al4V. Based on the methodology and regression relation achieved by the ANN, an “invasion model” is proposed to numerically simulate the transient competitive grain growth behaviour under the solidification conditions of a melt pool. The solidification background is first detailedly discussed. The boundary conditions including the crystal orientations and local solidification conditions are then described. The implementation of this invasion model goes through a model verification (cell size and timestep) before the experimental validation. A section of laser wire DED fabricated thin wall is selected for the validation and the results show the unique capacities of this novel method.

5.2. Solidification Background

Considering the nature of a constrained epitaxial grain growth under a steep thermal gradient condition, the ambient environment of a bi-crystal solidification in MAM is shown in Figure 4-2. The two grains within a bi-crystal system are depicted with different colours with the grids representing their crystal orientations, respectively. The solute concentration field is schematically shown above the liquidus line which can be influenced by the movement of the fusion driven by the Marangoni effect. The large thermal gradient value generated from MAM processes compresses the mushy zone of solidification at the melt pool bottom into a very thin film. Based

on the knowledge of welding for reference [254], the primary arm spacing under different cooling conditions is described by:

$$\lambda_1 = a(G^2R)^{-1/4} \quad \text{Equation 5-1}$$

Where λ_1 refers to the primary arm spacing, a is the material-dependent coefficient, G is thermal gradient and R is the solidification rate. In the case of MAM, λ_1 usually becomes very small with large G & R because of the negative correlation embodied in equation (1).

Under the condition of rapid solidification in the DED process, the primary spacing of dendritic grains is very small, and they are paratactic within a single columnar grain domain as a result of epitaxial grain growth. In the case of DED fabricated Ti6Al4V, the original solidification microstructural features are eliminated by the solid-phase transformation. However, evidence can be found in the simulation studies showing that the primary dendritic grains have a periodic behaviour occupying their neighbouring grains [166]. With a proper selection of the length scale, this periodic behaviour can be shown as a straight line as the waving curves generated at the grain boundary is usually less important when grain selection and grain size change are investigated at part-scale.

As for how a grain boundary is developed between a bi-crystal system under MAM solidification conditions, a hypothetical situation is first assumed where crystal orientations within a bi-crystal system are perfectly symmetrical. The total supercooling ΔT , which is the driving force of solidification front development, can be attributed to the sum of four contributions:

$$\Delta T = \Delta T_{th} + \Delta T_c + \Delta T_k + \Delta T_r \quad \text{Equation 5-2}$$

where ΔT_{th} is the pure thermal undercooling at solid/liquid interface caused by thermal diffusion, ΔT_c stands for the undercooling contributions associated with solute diffusion, ΔT_k is the kinetic supercooling influenced by the rate at which atoms attach to the solid phase, ΔT_r is the curvature supercooling due to curvature of the solid-liquid interface, also called Gibbs-Thomson supercooling. Based on the symmetry principle of the hypothetical situation, ΔT_{th} , ΔT_k and ΔT_c on the right-hand side of equation (2) are not able to make the grain boundary tilt from the initial normal direction of the solidification front. The three contributions all make the grain growth normal to the original liquidus line, which means the column grains (cluster of small dendritic columnar grain with same crystal orientations) are always perfectly parallel with each other if the solidification front is stable. However, for the solidification of metal alloys, the Marangoni effect influences the solute concentration in fusion and leads to different constitutional supercooling (ΔT_c) that breaks the symmetry of the system. In the case of DED fabricated Ti6Al4V, the surface tension-temperature coefficient is negative and the fusion from the laser exposure area with higher temperature tends to flow toward the boundary of the melt pool. And the flow direction near the mushy zone driven by the Marangoni effect has important implications for the grain growth direction as well as the development direction of grain boundaries in the solidification process of metal alloys.

In another solidification case of the bi-crystal system, if the two grains with different crystal orientations are solidified under the directional solidification condition (constant isotherm normal to solidification direction and without flow velocity at solidification front), the crystal orientation relation decides the grain boundary development direction, also called anisotropic growth effect. In general, the crystals with preferred crystal orientation (e.g., one of $\langle 001 \rangle$ directions in cubic crystals go most closely aligned with the normal direction of solidification front) have the

advantage to win the competitive grain growth. This phenomenon is widely found in metallic alloy materials under the directional solidification experiments, the grain boundaries are found to tilt from the normal direction of the solidification front because of the different crystal orientation relations among the adjacent grains [255]. Between these two extremes, conditions of solidification microstructure development in MAM are usually a combination of the two cases and some key physical realities and phenomena are detailly described below. In this work, dendritic columnar grains are referred to as column grains or grains for simplicity, and angles in a two-dimensional (2D) model are defined as negative in a clockwise direction and positive in a counterclockwise with regard to the normal direction of the solidification front.

5.2.1. Dendritic Columnar Grains

The columnar dendritic growth is characterized by the constrained growth of a packet of dendrites along the same general direction. Studies have shown that the columnar grain is a universal phenomenon in solidification microstructure not limited to DED but most MAM technologies [69]. This can be addressed to the cooling condition at the melt pool bottoms in terms of the thermal gradient (G) and solidification rate (R) as the solidification conditions of DED technology are mostly located at the columnar grain area of the G - R diagram. In DED fabricated Ti6Al4V, the column grains, as well as grain boundaries, tend to elongate along the built direction penetrating multiple layers, but they do not always strictly follow the thermal gradient direction. Based on experimental observation, the grain boundaries can maintain a straight line in a long range between the same bi-crystal system under a relatively constant cooling condition (stable melt pool geometry). This is the basic evidence indicating that the tilting of grain boundaries and grain size change can be modelled quantitatively.

A finer microstructure is usually desired in material science to achieve a better mechanical property according to the famous Hall-Patch relationship and as a result of the cleavage cracking resistance effect. Thus, a great amount of work focuses on achieving the CET for different materials in MAM [22, 256]. This can be accomplished by process parameter control, process optimization, promoting nucleation, and so on. From the modelling point of view, if fully equiaxial grain structures are achieved, the average grain size or the grain size change is usually of more importance which is determined by the maximum nucleation number (n_{max} , usually measured from the experimental result) arranged in the simulation domain. A simple Voronoi diagram is a good representation of the equiaxial solidification microstructure with a random nucleation position and crystal orientation assumption. However, for some types of material, the process parameter is only achieved in a certain range to get a successful print without defects like cracks or porosity. In this case, the columnar grains are inevitably produced. For DED fabricated Ti6Al4V, constitutional supercooling cannot achieve the amount requested for nucleation and there is no refiner for this type of material. The columnar grains can then grow into several millimetres thick penetrating hundreds of deposition layers, therefore, accurate modelling and controlling of the columnar grain structures becomes important.

5.2.2. Nucleation and epitaxial grain growth

According to the independent nucleation theory [22], Ti6Al4V is a material that has inadequate constitutional supercooling for nucleation. Thus, in most cases of DED fabricated Ti6Al4V parts, the added material epitaxially grows from the existing half-melt crystals to save free energy instead of creating a new nucleus. This was also approved by the experimental observation that only a limited number of new crystals with random crystal orientations generate along the material

deposition process. In the wire DED Ti6Al4V fabrication studied in this work, the nucleation rule is set based on the “no nucleation assumption”. This assumption believes there are all epitaxial grain growth and no grains with new crystal orientation are introduced in the simulation domain during the material deposition process. However, this assumption is not suitable for cases like PBF and DED processed Ti6Al4V with powder feedstock, as the unmelt powders or external material inevitably become the substrate for epitaxial grain growth and introduce grains with new crystal orientation into the printed zone. In this case, the random crystal orientation rule should be set as a boundary condition to investigate the competitive grain growth as it is almost impossible to measure the exact crystal orientations as boundary conditions for simulation.

For materials that CET can be achieved during MAM processes, traditional nucleation rules (e.g., continuous nucleation) should be applied which arranges nucleation numbers according to the density of grains in each time step with random crystal orientations. Due to the remelting effect of MAM techniques, even the CET can be achieved within the melt pool, it is still possible that remelting eliminates the equiaxial grain area (typically located at the top area of a melt pool), and the columnar grain dominates the printing area. In this case, the competitive grain growth can still be analyzed quantitatively under the “no nucleation assumption”.

5.2.3. Preferred grain growth direction and grain selection mechanism

Starting from the research conducted by Walton and Chalmers [257], people recognized that metallic materials have their preferred grain growth directions ($\langle 100 \rangle$ of cubic crystal systems and $\langle 1010 \rangle$ for hexagonal closed pack). This means on the preferred grain growth directions there is a higher grain growth velocity compared to other directions. This is a result of anisotropic surface energy in different packing manners of metal atoms. According to crystallographic symmetry,

$\langle 001 \rangle$ directions are 90 degrees apart in bcc and fcc crystals which are also referred to as four-fold symmetry. Under a 2D bi-crystal system, the grain selection mechanism is intensively investigated and there are two situations namely diverging and converging based on crystal orientation relations. In general, the grains with their preferred grain growth directions align with the solidification front (favourably oriented grains) have the advantage to win the competitive grain growth. Under a converging situation of a bi-crystal system, the unpreferred grain needs a higher supercooling to catch up with the solidification front compared to the preferred one. The small lag caused by this phenomenon makes the unpreferred grain hit the side of the preferred one and results in a grain boundary perfectly align with the $\langle 01 \rangle$ direction of the preferred one. If the two grains in a bi-crystal system are diverging, secondary and higher-order dendrites can develop into the open region and generate a grain boundary within the angle between the $\langle 01 \rangle$ directions of the two grains. Following this, the most famous grain selection mechanism is called best align criterion with the following formula:

$$\theta_{GB} = \begin{cases} \alpha_1 & \text{if } |\alpha_1| < |\alpha_2| \\ \alpha_2 & \text{if } |\alpha_2| < |\alpha_1| \end{cases} \quad \text{Equation 5-3}$$

In the best align grain selection mechanism, three criteria are followed according to the symmetric principle in its selection map: 1. the value of the grain boundary angle is centrosymmetric. 2. the value is continuous except for the diagonal line. 3. θ_{GB} is zero when the two grains have symmetrical crystal orientation. Together with the criterion, selection maps are depicted and compared with CA and PF models [239] which show the significant differences in between. In this work, as the directional solidification experiments for Ti6Al4V under rapid solidification condition of MAM is still pending based on the knowledge of the authors, the selection map under

a certain rapid solidification condition range in wire DED process is depicted from experimental data, and regression is achieved with the help of ANN (methodology can be found in Chapter 4).

Based on the physical realities of solidification conditions in MAM described above, an “invasion model” for Ti6Al4V is established in this work to simulate the solidification microstructure evolution in DED processes. Instead of chasing for methods to directly mimic the grain growth, the invasion model focuses on the interaction between the neighbouring grains within bi-crystal systems under different local solidification conditions and quantitatively analysis the grain boundary angles. The invasion model introduced an “invasion factor” to describe a transient grain boundary behaviour between a bi-crystal, as the parameter angle is a non-dimensional number that can be easily adapted into models where multiple scales are involved. The competitive grain growth behaviour of columnar grains in DED fabricated Ti6Al4V is considered as a sum-up of all the invasion behaviour in bi-crystal systems. According to physical realities discussed in the previous sector, the grain boundary angle between two adjacent grains from the normal direction of the solidification front is a result of the Marangoni effect (θ_M) and grain selection (θ_c), and these two effects are considered to be independent of each other in the invasion model. Under different cooling conditions ($G&R$), these two effects can be summed up for the competitive grain growth within a bi-crystal model. Regarding the normal direction of the solidification front, the transient grain boundary angle (θ_{GBt}) within a bi-crystal system under a certain solidification condition is given by:

$$\theta_{GBt} = \theta_c + \theta_M \quad \text{Equation 5-4}$$

The solidification in MAM is highly non-equilibrium as it takes place in a rapid manner, and the solutes of alloy systems cannot fully diffuse towards or away from the solidification front (solute trapping effect). Recent PF models have considered how to consistently and quantitatively integrate non-equilibrium effects [118], however, for extreme solidification conditions in MAM, it is still difficult in traditional solidification microstructure simulation methods. In this work, a data-driven method is chosen to describe the competitive grain growth behaviour within bi-crystal systems under different rapid solidification conditions. Here, we considered a limited solidification condition range in the DED process with an imposed solidification rate of 0-50 mm/s and a thermal cooling rate of $10^3 - 10^4$ K/s. The grain selection map is depicted with the help of the ANN model where the training data comes from the experiment matrix, additional details can be found in [258]. Then the generated dataset becomes one engine of a continuous solidification microstructure simulation to describe the anisotropic growth effect of the two grains in a bi-crystal system under different local solidification conditions.

Studies have shown that $\langle 001 \rangle$ texture can generate along the buildup direction after passing the initial tens layers of material deposition, the grain size inherited from substrate growth into a relatively stable level and “invasion model” can be applied into the columnar grain dominating areas where the constrained solidification condition is achieved. Within a timestep of invasion model, first, the investigated area is discrete into a regular lattice arrangement. Based on the transient melt pool geometry, the cells are divided into different types including fusion, mushy and solid cells. Then, the crystal orientation information on the bottom of the simulation domain is extracted from EBSD experimental result. As shown in Figure 5-1, the cells located on the grain boundary at the solidification front are recognized. Based on the position of the grain boundary cell, the solidification condition is extracted either from the experiment or the other transfer

phenomenon simulation models. Finally, the grain boundary angle is calculated from the invasion model, and the tangent value of the grain boundary angle is set at the grain boundary cell (mushy cells located at grain boundary positions) to describe the transient grain boundary invasion behaviour within a timestep.

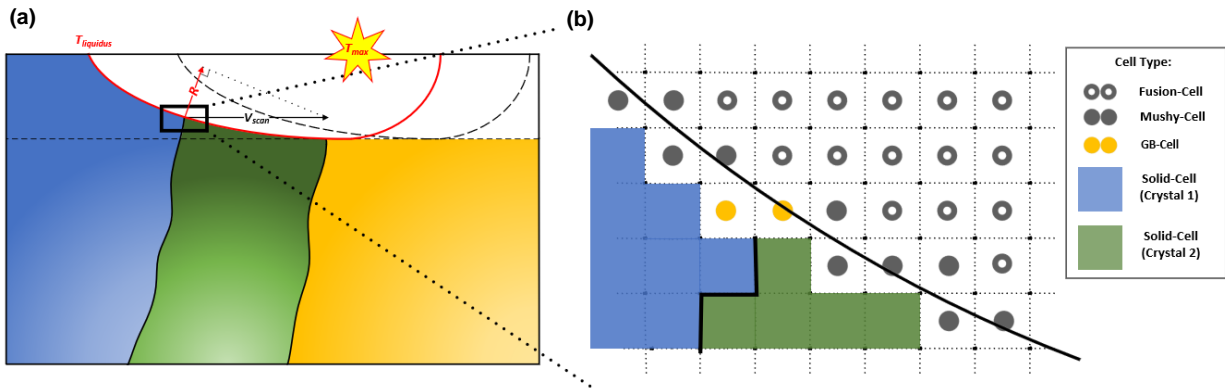


Figure 5-1 One timestep in the invasion model. a. Schematic of local solidification condition. b. Numerical representation of the simulation domain.

According to the simulation target and surrounding environment described above, the main assumptions adopted in this Chapter include:

- All the sub-grain microstructures are ignored
- Melt pool geometry is considered relatively stable in each scanning pass and the fluctuation at the start and end position of the scanning track is ignored
- No nucleation assumption with all epitaxial grain growth dominating the deposition process
- Columnar grain size is much bigger than primary arm spacing
- Solidification front can always catch up with the scanning speed of the DED process

Overall, the invasion model believes the tilt of grain boundary angles w.r.t the solid and liquid interface in the DED process is a sum-up of Marangoni and anisotropic growth effect. The

important features are detailed in the following sections to describe the boundary condition, grain growth environment, and grain boundary development.

5.3. Crystal orientations

For crystal orientations, columnar grains inherit the crystal information (including crystal orientation and size) from the previous layers of materials and nuclei on the existing half-melted crystals because of the epitaxial grain growth behaviour. To achieve a quantitative microstructure simulation, an accurate boundary condition of crystal orientation and initial grain topological structure is required. When the printed part has passed the initial several layers (5-10 layers) of competitive grain growth, a texture appears which decreases the intensity of grain competition, so the columnar grain size in the X-Y plane becomes relatively stable. In this case, the boundary condition is set based on crystal reconstruction result, and $\langle 001 \rangle$ directions reflection on the corresponding plate is used in 2D models. In real practice, the bottom area of printing is usually left for cutting or support structures making the microstructure inside less important. For the cases in which new crystals or nucleation are introduced in the process (SLM or laser powder DED), the boundary condition with random crystal orientations and grain structure using Voronoi diagram is acceptable because it is impossible to set the boundary condition based on the experiment considering the complexity of the process.

5.4. Local Solidification Condition

In most MAM cases, the melt pool is generated by a high-energy beam. As MAM fabricated part is composed of a mass of welds, the microstructure in a single weld bead decides the final solidification microstructure of the fabricated part. The transient melt pool geometries are crucial

and are the prerequisite to getting an accurate simulation result. To capture the melt pool geometrical along the building process, a well-tested CFD model is used to reproduce transient melt pool geometries with experimental validation. Details of the establishment of the CFD model can be found in [259]. The key attributes of the melt pool geometry can also be adopted from the FEM result or analytical solutions [234].

The melt pool geometry is considered as the isothermal surface along the liquidus line, closely attached to the mushy zone. It is a direct reflection of the local solidification conditions. The cooling condition along the melt pool bottom changes dramatically in terms of $G&R$, and in turn, influences the solidification microstructure developed subsequently. To calculate the transient solidification condition for the bi-crystal systems, the attributes of a transient fusion zone include melt pool length (L_m), width (W_m), depth (D_m), and displacement (d_m) are extracted from the melt pool geometry of CFD simulation after experimental validation. Then, the “double ellipsoid approximation” is used to mathematically represent the transient melt pool geometry. To accurately capture the normal direction and solidification condition of a solidification front, the segment of an ellipsoid is carefully matched with the simulated fusion zone at the melt pool tail. This ellipsoid can be defined by a simple equation (for thin wall structure, the tilt of melt pool is ignored) where the origin locates at the center of the laser beam:

$$\frac{x^2}{L_m^2} + \frac{y^2}{W_m^2} + \frac{(z-d_m)^2}{(D_m+d_m)^2} = 1, \quad (z \leq 0) \quad \text{Equation 5-5}$$

On the X-Z plane located at the center of the melt pool ($y=0$), we take the differential of Eq. (5) and obtain

$$\frac{dz}{dx} = -\frac{(D_m+d_m)^2}{L_m^2} * x, \quad (z \leq 0) \quad \text{Equation 5-6}$$

From the above mathematical model, solidification conditions in terms of $G&R$ are calculated. In terms of the thermal gradient, the maximum heat flux direction can be captured from the normal direction of isotherm as the negative reciprocal value of dz/dx is the tangent value of the thermal gradient direction on the X-Z plane. The thermal gradient value can also be generally calculated as $(T_{max} - T_{liquidus})/\sqrt{x^2 + z^2}$. For the solidification rate, it is represented by

$$R = -\frac{L_m^2}{(D_m + d_m)^2} * \frac{(z - d_m)}{x} * v_{scan}, \quad (z \leq 0) \quad \text{Equation 5-7}$$

The same principle can also be applied to Y-Z and X-Y planes. The grain boundary angle attributed by anisotropic growth effect under a local solidification condition is considered as a function of thermal gradient value, solidification rate, crystal orientations of the two grains in the bi-crystal system.

$$\theta_c = f(G, R, \alpha_1, \alpha_2) \quad \text{Equation 5-8}$$

As this function is highly nonlinear, in this work it is achieved by the regression of experimental data by ANN model with solidification condition and crystal orientations being the selected features. The methodology and details can be found in [258]. Under this strategy, the effect of grain boundary energy and force balance on grain boundary triple junctions [260] are implicitly included in the “invasion model” as they also can be considered as dependent features of the ANN model.

We now develop the theory a step further to consider the influence of the Marangoni effect on the grain boundary angle. Here, we assume there is perfect mixing in the liquid far from the solidification front because of the strong stirring effect and the alloy material added to the melt pool. Various simulation works have shown that the convection around a growing alloy crystal

can influence the grain growth behaviour dramatically [261]. Apparently, the stirring leads by the Marangoni effect change the concentration field near the solidification front and boundary layer thickness thus providing different constitutional supercooling which is the major contribution for alloy solidification.

Suggested by Papapetrou [262] that a parabolic isoconcentration interface geometry satisfies the shape-preserving condition as only a part of latent heat or solute is rejected ahead of growing dendrite to keep a constant dendritic tip grain growth velocity. For alloy solidification, the rest of the solute is dissipated along the sides which decreases the constitutional supercool and hinders the grain growth of secondary branches. Following this, the normal growth velocity approaches zero for the secondary dendrites far from the tip. This leads to the invariant thermal and solute concentration field condition in the directional solidification problem so that a parabolic dendrite can grow with a constant velocity (V). The invariant solute field can then be obtained for the steady-state diffusion equation with a moving coordinate system at the dendrite front:

$$\nabla^2 C + \left(\frac{V}{D}\right) \left(\frac{\partial C}{\partial z}\right) = 0 \quad \text{Equation 5-9}$$

With C stands for solute concentration, D is solute diffusion coefficient and z is the dendritic tip growth direction. The invasion model believes that the shape-preserving condition is rarely encountered in the practice of MAM, especially at the grain boundary area because of the asymmetrical solute concentration field led by Marangoni convection. Inevitably, the stirring effect of the moving fusion tends to reduce the solute concentration on the side facing against the liquid flow direction and provide an extra-constitutional supercooling and grain growth environment for a continuous generation and growth of secondary dendrites (as shown in Figure 5-2), thus generates a horizontal grain growth velocity and influence the grain boundary angle.

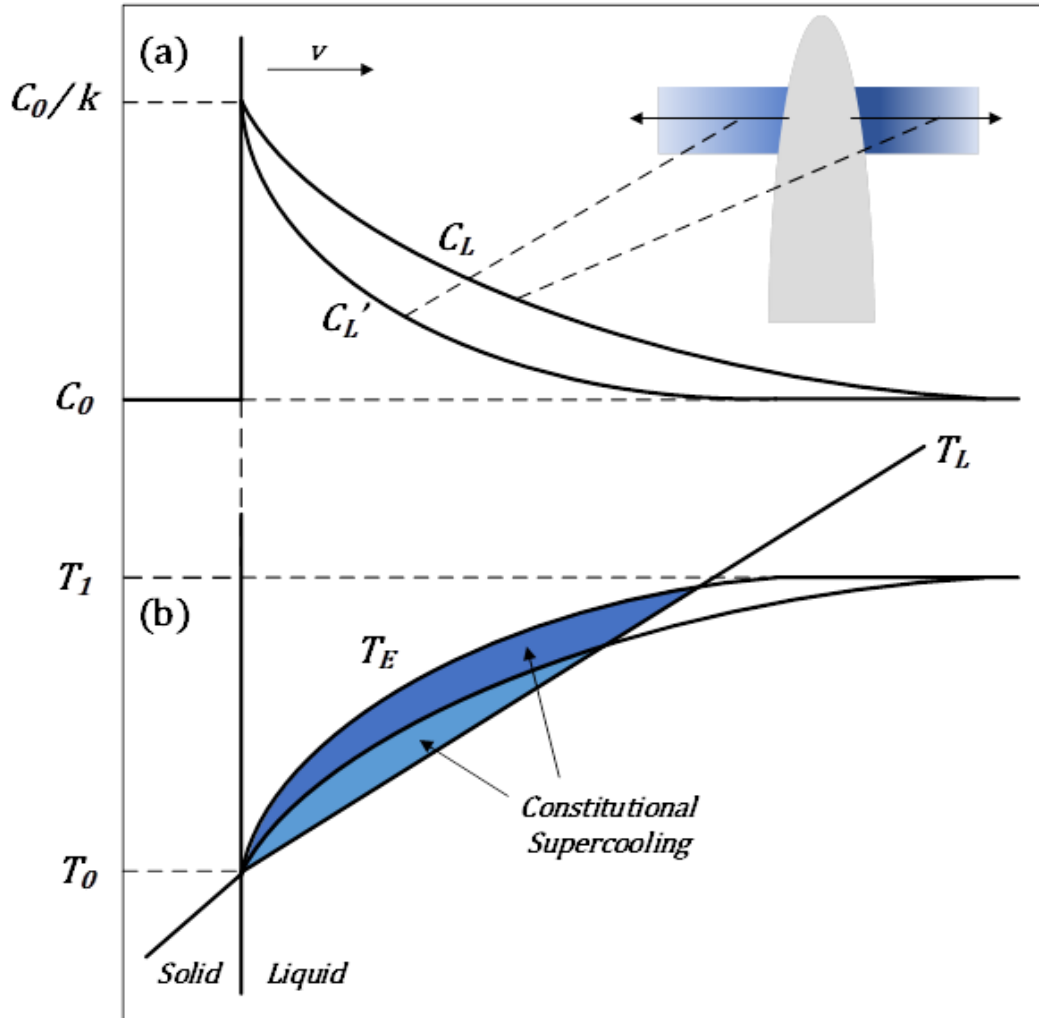


Figure 5-2 The origin of constitutional supercooling on both sides of dendrite under the Marangoni effect. (a) Composition profile across solid/liquid interface with direction point away from the interface. (b) The temperature profile (T_L) ahead of the interface with the difference between T_L and equilibrium liquidus temperature (T_E) represents the different constitutional supercooling on both sides. T_1 and T_0 stand for the equilibrium temperature of the solidus and liquidus line.

The growth velocity of these secondary dendritic tips (V_{tip}), with its reflection on solidification front, referred to as horizontal grain growth velocity (V_{GBh}), is adapted from the Kurz–Giovanola–Trivedi (KGT) model [199]. By using the solute supersaturation, Ω , as an intermediate variable

under Ivantsov function of the solute Peclet number: $Iv(Pe)$, the relationship between dendrite tip growth rate and undercooling yields to

$$V_{tip}(\Delta T) = \frac{D_L}{5.51\pi^2(-m(1-k)^{1.5})\Gamma} \left(\frac{\Delta T^{2.5}}{C_0^{1.5}}\right) \quad \text{Equation 5-10}$$

where D_L is the solute diffusion coefficient in the liquid, m is the liquidus slope, k is the partition coefficient, Γ is the Gibbs-Thomson coefficient, C_0 is the initial concentration, detailed steps and derivation can be found in [69, 200]. Then the grain boundary angle attributed to the Marangoni effect (θ_M) can be represented by

$$\theta_M = \tan^{-1}(V_{GBh}(\Delta T)/R) \quad \text{Equation 5-11}$$

Under the assumption that melt pool geometry is relatively constant within a single scan, the grain boundaries in each layer experienced similar solidification conditions from the bottom of the melt pool to its top in the X-Z plane. Thus, the influence of the Marangoni effect on grain boundary angles within a hole layer thickness can be taken as a general integral average value and subtracted from the total grain boundary angle when considering the anisotropic growth effect.

5.5. Grain Boundary Invasion

In each timestep of solidification microstructure simulation, the local solidification condition between the melt pool tails area is considered as constant, and the transient grain boundary is presented as a straight line. To accurately depict the grain boundary angle in a spatially discretized numerical model, the length of the meshing grid is decided based on the dimension of the simulation target. In the case of laser wire DED fabricated Ti6Al4V, as the columnar grain size can achieve several millimetres (characteristics feature size) and the layer thickness is around 0.7

mm, the cell size is set as 20 μm which is 35 times smaller than layer thickness to guarantee the simulation resolution.

This model is robust because an angle is a dimensionless number, and the angles representing anisotropic growth and Marangoni effects can be summed up without considering the magnitude of the discretized cells. After the grain boundary angle is calculated based on the above methodology at grain boundary positions, the grain boundary invasion behaviour in a numerical model becomes simple. Here we define the invasion factor (IF) of a grain boundary within a bi-crystal system as:

$$IF = \tan(\theta_{GBt}) \quad \text{Equation 5-12}$$

Under the cartesian coordinate system follows the convention of additive, the angle between a transient thermal gradient direction and build up direction in a 2D model is defined as θ_T and invasion factor becomes:

$$IF^{AM} = \tan(\theta_{GBt} + \theta_T) \quad \text{Equation 5-13}$$

The invasion factor is then assigned at a single track of cells straightly above the grain boundary cell and accumulates the value from bottom to top in each timestep. Once a positive integer is reached, the cells (based upon the integer value) at the left of the straight grain boundary line are changed into the grain index on the right, and vice versa. To avoid network dependence and converge the simulation result, the timestep length is determined based on trial and error to accurately represent the grain boundary curve and in the meantime guarantee the efficiency.

Altogether the invasion model considers the competitive grain growth behaviour in MAM as a summary of the grain boundary tilting among the adjacent crystals. The grain boundary angle is considered as a grain invading into its neighbour grains under the absolute coordinate system,

hence the “invasion model”. This grain boundary angle w.r.t. the thermal gradient direction under a local solidification condition is caused by anisotropic growth and the Marangoni effect. In the numerical application of the invasion model, an invasion factor is introduced to represent the tilting of transient grain boundary angles.

5.6. Model Verification

To verify the above methodology can accurately represent a grain boundary angle, model verification is carried out to determine the cell size and length of the time step. The cell size of the invasion model is inversely proportional to the number of discretized cells in characteristic length. In this work, the key factors of the melt pool (e.g., depth and width) are selected as the characteristic length because the solidification microstructure representation depends on the accurate depiction of grain boundary within the single tracks. Thus, a cell number within a domain of characteristic length should be decided first. Figure 5-3 shows the relation between the cell number and the deviation of the represented angle. The 5-, 10-, 20- and 30-degree angles are used for this test as their tangent value produces an irrational number considering the storage data type within the numerical simulation.

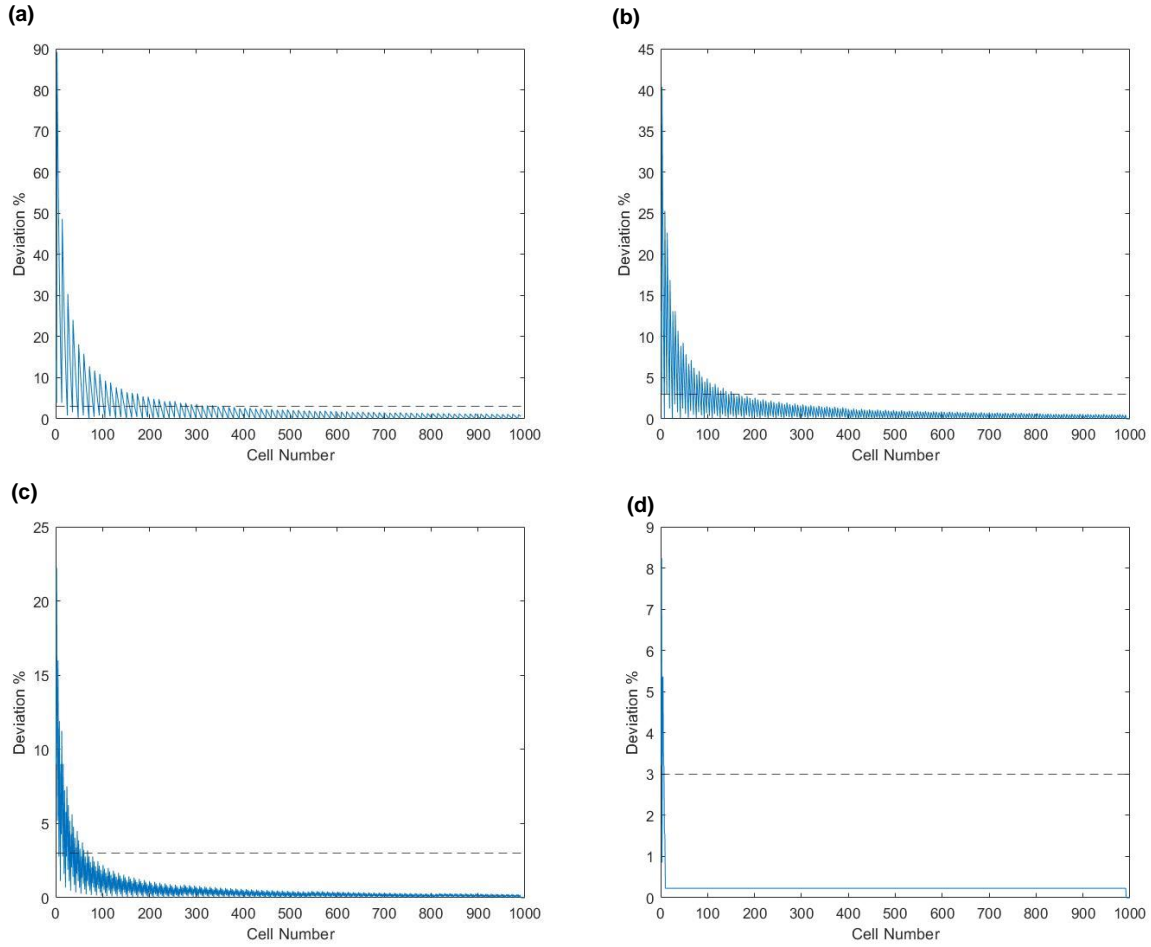


Figure 5-3 Deviation of the represented angle (percentage): (a) 5 degree (b) 10 degree (c) 20 degree (d) 30 degree

There is always a trade-off between the computational cost and the accuracy of a numerical simulation model. To limit the deviation to around 3% (horizontal dot line in Figure 5-3), a cell number higher than 200 is recommended within a domain of characteristic length. A series of angle representations is shown in Figure 5-4 with a discretized cell number of 200, the deviation is also shown in the figure.

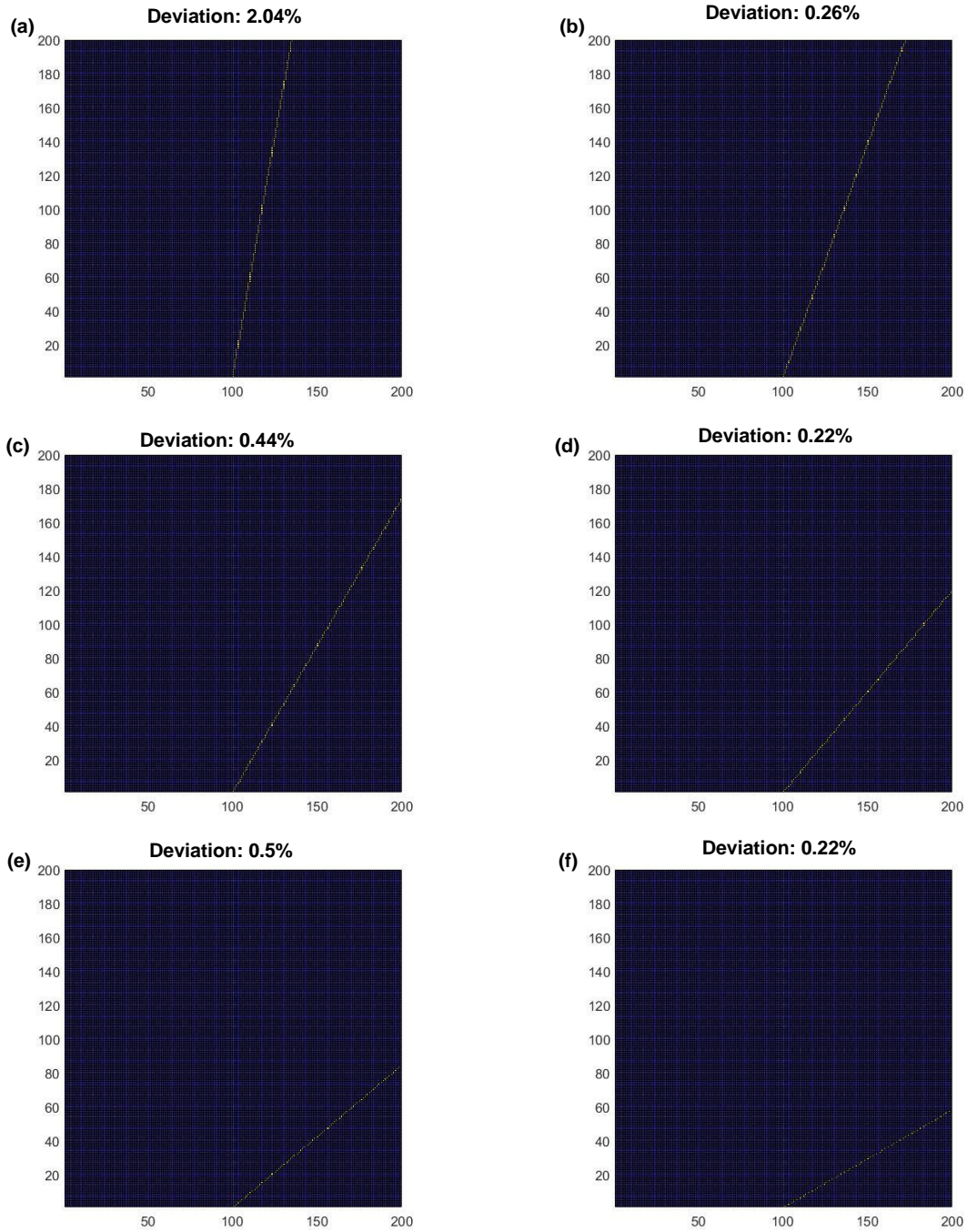


Figure 5-4 Representation of tilting angles with deviation (percentage): (a) 10 degree (b) 20 degree (c) 30 degree (d) 40 degree (e) 50 degree (f) 60 degree

According to equation 5-14, the size of the time step is decided based on the accurate representation of a curved grain boundary within the characteristic length.

$$R * \frac{\Delta t}{\Delta x} < 1 \quad \text{Equation 5-14}$$

Here, Δt is the time step size, Δx is the size of the cell and R is the solidification rate. In the following section, laser wire DED fabricated thin wall structure is used to validate the invasion model.

5.7. Experimental Validation

The building configuration wire DED process is shown in Figure 5-5a. The samples were fabricated using a LAWS 1000 automated welding system equipped with a 1 kW YAG solid fibre laser. The deposition with Ti6Al4V ELI wire feedstock was operated under an Argon gas protection environment. The process parameters are shown in Table 5-1. The case of wire DED fabricated Ti6Al4V is selected as a benchmark for this study because the epitaxial grain growth eliminates most of the random factors of nucleation. On the other hand, the thin wall structure fabricated is a good example for a pseudo-3D case simulation model as the columnar grains are able to develop extremely big into millimetre level, where the grain size exceeds the thickness of the thin wall and thus guarantee there is only one grain in the whole thickness direction. This eliminates the influences caused by the grains coming from the side and focuses on the competitive grain growth behaviour of a set of columnar grains. A comparison with the powder DED process is provided in Figure 5-5b, half-melt powders are found at the surface of the fabricated part (Figure 5-5d). These half-melted powders inevitably provide epitaxial growth positions introducing extra crystals and influencing the microstructure in the investigated domain. On the contrary, the wire

DED process is capable to fabricate an accurate thin wall structure with a clean surface on the side (Figure 5-5c), this indicates that melt pool geometry is relatively stable, and all the material experienced a melting and solidification process and eventually becomes the solidification microstructure in the fabricated part. To set up the boundary conditions based on the real experimental result and compare the simulation result with experiments, the following experimental activities are launched.

Table 5-1 Process parameters of the laser wire DED fabricated Ti6Al4V for model validation

Process Parameter	Laser Power	Scanning Speed	Wire Feeding Rate
Laser Wire DED	625 W	17ipm (431.8 mm/min)	35ipm (889 mm/min)

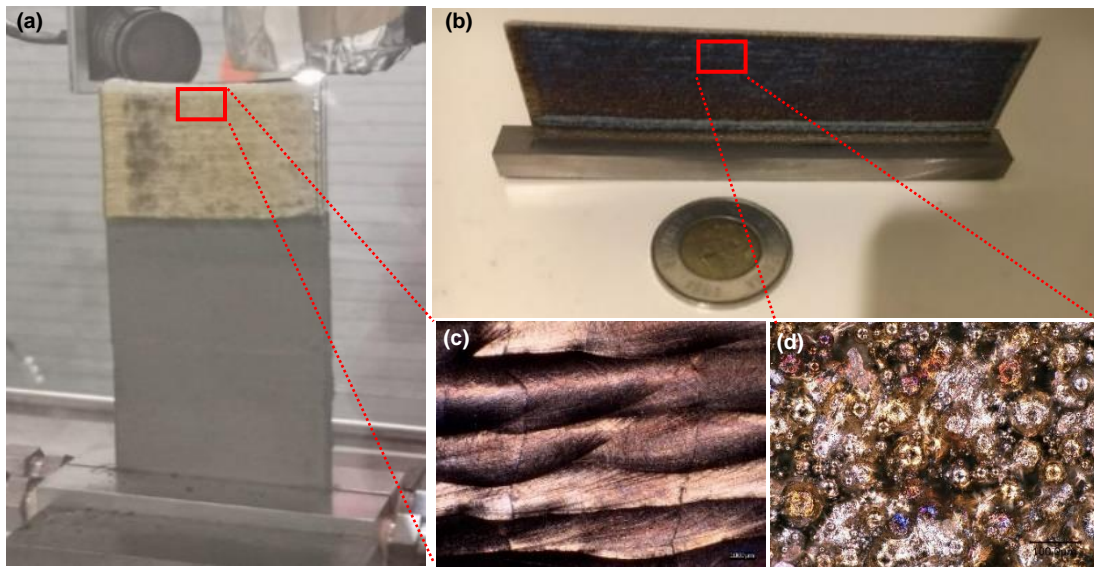


Figure 5-5 Building configuration and surface topology comparison of the wire (a, c) & powder (b, d) DED fabricated Ti6Al4V thin wall structures

5.7.1. Characterizations of microstructures

As can be seen from Figure 5-6a, the microstructure of wire DED fabricated Ti6Al4V at room temperature shows a full basketweave structure (alpha). In some cases of the DED process with

good cooling conditions, a full martensite structure (alpha prime) can be achieved. The solid phase transformation of Ti6Al4V eliminates most of the original crystal (prior beta) information with primary and higher-order branches of the same column grain merged with each other. The crystal orientation information can be captured from EBSD reconstruction techniques [76] as the solid phase transformation of Ti6Al4V strictly follows the BOR. Along the buildup direction, EBSD is carried out in three separate areas of each column grain for the reconstruction (Figure 5-6b). Maps of three Euler angle is shown in Figure 5-6c and the misorientation of the reconstruction result is lower than two degrees. This small misorientation can be attributed to the crystal deformation led by the high residual stress generated during the printing process. Also, the accuracy of the EBSD technique to distinguish a different crystal orientation is typically around 0.5 degrees, so the accuracy of the EBSD reconstruction technique is believed to be satisfied. However, the EBSD technique usually limits the size of the testing sample, and it is time and cost consumable. Thus, it is only used to capture the crystal orientation information of the solidification microstructure, and the grain topological structure reconstruction method in a part level is presented in the following section by extracting the grain boundaries of the column grains from sample surface and cross-sections.

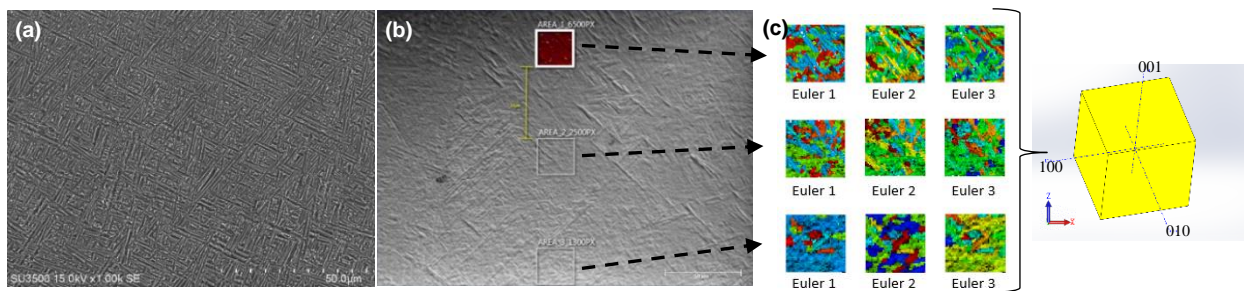


Figure 5-6 Microstructure of wire DED fabricated Ti6Al4V thin wall structure. (a) Electron microscope of the basketweave structure (fully alpha prime phase). (b) Three detected areas (spaced at 50µm) within the same prior beta grain. (c) The three corresponding Euler angle maps of alpha prime grain and the reconstructed crystal orientation present of the prior beta grain.

5.7.2. Grain boundary extraction & grain topological structure reconstruction

For the grain topological structure, the columnar grain morphologies cannot be reconstructed under a high amplification observation condition because of the solid phase transformation and the scale limitation. Luckily, different prior beta grains with different crystal orientations have different absorbance abilities of the visible light which can be recognized under an optical microscope. Distinguishing columnar grains with different crystal orientations is easier after chemical etching which can be observed with naked eyes. Moreover, the grain boundaries are areas filled with defects, for as the concentration of the dislocation in the low-angle tilt boundaries. These defects on the grain boundaries will also lead to different resistance to etchant and a contract between their neighbouring grains. On the surface of the printed part, grain boundaries also have a clear groove as they are the last solidified area compared to the inner area of grain, as shown in Figure 5-7.

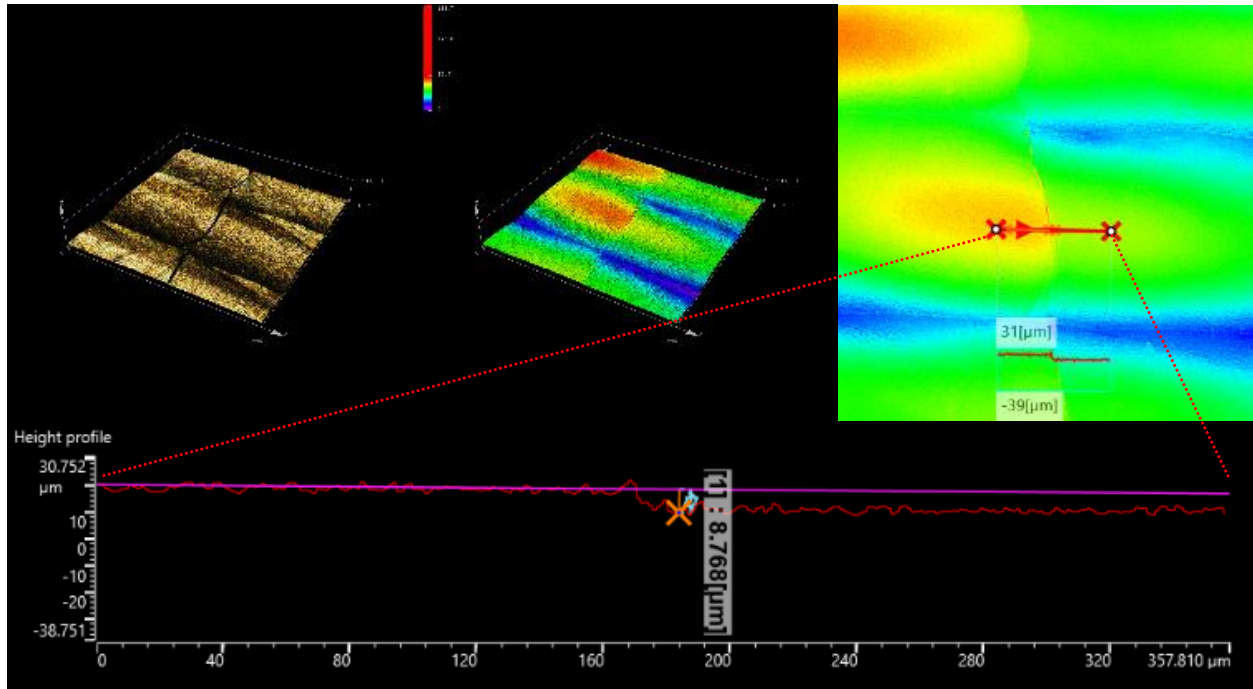


Figure 5-7 Laser confocal imaging and 3D optical image and contour map with the extracted cross-section height profile of grain boundary area.

The grain size and grain boundaries are extracted from the imaging results in a part scale under the help of image segmentation software (Figure 5-8 achieved by Dragonfly). For a 3D reconstruction of the grain topological structure, the thin wall samples are cut from the center on the X-Z plane and the above methods are used comprehensively to achieve a grain structure reconstruction on a large scale.

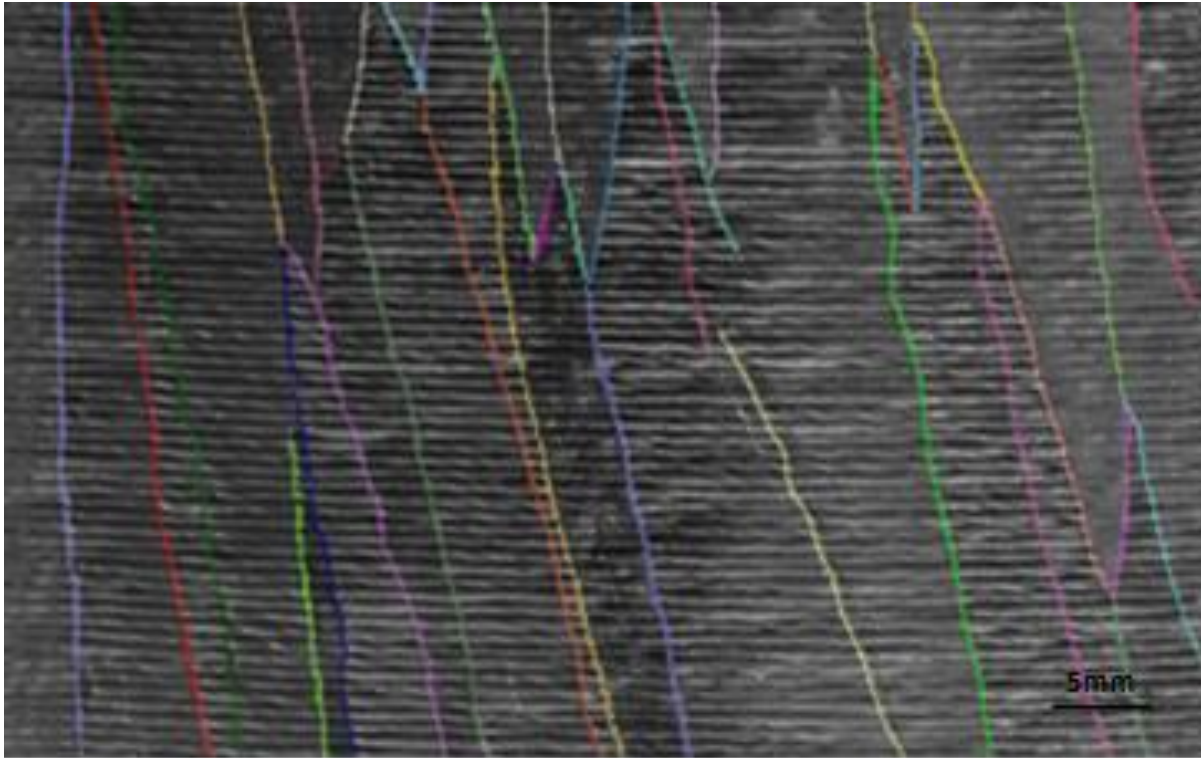


Figure 5-8 Grain boundary recognition under image segmentation from sample XZ_1.

5.7.3. Transient Melt Pool Geometry Attributes

We can never overestimate the importance of melt pool geometry to the resultant solidification microstructure in MAM. All solidification microstructure simulation works in part scale should carefully validate the melt pool geometry during the printing process to provide accurate solidification conditions and boundary conditions for the simulation domain. Figure 5-8a shows the laser positioning before the material deposition. A single track of material deposition in laser wire DED process includes the following steps: laser start and melt pool generation (Figure 5-9b&c), movement of a stable melt pool (Figure 5-9d-h), laser stop and cooling of the fabricated part (Figure 5-9i).

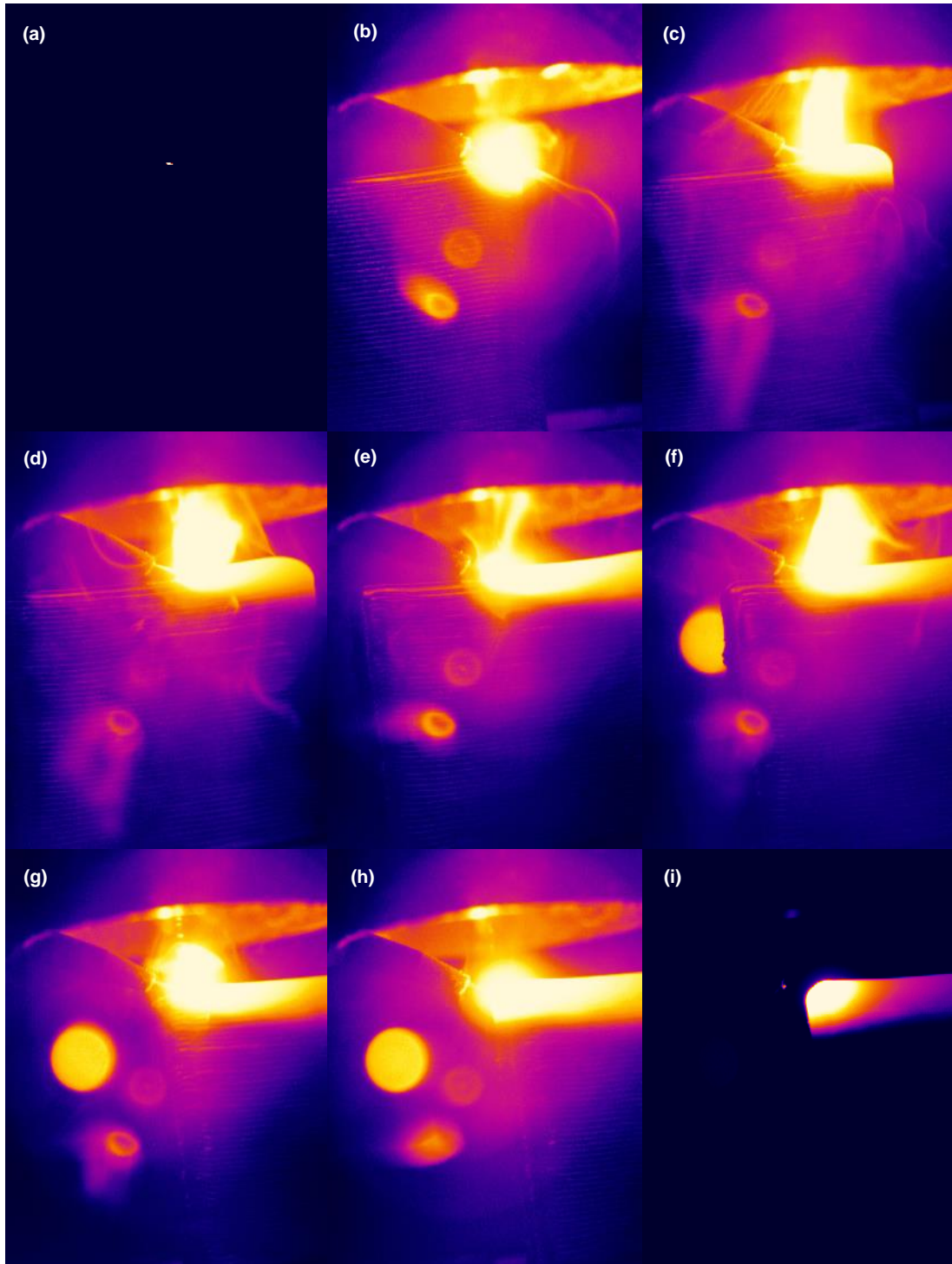


Figure 5-9 Deposition process of a single track: (a) Laser positioning at 0s (b) 1s (c) 2s (d) 3s (e) 4s (f) 5s (g) 6s (h) 7s (i) 8s

At the end of a single track of material deposition, the wire is retracted from feeding into the melt pool. This operation guarantees a flat fabrication and less distortion at the end of the bead. It takes around 0.2s as shown in Figure 5-10.

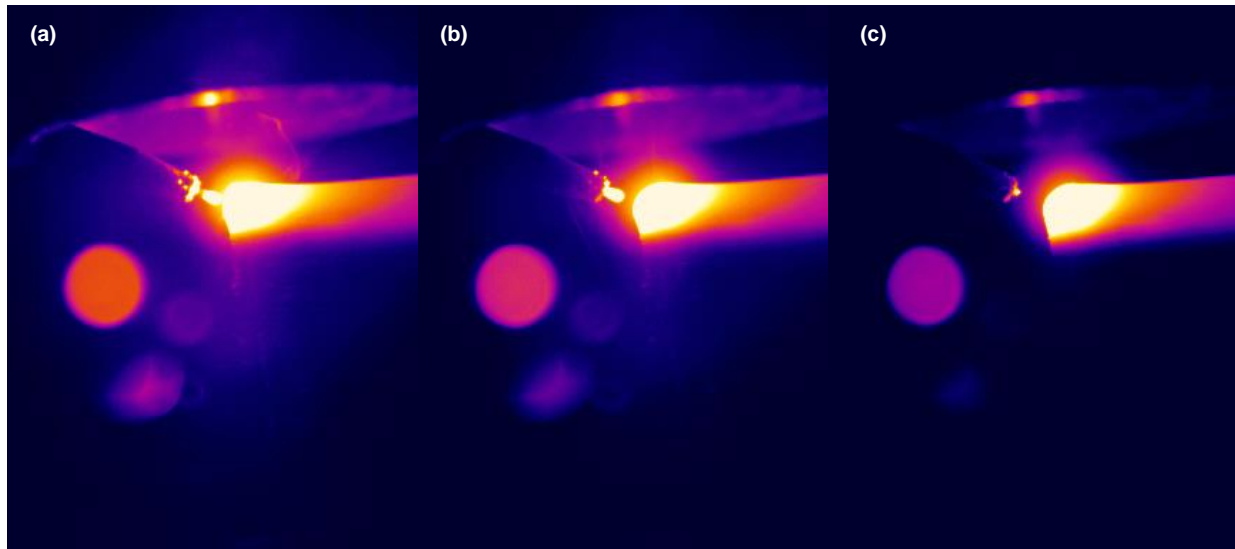


Figure 5-10 Laser stop and feeding wire retract at (a) 7.3s (b) 7.4s (c) 7.5s

In Figure 5-11a, a high-speed camera focusing on the melt pool domain is used for melt pool geometry validation. From the captured images and laser center position, the length and width of the fusion zone are measured. The depth of the melt pool and overlap between layers are measured from Y-Z cross-sections of the samples after chemical etching. The comparison between CFD simulation (Figure 5-11b) and experiment (both under single-track multi-layer configuration) is shown in Figure 5-11a where the melt pool geometry of the simulation coincides with experimental observation. For a more accurate melt pool geometry, the current research on ultrahigh-speed synchrotron X-ray imaging could provide more insights [238].

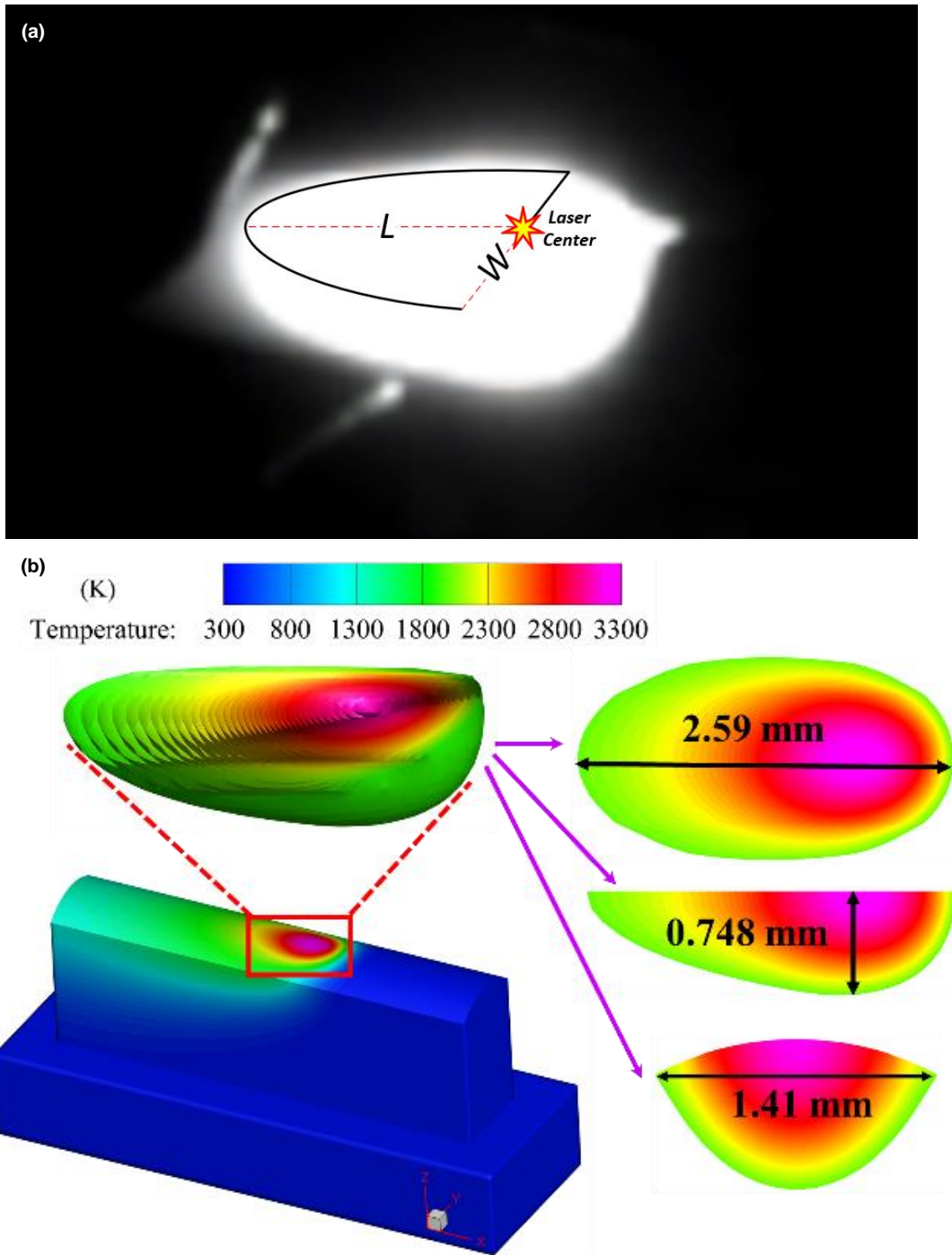


Figure 5-11 Melt pool geometry validation. (a) High-speed imaging of transient melt pool geometry with L and W representing the length and width of the melt pool. (b) Melt pool geometry extracted from the CFD simulation.

5.8. Results and discussion

The invasion model is carried out in a pseudo-3D case of a thin wall structure with a dimension of $22 \times 2.6 \times 7 \text{ mm}^3$ (10 layers). The solidification microstructure of the material deposited is simulated with a layer overlap of 38%. To keep the “relatively stable melt pool geometry” assumption valid, the simulation domain (shown in Figure 5-12a) is selected in the center (scanning direction) area of a thin wall to avoid melt pool geometry fluctuation and the printed part distortion located at both ends of a scanning track. For a quantitative comparison between the simulation and experimental result, the simulation domain is also located at the top of the printed part where the initial competitive grain growth inherits from the substrate is finished, and the columnar grains exceed the thickness of the thin wall eliminating the influence of the grains coming from the side.

Based on the integrated application of reconstruction techniques introduced in the experimental validation section, the image segmentation of different grains (Figure 5-12b) and the 3D reconstruction of grain geometrical structure (Figure 5-12c) in the target domain are achieved. The boundary condition of crystal orientation and initial grain structure are set directly based on the experimental result. After the initial several layers of material deposition, strong texture starts to emerge with $\langle 001 \rangle$ directions of the crystal generally parallel with the buildup direction. In this pseudo-3D model (a combination of multiple X-Z layers), the reflection of $[001]$ direction of the crystals is used to represent the crystal orientations in the 2D cases.

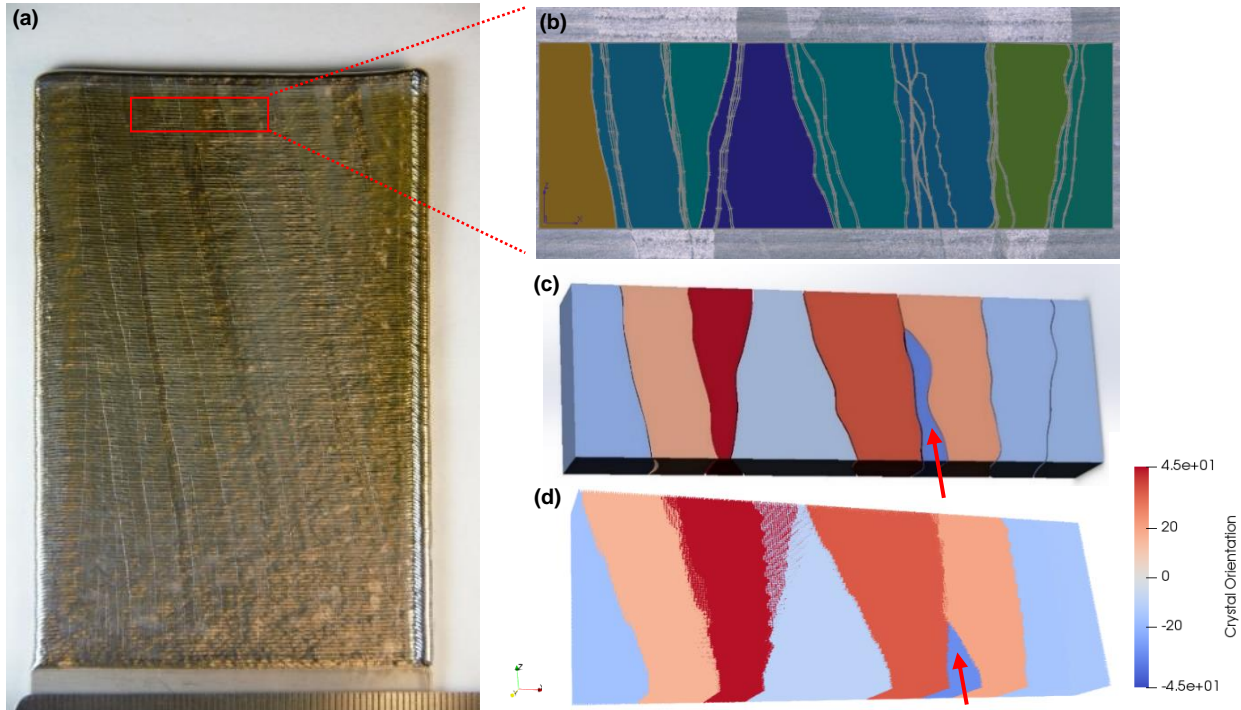


Figure 5-12 The application of the invasion model on the thin wall structure. (a) The simulation domain on a wire DED fabricated thin wall structure. (b) Grain boundary extraction on the three corresponding layers. (c) Grain structure reconstruction result. (d) Simulation result of the invasion model.

This invasion model was launched under a self-developed C++ environment and the simulation result is visualized by a data visualization software (ParaView). Under the 8 core CPU processor (Intel (R) Core (TM) i5-10300H), it took only 12 minutes to achieve the above simulation with a cell size of 20 μm . The simulation result of the solidification microstructure is shown in figure 8d which has a perfect match with the experimental result showing the increase and decrease of grain size along the material deposition process. It is also worth noting that the model accurately predicts the failure of the grain (highlighted in Figure 5-12c&d) during the competitive grain growth. This also indicates the application potential of the invasion model in other grain selection studies. The average grain size change of grain geometrical reconstruction and simulation along the material

deposition process in different layers is shown in Figure 5-13. The average grain size shows a perfect match between simulation and experimental reconstruction results in the first four and last two layers. However, vigorous increases are found at layer five and eight in simulation and experiment, respectively. This can be mainly attributed to the grain elimination at the corresponding layer, and the invasion model can rapidly recover its simulation accuracy within a short length range.

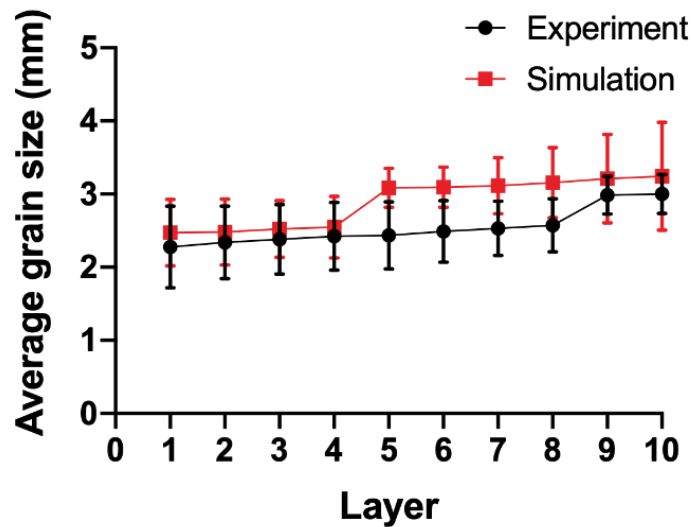


Figure 5-13 Average grain size comparison between experimental and simulation results.

According to the proposed methodological framework in Chapter 3, the predicted solidification microstructure from the invasion model can be combined with the solid phase prediction models for property prediction. The solid phase in the printed part can be extracted from the microstructural evolution map. In this strategy, the solid phase compositions are depicted as a microstructural evolution map showing the solid phase composition in each material deposition layer along the buildup direction of the DED process (e.g., the map developed by Kelly and Kampe [56]). In a more general case, the solid phase should be predicted from the experienced thermal

history. Based on arbitrary temperature history data, a model is proposed in [242] for a more accurate prediction of the solid phase composition.

For complex cases like solidification microstructure in MAM, the author believes there is no short path as many in-process parameters are not being quantified. In this simulation framework, experimental data is used as input to solve this problem by building up a database. A careful selection and coupling of various models with the appropriate application range is the only way to achieve an accurate, long-scale simulation with practical efficiency. The proposed invasion model is designed for constrained columnar grain growth like most cases in MAM when equiaxial grains are hard to achieve. However, the application field is not suitable for equiaxial grain growth with homogeneous nucleation in liquid as the invasion model cannot accurately track the grain boundary before the adjacent grains get in touch. The traditional methods such as the grain tip kinetic (CA) and deriving the field form (PF) are still very useful for the equiaxial grain growth and the invasion model can be a good complement when the prerequisite conditions are achieved.

The framework developed in this work also shows its practical importance when the solidification conditions are extreme, and the traditional solidification theory is invalid. This strategy of the invasion model is robust, and it can be applied to achieve an accurate solidification microstructure simulation for other types of material where current simulation methods are not suitable. It can also be coupled with other macroscale models or introduce data from models. When the invasion model is applied, the real problem becomes how to get the accurate local solidification condition, boundary condition and nucleation rules set up. In-situ characterization is a good way to provide accurate transient melt pool information [238], and the invasion model can be combined with the real-time experimental monitoring techniques to achieve a more accurate simulation result.

5.9. Conclusions

As many probabilistic models of solidification microstructure simulation are having difficulties when dealing with MAM processes, a deterministic model (named invasion model) is developed in this work to provide a quantitative prediction of solidification microstructure. With the wire DED process as a benchmark, the invasion model focuses on the grain boundary development within bi-crystal systems, and it believes the competitive grain growth behaviour is a sum-up of all the invasion behaviour of bi-crystal systems. By analyzing the effect of Marangoni and anisotropic growth, the transient grain boundary angles of columnar grains are represented by an invasion factor in the numerical model. To the best of the author's knowledge, the grain boundary angles of MAM fabricated Ti6Al4V has never been quantitatively studied before this work. Also, the invasion model provides a methodology to investigate the solidification microstructure for most of the alloy systems under a rapid solidification condition which is now still a difficulty for existing methods. When the traditional solidification theory frequently lost its efficacy on the simulation work (especially on the topics of nucleation), we realize that the establishment of databases for the key sub-processes is also important for a more accurate simulation. On the other hand, the invasion model is very practical as it can quantitatively depict the grain structure of columnar grains in a part scale with high accuracy and computational efficiency. The strategy is robust which can be combined with various existing mechanistic models. By combining with real-time monitoring data, we believe this model can be a good tool for process optimization in MAM and push the microstructural control into the next level of accuracy.

Chapter 6. Crystal Introducing Mechanism in Laser Wire DED fabricated Ti6Al4V

In the previous Chapters, a ‘no nucleation’ assumption is made based on the reality that laser wire DED fabricated Ti6Al4V mostly presents a fully columnar grain structure. However, there are still exceptions that disable this assumption even without reaching the critical undercooling. This Chapter discusses the importance of nucleation in MAM and investigates the crystal introducing mechanism in laser wire DED fabricated Ti6Al4V. Besides the term ‘nucleation’, this Chapter generalizes this phenomenon as the ‘crystal introducing’ as the crystals with different crystal orientations can be introduced to the printed domain without going through a nucleation scenario (growth from successful critical nuclei).

6.1. Introduction

Metal additive manufacturing has been rapidly developed for almost twenty years, however, the mechanism of nucleation (or crystal introducing) mechanism in MAM processes has been a long-term unsolved problem. Especially the solidification in MAM usually takes place under a rapid solidification condition with large supercooling, and the time lag is needed for structural relaxation into the steady-state regime which results in a time-dependent nucleation rate. Only limited works shed light on this area from an experimental and simulation point of view, and no unit solution has yet been addressed.

In MAM, there are several scenarios found that generates nucleation or introduce new grains with different crystal orientation into the fabricated part. First is the well-explored nucleation process which directly leads to the nucleation in the liquid phase. The embryos emerge in the liquid phase and the successful critical nuclei are able to continue growing into a new crystal. This effect is

mainly controlled by the constitutional effect attributed to the solute concentration in alloy systems. According to the interdependence theory [21, 22, 263], this process is controlled by the critical undercooling for nucleation [121], the amount of constitutional supercooling in front of the growing solid and the average spacing between the potent nucleation particles. A growth restriction factor Q was introduced by Hunt and Gaumann [264, 265] to evaluate the rate of developing a constitutional supercooling zone, where a large value of Q promotes nucleation. However, Ti6Al4V is a type of material with a low constitutional supercooling capacity which is very difficult to efficiently trigger this type of nucleation in MAM even with the addition of grain refiners (silicon or boron). Therefore, in most MAM fabricated Ti6Al4V studies, nucleation is believed to not exist as the epitaxial grain growth with no thermodynamic hindrance for nucleation dominates the whole material deposition process.

Another way to achieve the equiaxial grain structure in the fabricated part is by introducing the second phase particles (nanoparticles). By doing this, the energy barrier for a critical nucleus will be decreased thus promoting nucleation. This can be explained by the traditional nucleation theory as the introduced external surface decreased the free energy cost of generating a nucleus. However, this practice means a chemical composition change in the fabricated part. And the addition of the second phase particles leads to powder contamination which is a big problem in real practice.

There are other scenarios in MAM which introduce external nucleation sites into the printed domain without reaching the critical supercooling (epitaxial grain growth). In these scenarios, the crystals nucleate at the existing crystals and inherit the crystal orientations. Examples include the nucleation on the crystal surface of the half-melted feedstocks (powder or wire) or the breaking of growing dendrites (by introducing high-intensity ultrasound). These examples also approve that

the CET phenomenon is not a full solidification condition (G&R) controlled process, and even without bulk nucleation, CET is still achievable with proper process control.

Currently, one of the most important research trends on MAM is to refine the crystals in the printed part. In another word, to introduce more crystals into the printing domain. Thus, the study of nucleation, which eventually decides the grain size, becomes very important. Yet our understanding of the crystal introducing process in MAM is fragmented. Substantial amount of effort has been made to understand the mechanisms behind it. The rate, position and formation time of nucleation have a significant influence on the resultant solidification microstructure of the printed part. In most cases of structural materials, the microstructures as equiaxial grains are usually more desirable because the homogeneously distributed grain boundaries have the benefit to avoid the stress concentration during deformation thus providing more strength and reliability. Following this, how to promote nucleation during the material deposition process of MAM and achieve CET transformation becomes an important research topic. Some work shed lights on this topic, as the CET in MAM can be achieved by introducing external surfaces for nucleation, process improvement, process parameters or scanning strategy control, alloy component and phase design and so on. As suggested by Martin [256], introducing nanoparticles of nucleants that promote nucleation during MAM solidification can be a good strategy to improve the printability of conventional alloys. In their reported work, crack-free printing of 7075 and 6061 series aluminum alloys was achieved with equiaxial and fine-grained microstructure. A significant mechanical property improvement in terms of strength and ductility was found. In another work reported by Zhang [22], a titanium-copper alloy system was found to have promising mechanical properties with a fully equiaxed fine-grained microstructure when fabricated via MAM. Different from aluminum alloys, there is no effective commercial grain refiner for titanium that can promote the

nucleation process. So based on interdependence theory, a titanium-copper alloy system was designed as it has a high constitutional supercooling capacity which can override the negative effect of a high thermal gradient in the laser melting process and form an ultrafine eutectoid microstructure. In terms of process improvement, an interesting work from Todaro [266] employed high-intensity ultrasound to the SLM process. With the help of the acoustic cavitation effect, they successfully achieved the printing of equiaxed fine prior beta grains of Ti6Al4V, the yield stress and tensile strength were found to have 12% of improvement. With the established research on welding process, the controlling of these microstructural features turns out to be an important aspect to have a great influence on the resultant mechanical properties. Until now, to achieve the CET in MAM is still a research focus for the printing of different alloy systems for example the manipulating of process parameters, preheating the substrate and so on.

6.2. Nucleation in MAM solidification microstructure models

Almost all the phase transformation process in nature starts from nucleation. However, nucleation is a transient process, and the scale limits the researchers to get direct experimental evidence for the nucleation study. Great achievements have been made to experimentally observe the generation of early-stage nucleation in a solid phase [267], the shape of the critical nuclei can be observed experimentally in very few cases. As for the nucleation in the liquid metal, it is still an unachievable task especially in the extreme solidification condition of MAM.

Classical nucleation theories (CNT) believe that there are two kinds of nucleation processes: homogeneous and inhomogeneous. From the thermodynamic point of view, homogeneous nucleation is hard to achieve as the energy barrier request is very high, typically three times that in inhomogeneous nucleation. In the solidification process of MAM, homogeneous nucleation is

rarely encountered as impurity is inevitable during real practice. The main criticisms of the CNT include not only its capillary approximation but also it is unable to account for the grain density changes in different cooling conditions. That is why the instantaneous nucleation theory is broadly accepted which treats the nucleation phenomenon as a thermally activated process.

There is also no doubt that the treatment of nucleation in different microstructure simulation models has a significant influence on the solidification microstructure simulation result of MAM process. Unfortunately, the prevailing nucleation models in the solidification microstructure simulation models for laser wire DED fabricated Ti6Al4V processes are inappropriate which hinders the simulation results to be quantitative. In traditional models, nucleation is normally understood as an unpredictable process where the grain number is counted beforehand and manually arranged during the microstructure simulation process. Since 1993 when the most common solidification microstructure simulation method in MAM-cellular automata-was created by Dr. Rappaz in which the nucleation was treated as a continuous process. This means the nucleation number needs to be counted before doing the microstructure simulation. This could be more practical to be achieved by grain size analysis. The seed density model is then applied to describe the nucleation phenomenon in MAM [268]. However, this practice goes against the prediction nature of simulation and a single nucleation rule that cannot capture the real nature of the nucleation process in MAM processes. Thus, detailed work on the nucleation for MAM process needed to be applied to these models in order to guarantee the simulation accuracy. The study of the nucleation process is important also because the nucleation rate directly decides the grain size and grain structure. If the nucleation is eliminated during the whole MAM process, theoretically, the grain with growth advantages (e.g., preferred grain growth direction parallel with the thermal gradient direction) can develop into a very large scale after the competitive grain growth. It follows

that the solidification microstructure will eventually develop into a single crystal. However, this is never found in the cases of MAM Ti6Al4V. This indicates that our understanding of the crystal introducing mechanism is far from enough as it is a comprehensive result of the material properties (chemical component, purity, viscosity, interface energy and so on) and the forming environment (G&R, residual stress, solute concentration, thermal field, vibration, or other physical factors).

In this Chapter we demonstrate without reaching the CET curve, nucleation is possibly generated from the grain boundary position. And recrystallization is the reason which introduces the new crystals into the printed domain during the process of laser wire DED. The grains forming via solid-state recrystallization are then used as seeds when a subsequent layer solidifies thus giving rise to a refined grain structure. This study breaks grounds on understanding of the nucleation formation condition. It is an important step towards the formation of a unified understanding of the nucleation mechanism in MAM process.

6.3. Experimental Methods

6.3.1. Laser wire DED fabricated Ti6Al4V thin wall structure

To distinguish a nucleation spot from epitaxial grain growth is difficult in MAM processes. For example, the half-melted powders or the crystal growth from the side is usually confused with the real nucleation spot. In this work, laser wire DED processed thin wall structure is chosen as a benchmark to analyze the nucleation phenomenon in MAM. It is chosen as the benchmark because of two reasons: first, it eliminates the influence of the grains developed from half-melted metal powder, which is very typical in all the powder bed processes including SLM and EBSM. Second, the thin wall structure guarantees there is only one columnar grain in the whole thickness of the thin wall which leads the problem to a pseudo-3D problem and is easier to analyze. Also, if the

grain size exceeds the wall thickness, the influence of the grains coming from the side can be eliminated because there is only one grain in the Y direction.

As shown in Figure 6-1, a thin wall structure was cut from the center of the X-Z plane and compared on both sides. We found that the grain boundary from one side can always find its correspondence on the other side of the thin wall (Figure 6-1). This approves the statement that the thin wall structure can eliminate the grains that come from the side when the grain size exceeds the thickness of the fabricated wall. And even for crystals with their grain size in the X direction smaller than the thickness of the thin wall structure, they are still able to be found on both sides as a result of the epitaxial grain growth.

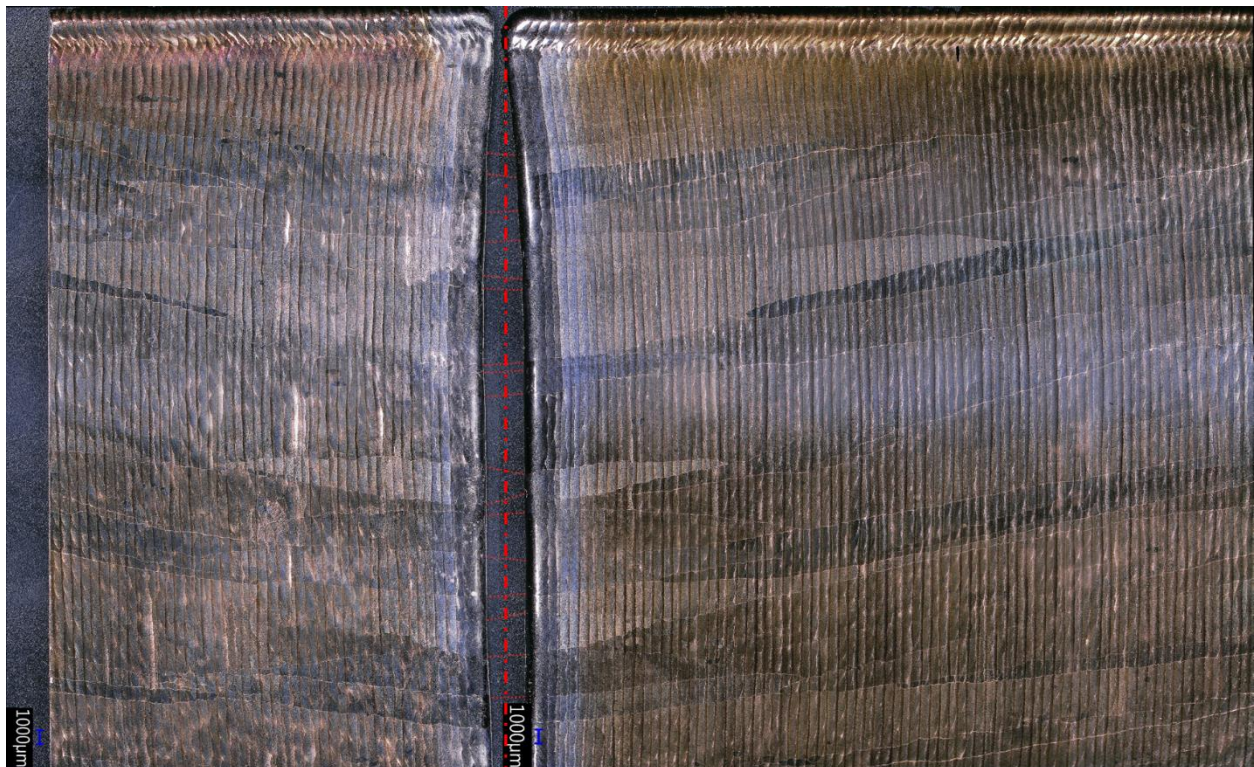


Figure 6-1 Comparison on both sides of a thin wall structure.

To get the first intuition of the crystal introducing mechanism in laser wire DED fabricated Ti6Al4V, the observation was made on the front surface of a continuously deposited thin wall structure (180 layers). A window (65mm * 45mm) at the top center section was used for analysis based on the image segmentation technique introduced in Chapter 4.3. The position recognized as the crystal start and end places is marked in Figure 6-2. Within the window, there are a total of 8 positions marked as the start place of a newly introduced crystal, and 9 places are marked as the end positions of crystal development because of competitive grain growth.

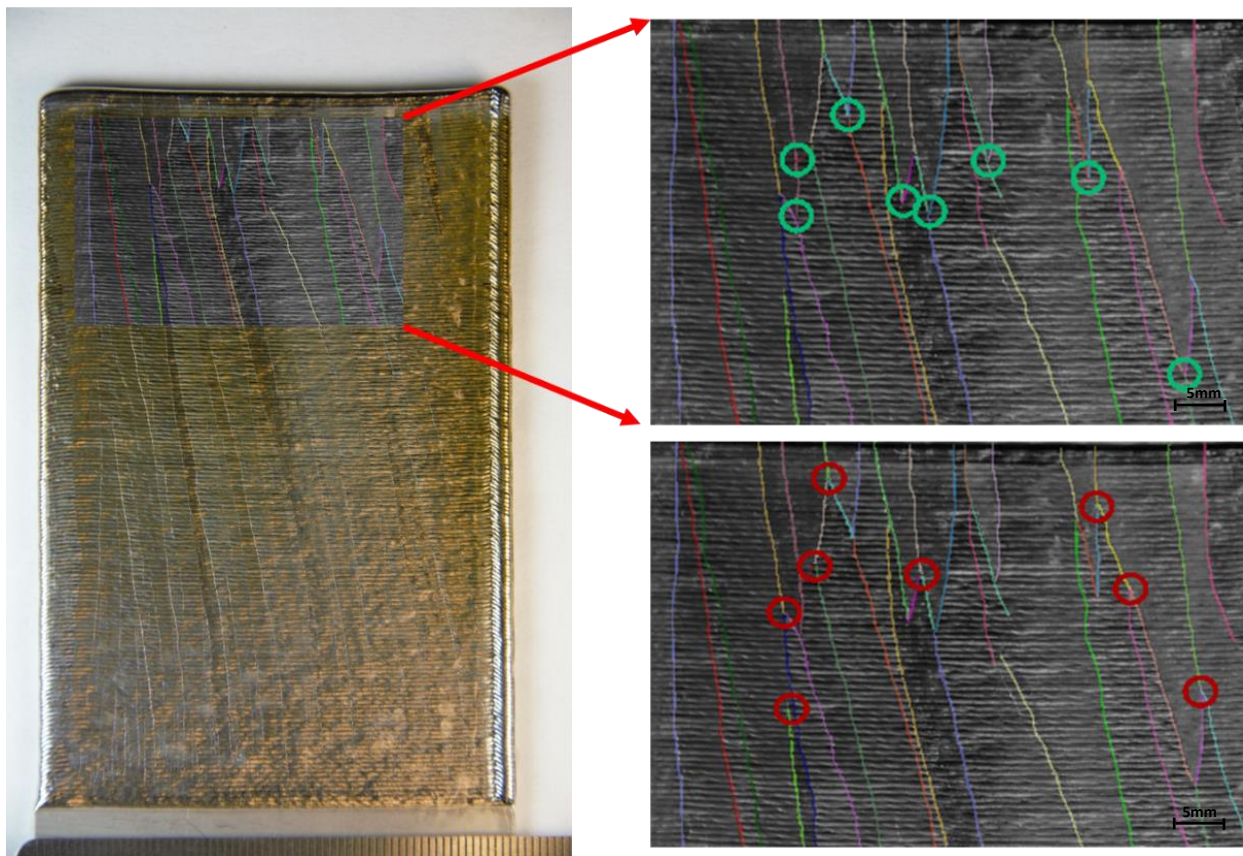


Figure 6-2 Crystal introducing (b) and end (c) position in a laser wire DED fabricated thin wall structure (a)

In the investigated window, seven out of the eight recognized crystal introducing sites are located at the grain boundary of the previous layers. Clearly, the distribution of the nucleation sites (or crystal introducing sites) does not follow a random manner suggested by the famous Johnson–Mehl–Avrami–Kolmogorov (JMAK) equation [269]. Instead of randomly distributed, the start places of crystal introducing process in laser wire DED fabricated Ti6Al4V has priority to locate at the grain boundaries.

By looking at the last several layers (176th - 180th layer) of material deposition in the fabricated part (Figure 6-3), the grain growth strictly follows epitaxial grain growth without any new crystal introduced. This approves that the solidification condition cannot provide efficient supercooling to generate nucleation in the liquid phase. Compared to the previous layers of material deposition, the last layer provides a lower thermal gradient value as a result of heat accumulation and a worse heat extraction condition. With a constant scanning velocity that gives the same solidification rate, theoretically, the solidification condition (G&R) in the previous layers moves even further in the columnar grain area. This experimental evidence suggests the solidification condition of laser wire DED processed Ti6Al4V under the mentioned process parameters fully located in the columnar grain area in the G&R map. Thus, the introducing of crystal in this process is believed to take place during the solid-state.

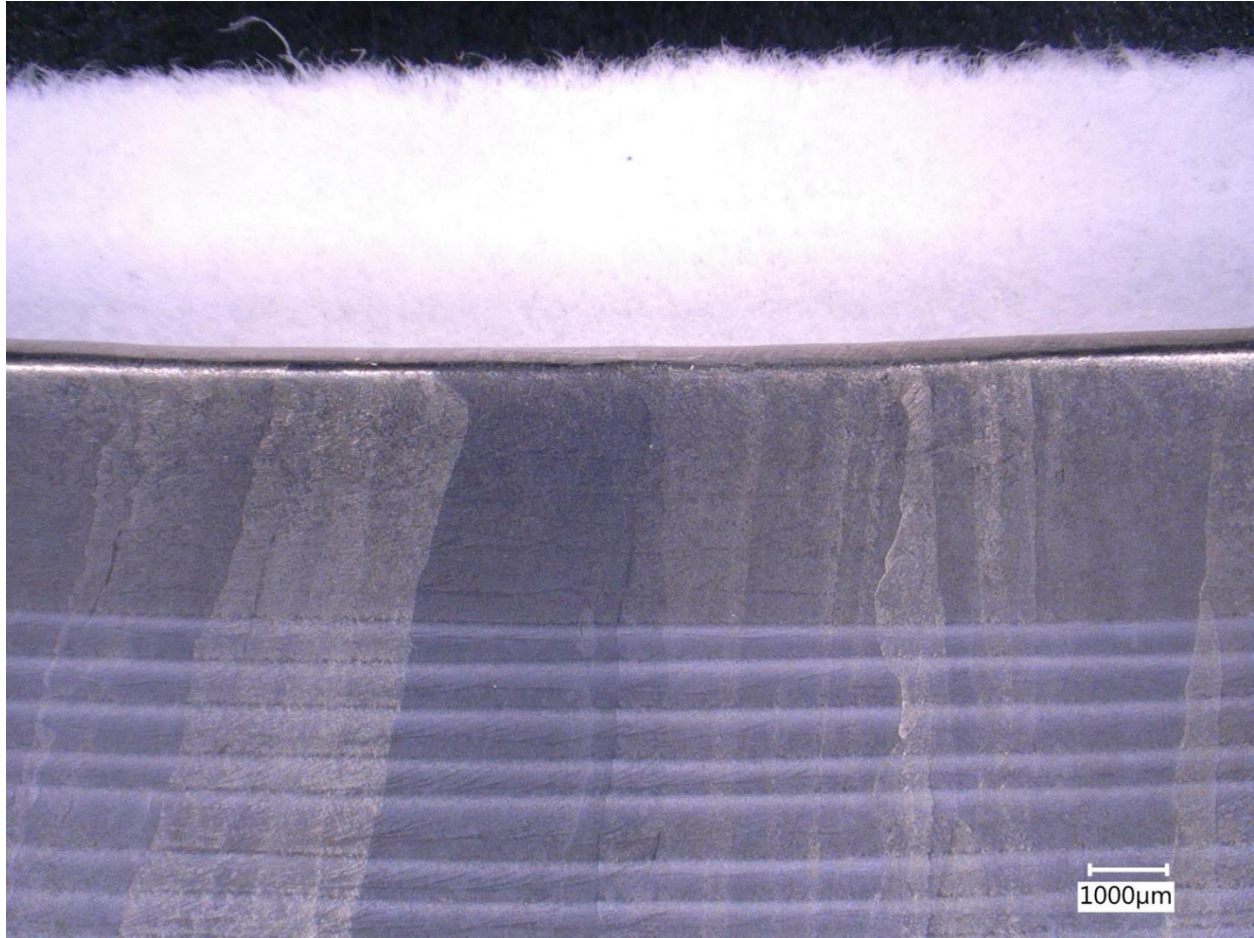


Figure 6-3 Solidification microstructure in the last 12 layers of material deposition

As shown in Figure 6-4, several introduced crystals which are able to win the competitive grain growth and develop into a millimetre scale are selected for a detailed grain geometrical structure reconstruction. The grain structure of these introduced crystals is reconstructed from image segmentation of the front, center, and back surfaces in the fabricated part. The accuracy of this reconstruction is guaranteed by using the layer number as a reference. The lowest point in these reconstructed crystal structures does not have a preference in the Y direction which means it can either take place at the surface or the internal areas of the fabricated part.

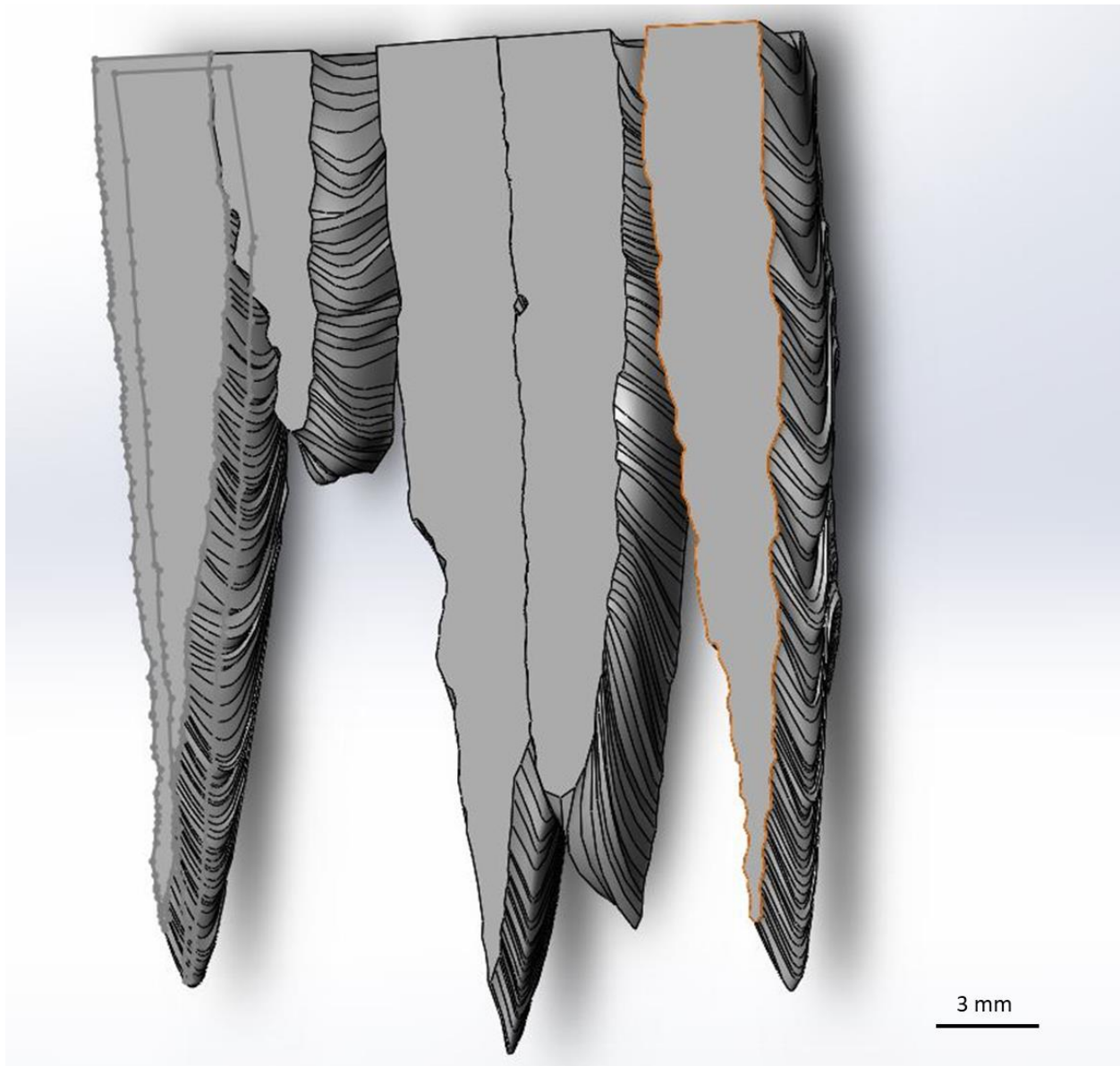


Figure 6-4 Grain structure reconstruction of the introduced crystal

6.3.2. Experimental design

Based on the observations in the previous section, the investigation of the crystal introducing mechanism in laser wire DED fabricated Ti6Al4V has focused on the recrystallization process in the previous deposition layers. As a section (35% - 40% in height) of the previously deposited

layer is remelted during the material deposition process of laser wire DED, the recrystallized crystals get a chance to epitaxially develop into the melt pool area and participate in the following competitive grain growth. This crystal introducing mechanism can also take place under other process parameters as most of the solidification conditions provided by laser wire DED are in the columnar area for Ti6Al4V alloy.

To further approve this theory, three hypotheses are proposed here to investigate the influence of different process conditions on the crystal introducing mechanism. According to the focus on the recrystallization process which the residual stress and reheating temperature are believed to be the driving force, laser wire DED fabricated Ti6Al4V thin wall structures were fabricated using a 1 kW YAG solid fibre laser automated welding system under Argon gas protection environment. The feedstock is selected to be Ti6Al4V ELI in the format of wire to eliminate the epitaxial grain growth from the half-melted powder. A laser power of 650 W with 16.9 ipm scanning speed and a feed rate of 50 ipm are used in the fabrication. The additive portion starts from the edge of a Ti6Al4V rolling sheet with a thickness of 1.26 mm. The scanning direction is constant during the deposition process and the material is deposited and builds up the thin wall structure (Figure 6-5) with a dimension of 95 ± 0.2 mm * 63 ± 0.5 mm * 2.5 ± 0.1 mm.

Four samples are fabricated for the investigation of the crystal introducing mechanism (CI samples). The sample CI_1 is the controlled group with a continuous deposition of 180 layers. The sample CI_2 is fabricated under the condition that the fabricated section is cooled down to room temperature for every 60 layers of material deposition. By doing this, it eliminates the influence of heat accumulation during the process. The sample CI_3 is annealed for every 60 layers at 600 degrees for 1 hour to eliminate the residual stress. The sample CI_4 is heat-treated above the alpha-beta transus temperature (under 1050 degrees for 2 hours) for every 60 layers. This sample

investigates the influence of the solid phase transformation of Ti6Al4V on the resultant solidification microstructure.

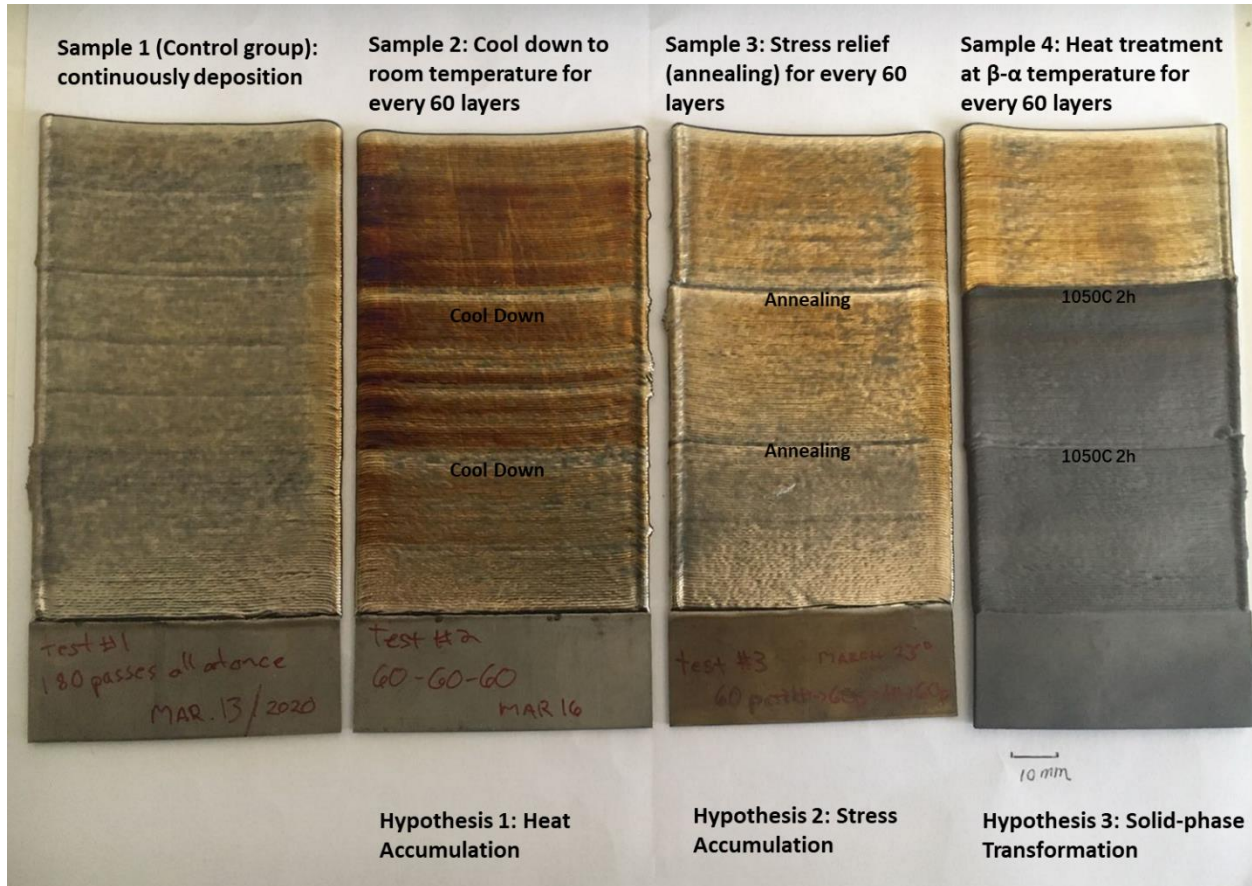


Figure 6-5 Sample matrix of the experimental design. Sample CI_1. continuous deposition of 180 layers (control group). Sample CI_2. Cool down to room temperature for every 60 layers (hypothesis 1). Sample CI_3. Annealing treatment for every 60 layers (hypothesis 2). Sample CI_4. Heat treatment at alpha-beta transform temperature for every 60 layers (hypothesis 3).

The samples for analysis and the observation are all under the as-built condition to eliminate the risk of introducing new nucleation positions and grain boundary migration caused by heat treatments. The samples are polished on the front and back surfaces and cut from the middle

surface of the X-Z plane. The microstructure observation was launched from both surfaces at the front and back as well as the etched middle plane.

6.3.3. Solidification microstructure and grain size analysis

Based on the observed solidification microstructure of DED fabricated Ti6Al4V, the grain structure and size analysis are carried out on the etched middle plane of the Y direction. As shown in Figure 6-6, the grain size is measured in the X direction for every ten layers of material deposition. According to the topological structure of the columnar grains, fabricated part geometry and the competitive grain growth mechanism, the grain size in the X direction directly reflects the influence of the introducing crystals on the solidification microstructure.

As this scale of grain size measurement is launched under an optical microscope, the microstructural features smaller than 100 μm is ignored. The small-size features are further analyzed in the following section of this Chapter. The reorganization of the grain boundaries of the columnar grains is achieved by a comprehensive analysis between the optical microscope image and the confocal laser scanning result. A more accurate grain boundary reorganization method is the EBSD. However, this technique is limited by scale and is not suitable for the grain size measurement task in this Chapter.

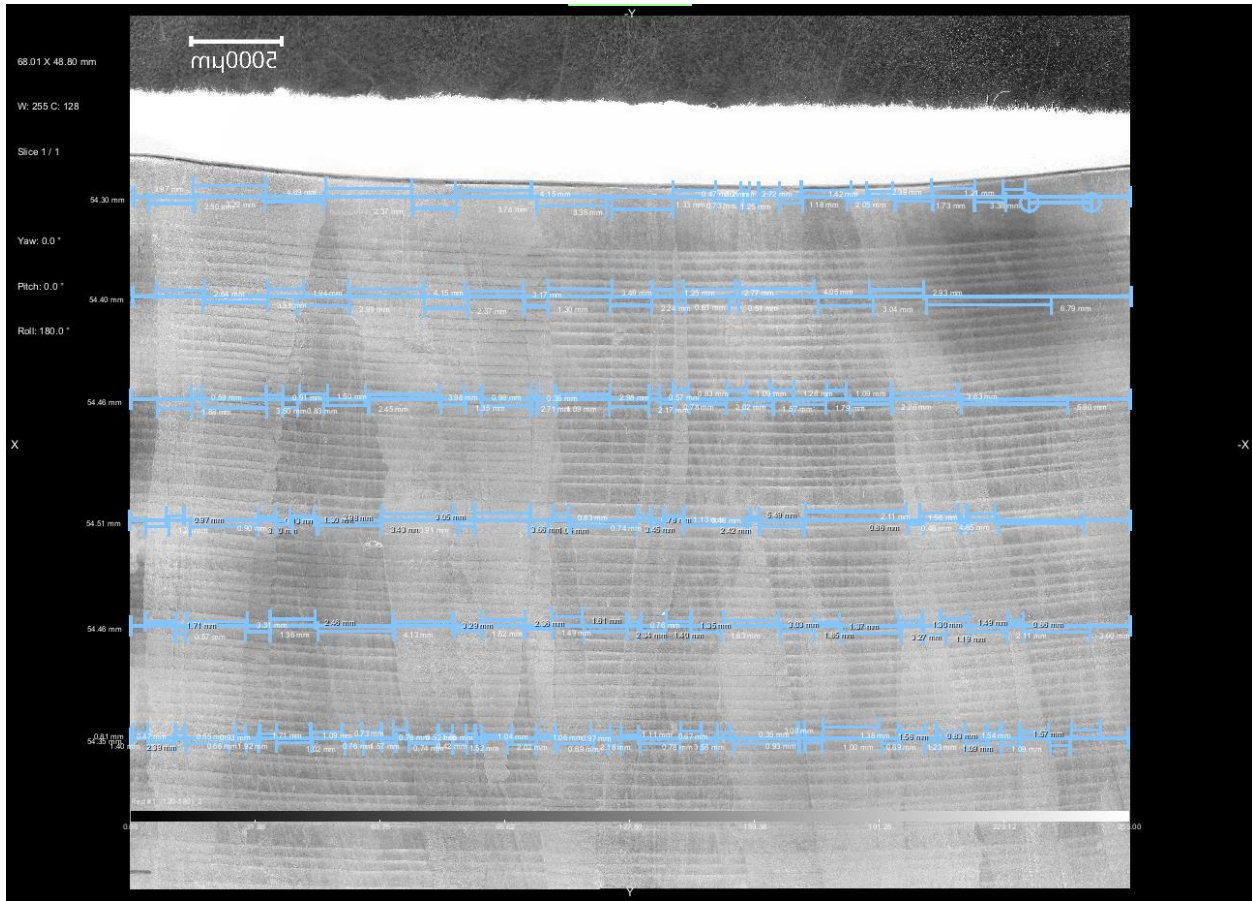


Figure 6-6 Grain size measurement of Sample NI_1 at 160th – 180th layers (every ten layers) on the middle plane of Y direction.

The grain size change of the control group (sample CI_1) along the build-up direction is shown in Figure 6-7. The average, standard deviation and scattering of the data points are shown in the figure. The average grain size is increasing along the build-up direction; however, the increasing speed of the average grain size is smaller than the maximum grain size in each layer. An increasing value of the standard deviation is also found, which can be attributed to the competitive grain growth effect that the preferred grains are eliminating the unpreferred ones during the process. However, the decreasing of average grain size is also found in some of the layers (e.g., layer 30, 40, 130, 160 and 180). This is clear evidence that the crystal introducing mechanism is limiting

the average grain size. Within the areas that the biggest crystal keeps developing, the difference between the maximum grain size change and the average grain size change can be considered as the influence of this crystal introducing mechanism on the grain size change during laser wire DED fabricated Ti6Al4V process.

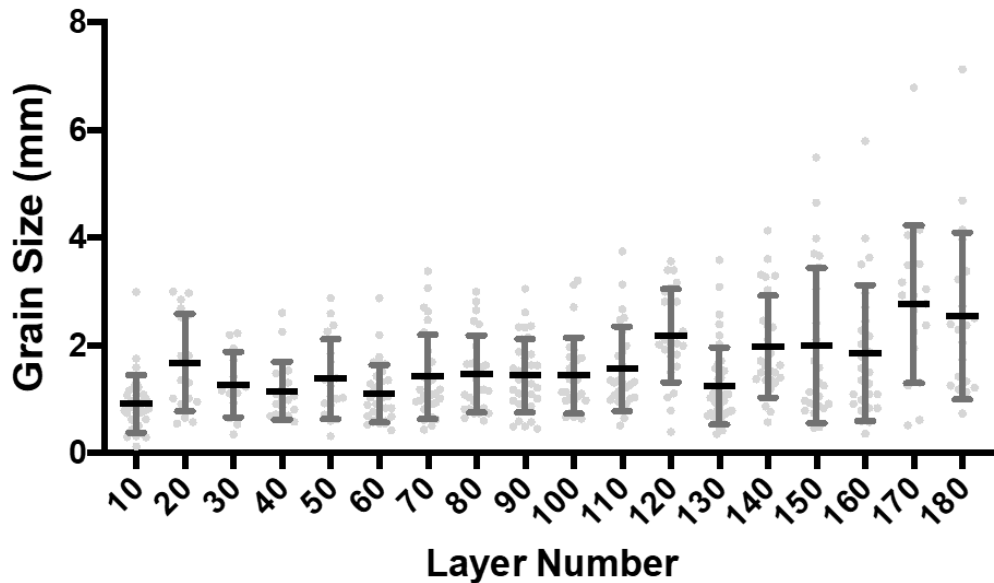


Figure 6-7 The grain size analysis of the control group (sample CI_1) along the build-up direction

The crystal introducing position is analyzed in Figure 6-8, the middle area in sample CI_1-4 (layer 60-120) is used for the optical microscope recognizable crystal introducing position marking. Apart from the priority at previous grain boundaries, the crystal introducing position still presents a random manner within the experimental sample matrix. The number of the crystal introducing position is found to be fewer in sample CI_3. This indicates the residual stress in the fabricated parts contributes to the generation of the introduced crystals. In Figure 6-8d, the heat treatment above the alpha-beta transformation temperature eliminates the original solidification

microstructure. The slow cooling rate along the chamber cooling provides the environment for the alpha grains to develop into a larger size, and a coarse basket weave microstructure emerges.

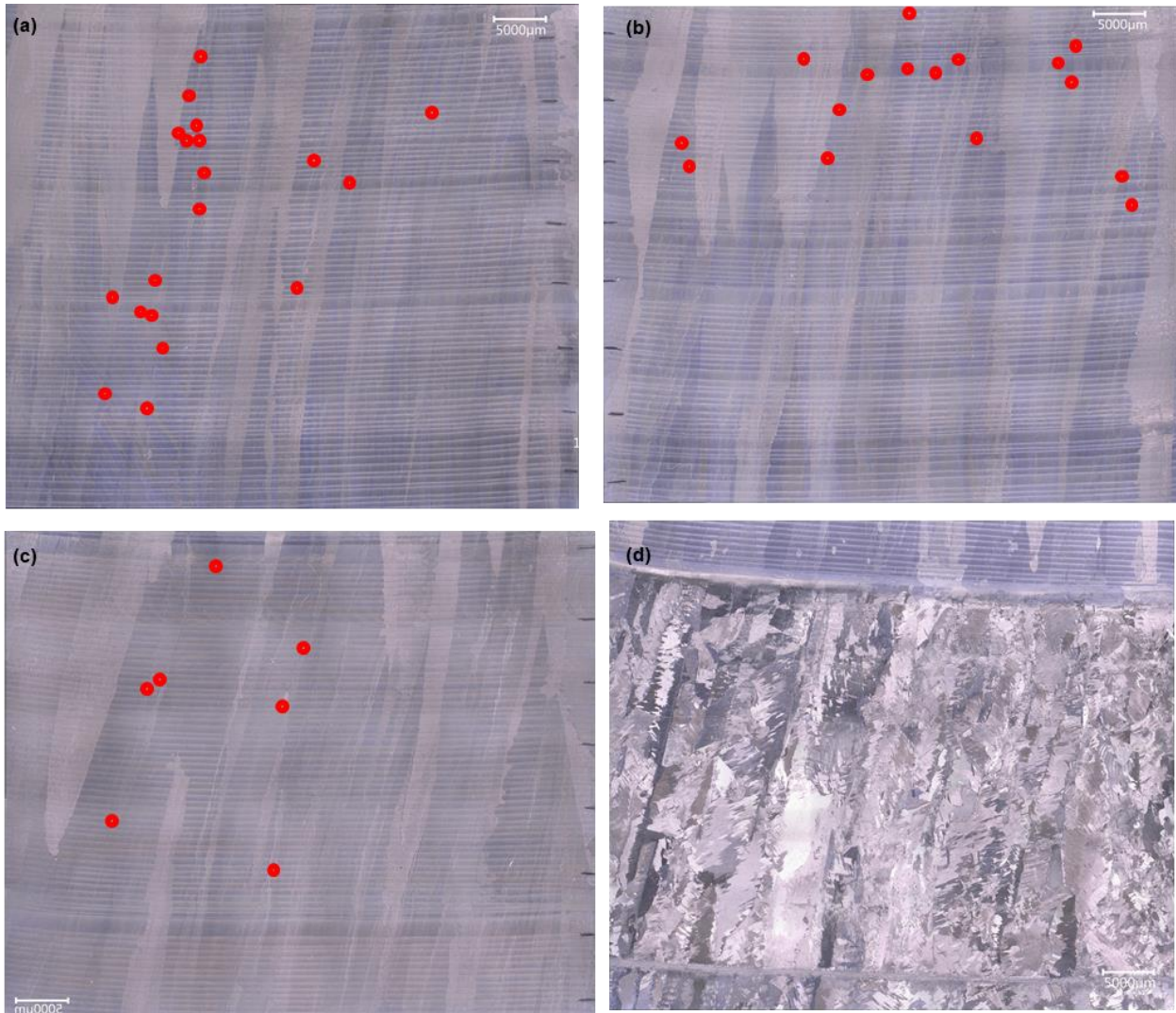


Figure 6-8 Crystal introducing position marking for the experimental sample matrix in layer 60-120: (a) CI_1 control group (b) CI_2 cooling to room temperature (c) CI_3 annealing (4) CI_4 heat treatment above the alpha-beta transformation temperature

A closer look at the sample CI_4 in layer 120-180 (without heat treatment) reveals another evidence that the residual stress contributes to the generation of the introduced crystals. According

to the literature [52, 270], the residual stress of the laser DED fabricated parts tends to concentrate at the center and bottom area in the fabricated thin wall structure. As shown in Figure 6-9, it is also the concentrated crystal introducing position fabricated from the alpha-beta transformation temperature heat-treated substrate. However, how the solid phase transformation influences the crystal introducing is still an open question which needs further investigation.

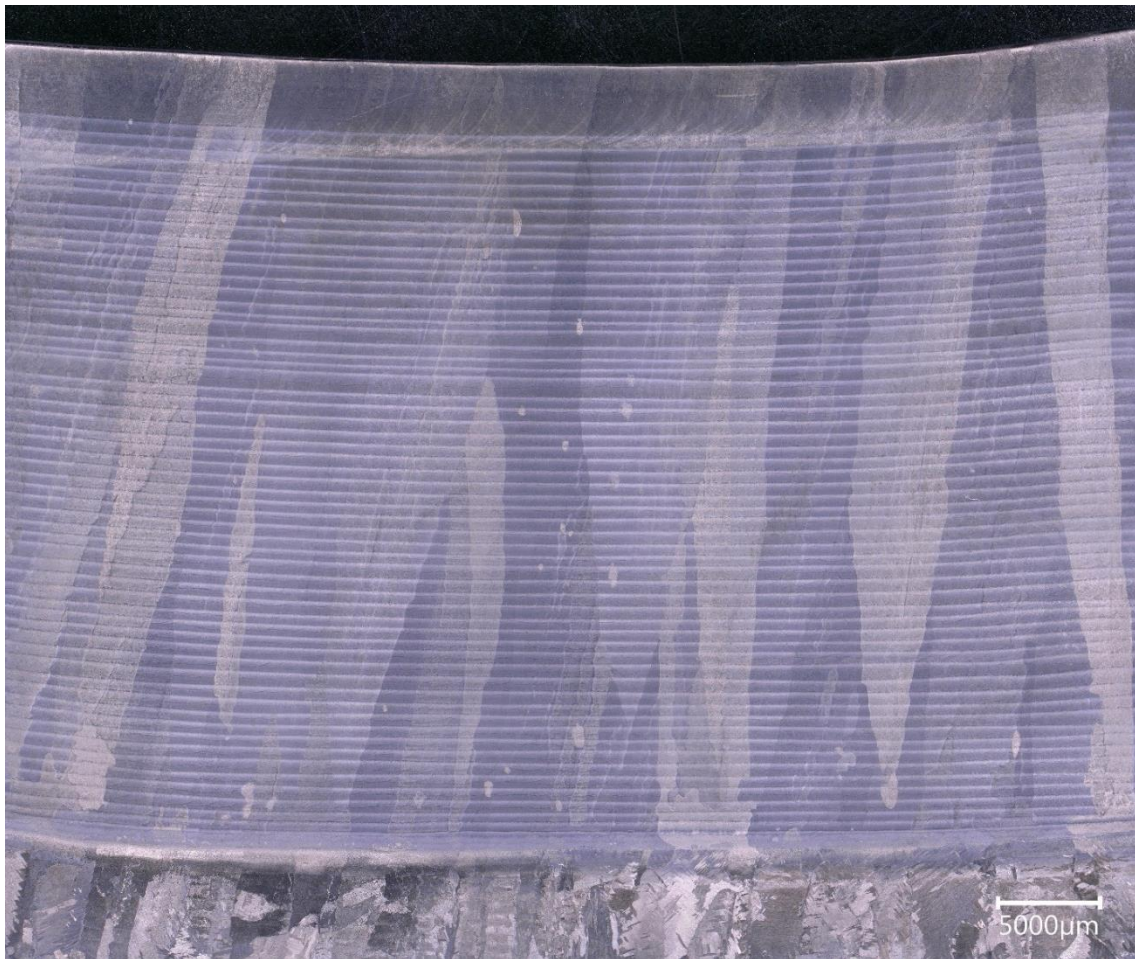


Figure 6-9 The crystal introducing position in sample CI_4 (layer 120-180).

6.4. Results

6.4.1. Contamination (gas impurities of oxygen, nitrogen)

Ti6Al4V is an active alloy that easily interacts with Oxygen and Nitrogen during solidification. To evaluate the effect of gas impurities on the crystal introducing mechanism. The X-Ray photoelectron spectroscopy (XPS Thermo Scientific K-Alpha) was used to analyze the chemical component difference between the intergrain and grain boundary area of a neighbouring bi-crystal system (Figure 6-10).

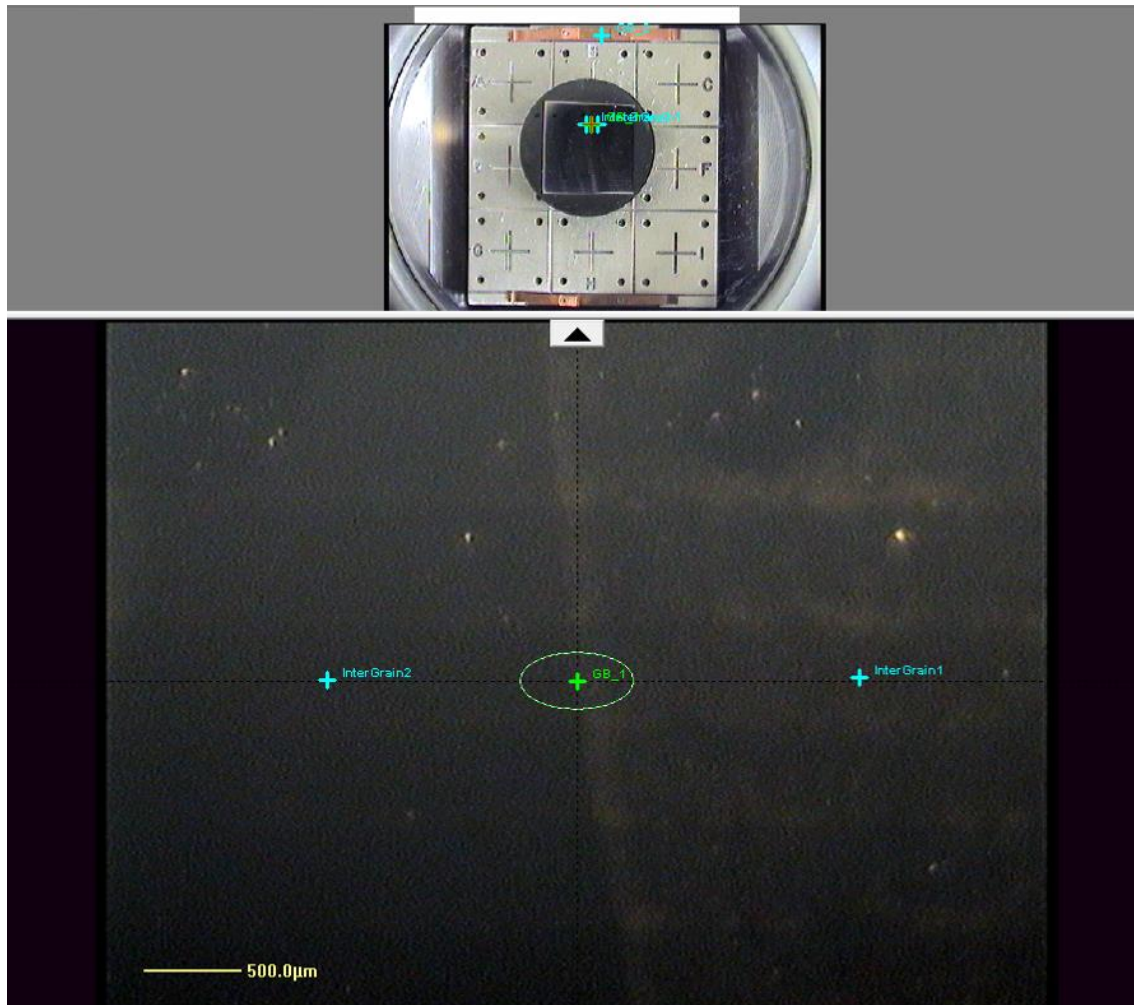


Figure 6-10 XPS testing position of intergrain and grain boundary area within a bi-crystal system (from sample CI_1)

The survey scan result of the intergrain and grain boundary area is shown in Figure 6-11. A perfect match between the two detected shows the stability of the chemical composition within this bi-crystal system. However, the content of the Oxygen is more than 30% in terms of the atomic percentage. This value is abnormal as the XPS testing only focuses on the several nanometers depth on the testing sample surface.

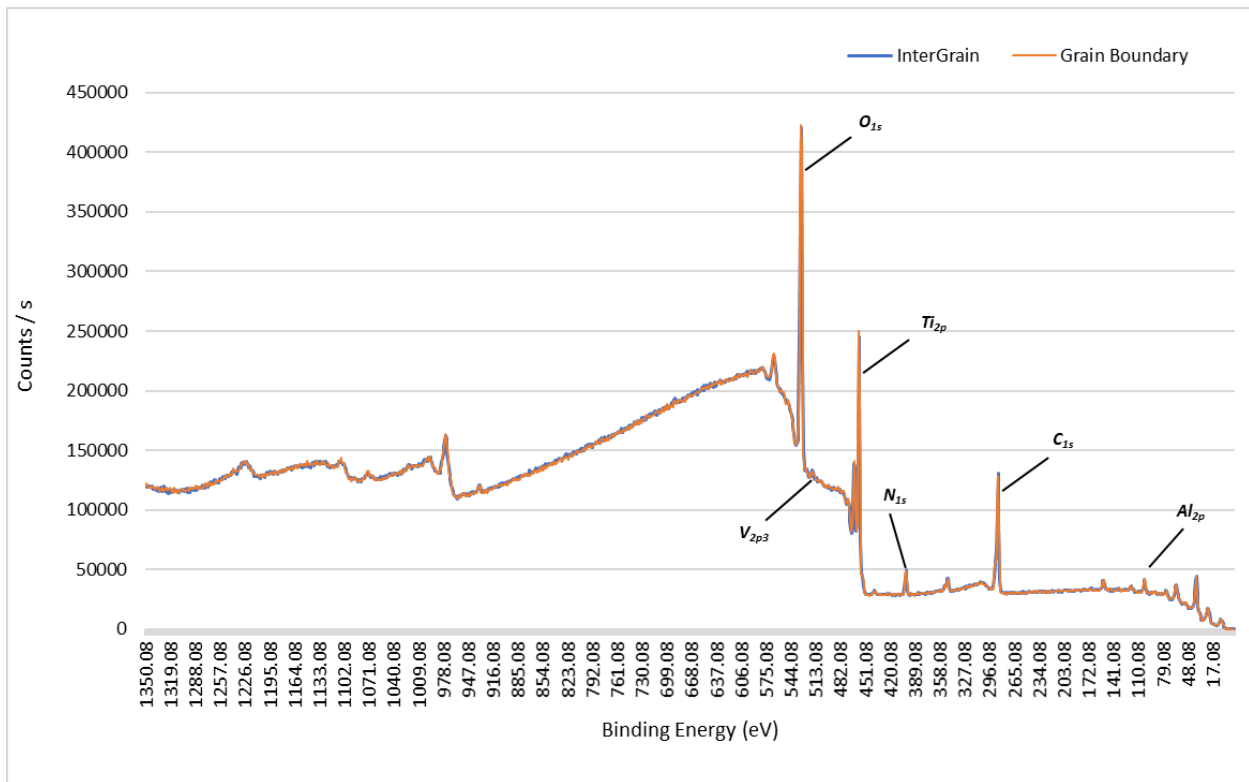


Figure 6-11 XPS survey of the intergrain and grain boundary area within a bi-crystal system

Cross-validation is carried out for a more accurate chemical composition testing of the sample. The focused ion beam (FIB) extreme high-resolution SEM was used to investigate the microstructure and the chemical component at the grain boundary area at a 3D level. As shown in Figure 6-12, the grain boundary area was milled down by the FIB by 40 μm . As the whole process

was carried out in a high vacuum environment, the analysis on the milled surface eliminates the influences of etching and gas contamination during the sample preparation process.

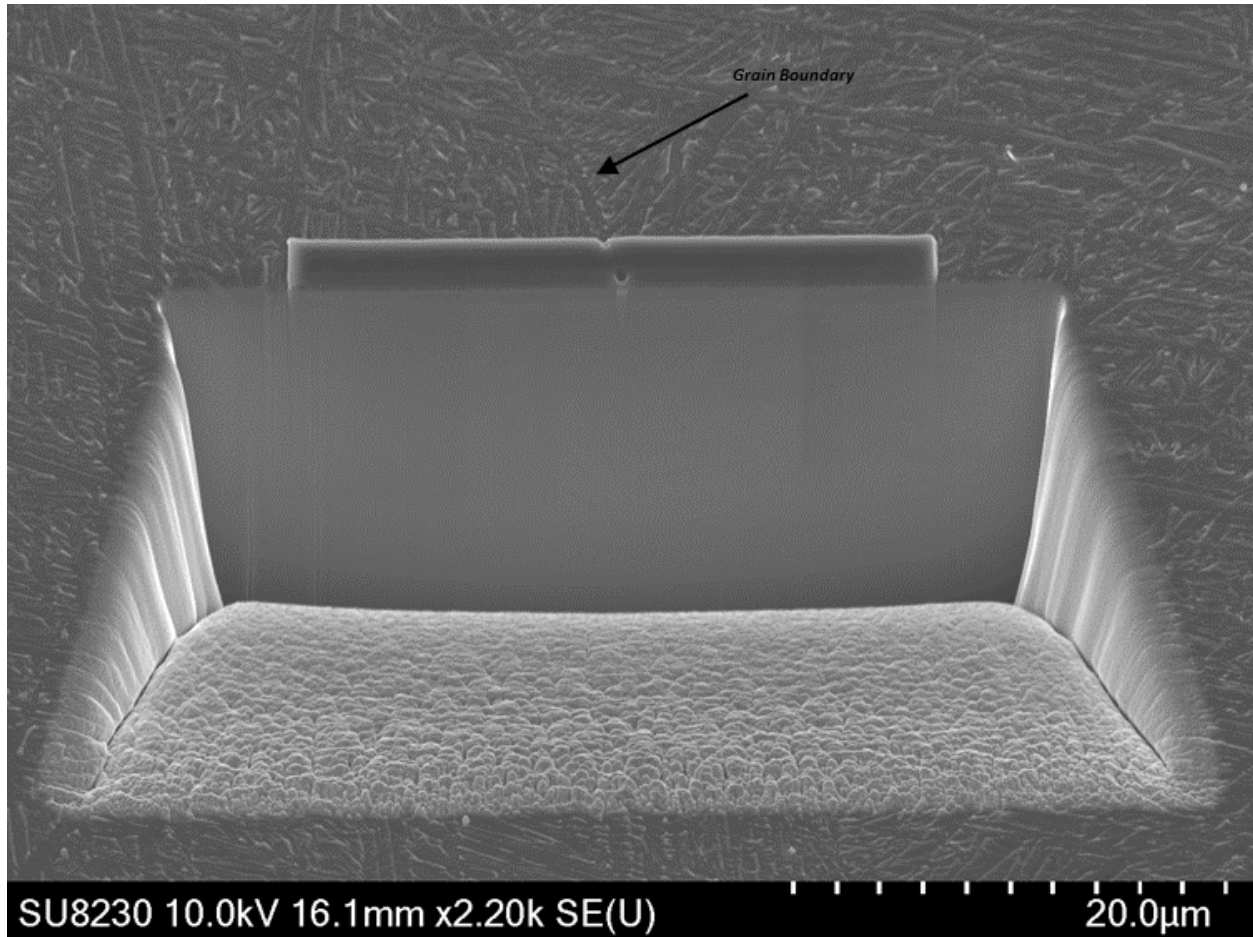


Figure 6-12 The FIB SEM of a grain boundary area.

The microstructure of the FIB milled area is shown in Figure 6-13. The grain boundary can be recognized penetrating along the Y direction in the sample.

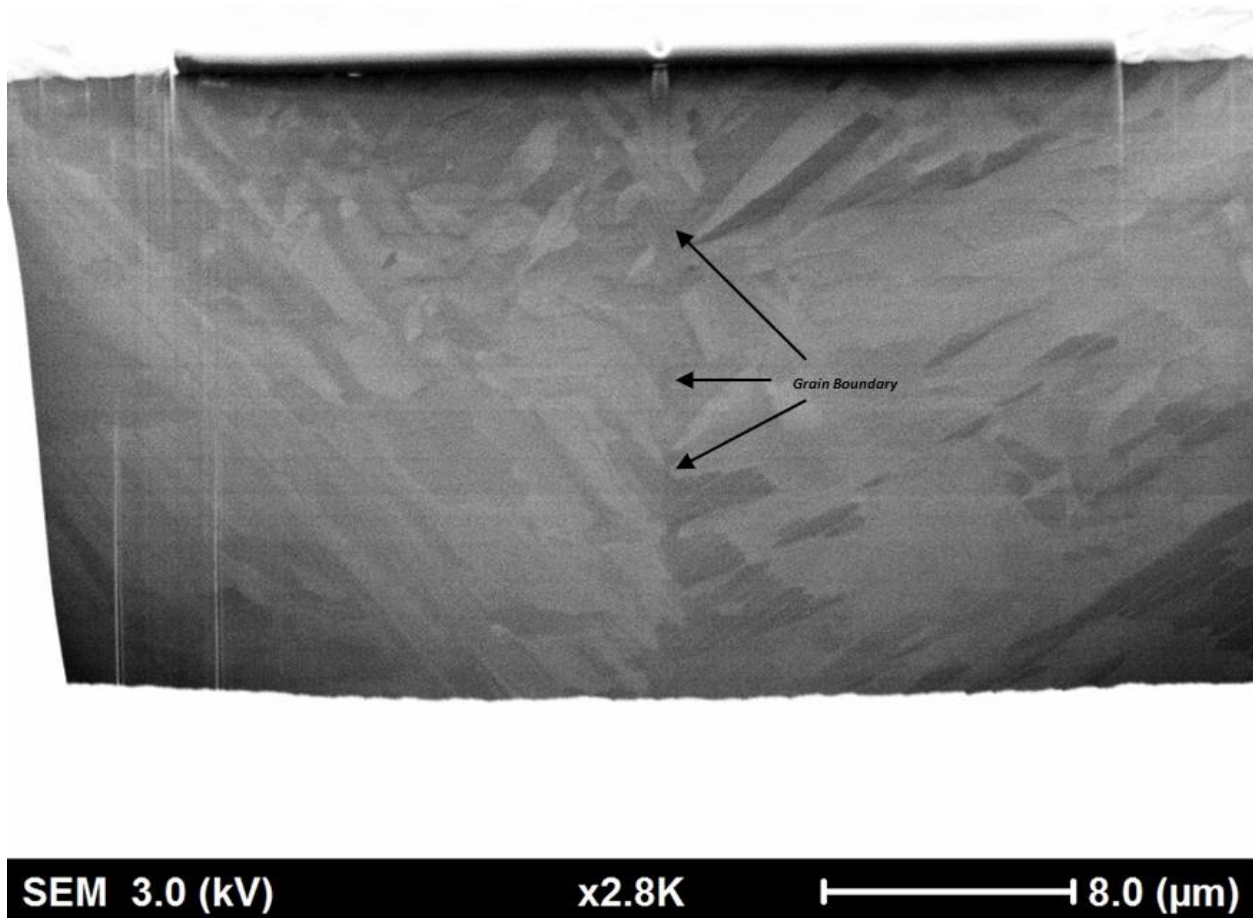


Figure 6-13 The grain boundary morphology in the XY plane in the fabricated part

The energy dispersive X-ray spectroscopy (EDX) testing result at the grain boundary area is shown in Figure 6-14. The element mapping result shows that the Al element (alpha stabilized element) tends to concentrate within the grain area of the alpha or prime alpha grains, while the V element distributes at the intergrain areas. The inhomogeneous distribution of the Al and V element is also found at the grain boundary of the prior beta grains. This indicates the existence or the emerging of the columnar grain boundary alpha phase.

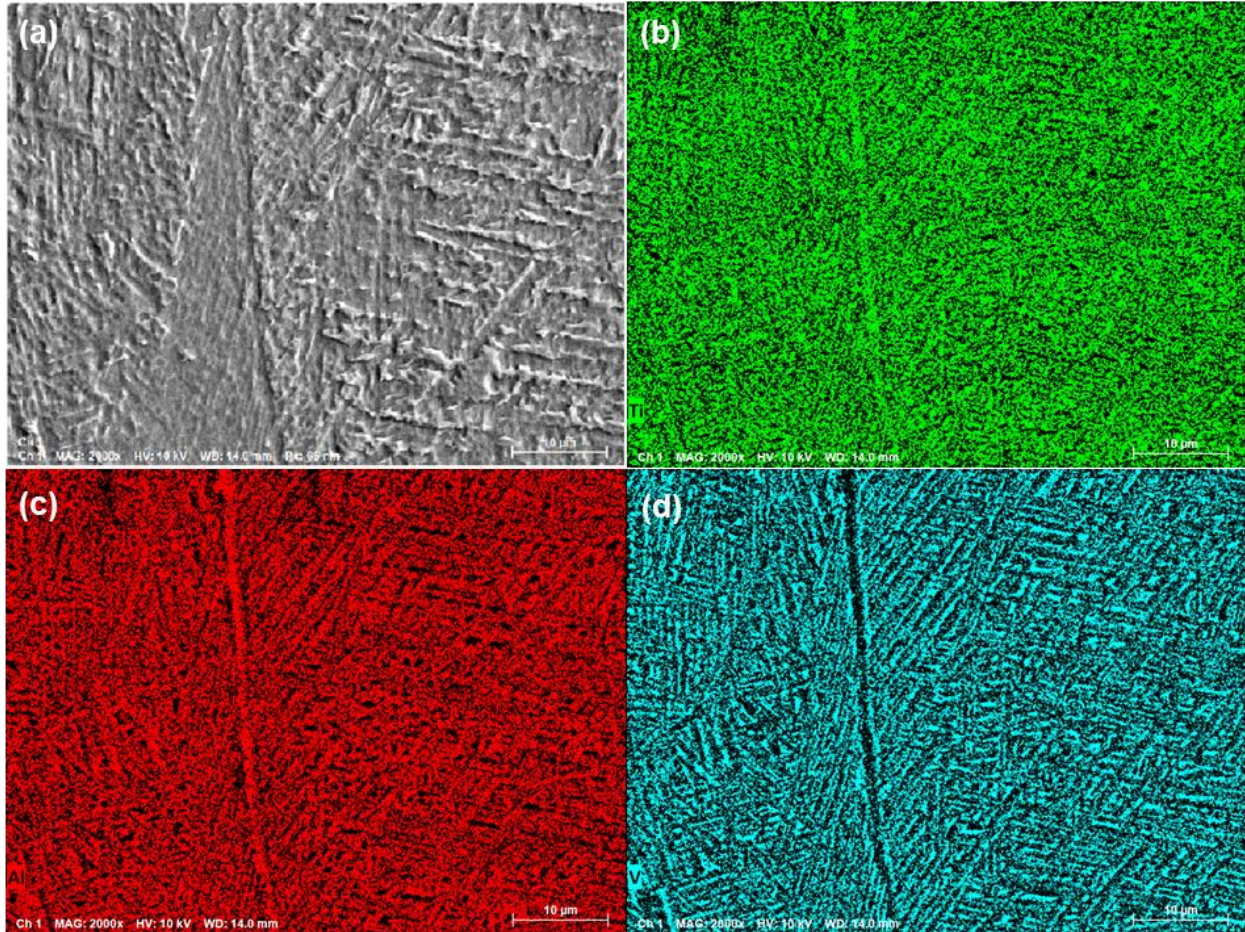


Figure 6-14 EDX result of the grain boundary area: (a) SEM image (b) Ti element map (c) Al element map (d) V element map

6.4.2. Early stage of crystallization at the grain boundary, 3D tomography analysis and chemical composition (segmentation)

To investigate the recrystallization process from its early stage, a recrystallized small size crystal (20 µm) was found at the grain boundary area of the prior beta grains. This crystal emerges during the material deposition process of laser wire DED and failed to develop into a bigger size (as shown in Figure 6-15). It did not participate in the competitive grain growth; however, it is a good example to reveal the crystal introducing mechanism.

Understandably, the recrystallized crystals have a preference at the grain boundary areas. In terms of crystallography, the grain boundary can be considered as a 2D phase concentrated with the stacking faults which also has higher free energy compared to its neighbouring area. As the recrystallization is a thermal controlled process, the initial grain boundary energy decreases the threshold value needed to generate a new crystal between the original bi-crystal system.

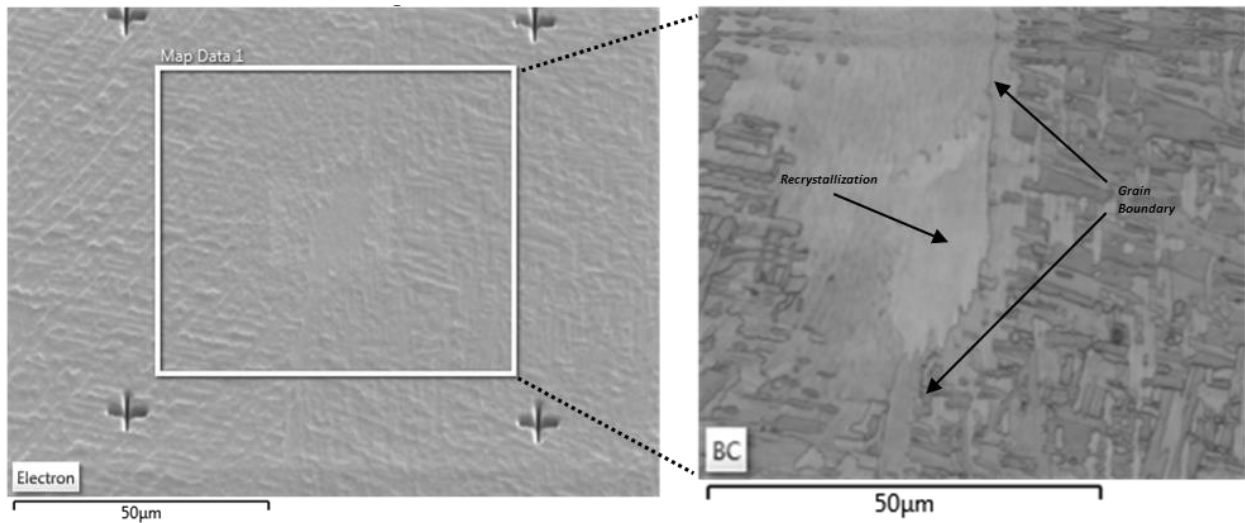


Figure 6-15 Forescatter diodes (FSD) mixed and band contract image of the recrystallized grain at the grain boundary

The EDX testing was used for the chemical component testing for the recrystallization area. As shown in Figure 6-16, the segregation of Al and V was found around the crystal. This solid solute segregation indicates the generation of this crystal starts from the prior alpha phase at the grain boundary and pushes the alpha stabilized element (Al) aside during the recrystallization process.

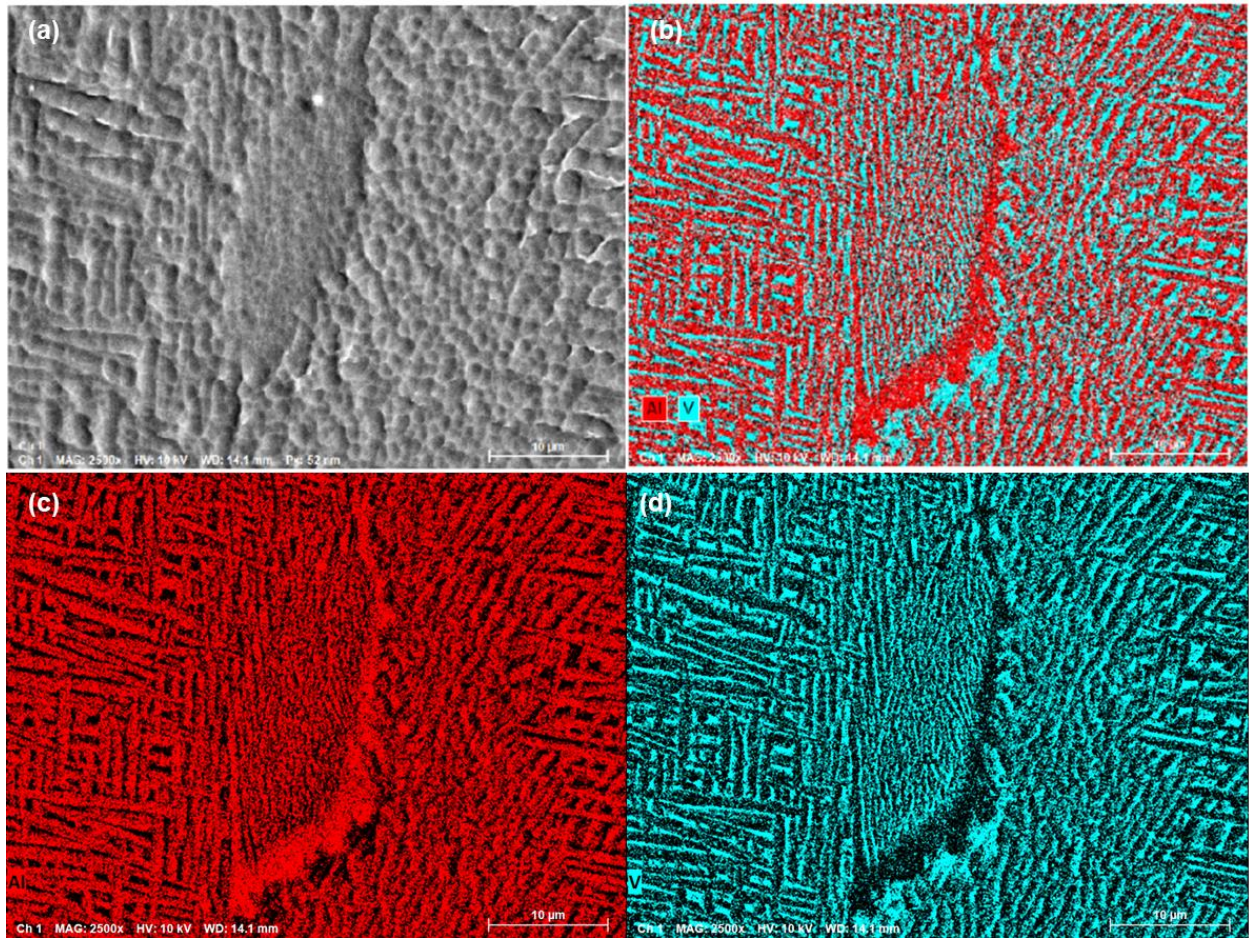


Figure 6-16 EDX mapping of the (a) small crystal area (b) combined Al and V mapping (c) Al mapping (d) V mapping

The EBSD was also used to detect the crystal orientations of the recrystallized grain and its neighbouring area. As shown in the Figure 6-17, the polar figure of the small crystal and its neighbouring area shows a strong dependency in terms of the crystal orientation. This further approves the grain boundary alpha being the mother phase of the recrystallized small grain detected.

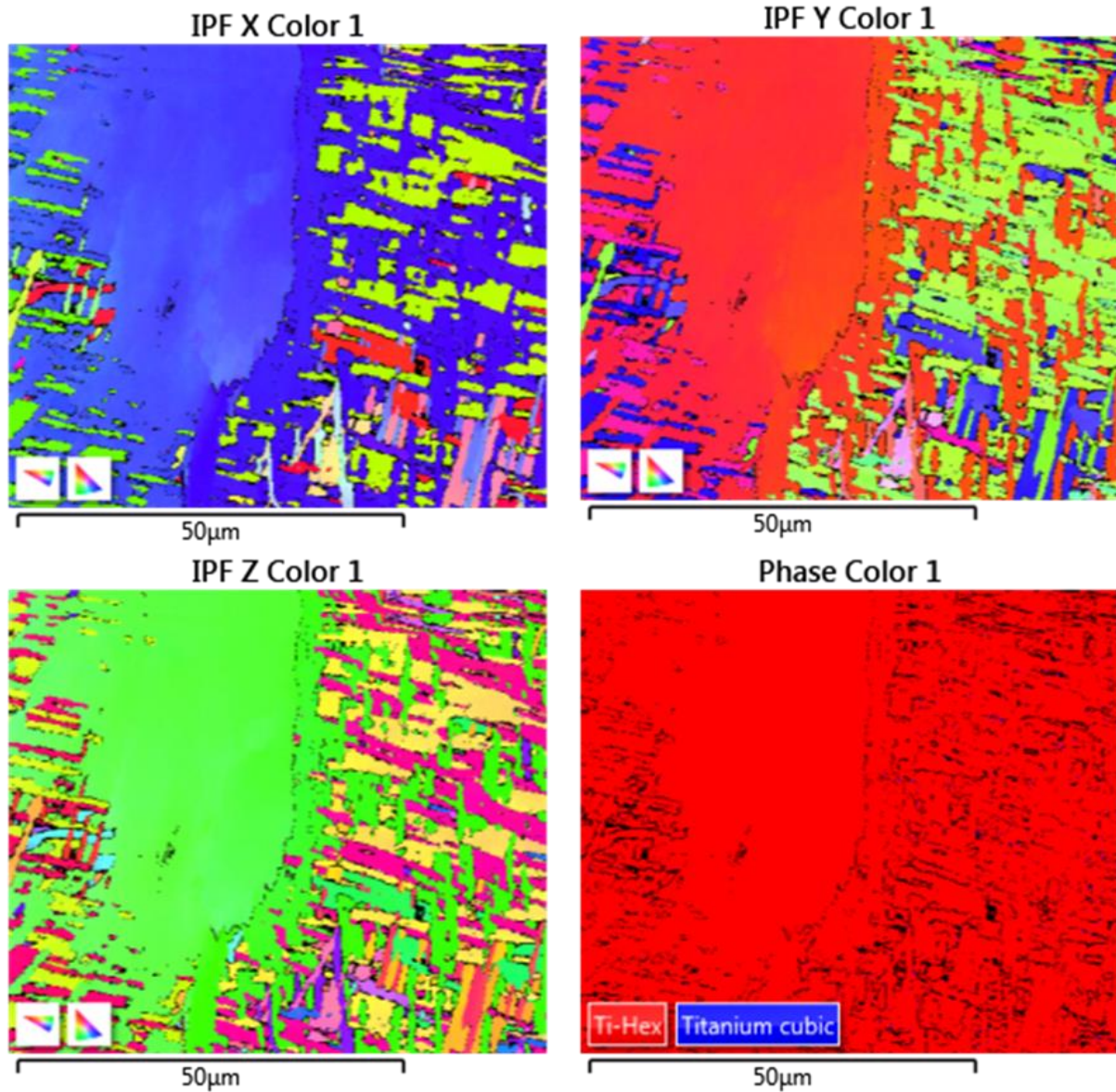


Figure 6-17 EBSD mapping of the small crystal and its neighbouring area.

The kernel average misorientation (KAM) map is used to evaluate the local grain misorientation of the newly emerged crystal area at the grain boundary (Figure 6-18). A misorientation around the small crystal is found with an average misorientation lower than 2° . Reconsider the EDX result in Figure 6-16, the alpha grain size in the small crystal area is obviously smaller than its surrounding area. It indicates the small crystal experiences a phase transformation back to the beta phase and cools to the room temperature again. On the other hand, its neighbouring columnar

grains do not experience such solid phase transformation and the alpha grain continuously grow under reheating. Combined with the KAM map, these misorientation indicates that the solid phase transformation indeed leaves an opportunity for introducing misorientations and recrystallization in laser wire DED fabricated Ti6Al4V. It is also believed that this mechanism is not limited for the DED, but all the MAM processed Ti6Al4V as the reheating and residual stress are common features in these techniques.

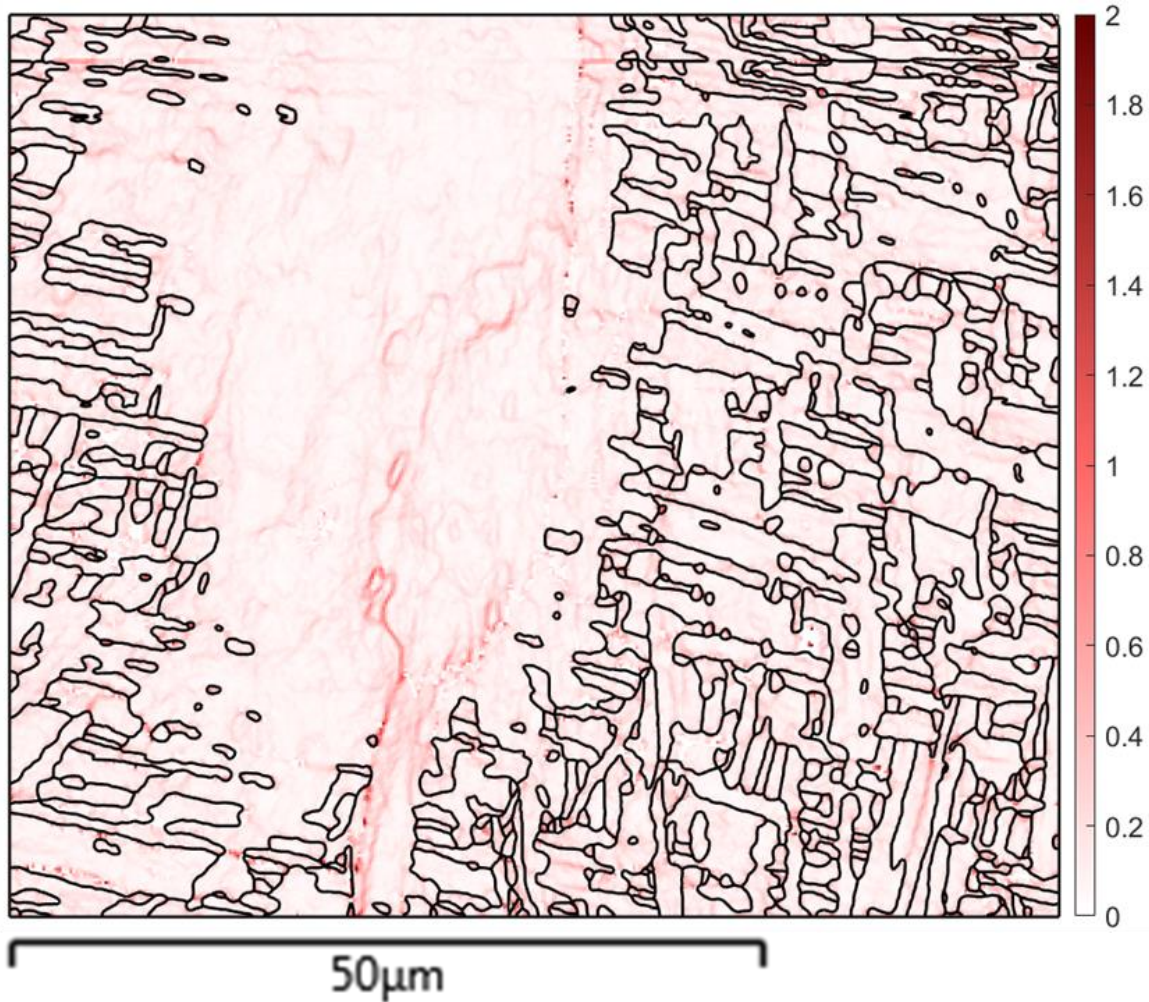


Figure 6-18 The KAM mapping of the recrystallized small crystal area showing the misorientation value of the subcrystals

6.4.3. Validation on a single beta grain substrate

To further investigate whether the prior beta grain boundary is necessary for recrystallization during the printing process, a two-step thin wall structure fabrication was carried out. In step one, the thin wall structure was fabricated under the previous condition, with a hot-roll Ti6Al4V metal sheet as substrate. After the columnar grains within this thin wall develops into a millimetre level, one columnar grain is selected to be cut from the center. As shown in Figure 6-19, the cut columnar grain is rotated 90 degrees and used as the fabrication substrate for step two. The process parameters are kept constant during the fabrication of the two steps with a laser power of 650 W, 16.9 ipm scanning speed and a feed rate of 50 ipm.

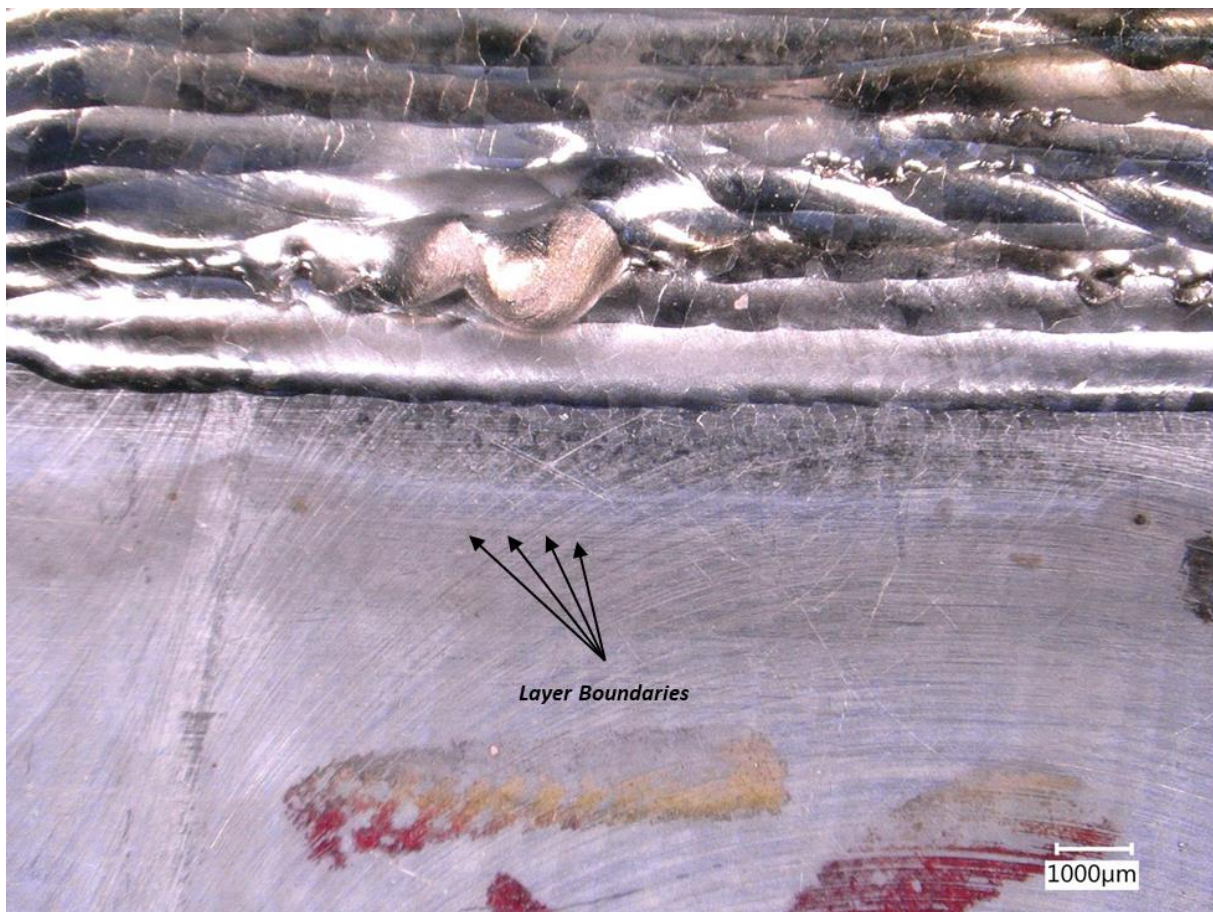


Figure 6-19 The two-step fabrication of a validation thin wall structure

By doing this two-step fabrication process, the effect of the prior beta grain boundary is removed as the substrate area belongs to a single prior beta grain. In the first layer of material deposition, the solidification microstructure presents a fully columnar structure as shown in Figure 6-20. And in the area below the fusion line which does not experience a solidification process, the microstructure presents an equiaxed grain structure instead of the provided single beta crystal. This further approves the possibility of recrystallization even without the grain boundaries, and the dislocation concentration within the layer boundaries can also promote the recrystallization during the material deposition process.

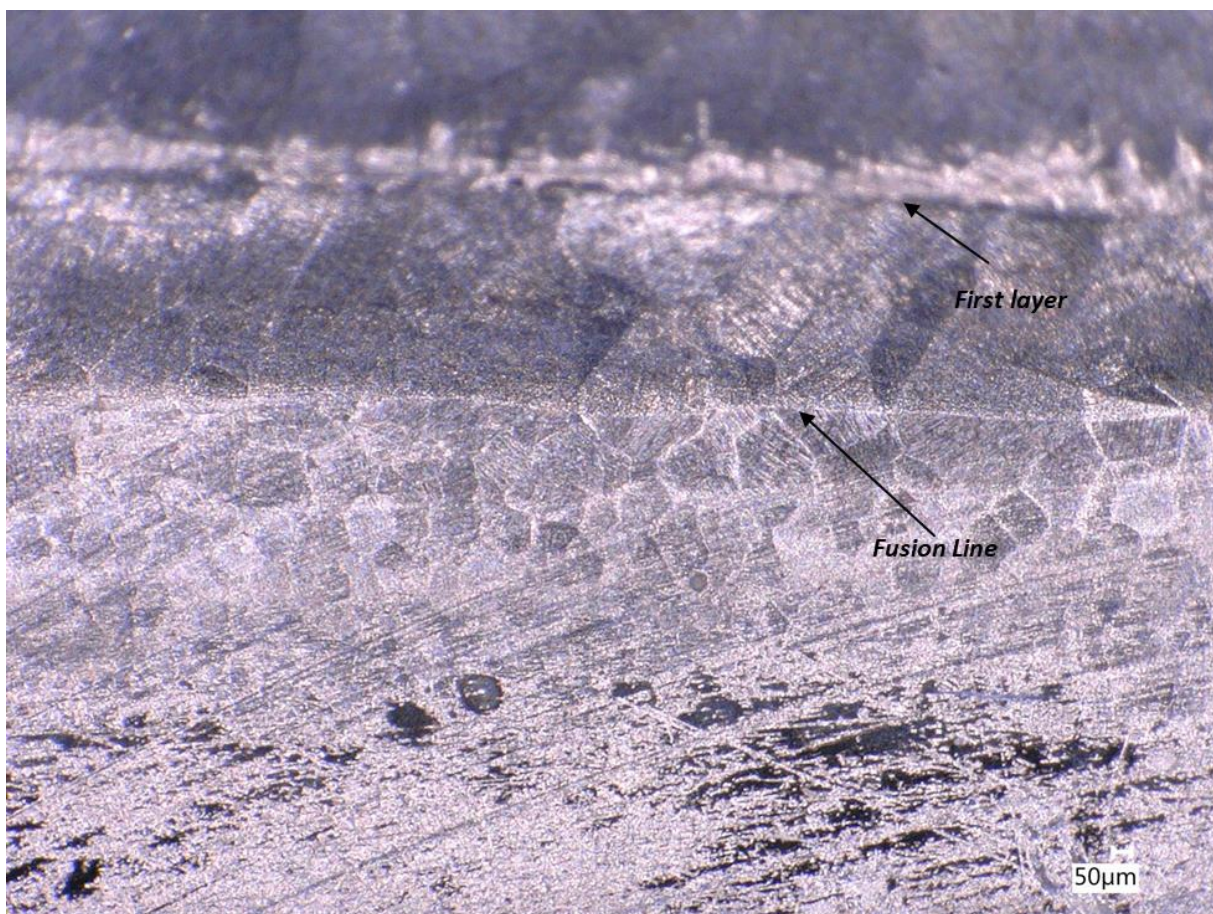


Figure 6-20 Grain structure at the first layer and the adjacent substrate

6.5. Conclusions

To investigate the crystal introducing mechanism in laser wire DED fabricated Ti6Al4V, a sample matrix under different fabrication conditions is fabricated regarding the three hypotheses. It is approved from different perspectives that recrystallization is the main reason for the crystal introducing, and it is a comprehensive result of the residual stress and reheating. A more detailed investigation was carried out on the early stage of a recrystallized grain at the grain boundary of the prior beta grain. The formation tendency of the recrystallized grain indicates its strong dependency on the grain boundary alpha phase. This study also approved that this type of recrystallization does not necessarily take place at the prior beta grain boundary area, even without grain boundaries, a single beta crystal can still be recrystallized into smaller grains under the fabrication condition of laser wire DED. Some of these recrystallized grains are able to participate in the following competitive grain growth, thus influencing the solidification microstructure in the fabricated part dramatically.

Chapter 7. Conclusions and future research

7.1. Conclusions

AM is changing the landscapes of current industrial practices and the simulation methods become more and more important to understand the mechanism and eliminate the uncertainties during AM fabrication process. The solidification microstructure simulation remains challenging because of the complex solidification conditions, especially in MAM. To address the difficulties in the solidification microstructure simulation of laser wire DED fabricated Ti6Al4V process, this thesis established a ML model to study the competitive grain growth behaviour of the columnar grains. Based on the database established, a deterministic model (named “invasion model”) was created to simulate the solidification microstructure. For the first time, the solidification microstructure was compared quantitatively with the experimental result in a practical scale of laser wire DED fabricated Ti6Al4V. As the crystal introducing mechanism in MAM process has been a long-term unsolved problem that limits the simulation accuracy, further research of this thesis was carried out to investigate the crystal introducing mechanism experimentally. The recrystallization that starts from the grain boundary is believed to be the main reason which introduces crystals during the deposition process. The efforts and conclusions made in each section of this thesis are elaborate as follow.

With a thorough review of the literature, the development of existing solidification microstructure simulation methods as well as their capacity and applicability on MAM are analyzed in Chapter 2. Traditional solidification microstructure simulation methods including CA, PF and KMC all have their merits as well as drawbacks when applied in MAM cases. Under the trade-off between the simulation accuracy and efficiency, how to develop a robust and practical simulation model on a long scale to describe the grain growth behaviour in a moving melt pool is still an open question

for the traditional models. The further discussion focuses on the sequential dependency of each physical process during the solidification of MAM which hinders the traditional methods from being deterministic on a practical scale. To achieve an accurate deterministic simulation, database establishment between the recognized phenomena is an ideal method to fill these gaps.

Following this conclusion, a database recording the competitive grain growth of laser wire fabrication of Ti6Al4V is established in Chapter 4. With the training sample extracted from the experiment (50 samples for Y-Z and X-Z each), the regression relation between the solidification condition, crystal orientation and the resultant grain boundary angle is achieved with the help of ANN. It is demonstrated that ANN is an efficient tool to investigate the competitive grain growth behaviour in laser wire DED fabricated Ti6Al4V. The ANN model developed in this work can be employed within a tolerance range of about $\pm 4^\circ$. An average prediction error of 2.43° shows that a feed-forward neural network is an appropriate tool for the task described in this thesis. This ANN can be used as an engine to support the microstructure simulation of laser wire DED fabricated Ti6Al4V.

Additionally, a deterministic solidification microstructure simulation model, named “invasion model”, is established in Chapter 5 to avoid the essential defects of traditional methods. This model focuses on the interaction between the neighbouring bi-crystals instead of simulating the growth kinetics of each columnar grain or deriving the field form of variables. Within a bi-crystal system, the grain boundary tilting from the vertical direction of solidification front is understood as a transient invasion behaviour of one grain to another, and the competitive grain growth behaviour along the buildup process of MAM is a summary of all the invasions in bi-crystal systems. For the validation of this novel solidification microstructure simulation model, laser wire DED fabricated Ti6Al4V thin wall samples with full dendritic columnar grains (prior beta) are selected as a

benchmark. The grain structure of reconstructed prior beta grains along the build-up direction has a good agreement with the simulation result which shows the unique capabilities of the invasion model compared to the traditional ones. As many probabilistic models of solidification microstructure simulation have difficulties when dealing with MAM processes, this deterministic model provides a quantitative prediction of solidification microstructure. To the best of the author's knowledge, the grain boundary angles of MAM fabricated Ti6Al4V has never been quantitatively studied before this work. Also, the invasion model provides a methodology to investigate the solidification microstructure for most of the alloy systems under a rapid solidification condition which is now still a difficulty to solve for existing methods. The strategy is robust which can be combined with various existing mechanistic models. By combining with real-time monitoring data, this model can be a good tool for process optimization in MAM and push the microstructural control into the next level of accuracy.

In the end, the crystal (prior beta grain) introducing mechanism in laser wire DED fabricated Ti6Al4V during the deposition process is investigated in Chapter 6. To investigate the crystal introducing mechanism in laser wire DED fabricated Ti6Al4V, a sample matrix under different fabrication conditions is fabricated regarding the three hypothesizes (heat and stress accumulation and the solid phase transformation). It is approved from different perspectives that recrystallization is the main reason for the crystal introducing which is a comprehensive result of the residual stress and reheating. A more detailed investigation was carried out on the early stage of a recrystallized grain at the grain boundary of the prior beta grain boundary. The formation tendency of the recrystallized grain indicates its strong dependency on the grain boundary alpha phase. And the solid-phase transformation plays an important role for generating the new crystals. The study also proved that the recrystallization does not necessarily take place at the prior beta grain boundary

area. Even without grain boundaries, a single beta crystal can still be recrystallized into smaller grains under the fabrication condition of laser wire DED. Some of these recrystallized grains are able to participate in the following competitive grain growth, thus influencing the solidification microstructure in the fabricated part dramatically.

In conclusion, this work sheds light on the current understanding of the solidification microstructure evolution in laser wire DED fabricated Ti6Al4V. A ML supported database is established for the competitive grain growth behaviour of laser wire fabricated Ti6Al4V, this methodology can be easily applied to other alloy systems. Besides, a novel solidification microstructure simulation method, the invasion model, is introduced to the community. The crystal introducing mechanism disclosed in this work also provides insights on how to set the nucleation rules in the simulation models or process control to achieve the desired microstructure and properties in real practise.

7.2. Future Research

Based on the knowledge of this research, further investigation includes the microstructure control from printing protocol manipulation according to the simulation result. Considering the limitations of the current research, it should also be extended to the following topics:

The CET mechanism study for the microstructural optimization and preprocess design in laser wire DED Ti6Al4V.

Apply the simulation scheme to other MAM techniques and alloy systems.

Establish a property prediction model based on microstructure, printing defects. With respect to microstructure, the treatment of the grain boundaries and interface between different phases is a critical problem to be considered for an accurate prediction.

As the solidification of alloys is fundamental research, the study of solidification microstructure has great significance for industrial production. Inspired by the methodology in this thesis, the competitive grain growth behaviour of different alloy systems under extreme solidification conditions should be established, furthermore, this topic should be generalized into the subject of material informatics.

References

- [1] M. Taufik, P.K. Jain, Role of build orientation in layered manufacturing: a review, *International Journal of Manufacturing Technology and Management* 27(1-3) (2013) 47-73.
- [2] M. Kumke, H. Watschke, P. Hartogh, A.K. Bavendiek, T. Vietor, Methods and tools for identifying and leveraging additive manufacturing design potentials, *International Journal on Interactive Design and Manufacturing (IJIDeM)* 12(2) (2018) 481-493.
- [3] L.J. Kumar, C.K. Nair, Current trends of additive manufacturing in the aerospace industry, *Advances in 3D printing & additive manufacturing technologies*, Springer2017, pp. 39-54.
- [4] R.B.S.C. GmbH, *ADDITIVE MANUFACTURING: A game changer for the manufacturing industry?*, 2013.
- [5] J.M. Wilson, C. Piya, Y.C. Shin, F. Zhao, K. Ramani, Remanufacturing of turbine blades by laser direct deposition with its energy and environmental impact analysis, *Journal of Cleaner Production* 80 (2014) 170-178.
- [6] B. Dutta, F.H.S. Froes, The additive manufacturing (AM) of titanium alloys, *Titanium powder metallurgy*, Elsevier2015, pp. 447-468.
- [7] B. Dutta, F.H. Froes, The additive manufacturing (AM) of titanium alloys, *Titanium Powder Metallurgy*2015, pp. 447-468.
- [8] B.-L. Chua, D.-G. Ahn, Estimation Method of Interpass Time for the Control of Temperature during a Directed Energy Deposition Process of a Ti-6Al-4V Planar Layer, *Materials* 13(21) (2020) 4935.
- [9] D. Greitemeier, C. Dalle Donne, A. Schoberth, M. Jürgens, J. Eufinger, T. Melz, Uncertainty of Additive Manufactured Ti-6Al-4V: Chemistry, Microstructure and Mechanical Properties, *Applied Mechanics and Materials* 807 (2015) 169-180.
- [10] M. Markl, C. Körner, Multiscale Modeling of Powder Bed-Based Additive Manufacturing, *Annual Review of Materials Research* 46(1) (2016) 93-123.
- [11] J.A. Dantzig, M. Rappaz, *Solidification: -Revised & Expanded*, EPFL press2016.
- [12] W. Oldfield, *A quantitative approach to casting solidification: freezing of cast iron*, (1966).
- [13] J.A. Dantzig, M. Rappaz, *Solidification*, EPFL press2009.
- [14] M. Rappaz, C.-A. Gandin, Probabilistic modelling of microstructure formation in solidification processes, *Acta metallurgica et materialia* 41(2) (1993) 345-360.
- [15] P. Thevoz, J. Desbiolles, M. Rappaz, Modeling of equiaxed microstructure formation in casting, *Metallurgical Transactions A* 20(2) (1989) 311-322.
- [16] W. Kurz, D.J. Fisher, *Fundamentals of solidification*, trans tech publications Aedermannsdorf, Switzerland1986.
- [17] P. Kobryn, S. Semiatin, The laser additive manufacture of Ti-6Al-4V, *JOM* 53(9) (2001) 40-42.
- [18] S. Kou, *Welding metallurgy*, 2003.
- [19] A. Clare, R. Mishra, M. Merklein, H. Tan, I. Todd, L. Chechik, J. Li, M. Bambach, Alloy design and adaptation for additive manufacture, *Journal of Materials Processing Technology* (2021) 117358.
- [20] A. Greer, A. Bunn, A. Tronche, P. Evans, D. Bristow, Modelling of inoculation of metallic melts: application to grain refinement of aluminium by Al-Ti-B, *Acta Mater.* 48(11) (2000) 2823-2835.

- [21] D. StJohn, M. Qian, M. Easton, P. Cao, The Interdependence Theory: The relationship between grain formation and nucleant selection, *Acta Materialia* 59(12) (2011) 4907-4921.
- [22] D. Zhang, D. Qiu, M.A. Gibson, Y. Zheng, H.L. Fraser, D.H. StJohn, M.A. Easton, Additive manufacturing of ultrafine-grained high-strength titanium alloys, *Nature* 576(7785) (2019) 91-95.
- [23] W.J. Sames, F.A. List, S. Pannala, R.R. Dehoff, S.S. Babu, The metallurgy and processing science of metal additive manufacturing, *International Materials Reviews* 61(5) (2016) 315-360.
- [24] N. Raghavan, R. Dehoff, S. Pannala, S. Simunovic, M. Kirka, J. Turner, N. Carlson, S.S. Babu, Numerical modeling of heat-transfer and the influence of process parameters on tailoring the grain morphology of IN718 in electron beam additive manufacturing, *Acta Materialia* 112 (2016) 303-314.
- [25] J.J. Lin, Y.H. Lv, Y.X. Liu, B.S. Xu, Z. Sun, Z.G. Li, Y.X. Wu, Microstructural evolution and mechanical properties of Ti-6Al-4V wall deposited by pulsed plasma arc additive manufacturing, *Materials & Design* 102 (2016) 30-40.
- [26] D. Herzog, V. Seyda, E. Wycisk, C. Emmelmann, Additive manufacturing of metals, *Acta Mater.* 117 (2016) 371-392.
- [27] W.E. Frazier, Metal Additive Manufacturing: A Review, *Journal of Materials Engineering and Performance* 23(6) (2014) 1917-1928.
- [28] F. Wang, S. Williams, P. Colegrove, A.A. Antonysamy, Microstructure and Mechanical Properties of Wire and Arc Additive Manufactured Ti-6Al-4V, *Metallurgical and Materials Transactions A* 44(2) (2012) 968-977.
- [29] F. Wang, S. Williams, M. Rush, Morphology investigation on direct current pulsed gas tungsten arc welded additive layer manufactured Ti6Al4V alloy, *The International Journal of Advanced Manufacturing Technology* 57(5-8) (2011) 597-603.
- [30] L. Thijs, F. Verhaeghe, T. Craeghs, J. Van Humbeeck, J.P. Kruth, A study of the microstructural evolution during selective laser melting of Ti-6Al-4V, *Acta Materialia* 58(9) (2010) 3303-3312.
- [31] S. Bontha, N.W. Klingbeil, P.A. Kobryn, H.L. Fraser, Thermal process maps for predicting solidification microstructure in laser fabrication of thin-wall structures, *Journal of Materials Processing Technology* 178(1-3) (2006) 135-142.
- [32] M. Gäumann, S. Henry, F. Cleton, J.-D. Wagniere, W. Kurz, Epitaxial laser metal forming: analysis of microstructure formation, *Materials Science and Engineering: A* 271(1-2) (1999) 232-241.
- [33] T. Wang, Y.Y. Zhu, S.Q. Zhang, H.B. Tang, H.M. Wang, Grain morphology evolution behavior of titanium alloy components during laser melting deposition additive manufacturing, *Journal of Alloys and Compounds* 632 (2015) 505-513.
- [34] A. Basak, S. Das, Epitaxy and Microstructure Evolution in Metal Additive Manufacturing, *Annual Review of Materials Research* 46(1) (2016) 125-149.
- [35] F. Wang, J. Mei, X. Wu, Microstructure study of direct laser fabricated Ti alloys using powder and wire, *Applied Surface Science* 253(3) (2006) 1424-1430.
- [36] B. Vrancken, L. Thijs, J.-P. Kruth, J. Van Humbeeck, Heat treatment of Ti6Al4V produced by Selective Laser Melting: Microstructure and mechanical properties, *Journal of Alloys and Compounds* 541 (2012) 177-185.
- [37] H. Xiao, P. Xie, M. Cheng, L. Song, Enhancing mechanical properties of quasi-continuous-wave laser additive manufactured Inconel 718 through controlling the niobium-rich precipitates, *Additive Manufacturing* 34 (2020) 101278.

- [38] M. Komarasamy, S. Shukla, S. Williams, K. Kandasamy, S. Kelly, R.S. Mishra, Microstructure, fatigue, and impact toughness properties of additively manufactured nickel alloy 718, *Additive Manufacturing* 28 (2019) 661-675.
- [39] L. Zhao, Y. Tan, S. Shi, X. You, P. Li, C. Cui, Microsegregation behavior of Inconel 718 superalloy prepared by electron beam smelting layered solidification technology, *Journal of Alloys and Compounds* 833 (2020) 155019.
- [40] K. Bertsch, G.M. de Bellefon, B. Kuehl, D. Thoma, Origin of dislocation structures in an additively manufactured austenitic stainless steel 316L, *Acta Materialia* 199 (2020) 19-33.
- [41] E. Liverani, S. Toschi, L. Ceschini, A. Fortunato, Effect of selective laser melting (SLM) process parameters on microstructure and mechanical properties of 316L austenitic stainless steel, *Journal of Materials Processing Technology* 249 (2017) 255-263.
- [42] Y. Zhong, L.-E. Rännar, L. Liu, A. Koptuyug, S. Wikman, J. Olsen, D. Cui, Z. Shen, Additive manufacturing of 316L stainless steel by electron beam melting for nuclear fusion applications, *Journal of nuclear materials* 486 (2017) 234-245.
- [43] J. Liu, A.C. To, Quantitative texture prediction of epitaxial columnar grains in additive manufacturing using selective laser melting, *Additive Manufacturing* 16 (2017) 58-64.
- [44] Y. Kok, X.P. Tan, P. Wang, M.L.S. Nai, N.H. Loh, E. Liu, S.B. Tor, Anisotropy and heterogeneity of microstructure and mechanical properties in metal additive manufacturing: A critical review, *Materials & Design* 139 (2018) 565-586.
- [45] J.J. Lewandowski, M. Seifi, Metal Additive Manufacturing: A Review of Mechanical Properties, *Annual Review of Materials Research* 46(1) (2016) 151-186.
- [46] P. Kontis, E. Chauvet, Z. Peng, J. He, A.K.d. Silva, D. Raabe, C. Tassin, J.-J. Blandin, S. Abed, R. Dendievel, Atomic-scale grain boundary engineering to overcome hot-cracking in additively-manufactured superalloys, Available at SSRN 3391502 (2019).
- [47] B.E. Carroll, T.A. Palmer, A.M. Beese, Anisotropic tensile behavior of Ti-6Al-4V components fabricated with directed energy deposition additive manufacturing, *Acta Materialia* 87 (2015) 309-320.
- [48] S. Kumar, W.A. Curtin, Crack interaction with microstructure, *Materials today* 10(9) (2007) 34-44.
- [49] P. Kontis, E. Chauvet, Z. Peng, J. He, A.K. da Silva, D. Raabe, C. Tassin, J.-J. Blandin, S. Abed, R. Dendievel, Atomic-scale grain boundary engineering to overcome hot-cracking in additively-manufactured superalloys, *Acta Materialia* 177 (2019) 209-221.
- [50] S.S. Al-Bermani, M.L. Blackmore, W. Zhang, I. Todd, The Origin of Microstructural Diversity, Texture, and Mechanical Properties in Electron Beam Melted Ti-6Al-4V, *Metallurgical and Materials Transactions A* 41(13) (2010) 3422-3434.
- [51] G.C. Obasi, S. Biroasca, J. Quinta da Fonseca, M. Preuss, Effect of β grain growth on variant selection and texture memory effect during $\alpha \rightarrow \beta \rightarrow \alpha$ phase transformation in Ti-6 Al-4 V, *Acta Materialia* 60(3) (2012) 1048-1058.
- [52] J. Wang, X. Lin, J. Wang, H. Yang, Y. Zhou, C. Wang, Q. Li, W. Huang, Grain morphology evolution and texture characterization of wire and arc additive manufactured Ti-6Al-4V, *Journal of Alloys and Compounds* 768 (2018) 97-113.
- [53] P. Liu, Z. Wang, Y. Xiao, M.F. Horstemeyer, X. Cui, L. Chen, Insight into the mechanisms of columnar to equiaxed grain transition during metallic additive manufacturing, *Additive Manufacturing* 26 (2019) 22-29.

- [54] X. Nong, X. Zhou, Y. Wang, L. Yu, J. Li, Effects of geometry, location, and direction on microstructure and mechanical properties of 15–5PH stainless steel fabricated by directed energy deposition, *Materials Science and Engineering: A* (2021) 141587.
- [55] T. Ahmed, H. Rack, Phase transformations during cooling in $\alpha + \beta$ titanium alloys, *Materials Science and Engineering: A* 243(1) (1998) 206-211.
- [56] S.M.K.a.S.L. KAMPE, Microstructural Evolution in Laser-Deposited Multilayer Ti-6Al-4V Builds, *Metallurgical and Materials Transactions A* 35(6) (2004) 1861-1867.
- [57] G. Lütjering, J.C. Williams, *Titanium*, 2nd ed ed., Springer Science & Business Media 2007.
- [58] F.H. Froes, Powder metallurgy of titanium alloys, *Advances in Powder Metallurgy* 2013, pp. 202-240.
- [59] D. Eylon, S. Seagle, dans "Titanium'99: Science and Technology", CRISM" Prometey", p37, St, Petersburg, Russia (2000).
- [60] M.A. Imam, F. Froes, K.L. Housley, *Titanium and titanium alloys*, Kirk-Othmer Encyclopedia of Chemical Technology (2000).
- [61] F. Froes, *Titanium: physical metallurgy, processing, and applications*, ASM International 2015.
- [62] <http://www.economist.com/node/374784>, Dr Chen and the philosopher's stone, 2000.
- [63] C. Qiu, G. Ravi, M.M. Attallah, Microstructural control during direct laser deposition of a β -titanium alloy, *Materials & Design* 81 (2015) 21-30.
- [64] A. Zafari, E.W. Lui, K. Xia, Deformation-free geometric recrystallisation in a metastable β -Ti alloy produced by selective laser melting, *Materials Research Letters* 8(3) (2020) 117-122.
- [65] Z. Liu, B. He, T. Lyu, Y. Zou, A Review on Additive manufacturing of titanium alloys for aerospace applications: directed energy deposition and beyond Ti-6Al-4V, *JOM* (2021) 1-15.
- [66] Y. Chen, S.J. Clark, L. Sinclair, C.L.A. Leung, S. Marussi, T. Connolley, R.C. Atwood, G.J. Baxter, M.A. Jones, I. Todd, Synchrotron X-ray imaging of directed energy deposition additive manufacturing of titanium alloy Ti-6242, *Additive Manufacturing* 41 (2021) 101969.
- [67] H. Fan, S. Yang, Effects of direct aging on near-alpha Ti-6Al-2Sn-4Zr-2Mo (Ti-6242) titanium alloy fabricated by selective laser melting (SLM), *Materials Science and Engineering: A* 788 (2020) 139533.
- [68] Y. Zhuo, C. Yang, C. Fan, S. Lin, Effects of trace Sn and Cr addition on microstructure and mechanical properties of TC17 titanium alloy repaired by wire arc additive manufacturing, *Journal of Alloys and Compounds* (2021) 161473.
- [69] S. Liu, Y.C. Shin, Additive manufacturing of Ti6Al4V alloy: A review, *Materials & Design* 164 (2019) 107552.
- [70] K.A. Lee, Y.K. Kim, J.H. Yu, S.H. Park, M.C. Kim, Effect of Heat Treatment on Microstructure and Impact Toughness of Ti-6Al-4V Manufactured by Selective Laser Melting Process, *Archives of Metallurgy and Materials* 62(2) (2017) 1341-1346.
- [71] B. Cai, J. Wang, A. Kao, K. Pericleous, A.B. Phillion, R.C. Atwood, P.D. Lee, 4D synchrotron X-ray tomographic quantification of the transition from cellular to dendrite growth during directional solidification, *Acta Materialia* 117 (2016) 160-169.
- [72] A.A. Antonysamy, P.B. Prangnell, J. Meyer, Effect of Wall Thickness Transitions on Texture and Grain Structure in Additive Layer Manufacture (ALM) of Ti-6Al-4V, *Materials Science Forum* 706-709 (2012) 205-210.
- [73] L. Thijs, M.L. Montero Sistiaga, R. Wauthle, Q. Xie, J.-P. Kruth, J. Van Humbeeck, Strong morphological and crystallographic texture and resulting yield strength anisotropy in selective laser melted tantalum, *Acta Materialia* 61(12) (2013) 4657-4668.

- [74] A.A. Antonysamy, J. Meyer, P.B. Prangnell, Effect of build geometry on the β -grain structure and texture in additive manufacture of Ti6Al4V by selective electron beam melting, *Materials Characterization* 84 (2013) 153-168.
- [75] M. Glavicic, P. Kobryn, T. Bieler, S. Semiatin, A method to determine the orientation of the high-temperature beta phase from measured EBSD data for the low-temperature alpha phase in Ti-6Al-4V, *Materials Science and Engineering: A* 346(1-2) (2003) 50-59.
- [76] C. Cayron, B. Artaud, L. Briottet, Reconstruction of parent grains from EBSD data, *Materials Characterization* 57(4-5) (2006) 386-401.
- [77] G. Welsch, R. Boyer, E. Collings, *Materials properties handbook: titanium alloys*, ASM international 1993.
- [78] A.M. Beese, B.E. Carroll, Review of Mechanical Properties of Ti-6Al-4V Made by Laser-Based Additive Manufacturing Using Powder Feedstock, *JOM* 68(3) (2015) 724-734.
- [79] G. Lütjering, Influence of processing on microstructure and mechanical properties of (α + β) titanium alloys, *Materials Science and Engineering: A* 243(1-2) (1998) 32-45.
- [80] T. Mitchell, *Machine learning*, (1997).
- [81] M. Kumke, H. Watschke, P. Hartogh, A.-K. Bavendiek, T. Vietor, Methods and tools for identifying and leveraging additive manufacturing design potentials, *International Journal on Interactive Design and Manufacturing (IJIDeM)* 12(2) (2018) 481-493.
- [82] T. DebRoy, H. Wei, J. Zuback, T. Mukherjee, J. Elmer, J. Milewski, A.M. Beese, A. Wilson-Heid, A. De, W. Zhang, Additive manufacturing of metallic components—process, structure and properties, *Progress in Materials Science* 92 (2018) 112-224.
- [83] J. Li, X. Zhou, M. Brochu, N. Provatas, Y.F. Zhao, Solidification Microstructure Simulation of Ti-6Al-4V in Metal Additive Manufacturing: A Review, *Additive Manufacturing* (2019) 100989.
- [84] T. DebRoy, T. Mukherjee, H. Wei, J. Elmer, J. Milewski, Metallurgy, mechanistic models and machine learning in metal printing, *Nature Reviews Materials* 6(1) (2021) 48-68.
- [85] T. DebRoy, T. Mukherjee, H. Wei, J. Elmer, J. Milewski, Metallurgy, mechanistic models and machine learning in metal printing, *Nature Reviews Materials* (2020) 1-21.
- [86] M. Bessa, R. Bostanabad, Z. Liu, A. Hu, D.W. Apley, C. Brinson, W. Chen, W.K. Liu, A framework for data-driven analysis of materials under uncertainty: Countering the curse of dimensionality, *Computer Methods in Applied Mechanics and Engineering* 320 (2017) 633-667.
- [87] J. Smith, W. Xiong, W. Yan, S. Lin, P. Cheng, O.L. Kafka, G.J. Wagner, J. Cao, W.K. Liu, Linking process, structure, property, and performance for metal-based additive manufacturing: computational approaches with experimental support, *Computational Mechanics* 57(4) (2016) 583-610.
- [88] W. Yan, S. Lin, O.L. Kafka, C. Yu, Z. Liu, Y. Lian, S. Wolff, J. Cao, G.J. Wagner, W.K. Liu, Modeling process-structure-property relationships for additive manufacturing, *Frontiers of Mechanical Engineering* 13(4) (2018) 482-492.
- [89] K.M. Kanti, P.S. Rao, Prediction of bead geometry in pulsed GMA welding using back propagation neural network, *Journal of materials processing technology* 200(1-3) (2008) 300-305.
- [90] F. Karimzadeh, A. Ebnonnasir, A. Foroughi, Artificial neural network modeling for evaluating of epitaxial growth of Ti6Al4V weldment, *Materials Science and Engineering: A* 432(1-2) (2006) 184-190.
- [91] I. Ghosh, S.K. Das, N. Chakraborty, An artificial neural network model to characterize porosity defects during solidification of A356 aluminum alloy, *Neural Computing and Applications* 25(3-4) (2014) 653-662.

- [92] T. Krol, C. Seidel, M. Zaeh, Prioritization of process parameters for an efficient optimisation of additive manufacturing by means of a finite element method, *Procedia CIRP* 12 (2013) 169-174.
- [93] S. Suryakumar, K. Karunakaran, A. Bernard, U. Chandrasekhar, N. Raghavender, D. Sharma, Weld bead modeling and process optimization in hybrid layered manufacturing, *Computer-Aided Design* 43(4) (2011) 331-344.
- [94] J. Xiong, G. Zhang, J. Hu, L. Wu, Bead geometry prediction for robotic GMAW-based rapid manufacturing through a neural network and a second-order regression analysis, *Journal of Intelligent Manufacturing* 25(1) (2014) 157-163.
- [95] A. Garg, K. Tai, M. Savalani, Formulation of bead width model of an SLM prototype using modified multi-gene genetic programming approach, *The International Journal of Advanced Manufacturing Technology* 73(1-4) (2014) 375-388.
- [96] D. Ding, Z. Pan, D. Cuiuri, H. Li, S. van Duin, N. Larkin, Bead modelling and implementation of adaptive MAT path in wire and arc additive manufacturing, *Robotics and Computer-Integrated Manufacturing* 39 (2016) 32-42.
- [97] V.V. Semak, Melt pool dynamics during laser welding, *Journal of Physics D: Applied Physics* 28 (1995) 2443.
- [98] S. David, S. Babu, J. Vitek, Welding: Solidification and microstructure, *JOM* 55(6) (2003) 14-20.
- [99] G.C. Sosso, J. Chen, S.J. Cox, M. Fitzner, P. Pedevilla, A. Zen, A. Michaelides, Crystal Nucleation in Liquids: Open Questions and Future Challenges in Molecular Dynamics Simulations, *Chemical Reviews* 116(12) (2016) 7078-116.
- [100] Y. Shibuta, S. Sakane, E. Miyoshi, S. Okita, T. Takaki, M. Ohno, Heterogeneity in homogeneous nucleation from billion-atom molecular dynamics simulation of solidification of pure metal, *Nature Communications* 8(1) (2017) 10.
- [101] S. David, S. Babu, Microstructure modeling in weld metal, Oak Ridge National Lab., 1995.
- [102] M. Rappaz, S.A. David, J.M. Vitek, L.A. Boatner, Analysis of solidification microstructures in Fe-Ni-Cr single-crystal welds, *Metallurgical Transactions A* 21(6) (1990) 1767-1782.
- [103] T. Zacharia, J. Vitek, J. Goldak, T. DebRoy, M. Rappaz, H. Bhadeshia, Modeling of fundamental phenomena in welds, *Modelling and Simulation in Materials Science and Engineering* 3(2) (1995) 265.
- [104] T. DebRoy, S. David, Physical processes in fusion welding, *Reviews of Modern Physics* 67(1) (1995) 85.
- [105] S. David, J. Vitek, Correlation between solidification parameters and weld microstructures, *International Materials Reviews* 34(1) (1989) 213-245.
- [106] M. Griffith, M. Schlienger, L. Harwell, M. Oliver, M. Baldwin, M. Ensz, M. Essien, J. Brooks, C. Robino, e.J. Smugeresky, Understanding thermal behavior in the LENS process, *Materials & Design* 20(2-3) (1999) 107-113.
- [107] M. Gouge, P. Michaleris, *Thermo-mechanical Modeling of Additive Manufacturing*, Butterworth-Heinemann 2017.
- [108] D.M. Keicher, J.E. Smugeresky, The laser forming of metallic components using particulate materials, *JOM* 49(5) (1997) 51-54.
- [109] L.E. Murr, S.M. Gaytan, D.A. Ramirez, E. Martinez, J. Hernandez, K.N. Amato, P.W. Shindo, F.R. Medina, R.B. Wicker, Metal Fabrication by Additive Manufacturing Using Laser and Electron Beam Melting Technologies, *Journal of Materials Science & Technology* 28(1) (2012) 1-14.

- [110] Y.C. Shin, N. Bailey, C. Katinas, W. Tan, Predictive modeling capabilities from incident powder and laser to mechanical properties for laser directed energy deposition, *Computational Mechanics* 61(5) (2018) 617-636.
- [111] J.C. Heigel, P. Michaleris, E.W. Reutzel, Thermo-mechanical model development and validation of directed energy deposition additive manufacturing of Ti-6Al-4V, *Additive Manufacturing* 5 (2015) 9-19.
- [112] A. Zinoviev, O. Zinovieva, V. Ploshikhin, V. Romanova, R. Balokhonov, Evolution of grain structure during laser additive manufacturing. Simulation by a cellular automata method, *Materials & Design* 106 (2016) 321-329.
- [113] J. Zhang, F. Liou, W. Seufzer, K. Taminger, A coupled finite element cellular automaton model to predict thermal history and grain morphology of Ti-6Al-4V during direct metal deposition (DMD), *Additive Manufacturing* 11 (2016) 32-39.
- [114] A. Rai, M. Markl, C. Körner, A coupled Cellular Automaton-Lattice Boltzmann model for grain structure simulation during additive manufacturing, *Computational Materials Science* 124 (2016) 37-48.
- [115] S.M. Thompson, L. Bian, N. Shamsaei, A. Yadollahi, An overview of Direct Laser Deposition for additive manufacturing; Part I: Transport phenomena, modeling and diagnostics, *Additive Manufacturing* 8 (2015) 36-62.
- [116] M.J. Aziz, T. Kaplan, Continuous growth model for interface motion during alloy solidification, *Acta Metallurgica* 36(8) (1988) 2335-2347.
- [117] N. Ahmad, A. Wheeler, W.J. Boettinger, G.B. McFadden, Solute trapping and solute drag in a phase-field model of rapid solidification, *Physical Review E* 58(3) (1998) 3436.
- [118] T. Pinomaa, N. Provatas, Quantitative phase field modeling of solute trapping and continuous growth kinetics in quasi-rapid solidification, *Acta Materialia* 168 (2019) 167-177.
- [119] D. Danilov, B. Nestler, Phase-field modelling of solute trapping during rapid solidification of a Si-As alloy, *Acta Materialia* 54(18) (2006) 4659-4664.
- [120] P. Galenko, E. Abramova, D. Jou, D. Danilov, V. Lebedev, D.M. Herlach, Solute trapping in rapid solidification of a binary dilute system: a phase-field study, *Physical Review E* 84(4) (2011) 041143.
- [121] X. Li, W. Tan, Numerical investigation of effects of nucleation mechanisms on grain structure in metal additive manufacturing, *Computational Materials Science* 153 (2018) 159-169.
- [122] J.A. Koepf, M.R. Gotterbarm, M. Markl, C. Körner, 3D multi-layer grain structure simulation of powder bed fusion additive manufacturing, *Acta Materialia* 152 (2018) 119-126.
- [123] O. Zinovieva, A. Zinoviev, V. Ploshikhin, Three-dimensional modeling of the microstructure evolution during metal additive manufacturing, *Computational Materials Science* 141 (2018) 207-220.
- [124] J. Koepf, D. Soldner, M. Ramsperger, J. Mergheim, M. Markl, C. Körner, Numerical microstructure prediction by a coupled finite element cellular automaton model for selective electron beam melting, *Computational Materials Science* 162 (2019) 148-155.
- [125] S. Chen, G. Guillemot, C.-A. Gandin, Three-dimensional cellular automaton-finite element modeling of solidification grain structures for arc-welding processes, *Acta Materialia* 115 (2016) 448-467.
- [126] R. Shi, S. Khairallah, T.W. Heo, M. Rolchigo, J.T. McKeown, M.J. Matthews, Integrated Simulation Framework for Additively Manufactured Ti-6Al-4V: Melt Pool Dynamics, Microstructure, Solid-State Phase Transformation, and Microelastic Response, *JOM* (2019) 1-16.

- [127] A.R. Dezfoli, W.S. Hwang, W.C. Huang, T.W. Tsai, Determination and controlling of grain structure of metals after laser incidence: Theoretical approach, *Scientific Reports* 7 (2017) 41527.
- [128] C. Gu, Y. Wei, X. Zhan, Y. Li, A three-dimensional cellular automaton model of dendrite growth with stochastic orientation during the solidification in the molten pool of binary alloy, *Science and Technology of Welding and Joining* 22(1) (2016) 47-58.
- [129] W. Yan, Y. Lian, C. Yu, O.L. Kafka, Z. Liu, W.K. Liu, G.J. Wagner, An integrated process–structure–property modeling framework for additive manufacturing, *Computer Methods in Applied Mechanics and Engineering* 339 (2018) 184-204.
- [130] M. Rolchigo, R. LeSar, Application of alloy solidification theory to cellular automata modeling of near-rapid constrained solidification, *Computational Materials Science* 163 (2019) 148-161.
- [131] A. Rai, H. Helmer, C. Körner, Simulation of grain structure evolution during powder bed based additive manufacturing, *Additive Manufacturing* 13 (2017) 124-134.
- [132] O. Lopez-Botello, U. Martinez-Hernandez, J. Ramírez, C. Pinna, K. Mumtaz, Two-dimensional simulation of grain structure growth within selective laser melted AA-2024, *Materials & Design* 113 (2017) 369-376.
- [133] H. Yin, S.D. Felicelli, Dendrite growth simulation during solidification in the LENS process, *Acta Materialia* 58(4) (2010) 1455-1465.
- [134] Z.J. Wang, S. Luo, H.W. Song, W.D. Deng, W.Y. Li, Simulation of Microstructure during Laser Rapid Forming Solidification Based on Cellular Automaton, *Mathematical Problems in Engineering* 2014 (2014) 1-9.
- [135] H. Yin, S.D. Felicelli, L. Wang, Simulation of a dendritic microstructure with the lattice Boltzmann and cellular automaton methods, *Acta Materialia* 59(8) (2011) 3124-3136.
- [136] T. Carozzani, C.-A. Gandin, H. Dignonnet, M. Bellet, K. Zaidat, Y. Fautrelle, Direct Simulation of a Solidification Benchmark Experiment, *Metallurgical and Materials Transactions A* 44(2) (2012) 873-887.
- [137] C.A. Gandin, J.L. Desbiolles, M. Rappaz, P. Thevoz, A three-dimensional cellular automation-finite element model for the prediction of solidification grain structures, *Metallurgical and Materials Transactions A* 30(12) (1999) 3153-3165.
- [138] T. Carozzani, H. Dignonnet, C.-A. Gandin, 3D CAFE modeling of grain structures: application to primary dendritic and secondary eutectic solidification, *Modelling and Simulation in Materials Science and Engineering* 20(1) (2011) 015010.
- [139] C.A. Gandin, T. Carozzani, H. Dignonnet, S. Chen, G. Guillemot, Direct Modeling of Structures and Segregations Up to Industrial Casting Scales, *JOM* 65(9) (2013) 1122-1130.
- [140] W. Wang, P.D. Lee, M. Mclean, A model of solidification microstructures in nickel-based superalloys: predicting primary dendrite spacing selection, *Acta Materialia* 51(10) (2003) 2971-2987.
- [141] L. Nastac, Numerical modeling of solidification morphologies and segregation patterns in cast dendritic alloys, *Acta Materialia* 47(17) (1999) 4253-4262.
- [142] X. Zhan, Y. Wei, Z. Dong, Cellular automaton simulation of grain growth with different orientation angles during solidification process, *Journal of Materials Processing Technology* 208(1-3) (2008) 1-8.
- [143] B. Radhakrishnan, S.B. Gorti, J.A. Turner, R. Acharya, J.A. Sharon, A. Staroselsky, T. El-Wardany, Phase Field Simulations of Microstructure Evolution in IN718 using a Surrogate Ni–Fe–Nb Alloy during Laser Powder Bed Fusion, *Metals* 9(1) (2019) 14.

- [144] S. Ghosh, K. McReynolds, J.E. Guyer, D. Banerjee, Simulation of temperature, stress and microstructure fields during laser deposition of Ti-6Al-4V, *Modelling and Simulation in Materials Science and Engineering* 26(7) (2018) 075005.
- [145] L.X. Lu, N. Sridhar, Y.W. Zhang, Phase field simulation of powder bed-based additive manufacturing, *Acta Materialia* 144 (2018) 801-809.
- [146] R. Acharya, J.A. Sharon, A. Staroselsky, Prediction of microstructure in laser powder bed fusion process, *Acta Materialia* 124 (2017) 360-371.
- [147] T. Keller, G. Lindwall, S. Ghosh, L. Ma, B.M. Lane, F. Zhang, U.R. Kattner, E.A. Lass, J.C. Heigel, Y. Idell, Application of finite element, phase-field, and CALPHAD-based methods to additive manufacturing of Ni-based superalloys, *Acta Materialia* 139 (2017) 244-253.
- [148] D. Liu, Y. Wang, Mesoscale Multi-Physics Simulation of Solidification in Selective Laser Melting Process Using a Phase Field and Thermal Lattice Boltzmann Model, *ASME 2017 International Design Engineering Technical Conferences and Computers and Information in Engineering Conference*, American Society of Mechanical Engineers, 2017, pp. V001T02A027-V001T02A027.
- [149] X. Wang, P. Liu, Y. Ji, Y. Liu, M. Horstemeyer, L. Chen, Investigation on microsegregation of IN718 alloy during additive manufacturing via integrated phase-field and finite-element modeling, *Journal of Materials Engineering and Performance* 28(2) (2019) 657-665.
- [150] L. Wu, J. Zhang, Phase Field Simulation of Dendritic Solidification of Ti-6Al-4V During Additive Manufacturing Process, *JOM* 70(10) (2018) 2392-2399.
- [151] J. Kundin, A. Ramazani, U. Prah, C. Haase, Microstructure Evolution of Binary and Multicomponent Manganese Steels During Selective Laser Melting: Phase-Field Modeling and Experimental Validation, *Metallurgical and Materials Transactions A* 50(4) (2019) 2022-2040.
- [152] N. Xue, Y. Ren, X. Ren, N. Ren, Q. Lin, Q. Wang, K. Qin, Phase field simulation of dendritic growth of copper films irradiated by ultrashort laser pulses, *Computational Materials Science* 148 (2018) 60-68.
- [153] T. Takaki, T. Shimokawabe, M. Ohno, A. Yamanaka, T. Aoki, Unexpected selection of growing dendrites by very-large-scale phase-field simulation, *Journal of Crystal Growth* 382 (2013) 21-25.
- [154] C. Yang, Q. Xu, B. Liu, GPU-accelerated three-dimensional phase-field simulation of dendrite growth in a nickel-based superalloy, *Computational Materials Science* 136 (2017) 133-143.
- [155] P. Steinmetz, J. Hötzer, M. Kellner, A. Genau, B. Nestler, Study of pattern selection in 3D phase-field simulations during the directional solidification of ternary eutectic Al-Ag-Cu, *Computational Materials Science* 148 (2018) 131-140.
- [156] T. Gong, Y. Chen, Y. Cao, X. Kang, D. Li, Fast simulations of a large number of crystals growth in centimeter-scale during alloy solidification via nonlinearly preconditioned quantitative phase-field formula, *Computational Materials Science* 147 (2018) 338-352.
- [157] N. Bergeon, D. Tournet, L. Chen, J.-M. Debierre, R. Guérin, A. Ramirez, B. Billia, A. Karma, R. Trivedi, Spatiotemporal dynamics of oscillatory cellular patterns in three-dimensional directional solidification, *Physical Review Letters* 110(22) (2013) 226102.
- [158] A. Karma, D. Tournet, Atomistic to continuum modeling of solidification microstructures, *Current Opinion in Solid State and Materials Science* 20(1) (2016) 25-36.
- [159] A.J. Clarke, D. Tournet, Y. Song, S.D. Imhoff, P.J. Gibbs, J.W. Gibbs, K. Fezzaa, A. Karma, Microstructure selection in thin-sample directional solidification of an Al-Cu alloy: In situ X-ray imaging and phase-field simulations, *Acta Materialia* 129 (2017) 203-216.

- [160] R.-w. Geng, J. Du, Z.-y. Wei, G.-x. Zhao, Simulation of microstructure evolution in fused-coating additive manufacturing based on phase field approach, *China Foundry* 14(5) (2017) 346-352.
- [161] D. Tournet, A. Karma, Growth competition of columnar dendritic grains: A phase-field study, *Acta Materialia* 82 (2015) 64-83.
- [162] T. Takaki, M. Ohno, T. Shimokawabe, T. Aoki, Two-dimensional phase-field simulations of dendrite competitive growth during the directional solidification of a binary alloy bicrystal, *Acta Materialia* 81 (2014) 272-283.
- [163] H. Humadi, N. Ofori-Opoku, N. Provatas, J.J. Hoyt, Atomistic Modeling of Solidification Phenomena Using the Phase-Field-Crystal Model, *JOM* 65(9) (2013) 1103-1110.
- [164] W.J. Boettinger, J.A. Warren, C. Beckermann, A. Karma, Phase-Field Simulation of Solidification, *Annual Review of Materials Research* 32(1) (2002) 163-194.
- [165] S.G. Kim, W.T. Kim, Phase-field modeling of rapid solidification, *Materials Science and Engineering: A* 304 (2001) 281-286.
- [166] D. Tournet, Y. Song, A.J. Clarke, A. Karma, Grain growth competition during thin-sample directional solidification of dendritic microstructures: A phase-field study, *Acta Materialia* 122 (2017) 220-235.
- [167] N. Warnken, D. Ma, A. Drevermann, R.C. Reed, S.G. Fries, I. Steinbach, Phase-field modelling of as-cast microstructure evolution in nickel-based superalloys, *Acta Materialia* 57(19) (2009) 5862-5875.
- [168] H. Wei, G. Knapp, T. Mukherjee, T. DebRoy, Three-dimensional grain growth during multi-layer printing of a nickel-based alloy Inconel 718, *Additive Manufacturing* (2018).
- [169] Z. Yang, S. Sista, J. Elmer, T. DebRoy, Three dimensional Monte Carlo simulation of grain growth during GTA welding of titanium, *Acta Materialia* 48(20) (2000) 4813-4825.
- [170] H.L. Wei, J.W. Elmer, T. DebRoy, Three-dimensional modeling of grain structure evolution during welding of an aluminum alloy, *Acta Materialia* 126 (2017) 413-425.
- [171] H. Wei, J. Elmer, T. DebRoy, Crystal growth during keyhole mode laser welding, *Acta Materialia* 133 (2017) 10-20.
- [172] H.L. Wei, J. Mazumder, T. DebRoy, Evolution of solidification texture during additive manufacturing, *Scientific Reports* 5 (2015) 16446.
- [173] H.L. Wei, J.W. Elmer, T. DebRoy, Origin of grain orientation during solidification of an aluminum alloy, *Acta Materialia* 115 (2016) 123-131.
- [174] D. Raabe, *Computational Materials Science*, WILEY-VCH1998.
- [175] S. Wolfram, Cellular automata as models of complexity, *Nature* 311(5985) (1984) 419.
- [176] S. Wolfram, Computation theory of cellular automata, *Communications in mathematical physics* 96(1) (1984) 15-57.
- [177] Y. Zhuang, W. LI, H. Wang, S. Hong, H. Wang, A Bibliographic Review of Cellular Automaton Publications in the Last 50 Years, *Journal of Cellular Automata* 12(6) (2017) 475-492.
- [178] L.O. Chua, L. Yang, Cellular neural networks: Applications, *IEEE Transactions on circuits and systems* 35(10) (1988) 1273-1290.
- [179] D. Raabe, Cellular Automata in Materials Science with Particular Reference to Recrystallization Simulation, *Annual Review of Materials Research* 32(1) (2002) 53-76.
- [180] D. Raabe, R.C. Becker, Coupling of a crystal plasticity finite-element model with a probabilistic cellular automaton for simulating primary static recrystallization in aluminium, *Modelling and Simulation in Materials Science and Engineering* 8(4) (2000) 445.

- [181] D. Raabe, L. Hantcherli, 2D cellular automaton simulation of the recrystallization texture of an IF sheet steel under consideration of Zener pinning, *Computational Materials Science* 34(4) (2005) 299-313.
- [182] D. Raabe, Mesoscale simulation of recrystallization textures and microstructures, *Advanced Engineering Materials* 3(10) (2001) 745.
- [183] D. Raabe, Introduction of a scalable three-dimensional cellular automaton with a probabilistic switching rule for the discrete mesoscale simulation of recrystallization phenomena, *Philosophical Magazine A* 79(10) (1999) 2339-2358.
- [184] M. Qian, Z.X. Guo, Cellular automata simulation of microstructural evolution during dynamic recrystallization of an HY-100 steel, *Materials Science and Engineering: A* 365(1-2) (2004) 180-185.
- [185] T. Zhang, S. Lu, Y. Wu, G. Hai, Optimization of deformation parameters of dynamic recrystallization for 7055 aluminum alloy by cellular automaton, *Transactions of Nonferrous Metals Society of China* 27(6) (2017) 1327-1337.
- [186] C. Gu, Y. Wei, F. Yu, X. Liu, L. She, Cellular Automaton Study of Hydrogen Porosity Evolution Coupled with Dendrite Growth During Solidification in the Molten Pool of Al-Cu Alloys, *Metallurgical and Materials Transactions A* 48(9) (2017) 4314-4323.
- [187] M. Picasso, C. Marsden, J. Wagniere, A. Frenk, M. Rappaz, A simple but realistic model for laser cladding, *Metallurgical and Materials Transactions B* 25(2) (1994) 281-291.
- [188] C.A. Gandin, M. Rappaz, R. Tintillier, 3-dimensional simulation of the grain formation in investment castings, *Metallurgical and Materials Transactions A* 25(3) (1994) 629-635.
- [189] C.A. Gandin, M. Rappaz, A coupled finite element-cellular automaton model for the prediction of dendritic grain structures in solidification processes, *Acta metallurgica et materialia* 42(7) (1994) 2233-2246.
- [190] C.A. Gandin, M. Rappaz, A 3D cellular automaton algorithm for the prediction of dendritic grain growth, *Acta Materialia* 45(5) (1997) 2187-2195.
- [191] M. Rappaz, Modeling and characterization of grain structures and defects in solidification, *Current Opinion in Solid State and Materials Science* 20(1) (2016) 37-45.
- [192] L. Yuan, P.D. Lee, A new mechanism for freckle initiation based on microstructural level simulation, *Acta Materialia* 60(12) (2012) 4917-4926.
- [193] J.Z. Yi, P.D. Lee, T.C. Lindley, T. Fukui, Statistical modeling of microstructure and defect population effects on the fatigue performance of cast A356-T6 automotive components, *Materials Science and Engineering: A* 432(1-2) (2006) 59-68.
- [194] H.B. Dong, P.D. Lee, Simulation of the columnar-to-equiaxed transition in directionally solidified Al-Cu alloys, *Acta Materialia* 53(3) (2005) 659-668.
- [195] N. D'souza, P. Jennings, X. Yang, P. Lee, M. McLean, H. Dong, Seeding of single-crystal superalloys—Role of constitutional undercooling and primary dendrite orientation on stray-grain nucleation and growth, *Metallurgical and Materials Transactions B* 36(5) (2005) 657-666.
- [196] R.C. Atwood, P.D. Lee, Simulation of the three-dimensional morphology of solidification porosity in an aluminium-silicon alloy, *Acta Materialia* 51(18) (2003) 5447-5466.
- [197] P. Lee, A. Chirazi, D. See, Modeling microporosity in aluminum-silicon alloys: a review, *Journal of light metals* 1(1) (2001) 15-30.
- [198] A. Shterenlikht, L. Margetts, Three-dimensional cellular automata modelling of cleavage propagation across crystal boundaries in polycrystalline microstructures, *Proceedings of the Royal Society A: Mathematical, Physical and Engineering Sciences* 471(2177) (2015) 20150039-20150039.

- [199] W. Kurz, B. Giovanola, R. Trivedi, Theory of microstructural development during rapid solidification, *Acta Metallurgica* 34(5) (1986) 823-830.
- [200] D.C. Tsai, W.S. Hwang, A three dimensional cellular automaton model for the prediction of solidification morphologies of brass alloy by horizontal continuous casting and its experimental verification, *Materials transactions* 52(4) (2011) 787-794.
- [201] J. Warren, Dendritic crystals: rule of thumb breaks down, *Nature materials* 5(8) (2006) 595.
- [202] T. Haxhimali, A. Karma, F. Gonzales, M. Rappaz, Orientation selection in dendritic evolution, *Nature materials* 5(8) (2006) 660.
- [203] I. Steinbach, Why Solidification? Why Phase-Field?, *JOM* 65(9) (2013) 1096-1102.
- [204] L. Wang, N. Wang, N. Provatas, Liquid channel segregation and morphology and their relation with hot cracking susceptibility during columnar growth in binary alloys, *Acta Materialia* 126 (2017) 302-312.
- [205] V. Fallah, A. Korinek, N. Ofori-Opoku, B. Raeisia, M. Gallerneault, N. Provatas, S. Esmaili, Atomic-scale pathway of early-stage precipitation in Al–Mg–Si alloys, *Acta Materialia* 82 (2015) 457-467.
- [206] N. Provatas, J. Dantzig, B. Athreya, P. Chan, P. Stefanovic, N. Goldenfeld, K. Elder, Using the phase-field crystal method in the multi-scale modeling of microstructure evolution, *JOM* 59(7) (2007) 83-90.
- [207] K. Ahmed, T. Allen, A. El-Azab, Phase field modeling for grain growth in porous solids, *Journal of Materials Science* 51(3) (2015) 1261-1277.
- [208] S. Hu, L. Chen, Solute segregation and coherent nucleation and growth near a dislocation—a phase-field model integrating defect and phase microstructures, *Acta Materialia* 49(3) (2001) 463-472.
- [209] T.T. Nguyen, J. Yvonnet, Q.Z. Zhu, M. Bornert, C. Chateau, A phase field method to simulate crack nucleation and propagation in strongly heterogeneous materials from direct imaging of their microstructure, *Engineering Fracture Mechanics* 139 (2015) 18-39.
- [210] N. Provatas, K. Elder, *Phase-field methods in materials science and engineering*, John Wiley & Sons 2011.
- [211] G. Nash, M. Glicksman, Capillary-limited steady-state dendritic growth—I. Theoretical development, *Acta Metallurgica* 22(10) (1974) 1283-1290.
- [212] J. Langer, H. Müller-Krumbhaar, Theory of dendritic growth—I. Elements of a stability analysis, *Acta Metallurgica* 26(11) (1978) 1681-1687.
- [213] D.A. Kessler, J. Koplik, H. Levine, Pattern formation far from equilibrium: the free space dendritic crystal, *Patterns, Defects and Microstructures in Nonequilibrium Systems*, Springer 1987, pp. 1-11.
- [214] J.-J. Xu, *Interfacial Wave Theory of Pattern Formation in Solidification*, Springer Series in Synergetics (Complexity) (2017) 16-21.
- [215] J.W. Cahn, J.E. Hilliard, Spinodal decomposition: A reprise, *Acta Metallurgica* 19(2) (1971) 151-161.
- [216] J.W. Cahn, J.E. Hilliard, Free energy of a nonuniform system. I. Interfacial free energy, *The Journal of Chemical Physics* 28(2) (1958) 258-267.
- [217] L.P. Gor'kov, Microscopic derivation of the Ginzburg-Landau equations in the theory of superconductivity, *Sov. Phys. JETP* 9(6) (1959) 1364-1367.
- [218] L.Q. Chen, Phase-field models for microstructure evolution, *Annual review of materials research* 32(1) (2002) 113-140.

- [219] L. Feng, B. Jia, C. Zhu, G. An, R. Xiao, X. Feng, Multi-phase field simulation of grain growth in multiple phase transformations of a binary alloy, *Chinese Physics B* 26(8) (2017).
- [220] K. Elder, M. Katakowski, M. Haataja, M. Grant, Modeling elasticity in crystal growth, *Physical Review Letters* 88(24) (2002) 245701.
- [221] N. Metropolis, A.W. Rosenbluth, M.N. Rosenbluth, A.H. Teller, E. Teller, Equation of State Calculations by Fast Computing Machines, *The Journal of Chemical Physics* 21(6) (1953) 1087-1092.
- [222] M. Anderson, D. Srolovitz, G. Grest, P. Sahni, Computer simulation of grain growth—I. Kinetics, *Acta Metallurgica* 32(5) (1984) 783-791.
- [223] O. Ivasishin, S. Shevchenko, S. Semiatin, Implementation of Exact Grain-Boundary Geometry Into a 3D Monte-Carlo (POTTS) Model for Microstructure Evolution (Preprint), AIR FORCE RESEARCH LAB WRIGHT-PATTERSON AFB OH MATERIALS AND MANUFACTURING DIRECTORATE, 2008.
- [224] J.K. Mason, J. Lind, S.F. Li, B.W. Reed, M. Kumar, Kinetics and anisotropy of the Monte Carlo model of grain growth, *Acta Materialia* 82 (2015) 155-166.
- [225] S. Mishra, T. DebRoy, Measurements and Monte Carlo simulation of grain growth in the heat-affected zone of Ti–6Al–4V welds, *Acta Materialia* 52(5) (2004) 1183-1192.
- [226] P.E. Goins, E.A. Holm, The Material Point Monte Carlo model: A discrete, off-lattice method for microstructural evolution simulations, *Computational Materials Science* 124 (2016) 411-419.
- [227] L. Wang, P. Clancy, Kinetic Monte Carlo simulation of the growth of polycrystalline Cu films, *Surface Science* 473(1-2) (2001) 25-38.
- [228] L. Zhang, A.D. Rollett, T. Bartel, D. Wu, M.T. Lusk, A calibrated Monte Carlo approach to quantify the impacts of misorientation and different driving forces on texture development, *Acta Materialia* 60(3) (2012) 1201-1210.
- [229] D. Tourret, A. Karma, Multi-scale needle-network model of complex dendritic microstructure formation, *IOP Conference Series: Materials Science and Engineering* 33 (2012).
- [230] B. Derrida, V. Hakim, Needle models of Laplacian growth, *Physical Review A* 45(12) (1992) 8759.
- [231] D. Tourret, A. Karma, Multiscale dendritic needle network model of alloy solidification, *Acta Materialia* 61(17) (2013) 6474-6491.
- [232] D. Tourret, A. Karma, A. Clarke, P. Gibbs, S. Imhoff, Three-dimensional Dendritic Needle Network model with application to Al-Cu directional solidification experiments, *IOP Conference Series: Materials Science and Engineering*, IOP Publishing, 2015, p. 012082.
- [233] L. Costa, R. Vilar, T. Reti, A.M. Deus, Rapid tooling by laser powder deposition: Process simulation using finite element analysis, *Acta Materialia* 53(14) (2005) 3987-3999.
- [234] M.N. Ahsan, A.J. Pinkerton, An analytical–numerical model of laser direct metal deposition track and microstructure formation, *Modelling and Simulation in Materials Science and Engineering* 19(5) (2011) 055003.
- [235] L.E. Criales, Y.M. Arısoy, B. Lane, S. Moylan, A. Donmez, T. Özel, Laser powder bed fusion of nickel alloy 625: experimental investigations of effects of process parameters on melt pool size and shape with spatter analysis, *International Journal of Machine Tools and Manufacture* 121 (2017) 22-36.
- [236] B. Regaard, S. Kaierle, W. Schulz, A. Moalem, Advantages of coaxial external illumination for monitoring and control of laser materials processing, *International Congress on Applications of Lasers & Electro-Optics*, Laser Institute of America, 2018, p. 2307.

- [237] C.L.A. Leung, S. Marussi, R.C. Atwood, M. Towrie, P.J. Withers, P.D. Lee, In situ X-ray imaging of defect and molten pool dynamics in laser additive manufacturing, *Nature Communications* 9(1) (2018) 1355.
- [238] R. Cunningham, C. Zhao, N. Parab, C. Kantzos, J. Pauza, K. Fezzaa, T. Sun, A.D. Rollett, Keyhole threshold and morphology in laser melting revealed by ultrahigh-speed x-ray imaging, *Science* 363(6429) (2019) 849-852.
- [239] A. Pineau, G. Guillemot, D. Tournet, A. Karma, C.-A. Gandin, Growth competition between columnar dendritic grains—Cellular automaton versus phase field modeling, *Acta Materialia* 155 (2018) 286-301.
- [240] A. Choudhury, K. Reuther, E. Wesner, A. August, B. Nestler, M. Rettenmayr, Comparison of phase-field and cellular automaton models for dendritic solidification in Al–Cu alloy, *Computational Materials Science* 55 (2012) 263-268.
- [241] A. Suárez, M.J. Tobar, A. Yáñez, I. Pérez, J. Sampedro, V. Amigó, J.J. Candel, Modeling of phase transformations of Ti6Al4V during laser metal deposition, *Physics Procedia* 12 (2011) 666-673.
- [242] C.C. Murgau, R. Pederson, L.E. Lindgren, A model for Ti–6Al–4V microstructure evolution for arbitrary temperature changes, *Modelling and Simulation in Materials Science and Engineering* 20(5) (2012) 055006.
- [243] E. Salsi, M. Chiumenti, M. Cervera, Modeling of microstructure evolution of ti6al4v for additive manufacturing, *Metals* 8(8) (2018) 633.
- [244] J. Irwin, E.W. Reutzel, P. Michaleris, J. Keist, A.R. Nassar, Predicting microstructure from thermal history during additive manufacturing for Ti-6Al-4V, *Journal of Manufacturing Science and Engineering* 138(11) (2016) 111007.
- [245] Q. Zhang, J. Xie, Z. Gao, T. London, D. Griffiths, V. Oancea, A metallurgical phase transformation framework applied to SLM additive manufacturing processes, *Materials & Design* 166 (2019) 107618.
- [246] G. Vastola, G. Zhang, Q.X. Pei, Y.W. Zhang, Modeling the microstructure evolution during additive manufacturing of Ti6Al4V: a comparison between electron beam melting and selective laser melting, *JOM* 68(5) (2016) 1370-1375.
- [247] C. Baykasoglu, O. Akyildiz, D. Candemir, Q. Yang, A.C. To, Predicting microstructure evolution during directed energy deposition additive manufacturing of Ti-6Al-4V, *Journal of Manufacturing Science and Engineering* 140(5) (2018) 051003.
- [248] L.E. Lindgren, A. Lundbäck, M. Fisk, R. Pederson, J. Andersson, Simulation of additive manufacturing using coupled constitutive and microstructure models, *Additive Manufacturing* 12 (2016) 144-158.
- [249] W. Liu, J. DuPont, Effects of melt-pool geometry on crystal growth and microstructure development in laser surface-melted superalloy single crystals: Mathematical modeling of single-crystal growth in a melt pool (part I), *Acta materialia* 52(16) (2004) 4833-4847.
- [250] H. Wei, G. Knapp, T. Mukherjee, T. DebRoy, Three-dimensional grain growth during multi-layer printing of a nickel-based alloy Inconel 718, *Addit. Manuf.* (2018).
- [251] Y. Lee, M. Nordin, S.S. Babu, D.F. Farson, Effect of fluid convection on dendrite arm spacing in laser deposition, *Metall. Mater. Trans. B* 45(4) (2014) 1520-1529.
- [252] M.F. Zhu, S.Y. Lee, C.P. Hong, Modified cellular automaton model for the prediction of dendritic growth with melt convection, *Phys. Rev. E: Stat., Nonlinear, Soft Matter Phys.* 69(6 Pt 1) (2004) 061610.

- [253] C. Cayron, ARPGE: a computer program to automatically reconstruct the parent grains from electron backscatter diffraction data, *Journal of applied crystallography* 40(6) (2007) 1183-1188.
- [254] S. Kou, *Welding metallurgy*, New Jersey, USA (2003) 431-446.
- [255] A. Wagner, B. Shollock, M. McLean, Grain structure development in directional solidification of nickel-base superalloys, *Materials Science and Engineering: A* 374(1-2) (2004) 270-279.
- [256] J.H. Martin, B.D. Yahata, J.M. Hundley, J.A. Mayer, T.A. Schaedler, T.M. Pollock, 3D printing of high-strength aluminium alloys, *Nature* 549(7672) (2017) 365.
- [257] D. Walton, u.B. Chalmers, The origin of the preferred orientation in the columnar zone of ingots, *Transactions of the American Institute of Mining and Metallurgical Engineers* 215(3) (1959) 447-457.
- [258] J. Li, M. Sage, X. Guan, M. Brochu, Y.F. Zhao, Machine Learning-Enabled Competitive Grain Growth Behavior Study in Directed Energy Deposition Fabricated Ti6Al4V, *JOM* 72(1) (2020) 458-464.
- [259] Q. Meng, X. Zhou, J. Li, Z. Cui, Y. Wang, H. Zhang, Z. Li, C. Qiu, High-throughput laser fabrication of Ti-6Al-4V alloy: Part I. Numerical investigation of dynamic behavior in molten Pool, *Journal of Manufacturing Processes* 59 (2020) 509-522.
- [260] S. Ghosh, A. Karma, M. Plapp, S. Akamatsu, S. Bottin-Rousseau, G. Faivre, Influence of morphological instability on grain boundary trajectory during directional solidification, *Acta Materialia* 175 (2019) 214-221.
- [261] H. Wei, G. Knapp, T. Mukherjee, T. DebRoy, Three-dimensional grain growth during multi-layer printing of a nickel-based alloy Inconel 718, *Additive Manufacturing* 25 (2019) 448-459.
- [262] A. Papapetrou, Untersuchungen über dendritisches Wachstum von Kristallen, *Zeitschrift für Kristallographie-Crystalline Materials* 92(1-6) (1935) 89-130.
- [263] M. Bermingham, D. StJohn, M. Easton, L. Yuan, M. Dargusch, Revealing the Mechanisms of Grain Nucleation and Formation During Additive Manufacturing, *JOM* (2020).
- [264] M. Gäumann, C. Bezencon, P. Canalis, W. Kurz, Single-crystal laser deposition of superalloys: processing–microstructure maps, *Acta materialia* 49(6) (2001) 1051-1062.
- [265] Y.-Y. Zhu, H.-B. Tang, Z. Li, C. Xu, B. He, Solidification behavior and grain morphology of laser additive manufacturing titanium alloys, *Journal of Alloys and Compounds* 777 (2019) 712-716.
- [266] C. Todaro, M. Easton, D. Qiu, D. Zhang, M. Bermingham, E. Lui, M. Brandt, D. StJohn, M. Qian, Grain structure control during metal 3D printing by high-intensity ultrasound, *Nature Communications* 11(1) (2020) 1-9.
- [267] J. Zhou, Y. Yang, Y. Yang, D.S. Kim, A. Yuan, X. Tian, C. Ophus, F. Sun, A.K. Schmid, M. Nathanson, Observing crystal nucleation in four dimensions using atomic electron tomography, *Nature* 570(7762) (2019) 500-503.
- [268] B. Böttger, J. Eiken, I. Steinbach, Phase field simulation of equiaxed solidification in technical alloys, *Acta materialia* 54(10) (2006) 2697-2704.
- [269] M. Fanfoni, M. Tomellini, The johnson-mehl-avrami-kohnogorov model: a brief review, *Il Nuovo Cimento D* 20(7) (1998) 1171-1182.
- [270] B.A. Szost, S. Terzi, F. Martina, D. Boisselier, A. Prytuliak, T. Pirling, M. Hofmann, D.J. Jarvis, A comparative study of additive manufacturing techniques: Residual stress and microstructural analysis of CLAD and WAAM printed Ti–6Al–4V components, *Materials & Design* 89 (2016) 559-567.

APPENDIX I: Lists of publications

Journal papers

1. **Li, Jinghao**, Xianglin Zhou, Mathieu Brochu, Nikolas Provatas, and Yaoyao Fiona Zhao. "Solidification microstructure simulation of Ti-6Al-4V in metal additive manufacturing: A review." *Additive Manufacturing* 31 (2020): 100989.
2. **Li, Jinghao**, Manuel Sage, Xiaoyi Guan, Mathieu Brochu, and Yaoyao Fiona Zhao. "Machine Learning-Enabled Competitive Grain Growth Behavior Study in Directed Energy Deposition Fabricated Ti6Al4V." *JOM* 72, no. 1 (2020): 458-464.
3. **Li, Jinghao**, Xianglin Zhou, Qingbo Meng, Mathieu Brochu, Nejib Chekir, J. J. Sixsmith, J. Y. Hascoët, and Yaoyao Fiona Zhao. "Deterministic modeling of solidification microstructure formation in directed energy deposition fabricated Ti6Al4V." *Additive Manufacturing* 46 (2021): 102182.
4. Nong, X. D., X. L. Zhou, Y. D. Wang, L. Yu, and **J. H. Li**. "Effects of geometry, location, and direction on microstructure and mechanical properties of 15–5PH stainless steel fabricated by directed energy deposition." *Materials Science and Engineering: A* (2021): 141587.
5. Qi, Hang, Xianglin Zhou, **Jinghao Li**, Yunfei Hu, and Lianghui Xu. "Performance Testing and Rapid Solidification Behavior of Stainless Steel Powders Prepared by Gas Atomization." *Materials* 14, no. 18 (2021): 5188.
6. Wang, Jibing, Xianglin Zhou, and **Jinghao Li**. "Evolution of microstructures and properties of SLM-manufactured Cu–15Ni–8Sn alloy during heat treatment." *Additive Manufacturing* 37 (2021): 101599.
7. Hu, Yunfei, Xiang-lin Zhou, Liang-hui Xu, **Jing-hao Li**, Hang Qi, Kai-ping Du, Yao Ma, and Yue-guang Yu. "Motion and Solidification Behavior Analysis of Fe-Based Alloy Droplets During Gas Atomization." *Metallurgical and Materials Transactions B* 51, no. 6 (2020): 2935-2945.
8. Meng, Qingbo, Xianglin Zhou, **Jinghao Li**, Ziqi Cui, Yandong Wang, Hailong Zhang, Zhuo Li, and Chunlei Qiu. "High-throughput laser fabrication of Ti-6Al-4V alloy: Part I. Numerical investigation of dynamic behavior in molten Pool." *Journal of Manufacturing Processes* 59 (2020): 509-522.
9. Xu, Lianghui, Xianglin Zhou, **Jinghao Li**, Yunfei Hu, Hang Qi, Wei Wen, Kaiping Du, Yao Ma, and Yueguang Yu. "Numerical simulations of molten breakup behaviors of a de laval-type nozzle, and the effects of atomization parameters on particle size distribution." *Processes* 8, no. 9 (2020): 1027.

10. Nong, X. D., X. L. Zhou, **J. H. Li**, Y. D. Wang, Y. F. Zhao, and M. Brochu. "Selective laser melting and heat treatment of precipitation hardening stainless steel with a refined microstructure and excellent mechanical properties." *Scripta Materialia* 178 (2020): 7-12.
11. Wang, Jibing, X. L. Zhou, **Jinghao Li**, Mathieu Brochu, and Yaoyao Fiona Zhao. "Microstructures and properties of SLM-manufactured Cu-15Ni-8Sn alloy." *Additive Manufacturing* 31 (2020): 100921.
12. Zhang, Mina, Xianglin Zhou, Dafeng Wang, Wuzhi Zhu, **Jinghao Li**, and Yaoyao Fiona Zhao. "AlCoCuFeNi high-entropy alloy with tailored microstructure and outstanding compressive properties fabricated via selective laser melting with heat treatment." *Materials Science and Engineering: A* 743 (2019): 773-784.

Publication under review or revision

1. **Jinghao Li**, Mathieu Brochu and Yaoyao Fiona Zhao. " Microstructural features in metallic parts made by AM " (book chapter of *Quality Analysis for Additive Manufactured Metals, under review of editor*).
2. **Jinghao Li**, Xianglin Zhou, Mathieu Brochu and Yaoyao Fiona Zhao. "Crystal Introducing Mechanism in Laser Wire Directed Energy Deposition Fabricated Ti6Al4V" (Submitting to *Additive Manufacturing*)

Peer-reviewed conference papers

1. **J. H. Li**, Z. B. Luo, X. Y. Guan, X. L. Zhou, M. Brochu, Y. F. Zhao*. A Novel Microstructure Simulation Model for Direct Energy Deposition Process. 2018 Annual Int'l Solid Freeform Fabrication Symposium. Hilton Austin Hotel, Austin, TX, United States Aug 13-15, 2018
2. **J. H. Li**, M. Sage, X. L. Zhou, M. Brochu, Y. F. Zhao*. Machine Learning for Competitive Grain Growth Behavior in Additive Manufacturing. The 14th World Conference on Titanium. La Cite Nantes Events Center, Pays de la Loire, Nantes, France June 10-14, 2019

APPENDIX II: Abstract of major journal publications

Journal publication D1

Additive Manufacturing 31 (2020) 100989



Contents lists available at ScienceDirect

Additive Manufacturing

journal homepage: www.elsevier.com/locate/addma



Solidification microstructure simulation of Ti-6Al-4V in metal additive manufacturing: A review



Jinghao Li^a, Xianglin Zhou^{b,*}, Mathieu Brochu^c, Nikolas Provatas^d, Yaoyao Fiona Zhao^{b,*}

^a Department of Mechanical Engineering, McGill University, Montreal, Quebec, H2A0C3, Canada

^b State Key Laboratory for Advance Metals and Materials, University of Science and Technology Beijing, 10083, China

^c Department of Mining and Materials Engineering, McGill University, Montreal, Quebec, H3A0C5, Canada

^d Department of Physics, McGill University, Montreal, Quebec, H3A 2T8, Canada

ARTICLE INFO

Keywords:
Additive manufacturing
Microstructure
Simulation
Solidification

ABSTRACT

Metal additive manufacturing (MAM) technology is now changing the pattern of the high-end manufacturing industry, among which microstructure simulation gradually shows its importance and attracts many research interests. As the simulation targets, this paper summarizes the unique microstructure characteristics in MAM fabricated parts, Ti-6Al-4V as an example. Further discussions are focused on the development of solidification microstructure simulation methods as well as their capacity and applicability on MAM. Finally, the difficulties and suggested future research topics in MAM microstructure simulation are addressed.

1. Introduction

Additive manufacturing (also known as 3D printing) refers to a process by which digital 3D design is fabricated in a layer by layer fashion. Metal additive manufacturing (MAM) methods based on powder, wire, sliced metals and alloys are famous for their flexibility, efficiency, and accuracy [1]. Due to the nature of MAM process, which adds material only at the desired place, the lead-time and material waste are reduced to a relatively low level. More importantly, since the tooling is no longer needed, MAM unlocks a significant amount of constraints for the designers to design products with complex geometry [2]. The technical features of MAM make it suitable for industries with small batch and high complexity part geometry, especially hollow structures and complex curved surfaces. There are already relatively mature applications at present in the area of aerospace, re-manufacturing, medical industries and so on. MAM technologies can be roughly divided into two categories, namely, direct energy deposition (DED) and powder bed fusion (PBF). There are several technologies under each category branded by different manufacturers [3,4]. MAM technologies based on different types of high energy beam (laser and electron beam) are operated under different environment: vacuum environment is needed for the electron beam to travel through and laser can propagate in an inert atmosphere. Also, the cooling rate (product of thermal gradient and solidification rate) in MAM can changes from 10^3 K/s in DED to 10^5 K/s in PBF. The different energy sources, process parameters as well as the cooling conditions in MAM technologies lead

to significant differences among the resultant melt pool geometries, which will further influence the fabricated microstructures. Consider the melt pool size alone can change from hundreds of micrometers in PBF to several millimeters in DED. Uncertainties in the process-structure-property (PSP) linkage are restricting the development and application of MAM techniques [5]. Thus, recognizing the interplay between PSP linkage in MAM is crucial for quality control and development of this technology. Modeling approaches and numerical simulations are the ideal tools to fill the gap by saving time and experimental costs [6]. These models enable mechanical property predictions from the process and material parameters and serve as a guideline for design, process control, and optimization.

Among the limited number of printable alloy systems including Ti-based, Fe-based, Al-based, Ni-based and Co-based alloys, MAM technologies inevitably lead to unique microstructural characteristics w.r.t. traditional forming and manufacturing methods. These differences are inevitable results of the melting, solidification and cooling condition provided by MAM, and the material properties including nucleation, grain growth behaviors and solid phase transformation, hence the different resultant mechanical properties and defects. In the past few decades, titanium alloys were found to be suitable for additive manufacturing and attracted a lot of research interest [7]. In this paper, the Ti-6Al-4V alloy is selected to explain the common microstructural characteristics in MAM, including columnar grains, nucleation and epitaxial grain growth behavior as well as the solid phase composition. These characteristics are also frequently observed in other printable

* Corresponding authors.

E-mail addresses: bxixi@gmail.com (X. Zhou), yaoyao.zhao@mcgill.ca (Y.F. Zhao).

<https://doi.org/10.1016/j.addma.2019.100989>

Received 5 July 2019; Received in revised form 28 November 2019; Accepted 4 December 2019

Available online 06 December 2019

2214-8604/© 2019 Elsevier B.V. All rights reserved.



Machine Learning-Enabled Competitive Grain Growth Behavior Study in Directed Energy Deposition Fabricated Ti6Al4V

JINGHAO LI,¹ MANUEL SAGE,¹ XIAOYI GUAN,¹ MATHIEU BROCHU,²
and YAOYAO FIONA ZHAO ^{1,3}

1.—Department of Mechanical Engineering, McGill University, Montreal, QC H2A0C3, Canada.
2.—Department of Mining and Materials Engineering, McGill University, Montreal, QC H3A0C5,
Canada. 3.—e-mail: yaoyao.zhao@mcgill.ca

Directed energy deposition (DED) of titanium alloys is a rapidly developing technology because of its flexibility in freeform fabrication and remanufacturing. However, the uncertainties of a solidification microstructure during the deposition process are limiting its development. This article presents an artificial neural network (ANN) to investigate the relation between the grain boundary tilt angle and three causative factors, namely the thermal gradient, crystal orientation and Marangoni effect. A series of wire feedstock DED, optical microscope and electron backscatter diffraction experiments was carried out under the Taguchi experimental design to gather the training and testing data for the ANN. Compared with conventional microstructure simulation methods, the strategy and ANN model developed in this work were demonstrated to be a valid way to describe the competitive grain growth behavior in DED fabricated Ti6Al4V. They can be deployed to achieve a quantitative microstructure simulation and extended to other polycrystal material solidification processes.

INTRODUCTION

Titanium alloys are famous for their light weight, high strength, and heat and corrosion resistant properties.¹ In the past few decades, titanium and its alloys were found to be suitable for metal additive manufacturing (MAM). Until now, only a limited number of commercial alloys has been used in MAM, among which Ti6Al4V has attracted lots of research efforts. Directed energy deposition (DED) is an important branch within MAM techniques. It refers to a process that focuses high energy beams to melt metal materials exactly where they are being deposited and directly fabricate the designed structure. DED is now widely applied in the remanufacturing industry; however, uncertainties regarding the microstructure, texture and mechanical properties of DED fabricated Ti6Al4V are restricting its development and application.²

It has been observed in research that dendritic column grains grow approximately along the buildup direction in DED fabricated Ti6Al4V.^{3–11} They can grow through multiple layers of the fabricated part. This is an overall result of the

cooling condition, nucleation and epitaxial grain growth behavior.¹² In most cases, grains with their preferred growing directions aligned with the thermal gradient will kill their adjacent grains and even develop to the millimeter level after the competitive grain growth. This will become a serious problem and degrade the mechanical properties of the part built. Cracks have the priority to propagate along these grain boundaries, which results in anisotropic mechanical properties in as-built condition. An example is the change of ductility in different loading directions.^{13–15}

Recognizing the interplay between the material deposition phenomena and resultant microstructure in MAM is crucial for quality control. Modeling approaches and numerical simulations on multiple scales are ideal tools to save time and experimental cost compared with traditional trial and error methods. These models enable mechanical property predictions from process and material parameters and serve as a guideline for further property optimization. Currently, three methods are used in the area of microstructure simulation for MAM, namely cellular automata (CA), phase field (PF) and



Research Paper



Deterministic modeling of solidification microstructure formation in directed energy deposition fabricated Ti6Al4V

Jinghao Li^a, Xianglin Zhou^{b,*}, Qingbo Meng^b, Mathieu Brochu^c, Nejib Chekir^{c,d}, J. J. Sixsmith^d, J.Y. Hascoët^e, Yaoyao Zhao^{a,*}

^a Department of Mechanical Engineering, McGill University, Montreal, Québec H2A 0C3, Canada

^b State Key Laboratory for Advanced Metals and Materials, University of Science and Technology, Beijing 10083, China

^c Department of Mining and Materials Engineering, McGill University, Montreal, Québec H3A 2B2, Canada

^d Libardi Automation Inc., Dundas, Ontario L9H 7K4, Canada

^e Institut de Recherche en Génie Civil et Mécanique (GeM), UMR CNRS 6183 Ecole Centrale de Nantes, Nantes 44321, France

ARTICLE INFO

Keywords:
Additive manufacturing
Microstructure
Modeling
Solidification

ABSTRACT

Metal additive manufacturing (MAM) technology is now widely applied in the manufacturing and remanufacturing industry, among which microstructure simulation gradually shows its importance. Traditional solidification microstructure simulation methods all have their merits as well as drawbacks when applied in MAM cases. In this work, a deterministic solidification microstructure model, named "invasion model", is established to avoid the essential defects of traditional methods. This model focuses on the interaction between the neighboring bi-crystals instead of simulating the growth kinetics of each columnar grain or deriving the field form of variables. Within a bi-crystal system, the grain boundary tilt from thermal gradient direction is understood as a transient invasion behavior of one grain to another, and the competitive grain growth behavior along the buildup process of MAM is a summary of all the invasions in bi-crystal systems. To fill the gaps in the rapid solidification theory, a database recording the anisotropic growth effect under a rapid directional solidification condition was established with the help of an artificial neural network (ANN). Wire feed directed energy deposition (DED) fabricated Ti6Al4V thin-wall samples with full dendritic columnar grains (prior beta) are used as a benchmark to test the validation of the novel simulation model. The grain geometrical structure of reconstructed prior β grains along the build-up direction has a good agreement with the simulation result. The model can also be applied to other cases of MAM or combine with various models to achieve real-time as-solidified crystallographic feature prediction when it meets the scope of application.

1. Introduction

Metal additive manufacturing (MAM) technology is now changing the pattern of the high-end manufacturing industry, among which MAM fabricated Ti6Al4V has been by far the most extensively investigated material and attracts a lot of research interests. MAM has a unique ability to create complex components, such as hollow and complex curved surfaces that may otherwise be impossible to other manufacturing methods. However, uncertainties in MAM such as chemical composition, microstructure, texture, and mechanical properties are restricting its development and application. Recognizing the interplay between material deposition phenomena and process factors in AM is crucial for component quality control. Modeling approaches and

numerical simulations on multiple length scales and timescales are the ideal tools to save time and experimental costs. These models enable mechanical property predictions from the process and material parameters and serve as a guideline for further property optimization.

Microstructure simulation for MAM is blooming recently as a result of the rapid development of MAM techniques and microstructure simulation methods. Now, there are three methods widely applied to achieve the solidification microstructure simulation for MAM, namely cellular automata (CA), phase-field (PF), and kinetic Monte Carlo (KMC). Among these three methods, CA is the first commercialized method because it is capable to provide the microstructure information in meso- and macro-scale where many practical significances can be found. It has already been used for the MAM cases at a three-

* Corresponding authors.

E-mail addresses: bxixl@ustb.edu.cn (X. Zhou), yaoyao.zhao@mcgill.ca (Y.F. Zhao).

<https://doi.org/10.1016/j.addma.2021.102182>

Received 2 March 2021; Received in revised form 10 June 2021; Accepted 12 July 2021

Available online 27 July 2021

2214-8604/© 2021 Elsevier B.V. All rights reserved.